Fundamental Physics Measurements and the Gamma-Ray Emission of Pulsars and Globular Clusters

LLOYD, SHERIDAN,JAMES

Fundamental Physics Measurements and the Gamma-Ray Emission of Pulsars and Globular Clusters

Sheridan James Lloyd

Abstract

Globular clusters (GCs) with high encounter rates and dense cores favour the production of millisecond pulsars (MSPs) which are gamma-ray sources and are thought to account for GC emission overall. The evidence for this is largely indirect and no detailed spectral comparison between GCs and MSPs has been attempted.

I analyse the gamma-ray emission of 111 GCs, detecting 34 (100 MeV$-$10GeV), with emission from inside the tidal radius. GC luminosity is positively correlated with encounter rate and mass-encounter rate product as expected for MSP emission but uncorrelated with metallicity which is at odds with MSPs being the emission source. Most GCs have a spectrum consistent with MSPs but there are exceptions. I find that GC unresolved diffuse X-ray emission is correlated with GC gamma-ray emission, possibly due to unresolved sources or relativistic electron propulation from MSPs.

I exclude a shock front emission mechanism in Terzan 5. I stack the spectrum of 98 MSPs, which is a good fit of one to two-thirds of GCs, but this fit is uncorrelated with GC characteristics impacting MSP formation. A spectral colour comparison shows GC emission is harder than the MSP model at 4$-$8 GeV, suggesting an additional non-MSP component. I conclude MSPs are important but not the only emission source in GCs.

I derive upper limits to the gamma-ray emission from 17 pulsars, and use a previously reported axion emissivity model, to determine an upper limit to the mass (m_a) of the Axion of 9.6×10^{-3} eV which is strongly temperature dependent. I obtain an upper limit m_a of 8.05×10^{-3} eV by applying an axion power model to magnetars.

Finally, I show that GCs with hard spectral models up to 100 GeV are prime future targets for the Cherenkov Telescope Array and such observations will be vital to determine sources of GC emission.

Fundamental Physics Measurements and the Gamma-Ray Emission of Pulsars and Globular Clusters

Sheridan James Lloyd

Department of Physics
University of Durham

This dissertation is submitted for the degree of
Doctor of Philosophy

Ustinov College January 2021

Table of contents

List of tables

List of figures

Declaration

I hereby declare that except where specific reference is made to the work of others, the contents of this dissertation are original and have not been submitted in whole or in part for consideration for any other degree or qualification in this, or any other university. This dissertation is my own work and contains nothing which is the outcome of work done in collaboration with others, except as specified in the text and Acknowledgements.

Sheridan James Lloyd
January 2021

Statement of Copyright

Acknowledgements

I would like to thank my supervisors and super advisors, Paula Chadwick and Anthony Brown whose unfailing support and guidance over the last four years have made this PhD such an interesting journey and a genuine pleasure.

I would also like to thank Kuver Sinha, of the University of Oklahoma, who generously gave me the opportunity to collaborate on further axion studies in magnetars.

I would like to dedicate this thesis to my wife Uma, without whose generous and loving support this PhD would not have been possible and to my mother Joan, who demonstrates by example, the importance and joy of lifelong learning.

Chapter 1

Introduction

1.1 Interesting Properties of Globular Clusters

The 157 known [124, 125] Galactic globular clusters (GCs) are bound, spherical stellar systems of masses $10^4 - 10^6$ $M_\odot$ [48]. They are old (of the order of 10^{10} years), dust-free satellites of the Milky Way galaxy, characterised by dense cores of 100 to 1000 stars per cubic parsec and consequently high stellar encounter rates. The GC population has a distribution as seen in Fig. 1.1, and their dense stellar environment is seen in Hubble Space Telescope images, such as the well-known GC 47 Tuc (Fig. 1.2). Around two-thirds of the Galactic GCs are at helio-centric distances of 15 kpc or less and 131 GCs have negative declination.

GCs are very important and interesting objects for a variety of reasons. Due to their great age and distinct stellar populations, they are probes of galaxy formation and evolution with two distinct GC populations recognised: the metal-poor, "blue" colour population (metallicity [Fe/H] peak ~ -1.5), thought to be accreted onto the Milky Way Galaxy from satellite galaxies and the metal-rich, "red" colour population (metallicity [Fe/H] peak ~ -0.5), thought to have formed in-situ with the Milky Way [232].

GCs may also have formed within DM sub-halos and *N*-body modelling can reproduce some feature of GC systems such as the scaling of GC number with galaxy-halo virial mass and the highly-clustered nature of GCs today [85]. Some GCs also have tidal tails, aligned in the direction of the Galactic centre and its gravitational potential [245] while GC proper-motions allow an estimate of Galactic mass and the mass and shape of the Galactic dark matter (DM) halo [223].

The dense cores of GCs may also favour the creation of a central intermediate mass black hole (IMBH) of mass $10^3 - 10^4$ $M_\odot$, which, if found, would confirm IMBHs as an

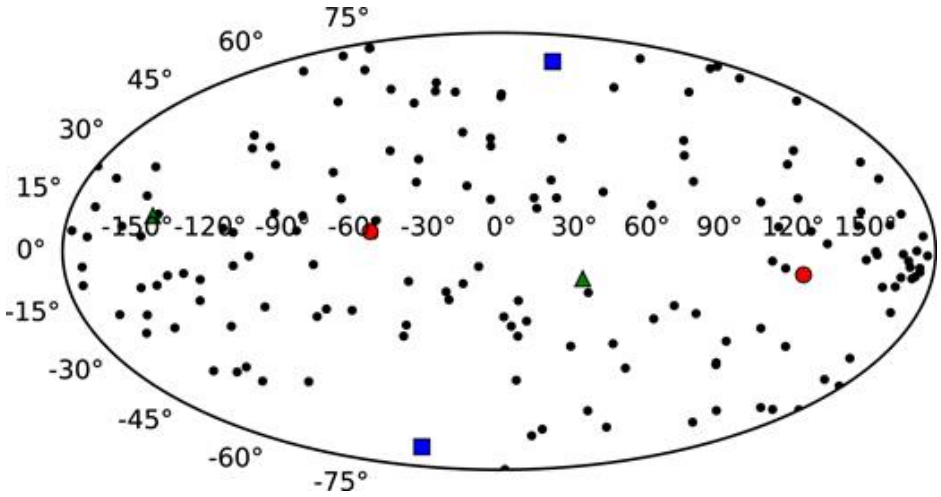

Fig. 1.1 Globular cluster sky-map, in Galactic co-ordinates, showing distribution of GCs (black dots). The symmetry of the GC distribution, with respect to the Galactic plane, is shown by points marking minor (red circles), intermediate (green triangles), and major (blue squares) axes. Figure taken from taken from [34]

Fig. 1.2 HST image of the globular cluster 47 Tuc (centre) showing the self-contained and dense stellar population. Image taken from hubblesite.org.

astrophysical class in their own right[1]. 47 Tuc may have a central IMBH of 2300 $M_\odot$ based on pulsar acceleration measurements [159] whilst NGC 6624 may have an IMBH of >7500 $M_\odot$ [217]. However, this is not a consensus view, as no electromagnetically active IMBH has been observed in 50 GCs [258] and alternative pulsar models and observations of central surface brightness and velocity dispersion can also account for the proposed IMBHs in GCs [144, 50]. At least 5 GCs are predicted to have a population of $\sim$ 100 BHs, with total mass $\sim$ 1000 $M_\odot$ [269].

GCs can also contain significant numbers of cataclysmic variables (CVs), with 43 CVs detected in 47 Tuc [237], and 18 in Omega Centauri [128], and the mysterious blue-straggler stars [230], bluer and more luminous than the older GC stellar populations. As a consequence of high encounter rates, GCs are noted for hosting low mass X-ray binaries (LMXB) which are possible progenitors to millisecond pulsars (MSPs) [30], recycled pulsars with periods of $<$ 30 ms which arise from binary interactions, where the neutron star is spun up by accreting material from its companion via Roche-lobe overflow. 157 pulsars, 82 of them in binary systems, and predominantly MSPs (with just 9 pulsars with periods $>$ 30 ms), are resolved in 30 GCs[2], with the GCs Terzan 5 and 47 Tuc having the highest number of phase resolved MSPs (38 and 25 respectively).

1.2 Millisecond Pulsar Properties and Evolution

The Australia Telescope National Facility Catalogue (ATNF)[3] lists 389 radio-resolved MSPs (including those in GCs above) of which 234 have companion stars which range in type from ultra-light objects of mass $<$ 0.08 $M_\odot$, to main sequence stars, neutron stars or white dwarves. The MSPs in the ATNF also have weaker magnetic B fields than conventional pulsars ($10^{11}-10^{12}$ G), with 246 having B fields of ($0.45-95.2\times10^8$ G (average 6.5×10^8 G)), due to their greater age, but exhibit fast rotation (normally a feature of younger pulsars), having been spun up by accretion from a companion. Isolated MSPs and MSPs with companions are as expected from an evolutionary scenario where the secondary companion in a compact binary (orbital period $<$ 1 d) is of very low mass ($<$ 0.1 $M_\odot$), and is eventually evaporated by the gamma-ray emission or pulsar wind to leave the primary as an isolated MSP. A dynamical channel is also possible where isolated MSPs in GCs can acquire new companions by an encounter process [91].

[1] During final preparation of this thesis, LIGO and Virgo have observed creation of a 142 $M_\odot$ IMBH [3].
[2] Catalogue of pulsars in globular clusters at http://www.naic.edu/~pfreire/GCpsr.html
[3] ATNF Version 1.63 accessed 2nd Sept 2020 https://www.atnf.csiro.au/research/pulsar/psrcat/

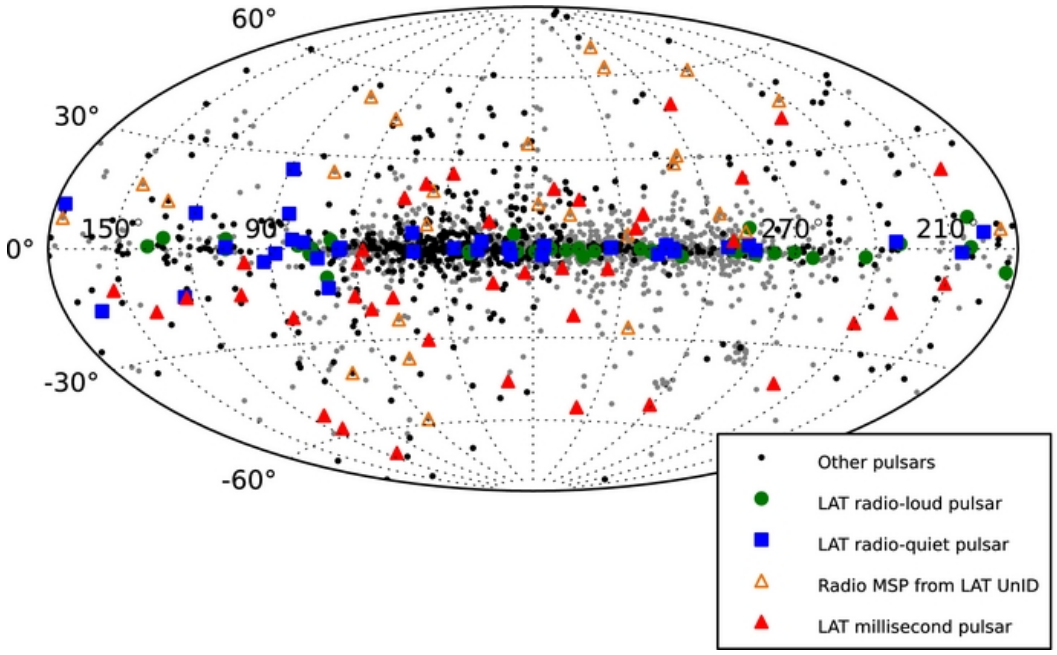

Fig. 1.3 The distribution of gamma-ray detected pulsars in the 2PC, in Galactic co-ordinates showing that MSPs are distributed to higher latitudes than other gamma-ray emitting (LAT) pulsars. Figure taken from [11].

Observations with the Large Area Telescope (LAT) instrument on the space-borne *Fermi* gamma-ray observatory, over a decade ago, established that MSPs are strong gamma-ray sources [6], emitting gamma-rays through curvature radiation and electron / positron pair production cascades in their compact magnetospheres. The 2013 Second *Fermi* Large Area Telescope catalog of Gamma-Ray pulsars, the 2PC [11], based on 3 yrs of observations, lists 40 gamma-ray emitting MSPs, which are spatially distributed off the plane in comparison to other pulsars. (Fig. 1.3).

1.3 The Gamma-Ray Connection of Millisecond pulsars and Globular Clusters

About a quarter of the known MSP population are gamma-ray emitters, and so it is not surprising that *Fermi*-LAT observations of GCs, with their MSP populations, demonstrate that GCs are also gamma-ray emitters, beginning with the detection of 47 Tuc [7], followed by 8 other GCs including Terzan 5, shortly thereafter [10]. The direct connection of MSP and GC gamma-ray emission is shown by the cases NGC 6624 and NGC 6626, where the pulsed emission of a single MSP can account for 100 and 25% of the GC emission respectively

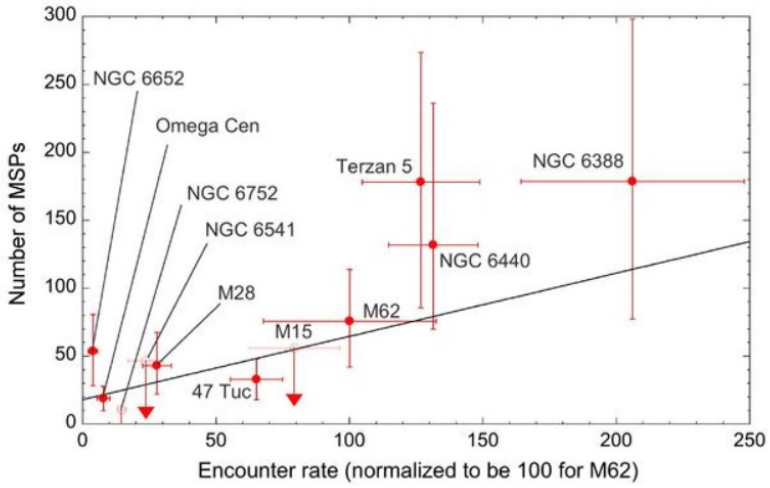

Fig. 1.4 The correlation of millisecond pulsar numbers in globular clusters with encounter rate. The assumed number of MSPs is based on the globular cluster gamma-ray luminosity. Figure taken from [10].

[109, 277]. X-ray and radio observations of the MSP and X-ray transient, IGR J18245–2452, in NGC 6626 also show that it can switch between an X-ray luminous accretion powered mode and an X-ray quiet but radio loud, rotation powered mode demonstrating a state transition and the link between LMXBs and MSPs on observation timescales of a few yrs in GCs. However, more generally, the case for MSPs being sources of GC gamma-ray emission has relied on long-standing qualitative comparisons such as GCs exhibiting MSP-like spectra with cut-offs of a few GeV, the positive correlation of GC gamma-ray luminosity with encounter rate, presumed to encourage MSP formation, and the fact that an average $\dot{E}$ (based on the Galactic field MSP population), combined with a canonical gamma-ray efficiency and the observed GC gamma-ray luminosity, yields MSP numbers in GCs as predicted by other studies (Fig. 1.4, [10]). To-date no spectral comparison has been attempted between the MSP and GC population.

Currently the latest *Fermi*-LAT 4FGL source catalogue lists 30 source associations with GCs, one source that has an alternative association as a GC and two sources that are very bright pulsars in GCs (i.e. NGC 6624 and NGC 6626). In this work I will re-analyse the complete Galactic GC population (whether currently detected in gamma-rays or not) out to the furthest gamma-ray GC detection, using 10.5 yr of *Fermi*-LAT data and the most recent 4FGL source catalogue along with its improved background models. This analysis will be the most up to-date GC gamma-ray survey, yet attempted, and produce the most refined spectra for comparison with MSPs.

1.4 Generic Models of Millisecond Pulsar Emission

At the time of this work, 103 gamma-ray emitting MSPs are listed in the Public List of LAT Detected Gamma-Ray Pulsars[4]. Of these MSPs, 92 have a defined $\dot{E}$ in the range (0.14−220) $\times$ 10^{34} erg s^{-1}, with the distribution skewed towards $\dot{E}$ of a few $\times$ 10^{34} erg s^{-1} (Fig 1.5). This large sample represents a considerable improvement on the 40 MSPs of the 2PC from which a MSP sample was drawn, analysed and stacked, to construct a representative generic model of MSP emission by Xing and Wang [278] and McCann [194]. If the gamma-ray emission from a GC results from the sum of its unresolved MSP population then, (as there is no evidence to suggest that Galactic field MSPs are different from their GC counterparts), it seems reasonable to use these model MSP spectra as an analogue of the ensemble emission of the GC MSP population as a whole, to a first order, and therefore to comment to what extent MSPs are sources of emission in GCs. Surprisingly, this is an approach that has received no attention in the literature with the exception of my contribution to understanding the gamma-ray emission from 47 Tuc [63] in which I used the Xing and Wang model as an analogue for the combined emission of unresolved MSPs, and, on a more qualitative level, where I used the spectral cut-off of the McCann model to comment on MSP-like emission in 6 high latitude Galactic GCs [181]. The creation of my own stacked MSP model by analysing 2.5$\times$ the number of MSPs and employing 7.5 yr of additional event data, combined with the latest 4FGL *Fermi* source catalogue and background model is likely to improve considerably on the existing stacked models and it application to GCs at a detailed spectral level, which has not been attempted previously, is long-overdue.

1.5 Axion and Magnetars

If GCs contain central IMBHs, and reside within DM halos [216], then this could lead to a higher density of DM around the IMBH and enhanced DM annihilation to gamma-rays [139].

Although it is not possible, for reasons of time, to consider specific GC DM candidates or IMBH scenarios in this work, it is natural that given the focus on pulsars elsewhere in this thesis, that I should consider the case of the axion, which may be produced via nucleon-nucleon Bremsstrahlung in *hot* pulsar cores. The hypothetical axion is a Nambu-Goldstone boson, that might be very light and coupled only very weakly to Standard-Model particles. The axion is important in particle-physics as a plausible solution to the strong charge-parity

[4]https://confluence.slac.stanford.edu/display/GLAMCOG/Public+List+of+LAT-Detected+Gamma-Ray+Pulsars, accessed on 2nd April 2019

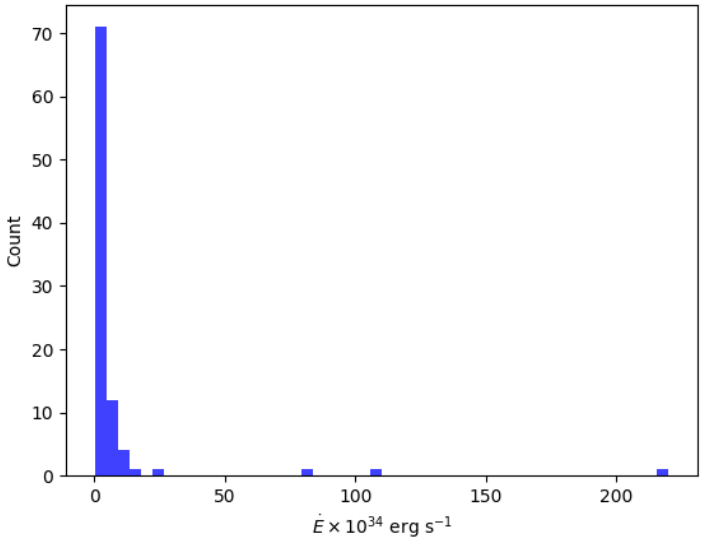

Fig. 1.5 The distribution of $\dot{E}$ for 92 millisecond pulsars in my sample.

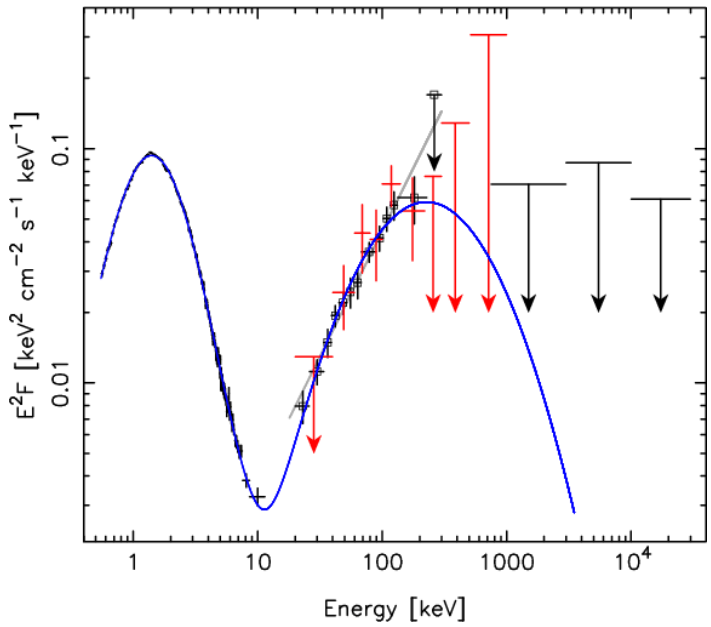

Fig. 1.6 The spectral energy distribution of magnetar 4U 0142+61 showing up-turn of spectrum to 300 keV. Above 300 keV, ULs imply a spectral break. Fluxes and ULs are from instruments XMM-Newton (black), *INTEGRAL*-ISGRI (black open square) and SPI (red) and CGRO-COMPTEL (black ULs above 1 MeV). Figure taken from [97].

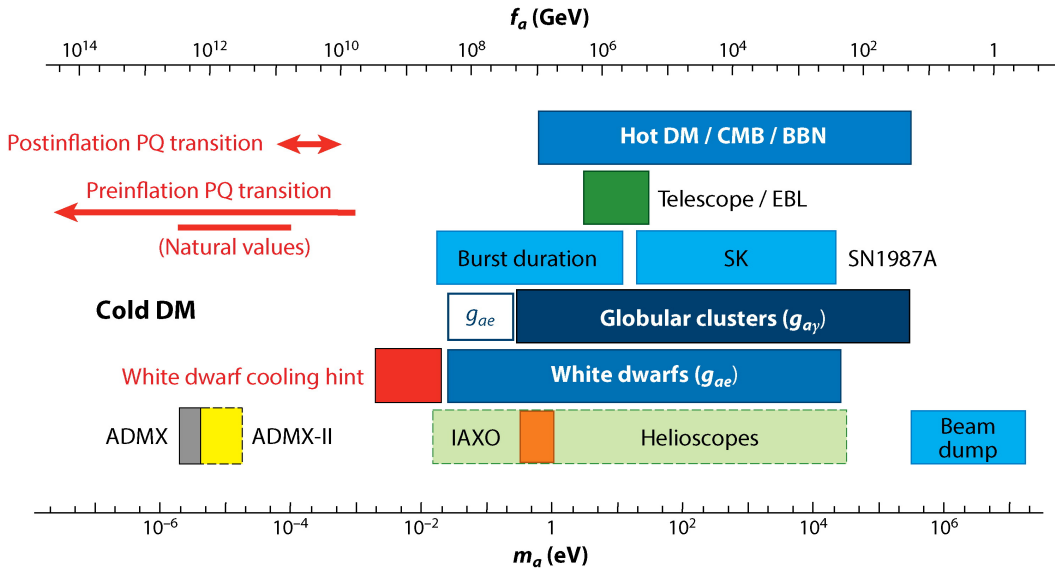

Graham PW, et al. 2015.
Annu. Rev. Nucl. Part. Sci. 65:485–514

Fig. 1.7 The axion mass (m_a) search space with excluded regions from astrophysical and cosmological hints, and indirect search methods. Figure taken from [113].

(CP) problem of quantum chromodynamics (QCD), where expected CP symmetry violations are not observed. The preservation of CP symmetry can be measured experimentally to a high order and to match observations unreasonable fine-tuning of the theory is required. Axions are also of interest to the Cosmology community as a plausible cold dark matter candidate through their non-thermal production in the early Universe [215, 272, 98]. In the current epoch and nearer to home, the axion may also be produced by the Primakoff scattering of thermal photons, in the core of the Sun and be detectable by the CERN Axion Solar Telescope (CAST), a "helioscope", which sets axion-photon coupling constraints based on the conversion of these solar axions into X-ray photons inside a 9 T magnet [80].

The properties of the axion, such as mass (Fig 1.7), or the axion-photon coupling constant, may be constrained through the lifetime of astrophysical phenomena combined with cooling arguments, hints obtained from cosmology, indirect-detection methods or by considering the gamma-ray emission produced by axion radiative-decay or by conversion of the axion to gamma-ray photons in the B field of the star. However, the production of axions in the pulsar core is exceptionally temperature (T_c) dependant (proportional to T_c^6) and as such the pulsar core temperature must be realistic in any determination.

These temperature arguments lead me to consider axion emission from magnetars. Magnetars are a pulsar class with properties diametrically opposed to those of MSPs. Originally

classified as two distinct pulsar types; soft-gamma-ray repeaters and anomalous X-ray pulsars, but now recognised as the same object class, magnetars display persistent high X-ray luminosity which exceeds their spin down power by a factor of > 10. This fact, combined with their slow periods of a few seconds and lack of Doppler modulation of their X-ray pulses, implying a lack of binary companions, excludes an accretion powered rotation interpretation. Rather, it is thought they are powered by the dissipation of their super-strong B fields ($> 10^{14}$ G) (For a recent review see [106]). Magnetars exhibit a spectral up-turn to $\sim$300 keV, above which it is presumed there is a spectral break (e.g. the case of 4U 0142+61 in Fig. 1.6) as no magnetar has been detected in quiescence above this energy [97, 166]. Flare events have been detected with the *Fermi*-Gamma Ray Burst monitor up to 200 keV[82] and magnetars remain undetected by the *Fermi*-LAT [177]. Magnetars exhibit a black-body component flux of $0.3-0.5$ keV which is hotter than a typical rotation powered pulsar and implies an additional heating source. The McGill magnetar catalog lists 23 confirmed magnetars, mostly in the Galactic plane [212].

Magnetars with their hotter cores and stronger B fields which permit significant axion-to-photon conversion, should allow strong constraints to be placed on the axion, while other sources of soft-gamma ray background close to the star are suppressed.

1.6 Structure of this Work

I now describe briefly the structure and content of this thesis. In Chapter 2, I summarise the relevant techniques and instruments used in gamma-ray analysis. I describe the *Fermi*-LAT instrument and show how its angular resolution, sensitivity characteristics, source catalogue and background models are incorporated into the steps of the likelihood analysis method, which is the basis of the gamma-ray analysis in this work. I introduce ground based gamma-ray telescopes (IACTs), which use the atmosphere as a detection medium, and are able to probe higher energies than are possible with the LAT. I describe the next generation gamma-ray telescope, the Cherenkov Telescope Array (CTA), which when completed, is expected to offer an order of magnitude improvement in performance over existing ground-based instruments and I also introduce its prototype software simulation and analysis chain which I shall use to determine if GCs can be detected at higher energies by CTA.

In Chapter 3, I describe the main gamma-ray observations of GCs and MSPs using the *Fermi*-LAT, which establish MSPs as a plausible source of emission in GCs. I summarise the state of MSP emission modelling which can use simple physics input to generate MSP spectra that match observations. I then highlight how the modelling of MSP emission has allowed the spectra of individual GCs to be reproduced (but not, it must be said, predicted

a priori). I also summarise the modest number of IACT GC observations in the *Fermi* era which yield only one detection, Terzan 5. I discuss how the Galactic plane survey of one IACT, H.E.S.S., allows me to set constraints on the gamma-ray emission of 22 GCs above 200 GeV.

Next in Chapter 4, I analyse the well known GC, 47 Tuc, as an exemplar of my method. I produce a refined spectral energy distribution and spectral model for this GC and show that all gamma-ray sources have been accounted for in the analysis using test statistic and residual significance maps. I also demonstrate that 47 Tuc has no significant variability or extended emission.

I then apply the same methods to analyse 111 GCs in Chapter 5 to determine detection significance and fluxes. For the detected GCs, I produce spectral energy distributions (SEDs), and show the best fitted spectral models whose goodness-of-fit I assess. I also check for extended emission and localise the position of the GC emission to determine if the source is within the GC tidal radius. I also investigate using predicted counts maps, whether GC emission above 10 GeV could be due to a shock front mechanism. Then, I compare the gamma-ray luminosity for the detected GCs against GC characteristics which are expected to increase MSP formation and hence luminosity (i.e. stellar encounter rate, metallicity and my own quantity, the mass encounter rate product) to derive best fit relationships. Finally, I also show the connection between diffuse unresolved X-ray emission in GCs and gamma-ray emission and attempt to account for this.

Next, in Chapter 6, in order to assess the correlation between MSP and GC emission at a spectral level, I construct a general spectral model for MSPs using my own stacked spectral analysis of 103 gamma-ray emitting MSPs. I determine if my model is the preferred one in comparison to the stacked MSP models of Xing and Wang [278], and McCann [194], using the Akaike Information Criterion (AIC) statistic and test the goodness-of-fit of my derived MSP model to the stacked flux of the detected MSPs.

In Chapter 7, firstly I consider the spectral shapes of selected GCs to see if they are consistent with an MSP spectrum and assess if they have other gamma-ray counterparts, apart from MSPs. Next, I determine if the gamma-ray emission from 47 Tuc can be accounted for, as arising from its resolved MSP population and using an MSP X-ray / gamma-ray relation. I then choose the preferred stacked MSP model for the GC spectral models, again using the AIC statistic, and determine the goodness-of-fit of that preferred model to the GC SEDs and their spectral models. This allows me to identify two populations of GCs, those that are well fitted by an MSP model, and those that are not and then to determine if the distribution of GC characteristics relevant to MSP formation are different in these GC populations. Next I consider detailed spectral flux characteristics of the individual GCs and stacked MSP model

by constructing gamma-ray colours and determining if there is any first order correlation between these colours and GC characteristics relevant to MSP formation. I also use the GC colours to determine if there any systematic difference between GC SEDs and the preferred MSP model which might indicate other components of emission apart from MSPs. I predict through simulations whether the GC spectral models derived in this work will result in CTA detections, when extrapolated to TeV energies.

I examine axion production from pulsars in Chapter 8 as an exemplar of setting constraints on a dark matter candidate through gamma-ray observations. I firstly improve a previously published analysis which set constraints on the UL axion mass by analysis of UL gamma-ray emission arising from a radiative axion decay model. I analyse 17 gamma-ray dark pulsars and determine UL gamma-ray emission which I relate to the radiative decay model and derive an UL axion mass (m_a). I then assess whether the pulsar core temperature assumed in the model is appropriate and determine the axion emissivity that would result from more plausible temperatures. I also consider an alternative power model for axion production and determine the range of UL m_a obtained across a range of temperature and axion-to-photon conversion probabilities. I then apply this power model to the case of magnetars and through their published soft-gamma ray emission and axion-to-photon conversion probability obtain a value for UL m_a. I briefly list constraints on axion-photon coupling obtained from a collaborative work and suggest future observations with the *Fermi* Gamma Ray Burst Monitor.

Finally, in Chapter 9, I summarise my findings and make suggestions for future work.

Chapter 2

Gamma Ray Observation and Analysis

2.1 Introduction

In this chapter I discuss the detection methods of astrophysical gamma-rays with reference to *Fermi*, which is the definitive spaceborne gamma-ray observatory of the last ten years, and ground-based Cherenkov telescopes which probe higher gamma-ray energies than *Fermi* by using the atmosphere as a detection medium. I introduce the mathematics of the likelihood analysis method which has a long history, ranging from general hypothesis testing to the evaluation and optimisation of source models and their fitting to the gamma-ray observations, thus allowing the spectral form of individual sources to be characterised. I describe the Large Area Telescope or LAT which is the primary science instrument of *Fermi* and show how the characteristics and catalogue models of the *Fermi*-LAT are carried through into the analysis of gamma-ray observations using methods which form the basis of all *Fermi*-LAT analysis in this work. I introduce the Cherenkov Telescope Array (CTA), which is the next generation ground-based gamma-ray observatory and uses the existing technology set of current ground-based telescopes on a larger scale to deliver an order of magnitude increase in sensitivity. Finally I introduce the CTA analysis tools, CTOOLS and GAMMAPY, which allow observations and detections to be simulated from existing spectral models.

2.2 *Fermi* Gamma Ray Observatory

The spaceborne *Fermi* gamma-ray observatory (formerly GLAST), launched 2008 June 11 [5] and still operational at the time of writing, improves on its predecessor EGRET by a factor 6 increase in sensitivity and has made many groundbreaking discoveries such as demonstrating that globular clusters are sources of gamma-ray emission [7, 10], initially

finding a large population of 117 and now 250[1] gamma-ray emitting pulsars [11] and showing that diffuse gamma-ray emission is seen from bubble-like structures which extend on kpc scales above and below the Galactic plane in the eponymous *Fermi* bubbles [246].

Fermi has two science instruments on board: the first is the large area telescope or LAT which measures the energy and directionality of gamma-rays of energies 30 MeV$-$1 TeV in a sky survey mode[2], and the second is the gamma-ray burst monitor (GBM) which measures transient bright gamma-ray phenomena in the sky in the energy range from 8 keV to 40 MeV [5].

In this work my new gamma-ray data analysis has been undertaken using the *Fermi*-LAT rather than the GBM but I have used published GBM flux measurements of magnetars to determine an upper limit (UL) axion mass in Chapter 8. I therefore defer the discussion of the relevant characteristics of the GBM instrument to that point.

A schematic view of the *Fermi*-LAT is shown in Fig. 2.1 showing the main detector sub-systems of the tracker (TKR), calorimeter (CAL) and anti-coincidence detector (ACD) with the TKR/CAL combination arranged in a 4x4 grid to give 16 TKR/CAL stacks. The *Fermi*-LAT is fully described in [20] which deals with the LAT detectors, on-orbit calibration and point spread function (PSF) and I reproduce the main points of relevance to gamma-ray analysis here.

The TKR consists of 18 layers of paired x-y silicon strip detector planes interleaved with tungsten foils (the "paired layer"). The interaction of an incoming gamma-ray with the tungsten foil creates electron-positron pairs whose tracks are determined by the silicon strip detectors and allow the source direction of the gamma ray to be inferred. The TKR can be further divided into a "Front" or "thin" section of 12 paired layers, each layer having a 3% radiation length, and a further "Back" or "thick" section of 4 paired layers which has thicker tungsten providing an 18% radiation length. These Front and Back sections of the TKR are needed to balance the competing and somewhat mutually exclusive aims of good angular resolution and increasing pair conversion probability. Thus, the Front section, by virtue of less particle scattering, has better angular resolution but a poorer pair conversion probability, whereas in the Back section of the TKR the converse is true. Moreover the differing radiation length thicknesses of the Front and Back sections are chosen to ensure that 50% of incident photons convert in the Front section and 50% convert in the Back to mitigate against systematic bias. Below the TKR, the CAL, which is 8.6 radiation lengths, measures

[1] https://confluence.slac.stanford.edu/display/GLAMCOG/Public+List+of+LAT-Detected+Gamma-Ray+Pulsars, list last updated 27$^{\text{th}}$ Dec 2019, accessed on 1$^{\text{st}}$ April 2020

[2] https://fermi.gsfc.nasa.gov/ssc/data/analysis/LAT_caveats.html Caveats About Analyzing LAT Pass 8 (P8R3) Data, accessed on 1$^{\text{st}}$ April 2020

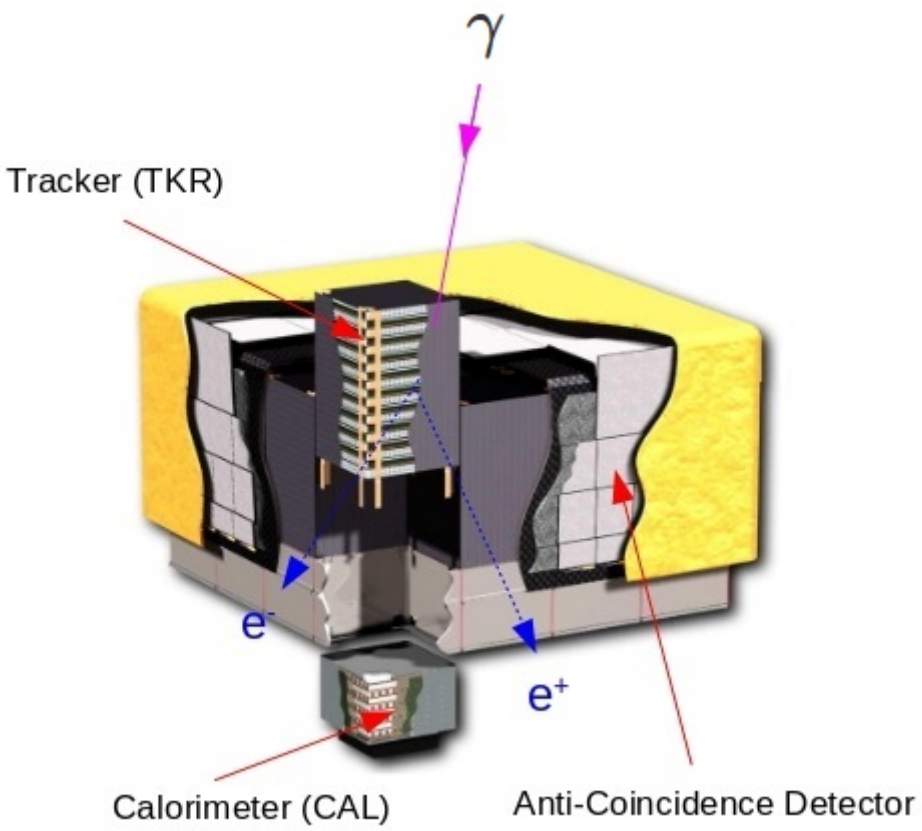

Fig. 2.1 Schematic view of the *Fermi*-Large Area Telescope, which is a pair production instrument. An incoming gamma-ray converts to electron-positron pairs which are detected by silicon strip micro-detectors in the tracker (TKR). The calorimeter (CAL) mainly measures the energy of the charged particles produced and also can detect photons. The anti-coincidence detector (ACD) acts to veto the far more numerous cosmic-ray events which can also trigger the tracker. This schematic image is adapted from [5].

the energy of the incoming gamma-ray. It is comprised of 8 layers with each layer consisting of 12 CsI scintillation crystal "logs" arranged at 90° to the layer above, with each "log" read by photodiodes sensitive to < 1 GeV and < 70 GeV ranges. Finally, the ACD, constructed of plastic scintillator tiles and wavelength shifting fibres read by photomultiplier tubes (PMTs), registers the passage of charged particles and acts as a veto mechanism rejecting more than 99.97% of cosmic rays striking the LAT, which could otherwise be erroneously recorded as an incident gamma-ray in the TKR.

The superior angular resolution of the TKR Front section compared to the Back section can be seen in Fig. 2.2[3] which is a plot of the PSF of the instrument applicable to the latest *Fermi*-LAT event data release (P8R3_V2). It can be seen that Front converting events have the smallest containment angle and hence best angular resolution across all energies, but that the PSF of the Front and Back converting events is not greatly poorer. The best angular resolution for all event types is at high energies of > 30 GeV. It is also clear that analysis at lower energies will be challenging, especially below 100 MeV, because the PSF worsens by a factor of 6 for each decade in energy when going from 10 GeV to 10 MeV. Thus, in the analysis performed in this work, Fig. 2.2 is the key, practical plot for deciding the angular size of the area to be directly analysed in a main "region of interest" or ROI and determining what larger area outside of this ROI should be modelled to account for peripheral bright gamma-ray sources whose emission may affect the analysis due to the PSF of the energy range being considered.

In terms of data collection, the *Fermi*-LAT is primarily used in an all sky survey mode where the entire sky is scanned, giving 30 minutes of livetime on each point in the sky every 2 orbits (approx 3 hrs). The gamma-ray event data from this survey for the whole mission are publicly available for analysis and download as weekly files of .fits format ("Weekly Files") from the *Fermi* Science Support Centre (FSSC)[4].

Since the launch of *Fermi* in 2008, the event data collected by the LAT has undergone revision and re-issue to the public in batched data releases to account for the continuously improving understanding of the LAT instrument performance (determined by simulations) and the astrophysical gamma-ray backgrounds present. The initial data release (which is described but not named in [39]) was PASS 6 which used the event analysis scheme determined prior to launch and applied for the first 3 years of science operations. This was supplanted by PASS 7 [20] on August 1 2011, which re-determined on-orbit PSFs from the first 2 years of observations, calibrated using the on-off pulses of the Vela pulsar, a population of bright active galactic nuclei (AGN) and the emission from the Earth limb and the Galactic Ridge. PASS 7 confirmed the validity of the gamma-ray direction reconstruction used in PASS 6 and increased the effective area of the LAT below 300 MeV. The latest data release, PASS 8 [38], improves TKR event reconstruction and hence PSF by considering the initiation and propagation of electron-positron shower paths as a series of tree structures that can be related to each other. The CAL reconstruction is also improved in PASS 8 by introducing a clustering stage to identify and reject "ghost" pileup events which interfere with the process of matching CAL and TKR events to the incident gamma-ray, potentially causing the rejection of valid

[3] https://www.slac.stanford.edu/exp/glast/groups/canda/lat_Performance.htm *Fermi*-LAT Performance Page, accessed on 2nd April 2020

[4] https://fermi.gsfc.nasa.gov/ssc/data/access/ Currently Available Data Products

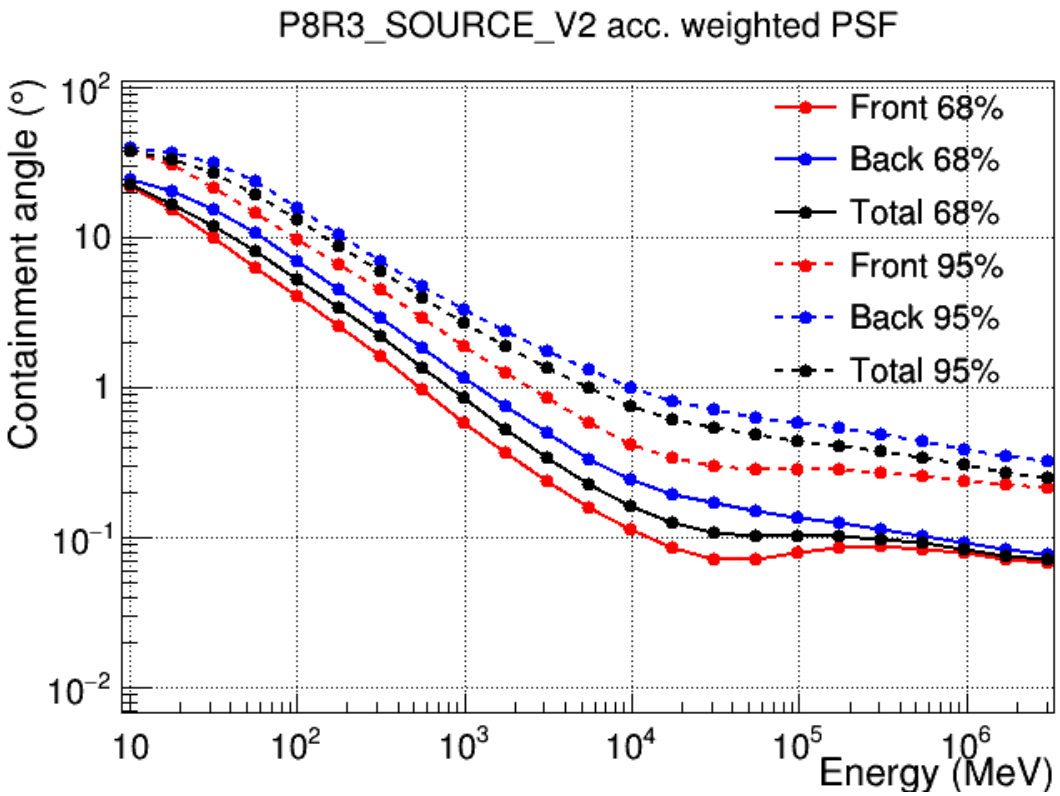

Fig. 2.2 Plot of the LAT PSF of containment angle in degrees vs gamma-ray energy for the cases where either 95% or 68% of the gamma-ray photons from a source are correctly attributed using the Front, Back or both Front and Back (Total) sections of the TKR. The lowest gamma-ray energies have the largest PSF and the Front converting events have the best angular resolution (lowest PSF). The PSF worsens by a similar factor of approximately 6 fold by decade of energy as the gamma-ray energy goes from 10 GeV to 10 MeV. This plot is taken from the *Fermi*-LAT performance page at https://www.slac.stanford.edu/exp/glast/groups/canda/lat_Performance.htm

events. This improved rejection algorithm increases gamma-ray acceptance (i.e. the effective area integrated over the solid angle) by a factor of 1.25 and $2-3$, for energies above and below 3 GeV, respectively.

PASS 8 also has further PSF event types (in addition to the event types for Front and Back converting events) defined for each event. The PSF event type indicates the quality of direction reconstruction and is divided into quartiles with PSF3 being the best direction reconstruction and PSF0 being the worst.

The latest event data sub-release of PASS 8 is P8R3 (at the time of writing) which eliminates a background systematic (where the diffuse isotropic background is ~ 2 times higher at $1-3$ GeV within $\sim 20^\circ$ of the Ecliptic compared to the poles) for only a modest 1% drop in acceptance [64]. A plot of differential energy flux sensitivity for this data release using a PL spectrum index 2.0 test source (Fig. 2.3) shows that the energy range $2-7$ GeV is where the LAT is most sensitive, with a decline in sensitivity going to lower energies below 2 GeV and higher energies above 7 GeV. Furthermore, the direction of observations with respect to the Galactic plane matters, so that observations taken towards the Galactic centre exhibit the worst sensitivity.

Within the weekly files above, each of the observed events is tagged with a photon event class determined by the *Fermi*-LAT team's event reconstruction. The photon event class is a nested hierarchy where each event class contains the photons in the next more stringent event class wherein the quality of reconstruction is greater, the astrophysical background less, the PSF narrower and the effective area reduced. The photon event classes for non transient sources in order of increasing reconstruction quality are "Source", "Clean", "Ultraclean" and "Ultracleanveto". The Source photon class is the least stringent but is the recommended FSSC class for most analysis and provides good sensitivity for analysis of point sources and moderately extended sources. The other photon event classes listed are of benefit in the detection of hard spectrum sources at high Galactic latitudes and in checking for cosmic-ray induced systematics but offer few benefits for the analysis of the types of sources in this work (as confirmed empirically by my own analysis but which for the sake of brevity I do not offer here) and make comparison with the literature difficult as the Source photon event class is most widely used. I therefore use the Source photon event class in this work throughout.

Separate from the weekly event files but uniquely associated with the PASS data releases are the files describing the gamma-ray background[5] which arises from Galactic interstellar (diffuse) emission and from extra-Galactic sources. The Galactic interstellar emission mode (IEM [252]) describes the spatial and spectral distribution of gamma-ray emission produced by cosmic-ray proton interactions with interstellar nuclei (followed by secondary pion decay)

[5]https://fermi.gsfc.nasa.gov/ssc/data/access/lat/BackgroundModels.html LAT Background Models

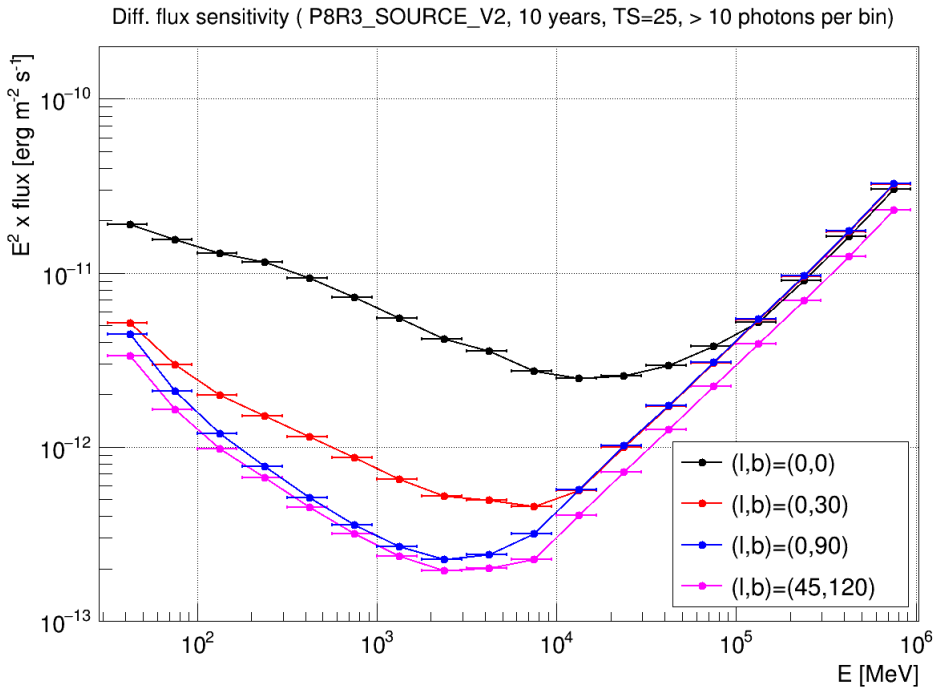

Fig. 2.3 The plot above is a P8R3_SOURCE_V2 differential sensitivity plot assuming ten years of observations between 31.6 MeV and 1 TeV and a point source with a power-law spectrum with index 2 and uniform background around it. The curves are for a presumed source in four different locations (shown in Galactic coordinates): Galactic centre, intermediate latitudes, north Galactic pole, and north Celestial pole. A minimum of 10 photons per energy bin is required for the sensitivity curve to be valid. The energy range between $2-7$ GeV is where the LAT has peak energy flux sensitivity with worsening sensitivity going to lower energies below 2 GeV and to higher energies above 7 GeV. Observations taken towards the Galactic centre exhibit the worst sensitivity. This plot is taken from the *Fermi*-LAT performance page at https://www.slac.stanford.edu/exp/glast/groups/canda/lat_Performance.htm

and cosmic-ray electron Bremsstrahlung interactions with nucleons or their inverse Compton scattering of soft interstellar photons (infrared-ultraviolet). The IEM is dependent on the spatial distribution of interstellar gas deduced by line surveys of HI and CO (as a tracer to H_2). The IEM is defined in the file gll_iem_v07.fits which gives the background energy flux for 28 energies between 50 MeV and 81.4 GeV along with their spatial co-ordinates. I show the IEM at 50 MeV in Fig. 2.5 for the whole sky along with an expanded view of the background towards the Galactic centre. The backgrounds at higher energies have a similar spatial extent predominantly in the plane although the background fluxes decrease for higher energies. The isotropic extra-Galactic diffuse emission is modeled more simply as a list of gamma-ray energies and background differential gamma-ray flux applicable to that energy with a separate list file for every combination of photon event class and PSF event type.

The final data products to consider are the 4 gamma-ray source catalogues, the 1FGL to the 4FGL [8, 209, 18, 13], which have been compiled during the *Fermi* mission using increasing integration times and improved background models and PSFs as described above. This has led to an increased number of source detections and an expanded energy range of the observations (Table 2.2). The catalogues define the gamma-ray spectral characteristics of all sources detected by the *Fermi*-LAT collaboration at greater than 4σ significance and identifies their possible counterpart astrophysical sources. A significant number of the detected sources are not associated with any known counterpart. These catalogues are a crucial part of the *Fermi*-LAT analysis as they provide a base-line model of the gamma-ray sky which is consistent for all researchers thus saving the effort of recreating this anew at each analysis and leaving us free to detect new sources outside of the catalogue or refine the spectra of existing sources. This thesis began by using the 3FGL and switched to the 4FGL on its initial release late in 2019. An updated version of the 4FGL, data release 2 [12] using 10 years of observations (rather than the 8 yr of the initial 4FGL catalogue) was released by the FSSC during preparation of my thesis in May 2020 but is not used in my analysis.

Description	Identified		Associated	
	Designator	Number	Designator	Number
Pulsar, identified by pulsations	PSR	232	···	···
Pulsar, no pulsations seen in LAT yet	···	···	psr	7
Pulsar wind nebula	PWN	11	pwn	6
Supernova remnant	SNR	24	snr	16
Supernova remnant/Pulsar wind nebula	SPP	0	spp	78
Globular cluster	GLC	0	glc	30
Star-forming region	SFR	3	sfr	0
High-mass binary	HMB	5	hmb	3
Low-mass binary	LMB	1	lmb	1
Binary	BIN	1	bin	0
Nova	NOV	1	nov	0
BL Lac type of blazar	BLL	22	bll	1109
FSRQ type of blazar	FSRQ	43	fsrq	651
Radio galaxy	RDG	6	rdg	36
Non-blazar active galaxy	AGN	1	agn	10
Steep spectrum radio quasar	SSRQ	0	ssrq	2
Compact Steep Spectrum radio source	CSS	0	css	5
Blazar candidate of uncertain type	BCU	2	bcu	1310
Narrow-line Seyfert 1	NLSY1	4	nlsy1	5
Seyfert galaxy	SEY	0	sey	1
Starburst galaxy	SBG	0	sbg	7
Normal galaxy (or part)	GAL	2	gal	1
Unknown	UNK	0	unk	92
Total	···	358	···	3370
Unassociated	···	···	···	1336

Note. The designation “spp” indicates potential association with SNR or PWN. Designations shown in capital letters are firm identifications; lower case letters indicate associations.

Table 2.1 A breakdown count of sources detected by *Fermi*-LAT as listed for the 4FGL catalogue with number of confirmed identifications in the "Identified" column and presumed associations in the "Associated" column. Table taken from [13]. AGN of various kinds are the predominant associated source class, whereas pulsars identified by pulsed emission are the largest number of confirmed identifications. All globular cluster associations are presumed associations highlighting the lack of an unambiguous diagnostic property for these sources.

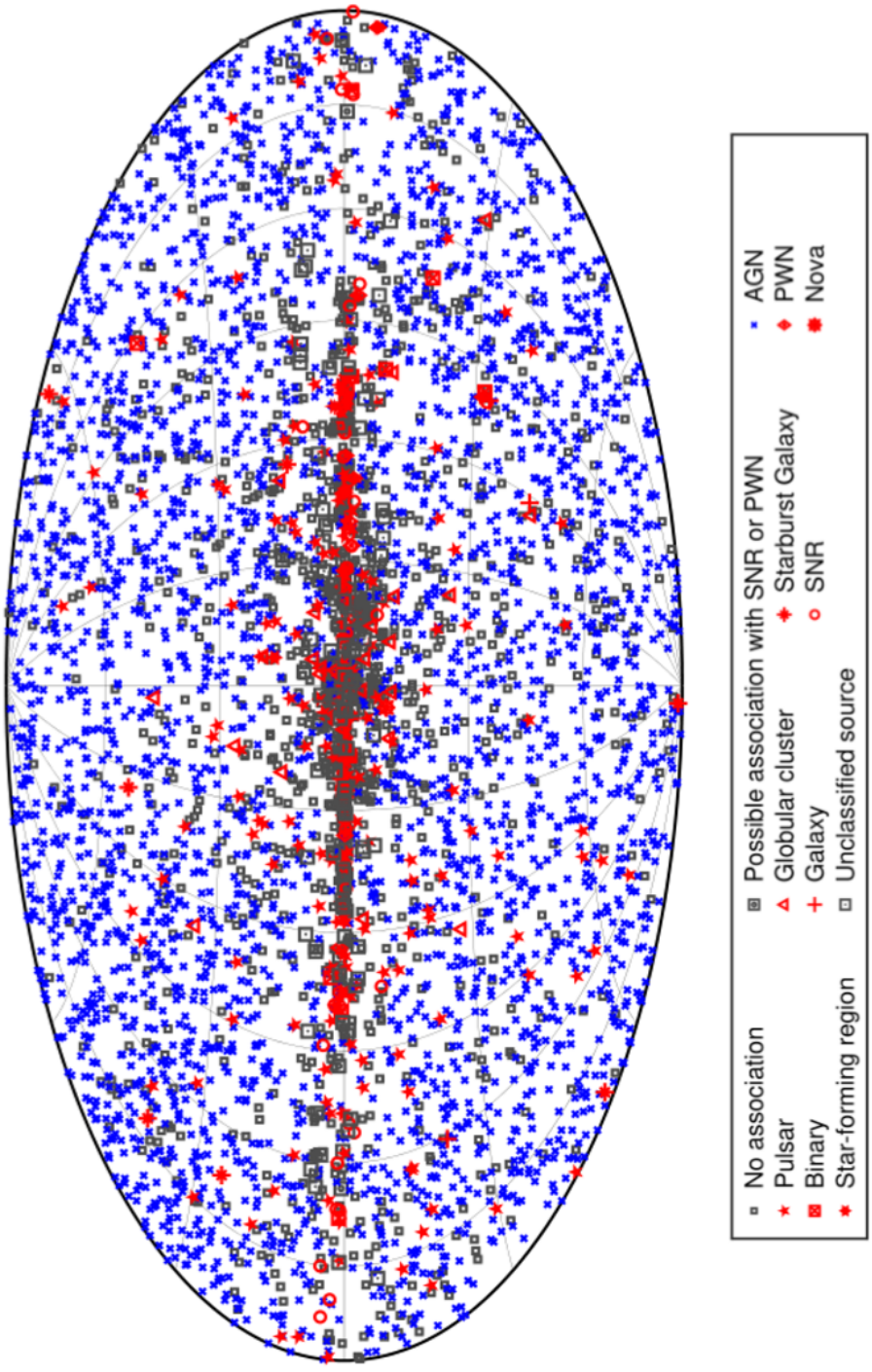

Fig. 2.4 A skymap of gamma-ray sources classified by *Fermi*-LAT showing Active Galactic Nuclei (AGN) as the predominant source class, isotropically distributed across the sky. Sources are more concentrated in the Galactic plane (middle band of the figure). SNR and PWN stand for Super-Nova Remnant and Pulsar Wind Nebula respectively. Figure taken from [13].

Catalogue	Integration Time	Year Published	No. of Detected Sources	Energy Range (GeV)	No. of Unassociated Sources	Data Release
1FGL	11 months	2010	1451	0.1−100	630	PASS 6
2FGL	2 yr	2012	1873	0.1−100	575	PASS 7
3FGL	4 yr	2015	3033	0.1−300	1009	PASS 7 (reprocessed)
4FGL	8 yr	2019	5064	0.05−1000	1336	PASS 8
4FGL DR2	10 yr	2020	5788	0.05−1000	-	PASS 8

Table 2.2 The 4 source catalogues of the *Fermi*-LAT showing the increasing number of 4σ sources detected over the increasing integration time of the mission and the improving energy range analysed. The catalogues have been compiled by the *Fermi*-LAT collaboration with specific data releases as shown. The 3FGL was produced with a reprocessed version of PASS 7. The 3FGL and 4FGL catalogues are used in the analysis in this work. The 4FGL DR2 catalogue was made available in May 2020 [12] during thesis preparation and so is not used in my analysis. The number of unassociated sources is not quoted in the 4FGL DR2 draft paper.

The diverse range of sources listed in the 4FGL [13] and their distribution on the sky is shown in a skymap (Fig. 2.4) where a concentration of sources in the Galactic plane is clearly visible, whilst the breakdown count of source associations is shown in Table 2.1. AGN of various kinds are the predominant associated source class, whereas pulsars identified by their pulsed emission are the largest number of confirmed identifications. It is interesting that all globular cluster associations are only presumed associations, which is suggestive of a lack of an unambiguous diagnostic property to distinguish these sources from others.

2.3 Likelihood Analysis

The quantitative analysis of *Fermi*-LAT event data requires the fitting of models to the data, with the visualisation of photon count statistics being of lesser importance. This requirement arises because the LAT is operated mostly in a sky-survey mode rather than by continuous fixed pointing at a target and hence the inclination of the LAT bore-sight to any source being measured will vary continuously and so the effective area of the LAT will also change with respect to the source. In addition the PSF of the LAT will vary as a function of photon energy, as will the gamma-ray background for the energy being considered and by position observed in the sky. The likelihood analysis method is used to fit models to event data with the likelihood being the probability of obtaining the photon event data observed given an

input model comprised of gamma-ray sources in the sky each with a given flux intensity and spectral model described by a functional form with parameterised values.

The likelihood analysis method is fundamentally based on Wilks' Theorem [273] which is formulated to test *composite hypotheses* which can be taken to be the models above. In his 1938 paper Wilks considers a population K with an observable x which has a distribution function $f(x, \theta_1, \theta_2, ...\theta_h)$ which depends on parameters $\theta_1, \theta_2, ...\theta_h$. A *simple hypothesis*, or in modern parlance a "model", is one where the θ parameters have specific values and further a set of *admissible hypotheses*, Ω, can be defined with each member of the set being a *simple hypothesis* with its own θ parameter values. Similarly a set, ω, can be defined with just one member, a single *simple hypothesis*. He then takes a random sample O_n of n individuals from K and gives the probability density function P associated with O_n, shown in Eqn. 2.1.

$$P = \prod_{\alpha=1}^{n} f(x_\alpha, \theta_1, \theta_2, ...\theta_h) \tag{2.1}$$

The maximum possible value of P for the set of *admissible hypotheses*, Ω, is then denoted by $P_\Omega(O_n)$ and by $P_\omega(O_n)$ for the single *simple hypothesis* in the set ω. A likelihood ratio, λ, is then defined as Eqn. 2.2.

$$\lambda = \frac{P_\omega(O_n)}{P_\Omega(O_n)} \tag{2.2}$$

The likelihood ratio λ is used to test the hypothesis, H, that O_n is from a population with a distribution whose values of θ_i are as in the *simple hypothesis* ω.

Wilks then goes on to show that when H is true then λ is related to the chi-squared distribution χ^2_0 for zero degrees of freedom as Eqn. 2.3 except for small terms of order $\frac{1}{\sqrt{n}}$.

$$-2\ln\lambda = \chi^2_0 \tag{2.3}$$

Finally Wilks shows that a more general case of Eqn. 2.3 applies so that when hypothesis H is true that the distribution of $-2\ln\lambda$ is as χ^2 with $h-m$ degrees of freedom (where $h-m$ is the number of additional parameters for the *simple hypothesis* as compared to hypothesis H [191]). This general case is Wilks' Theorem.

The χ^2 distribution of likelihood in Wilks' Theorem was first applied to the problem of parameter estimation in astronomy in [70], where consideration is given to photon counting and the localisation of weak X-ray sources. [70] also reformulated the likelihood ratio equation (Eqn. 2.2) into a computationally more useful form as the sum of log likelihoods for the models being compared. Subsequently a likelihood ratio test (LRT) was used in the analysis of gamma-ray data from the EGRET instrument aboard the *Compton Gamma-ray*

Observatory which was the predecessor instrument to the *Fermi-LAT* [191]. A null hypothesis (analogous to hypothesis H above) is proposed that no point source exists at a position under consideration whilst an alternative hypothesis (analogous to a set of admissible hypotheses: Ω, above) posits the converse. The *maximum* likelihood for the models is determined by the Newton-Raphson iteration of successive model estimates which determine when the partial differential of the log likelihoods with respect to a vector of parameters, Λ, (comprising the normalisation of the Galactic diffuse radiation model, the isotropic diffuse intensity and the proposed counts of an active source) is zero. [191] also demonstrates through Monte Carlo simulation that the range of gamma-ray fluxes predicted by the maximum likelihood estimate method are unbiased, with counts significance vs measured counts being distributed as a Gaussian curve around a peak significance for the true known counts of two test fluxes.

This iterative process to find maximum likelihood for a parameter set is implemented in [191] using a bespoke FORTRAN code. As an aside, the iterative traversal of the log likelihood parameter space to find a maximum is a common feature of the MLE method and now some 24 years after the work of [191], a choice of encapsulated software optimisers is available to perform this task, such as the MINUIT package.

Having obtained the maximum log likelihood for the null (L_0) and source detection (L_1) hypotheses the authors of [191] form a test statistic T_s (Eqn. 2.4) which they show by Monte Carlo simulation is distributed as $\frac{\chi^2_1}{2}$ as broadly expected by Wilks' Theorem, (Eqn. 2.3 above) with the factor of $\frac{1}{2}$ in the distribution arising from disregarding any predicted counts which are negative in sign. They also determine the significance of an EGRET source detection to be $\sqrt{T_s}$ in σ units.

$$T_s \equiv -2(\ln L_0 - \ln L_1) \tag{2.4}$$

2.4 *Fermi*-LAT Analysis

The analysis of *Fermi*-LAT data follows a conceptually similar model fitting procedure to that of EGRET above where spectral parameters of sources are varied until likelihood is maximised. This analysis process can be broken down into successive steps of event and source model selection followed by the pre-computation of LAT exposure and live-time and ending with spectral model fitting. The steps of the analysis chain are discussed below and are implemented using the *Fermi* Science Tools which can be either invoked directly or more conveniently through Python wrapper code such as FERMIPY. In my work I use the *Fermi* Science Tools directly for event selection and creating event files which I subsequently

analyse using FERMIPY. The FERMIPY configuration parameters discussed below are held in a single config.yaml file.

2.4.1 Event Selection

The *gtselect* command extracts event data from the Weekly Files within a specified observation time, energy range, photon event class, PSF event type, zenith cut and event radius around a central analysis target source whose location is described by right ascension and declination co-ordinates in decimal degrees. The event data are filtered on photon event class and PSF event type using the *evclass* and *evtype* parameters respectively. An *evclass* of 128 indicates "Source" photons. A PSF *evtype* of 1 or 3 indicates events that convert in just the Front or both the Front and Back of the TKR respectively. An *evtype* of 32 selects only events which have the PSF3 best quartile direction reconstruction. A 90° zenith cut is applied to the event data using the *zmax* parameter in order to prevent gamma-ray contamination from the Earth limb as per FSSC recommendations. The radius of event selection from the central target is specified by the *rad* parameter with a *rad* of 30° being sufficient to include all analysis scenarios in my work. The radius chosen is sufficiently large to encompass the sum of two individual radii, the first is the radius of the region of interest (ROI) which is an inner region set by the largest PSF of the energy range being considered whereas the Source Region of Interest (SROI) is a wider region where bright sources can contribute emission to the ROI within their PSF and need to be accounted for. The extracted event data returned by *gtselect* is output as a single file in *.fits* format.

Next, only events from good time intervals are selected from the single *.fits* file above using the *gtmktime* command. This uses a pointing and livetime spacecraft history file describing the position and orientation of *Fermi* throughout the mission to exclude poor quality events when *Fermi* is either within the South Atlantic Anomaly or not in a state to collect good science data. The poor quality events are filtered out by a *filter* parameter string specifying DATA_QUAL $>$ 0 and LAT_CONFIG=1. Again the output of this step is a single file of *.fits* format.

2.4.2 Source Model Selection

The next step is to choose the baseline model of known gamma-ray sources containing their spectral functional forms, spatial location and the appropriate version of the background emission model: the Galactic IEM and isotropic spectral template are paired with the data release used to compile the chosen catalogue. Typically the most up to date catalogue available is used, which initially is the 3FGL and subsequently the 4FGL. The catalogue in use

is specified by the FERMIPY *catalogs* configuration parameter while the model background is specified by *galdiff* and *isodiff* configuration parameters. For the latest 4FGL catalogue and an analysis with *source* class photons I use a *galdiff* filename value of "gll_iem_v07.fits" and an *isodiff* filename value of "iso_P8R3_SOURCE_V2_v1.txt" which is the isotropic spectral template matched with the photon event class. The choice of the *source* photon class has been discussed above and this requires a matching instrument response function (IRF) to be specified in the *irfs* configuration parameter of "P8R3_SOURCE_V2". The correct correspondence of photon class, IRF name and isotropic spectral template is listed in the FSSC LAT Background Models page referred to earlier and care must be taken as an incorrect pairing can fail silently and lead to erroneous analysis results. Finally the sizes of the ROI and SROI regions used in the model are set using the *roiwidth* and *src_roiwidth* FERMIPY configuration properties. For the energy ranges considered in this work of 60 MeV to 300 GeV I use a *roiwidth* of 25° and *src_roiwidth* of 40°. This is sufficient to allow for the PSF of the LAT and for gamma-ray contributions from all sources around the main one of interest, as can be deduced from Fig. 2.2. Finally, it should be noted that the source model is only a baseline model, current at the time of the catalogue compilation by the *Fermi*-Collaboration. As such it is necessary to account for additional sources which are not listed in the catalogue because they either fall below the significance threshold for inclusion at the time of catalogue compilation or are revealed in subsequent event observations made with the LAT since the catalogue was compiled. These additional sources are either identified by the FERMIPY *find_sources* command and automatically added to the source model during the analysis or can be manually added through the FERMIPY *add_source* command which allow the spectral model and source location to be specified.

2.4.3 Pre-compute Livetime and Exposure

The LAT IRF is a function of inclination angle, which is the angle between the source direction and the LAT normal. Therefore the count from a source depends on the time a source has spent at a given inclination angle during observation. This "livetime" or time spent observing at a given inclination angle depends only on the LAT orientation and not on any source model and so it can be pre-computed over a spatial HEALPix grid (which is the projection of a spherical surface where each pixel has the same surface area) and re-used in the analysis of multiple sources over the same time range, zenith angle and ROI. The pixel size of the spatial grid is set using the *binsz* configuration parameter at 0.1 °.

The "livetime cube" is pre-computed by the *gtltcube* command. The exposure map of emission from extended sources and the Galactic diffuse and isotropic background is then computed using the *gtexpcube2* command for the SROI using the livetime spent at each

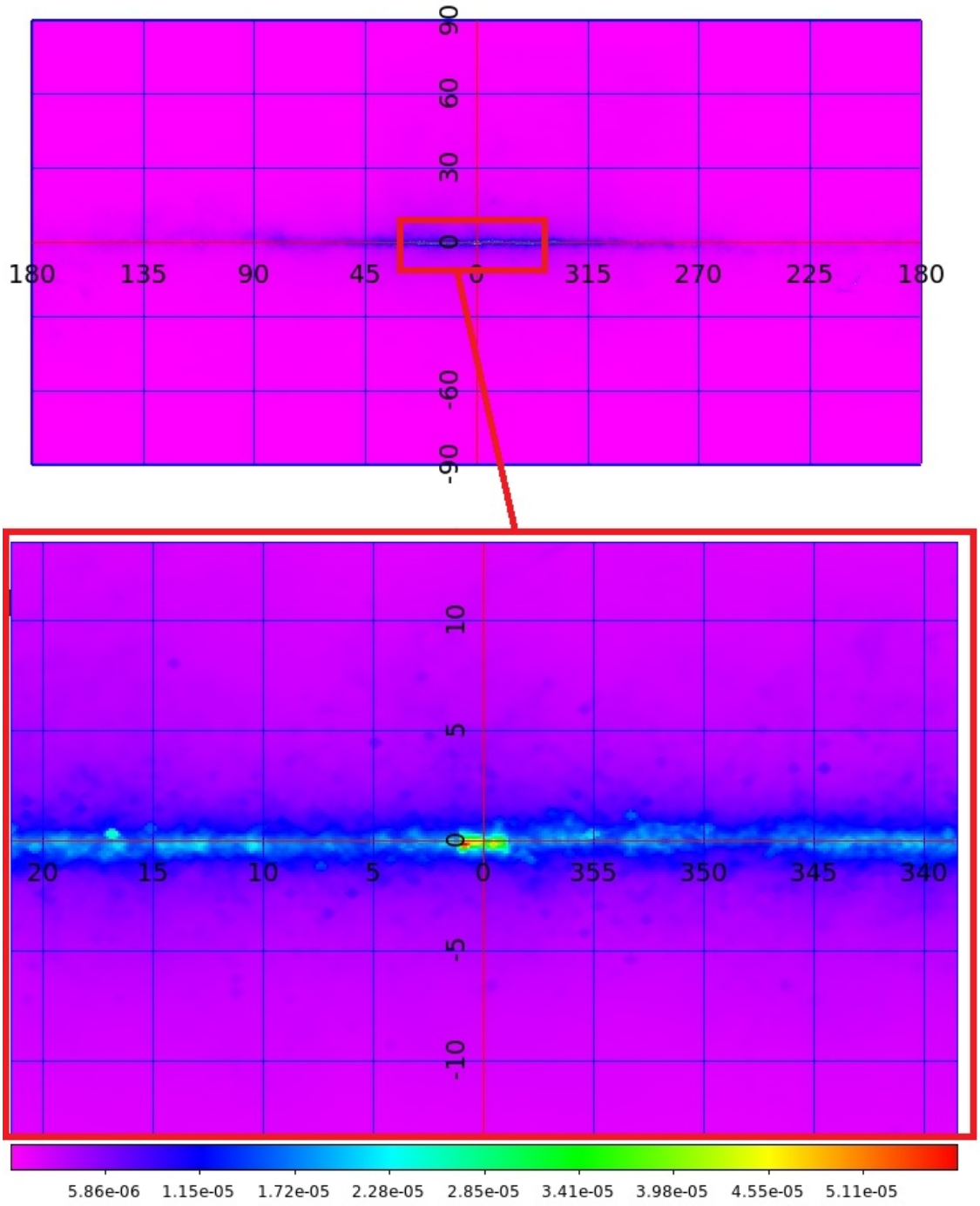

Fig. 2.5 The Galactic diffuse background model for energies of 50 MeV from gll_iem_v07.fits displayed using Galactic co-ordinates. The horizontal axis is Galactic longitude l and the vertical axis is latitude b. The top sub-figure shows the diffuse emission of the whole sky with the Galactic plane being an area of higher background while the expanded figure (bottom) shows the diffuse background emission towards the Galactic centre. The colour scale is a photon flux in units of ph cm^{-2} s^{-1}

inclination angle derived from the "livetime cube". In my analysis the SROI is $\sim 50\%$ greater than the ROI for exposure map generation in line with the FSSC recommendation to ensure that all source photons are included due to the broad PSF at low energies. The model count maps for each source are then computed using the *gtsrcmaps* command by scaling by the exposure and convolving with the PSF.

2.4.4 Spectral Model Fitting

In the spectral model fit process I determine the spectral parameter set that maximises likelihood through use of the FERMIPY *fit* and *optimize* methods which use the *pylikelihood* package and the MINUIT likelihood optimiser. During optimisation I allow spectral trial parameters on individual sources and the background to vary (also known as "freeing") whilst fixing or "freezing" others. The optimiser then iteratively determines likelihood for each trial set of parameters and searches for the maximum likelihood using the derivative of the likelihood function to find a stationary point. Typically, a key set of parameters (or "shape") for a source spectral model is freed for all significant sources (TS greater than 25), within the SROI during the fit process, while the normalisation (or "prefactor") is freed on all sources in the ROI and on the Galactic IEM and isotropic background. The remaining spectral parameters on SROI sources are kept fixed. The end results of the fit process are the spectral parameters of the spectral model of the source of interest, the significance of the detection as a TS value, energy and photon fluxes of the source along with the errors on the free model parameters and fluxes.

I will show in Chapter 4 how the above steps can be applied to the analysis of the globular cluster 47 Tuc, to determine its spectral model, detection significance and energy and photon fluxes.

2.5 Imaging Atmospheric Cherenkov Telescopes

2.5.1 Principle of Detection

The vertical thickness of the Earth's atmosphere is 28 radiation lengths and effectively blocks electromagnetic radiation of energies 10 eV and above. When a gamma-ray with energy greater than 10 MeV strikes the atmosphere, production of an electron-positron pair takes place, after travelling a radiation length, which shares the energy of the original gamma-ray and propagates in the forward direction. After another radiation length, the electron-positron pair interacts with air molecules to emit secondary gamma-rays by the Bremsstrahlung process. These secondary gamma-ray rays can also pair produce and the

pair-production / gamma-ray emission cycle continues in an electromagnetic cascade along the original gamma-ray path. This process continues until the average energy of all particles reaches a point where radiation and ionisation energy losses are equal, the so-called "shower maximum". The shower maximum varies from 10.3 km for gamma-rays of 100 GeV to 5.5 km at 100 TeV and thus the energy threshold varies with the zenith angle of observation, being lowest near the zenith and highest near the horizon. The development of the air shower occurs on nanosecond time scales and the direction of the air shower core allow the source gamma-ray emitter to be located on the celestial sphere. The air shower itself can be directly visualised by the faint Cherenkov light it emits, again on a nanosecond time scale. In addition the brightness of the Cherenkov light allow the energy of the incoming gamma-ray to be determined.

Cosmic rays also generate atmospheric air showers, initially producing pions of which one-third are neutral and two-thirds are charged [105]. The neutral pions decay immediately to two gamma-rays per pion, transferring one third of the energy of the primary cosmic ray to the development of an electromagnetic cascade of gamma-ray/ electron-positron pair production as previously described above. In contrast the charged pions decay to muon and neutrino species, with the muons propagating with small energy loss to reach the Earth's surface almost unattenuated whilst still producing their own Cherenkov light. The extended lateral morphology of cosmic-ray air showers as compared to gamma-ray air showers arises from the production of transverse muons from lower energy pions.

The Cherenkov light produced by much more numerous cosmic-ray events acts as a background in gamma-ray detection. Fortunately, the air showers resulting from cosmic rays can be distinguished from those of gamma-ray air showers due to their different morphologies and wider opening angle as seen in Monte Carlo simulations (Fig. 2.6).

Ground-based imaging atmospheric Cherenkov telescopes (IACTs) are able to probe much higher gamma-ray energies than *Fermi*-LAT, because they can view the Cherenkov light produced in air showers and make gamma-ray observations using the atmosphere as a detection medium. IACTs of the current generation follow the Davies-Cotton optical design [90]. They have a large light collection area and use tessellated arrays of mirrors, each of the same focal length, which are mounted on a telescope structure which has the same radius of curvature as the focal length (future telescopes of the Cherenkov Telescope Array will use both Davies-Cotton and Schwarzschild-Couder designs as explained below). Importantly, the Cherenkov light cast on the ground is large in extent ($\sim$ 100 m) and the so the collection area available to one or more widely spaced IACTs is much larger than their mirror area alone. In contrast the physical size of the telescope mirror of each individual IACT determines the brightness of the Cherenkov light being observed, so IACTs optimised for higher energy

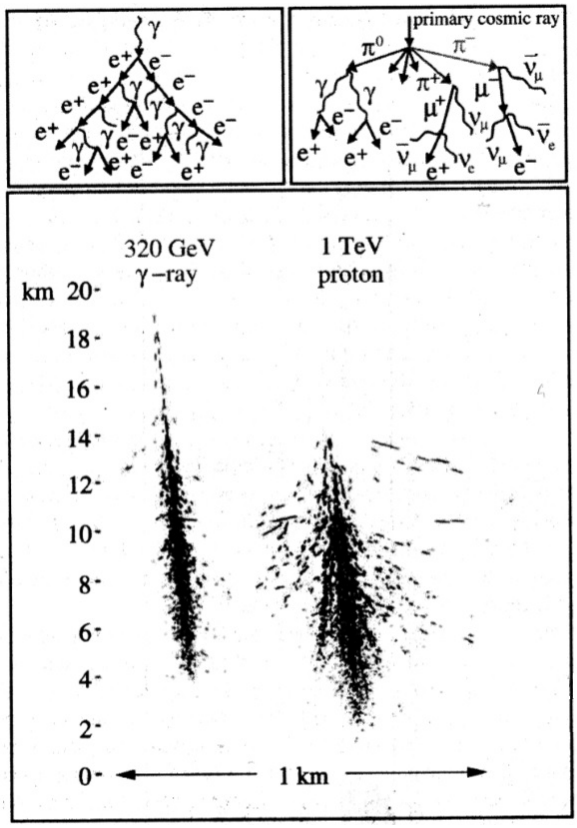

Fig. 2.6 Top panel shows particles produced in an air shower cascade from a gamma-ray (left) and cosmic-ray (right) interacting with the atmosphere. The main panel is a Monte Carlo simulation of air shower extent for 320 GeV gamma-ray (left) and 1 TeV proton cosmic-ray (right). The cosmic-ray shower has a larger opening-angle and will cast a more circular light flash on the ground and thus can be distinguished from the gamma-ray shower. This figure is from [270], originally credited to D. Horan.

observation have smaller mirror collection areas than IACTs detecting the lowest gamma-ray energies.

The detector of each IACT is a camera able to sense blue/UV Cherenkov light at nanosecond time-scales and down to the intensity level of a few photo-electrons. The detection element of the IACT camera has historically been an array of PMTs operating at high voltages and easily damaged by excessive light (such as moonlight) which usually limits observations to times when the moon is below the horizon. Recently, it has been possible to overcome this limitation to some degree and observe in conditions of up to 80 % moon illumination by either lowering the operating voltage of PMTs (with the loss of some sensitivity) or by using ultra-violet bandpass filters [35].

The 10 m Whipple telescope was built in 1968 as the first *large* optical reflector purpose-built for Cherenkov air shower observations. The use of a camera consisting of an array

Fig. 2.7 The H.E.S.S. array in Namibia (top) showing 28 m telescope (centre of image) flanked by the four 12 m telescopes and an open view of one of its 960 pixel PMT cameras as used on the 12 m telescope (bottom). Top image taken from H.E.S.S. Physics Working Group on Multiwavelength Observations at https://www.lsw.uni-heidelberg.de/projects/hess/HESS/hessmultnu.php. Bottom image take from [267]

of PMTs to record air-shower images was first suggested in 1977 by Turver and Weekes [259]. However, it was not until 1989 that Whipple observations made a significant detection of the Crab for the first time, at 9σ significance. This was the first significant detection of any astrophysical source by an IACT and employed a 37 pixel PMT camera combined with nanosecond time resolution [271]. In the modern era, the camera used in the 12 m telescopes of the H.E.S.S. array has 960 pixels or PMTs as can be seen in Fig. 2.7.

Also seen in Fig. 2.8, are examples of the different morphologies of optical images formed in the 960 pixel H.E.S.S. cameras, from cosmic rays (protons), gamma-rays, cosmic ray induced muons (which make characteristic rings) and noise, all of which can be distinguished by their different shapes. During observations with IACTs, elliptical shower images may be selected as resulting from incident gamma-rays through the use of Hillas parameters [133] which characterise the major axis and width-to-length ratios of the ellipses in the image (Fig. 2.9).

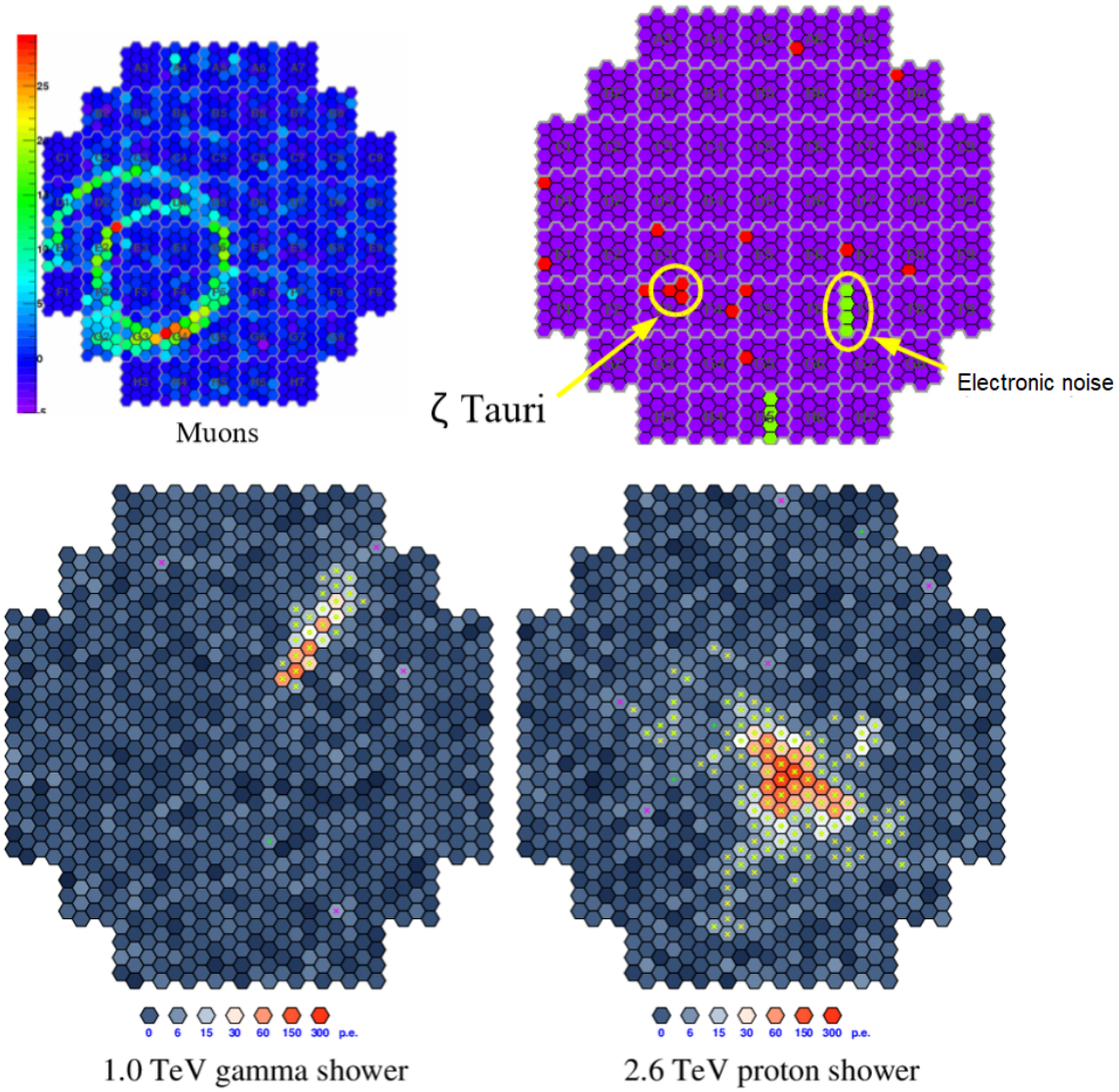

Fig. 2.8 Images recorded on the H.E.S.S. camera of the 12 m telescope. Top left, A muon ring, top right, noise from the star ζ Tauri and electronic glitches, bottom left, image of an gamma-ray which is more elliptical than that of a proton cosmic ray proton shower, bottom right. All scales are in photo-electrons. Top images taken from [175], bottom images from [267].

The arrangement of multiple IACTs in an array to catch the wider extent of the light cast by the air shower on the ground offers further advantages in detecting lower energies because multiple cameras can be triggered by the same flash and so any individual trigger threshold can be reduced. In addition, angular and energy resolution are improved as multiple camera images can be combined for source direction reconstruction. Finally, cosmic rays can be better rejected as multiple shower images are available for characterisation.

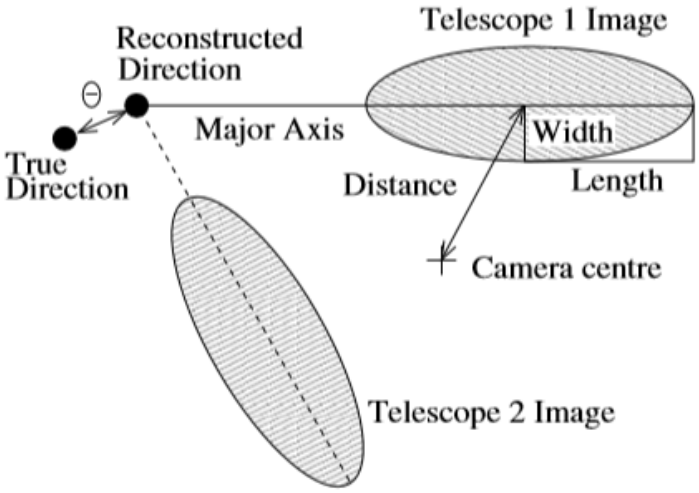

Fig. 2.9 Simple Hillas parameters for two gamma-ray images from different IACTs which allow a source direction to be reconstructed and for images to be classed as resulting from incident gamma-rays rather than cosmic rays. Image reproduced from [22].

The major axes of multiple images, each from a different IACT, can be used to reconstruct a direction to the source with the angle, θ, indicating the offset between a reconstructed and true direction to the source. Direction reconstruction is also applied in the opposite direction from the source into the plane perpendicular to the observing direction, which allow the centre of air shower light pool falling on the ground to be deduced, with the distance of that centre to the IACT being the "impact parameter". Comparison of the image amplitude, measured in photo-electrons, and its impact parameter with look-up tables summarising Monte Carlo simulations of air showers for different zenith observation angles and gamma-ray energies allow an accurate energy reconstruction of the originating gamma-ray to be made. The excess events for a source after background subtraction can be plotted against θ^2 (rather than θ to ensure a constant solid angle on the sky per bin) to show a peak in excess events as θ^2 tends to zero with excess counts decreasing to zero as θ^2 increases. This excess event distribution is thus an indication of the PSF of the instrument. However, it is now more common to show excess events in a sky map of excess counts.

The significance S of any gamma-ray excess after background subtraction is given by Eqn. 2.5 which is derived from a likelihood ratio method as presented by Li and Ma in their 1983 paper where they also verify the applicability of the result using Monte Carlo simulations conducted during their time at the University of Durham [178]. In Eqn. 2.5, α is the ratio of the time spent observing the source of interest to that of observing the background and N_{on} and N_{off} are the number of photons observed from the source and background respectively.

$$S = \sqrt{2}\Big\{N_{on}\ln\Big[\frac{1+\alpha}{\alpha}\Big(\frac{N_{on}}{N_{on}+N_{off}}\Big)\Big] + N_{off}\ln\Big[(1+\alpha)\Big(\frac{N_{off}}{N_{on}+N_{off}}\Big)\Big]\Big\}^{\frac{1}{2}} \tag{2.5}$$

2.5.2 Operational IACTs

I summarise the relevant characteristics of the *currently operational* IACT arrays in Table 2.3. The sensitivity quoted is the time to detect a given percentage of the flux of the Crab nebula. The Crab, although it shows some low energy variability with a flaring synchroton component (with *Fermi*-LAT detecting a factor 20 increase in flux for energies < 700 MeV in March 2013 [192]), is considered a "standard candle" in VHE gamma-ray astronomy with no variability observed with H.E.S.S. over the same flare period in, for example, 2013 [81]. Hence, it is often the source object of choice in any first light demonstration of an IACT. The specification shown is the latest specification at the time of writing, with both VERITAS and H.E.S.S having been upgraded after their globular cluster observations (which I summarise in Chapter 3) were performed. The IACTs listed are broadly comparable from a scientific perspective but there is a northerly location bias in their placement.

All sources detected using IACTs are listed in TeVCat[6], which is an online catalogue generated from reported TeV detections. It is seen that of the 227 sources in TeVCat, the largest source class is comprised of AGN of various kinds and that about a quarter of sources are unidentified (Table 2.5). TeVCat contains just one globular cluster: Terzan 5.

2.5.3 Water Cherenkov Detectors

In addition to IACTs, ground-based water Cherenkov tank experiments are also important for probing higher energy air showers. The High Altitude Water Cherenkov Experiment (HAWC) is a very high-energy gamma-ray observatory observing gamma-rays of energy 100 GeV$-$100 TeV and is situated at an altitude of 4100 m and latitude 18°59' N in Mexico. The

[6]TeVCat is available at https://heasarc.gsfc.nasa.gov/W3Browse/ground-based/tevcat.htmlsource_type, accessed on 14th June 2020

Telescope	Latitude	Altitude (m)	Time to detect 1% Crab Source (h)	Energy Threshold (TeV)	No. of Telescope in Array	Mirror Diameter (m)	Observable Energy Range (TeV)
VERITAS	31.7 ° N	1268	24 [227, 2]	0.24	4	12	0.1−10
H.E.S.S. II	23.2 ° S	1800	25 [136]	0.30	5	12 (4) 28(1)	0.05−100
MAGIC	28.7 ° N	2200	30 [28]	0.29	2	17	0.05−50

Table 2.3 Characteristics of the three major operational IACT arrays, VERITAS, H.E.S.S and MAGIC. Sensitivities are from the references given and apply to the energy threshold shown. H.E.S.S. is a mini-array with the number of telescopes of each size given in brackets.

Array Telescope	Latitude	Altitude (m)	No. of Telescope in Array	Mirror Diameter (m)	Observable Energy Range (TeV)
CTA-N	28.7 ° N	2200			
LST			4	23	0.02−0.15
MST			15	12	0.15−5
CTA-S	23.6 ° S	2100			
LST			4	23	0.02−0.15
MST			25	12	0.15−5
SST			70	4.3	> 5

Table 2.4 Baseline configuration of the next generation Cherenkov Telescope Array with two observatory sites CTA-N and CTA-S and three classes of telescope in the array, SST = Small Sized Telescope, MST = Medium Sized Telescope, LST = Large Sized Telescope which are optimised to probe different energy ranges. CTA-N is co-located on the same site as MAGIC.

Source Type	Count
AGN (unknown type)	2
Binary	11
BL Lac (class unclear)	1
Blazar	3
Composite SNR	2
FRI	4
FSRQ	8
Globular Cluster	1
GRB	3
HBL	51
IBL	8
LBL	2
Massive Star Cluster	3
PSR	4
PWN	32
PWN/TeV Halo	2
Shell	14
SNR/Molec. Cloud	10
Starburst	2
Superbubble	2
TeV Halo	3
Unidentified	59
Total	227

Table 2.5 Count of source types listed in TeVCat as of the 14th June 2020: FR I=Fanaroff-Riley type I radio galaxy, FSRQ=Flat-spectrum radio quasar, HBL, IBL, LBL=High, intermediate and low-frequency peaked BL Lac, PSR=Pulsar, PWN=Pulsar wind nebula, SNR=Supernova remnant

primary array consists of 300 identical optically isolated water Cherenkov tanks of height 5 m and diameter 7.32 m with 4 PMTs in each tank [184]. A secondary outrigger array added in late 2018 improves the direction reconstruction of events of energy > 10 TeV and consists of 345 smaller water tanks (each of diameter 1.55 m and height 1.6 m) with a single internal PMT. HAWC detects the particles of air showers that reach ground level by the Cherenkov light produced by electrons inside the water tank. Gamma-rays can also convert to detectable electrons by pair-production and Compton scattering processes in the tank itself. The identification of gamma-ray air showers and hadronic cosmic-ray background air showers uses their morphological characteristics in a similar way as IACTs with gamma-ray showers having a compact core and a smooth lateral distribution while hadronic showers are broader, with multiple or poorly defined cores and large muon/hadronic signals away from the primary shower core. HAWC is noteworthy for its large instantaneous field of view ($>$ 1.5 sr) and high duty cycle as it can observe day and night and in all weathers (maintenance interruptions notwithstanding) but has a bias towards the detection of harder sources. HAWC can view targets with declinations between -20° and 60° and has produced a source catalogue, the 2HWC [14], with 39 sources based on 507 days of observations. Of these 39 sources, 20 have associated counterparts in TeVCat (association defined as HAWC source $< 0°.5$ from TeVCat source) of which 10 are pulsar wind nebulae or supernova remnant sources whilst 2 others are blazars and 8 are unidentified. The remaining 19 sources in the 2HWC are not associated with any known source.

Another Cherenkov water detector of note, 3 times the instrument area of HAWC, is the Large High Altitude Air Shower Observatory (LHAASO) [42], based in Tibet, China, at latitude 29°21' N, and an altitude of 4410 m. LHAASO is being commissioned at the time of writing and has not yet reported any sources. The sensitivity of LHAASO is predicted to exceed that of HAWC [42] and will detect cosmic rays from 1 TeV to 1 EeV and gamma-rays from 100 GeV to 1 PeV.

2.5.4 The Cherenkov Telescope Array

The Cherenkov Telescope Array (CTA) is the next generation gamma-ray observatory and will be comprised of differing numbers of large, medium and small sized telescopes (LST, MST and SST respectively) to probe different energy ranges as listed in Table 2.4. CTA will be split across two sites, CTA North (CTA-N) and CTA-South (CTA-S). The first and most developed site, CTA-N, is on La Palma at the Roque de los Muchachos Observatory, co-located with the MAGIC IACT, and already has a prototype LST installed and running. CTA-S will be near the European Southern Observatory at Paranal, Chile and is at the site preparation stage at the time of writing.

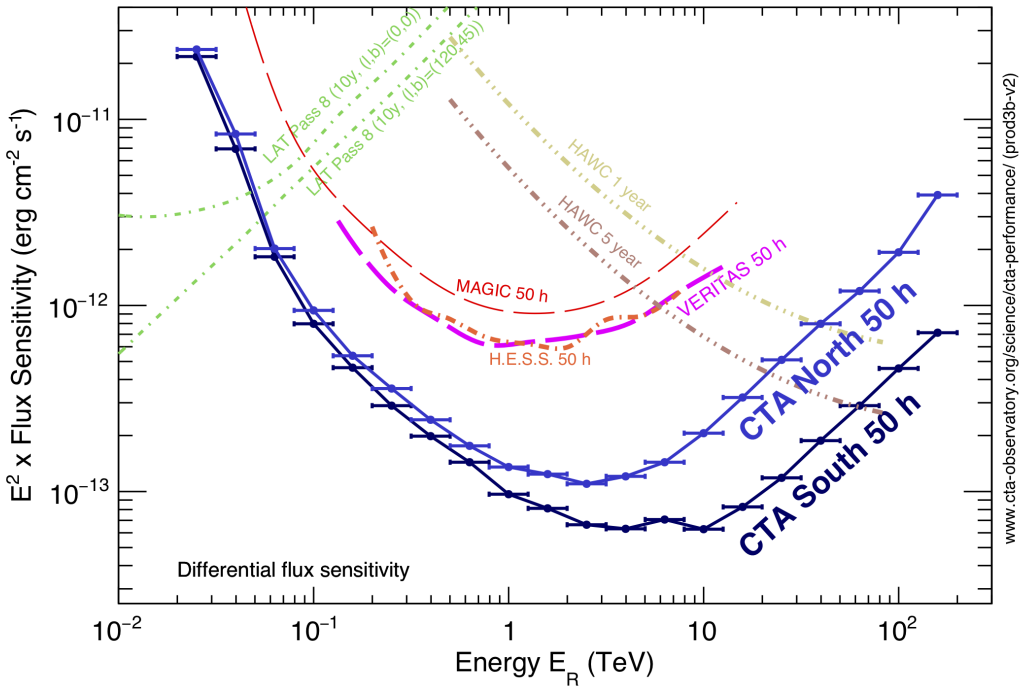

Fig. 2.10 The differential flux sensitivity of CTA-N and S for 50 h observations compared to *Fermi*-LAT and existing IACTs: H.E.S.S, MAGIC and VERITAS. Also shown is the sensitivity of HAWC, a Cherekov Water Tank experiment which detects very very high energy particles directly via the Cherenkov light within light proof water tanks with PMTs in-situ. This sensitivity curve is for the prod3b-v2 configuration.

The optimum differential flux sensitivity of CTA is in the $1-5$ TeV range for CTA-N and in the $3-10$ TeV range for CTA-S; this generally represents an order of magnitude improvement on existing IACTs as can be seen in Fig. 2.10. Below 1 TeV the sensitivity of CTA-N and CTA-S declines but is always a factor of a few greater than existing IACTs and 50 h of CTA observations are more sensitive than 10 yr of PASS 8 *Fermi*-LAT observations to a lower limit of $60-70$ GeV. At the higher energies, 50 h of CTA-N and CTA-S observations are more sensitive than 5 yr of HAWC observations below energies of 20 and 60 TeV respectively, with HAWC being more sensitive at the very highest energies.

The SST and the p-SCT telescope prototype of the MST are noteworthy for mounting the camera on a Schwarzschild-Couder (SC) telescope as opposed to Davies-Cotton. The SC design allows de-magnification of the image onto a smaller plate scale. The smaller plate scale makes it practical to employ a camera with compact silicon photo-multipliers (SiPMs, which are avalanche photodiode type devices), instead of larger PMTs, which improves angular resolution and off-axis sensitivity compared to the traditional Davies-Cotton design.

2.6 CTA Analysis Software

CTA offers 2 tools for gamma-ray analysis, CTOOLS [160][7] and GAMMAPY [95] [8]. Both tools are the equivalent of the *Fermi* science tools above and share many functional similarities. It is noteworthy that CTOOLS and GAMMAPY are exactly able to reproduce the results obtained by proprietary H.E.S.S. analysis tools when applied to the analysis of H.E.S.S. event data [199] and so can be considered functionally consistent with existing analysis tools and each other. I now summarise the relevant steps of the CTOOLS analysis chain which I use subsequently in my simulations of the CTA detection of globular clusters in Chapter 5.

2.6.1 Simulating Event Data

The *ctobssim* tool generates random events within a given energy range and ROI, which are drawn from a background model and the predicted spectral model of the source of interest and then convolved with the applicable IRF of the array, CTA-N or CTA-S, for the observation integration time being simulated. *ctobssim* is seeded with a seed value for its random number generator to generate statistically independent Monte Carlo samples of CTA event data. In simulating event data for analysis I use 880 different seeds to generate 880 independent event data samples for analysis which are each passed as input events to the event data selection step below. The *ctselect* tool is then used to select event data from the simulated event data within a given ROI, time and energy range. The selected event data is then binned into a *counts cube* using the *ctbin* tool. The *counts cube* is a 3-dimensional data cube with dimensions of right ascension, declination and logarithmically spaced energy.

2.6.2 Pre-computing the Binned Response

The IRF is then computed for the *counts cube* to produce an *exposure cube*, a *PSF cube* and a *background cube*. The *exposure cube* contains the effective area multiplied by the livetime of the observation, which is the exposure as a function of sky co-ordinates and energy. The *PSF cube* has dimensions of right ascension, declination, a true photon energy and an offset angle between and the true and reconstructed photon direction.Finally the *background cube* contains a predicted background rate as a function of sky position and energy. The *exposure cube*, *PSF cube* and the *background cube* are produced by *ctexpcube*, *ctpsfcube* and *ctbkgcube* tools respectively using the counts cube, the selected events and the applicable IRF for the integration time. The *ctbkgcube* tool also produced a model file

[7] CTOOLS available from http://cta.irap.omp.eu/ctools/index.html
[8] GAMMAPY available from https://gammapy.org/

using the original input model where the background model is changed to a model of type CTACubeBackground.

2.6.3 Fitting Binned Data with a Model

Model fitting using a log-likelihood method is then performed using the *ctlike* tool which takes the pre-computed cubes above, the *count cube*, and the input model updated with the CTACubeBackground model and performs a binned analysis. The model fitting determines the detection significance of the source of interest using the same method as the determination of an EGRET source significance in Eqn. 2.4 above.

2.7 Conclusion

In this chapter I have introduced *Fermi* and its main instrument, the LAT, along with listing its key discoveries and catalogues of gamma-ray sources. I have described the *Fermi* science tools and introduced the LAT data analysis method used elsewhere in this work. I have discussed the mathematical underpinning of the likelihood analysis method and how it is used to determine the significance and spectral models of sources. I have also discussed current ground-based gamma-ray observation techniques, current IACT arrays and their successor instrument the CTA, all of which probe higher energy gamma-rays than the LAT by using the atmosphere as a detection medium. Finally I have described a software analysis chain based on CTA CTOOLS which allow the simulation of source detectability with CTA given a spectral model and the instrument response functions applicable to CTA.

Chapter 3

Gamma-ray emission from Globular Clusters and Millisecond Pulsars

3.1 Introduction

In this chapter I summarise the main gamma-ray observations of GCs made in the *Fermi*-LAT era with both *Fermi* and IACTs. I also summarise models of GC gamma-ray emission based mainly on inverse Compton scattering processes powered by relativistic particles from MSPs in combination with the direct gamma-ray emission of MSPs themselves. Such models are worth considering here as they have had some success in predicting the observed GeV spectra of the well known GCs, 47 Tuc and Terzan 5, and hint at higher energy emission in the TeV range. For completeness I also summarise models of individual MSP gamma-ray emission which allow the spectra and lightcurves of catalogue MSPs characterised and discovered using *Fermi*-LAT to be recreated with simple physics inputs, thus showing that there is a reasonable consensus understanding of emission processes in MSPs to a first order. This allows the application of MSP emission models to overall GC emission to be considered valid. At the same time I highlight that the relationship between gamma-ray luminosity and MSP spin-down power is not clear cut and that faint MSPs themselves are not individually observable and so deriving a model of GC emission from pulsar characteristics alone is likely to be challenging. Throughout I draw attention to modelling and observational evidence that supports emission in both MSPs and GCs above 10 GeV (which I term high energy emission or HE) and above 50 GeV (which I call very high energy emission or VHE). VHE is a potential energy range to be probed with CTA to further elucidate the MSP and GC gamma-ray connection.

3.2 Gamma-ray emission from Globular Clusters

3.2.1 GC Observations Made with the *Fermi*-LAT

The detection of 47 Tuc with just 194 days of *Fermi*-LAT observations in 2009 established GCs as sources of gamma-ray emission for the first time [7] (Fig. 3.1) and showed that the gamma-ray spectrum of 47 Tuc was best fitted by a power-law with an exponential cut-off. This initial detection demonstrated the lack of gamma-ray variability on 2 week timescales and supported the supposition that MSPs in GCs are detectable en-masse by their gamma-ray emission. A folding of the gamma-ray signal with the ephemerides of 21 of the 25 MSPs in 47 Tuc failed to significantly detect any individual MSP, demonstrating that 47 Tuc is not dominated by a single gamma-ray bright MSP. By assuming an average $\dot{E}$ of 1.8×10^{34} erg s^{-1} for each MSP in the GC, a spin-down gamma-ray conversion efficiency of 12% was determined [7]. Subsequently, an analysis of 546 days of *Fermi*-LAT observations re-detected 47 Tuc and a further 7 GCs, Omega Centauri, Terzan 5, NGC 6626, NGC 6266, NGC 6388, NGC 6440 and NGC 6652, as point sources with detection significance ranging from $7-24$ σ [10]. The GC spectra were again fitted with an exponential cut-off power law and exhibited hard spectral power indices ($0.7< \Gamma <1.7$) with the exponential cut-off in the range $1.0-2.6$ GeV which is the characteristic signature of magnetospheric emission from MSPs. A positive correlation was also established between gamma-ray luminosity and stellar encounter rate in GCs. In [249], using 2 yr of *Fermi*-LAT observations, the GCs NGC 6624 and NGC 6752 were detected alongside evidence of gamma-ray emission within the tidal radius of NGC 6093, NGC 6139, Liller 1 and NGC 6541. These GCs (with the exception of Liller 1) are recognised as gamma-ray emitting GCs in the 4FGL catalog today. The authors of [284] used 2191 days of PASS 7 *Fermi*-LAT data to make 5σ detections of FSR 1735, 2MS-GC01 and IC 1257, although of these only 2MS-GC01 is now recognised as a gamma-ray emitting GC in the 4FGL catalog. In [283], 6 years of PASS 8 *Fermi*-LAT data was analysed with significant detections made of GCs NGC 7078, 6397, 5904, with these gamma-ray sources placed inside the tidal radii of the GCs. The GCs 6218 and 6139 were also detected at slightly less than 5σ significance and these are also now confirmed sources in the 4FGL.

In my own GC analysis paper [181], I analysed 30 high latitude GCs using 8 years of PASS 8 data in the 60 MeV$-$300 GeV energy range with the 3FGL catalog as a source model. My analysis confirmed the detections of 5 GCs, 47 Tuc, NGC 6093, 6752, 7078 and 6218, and made a new detection NGC 6254, not listed in the 3FGL. This GC displays emission offset from the core but still within the GC tidal radius. This source is now listed in the 4FGL catalog with source name 4FGL J1656.4-0410 (although its counterpart source type remains unclassified). I showed that there was no evidence for variability on a 6 month timescale

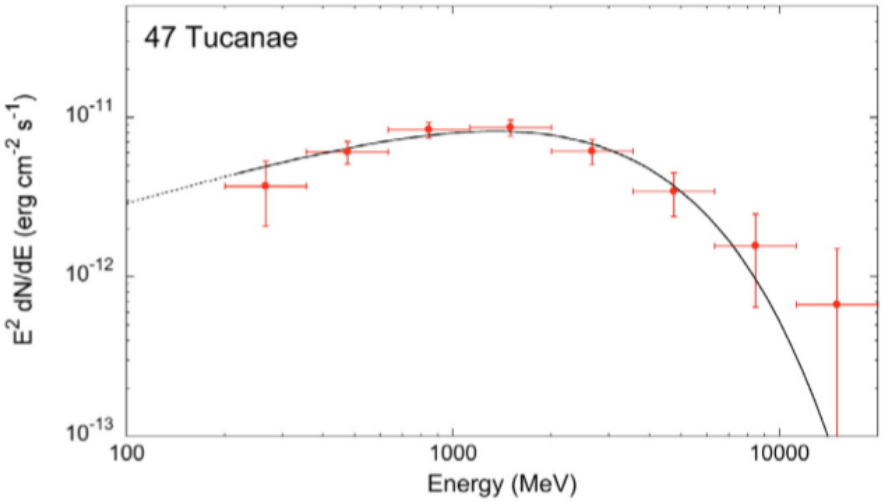

Fig. 3.1 The *Fermi*-LAT gamma-ray spectrum of 47 Tuc fitted with an exponential cut off power law. Figure taken from [10].

or spatial extension of the emission in these sources and that there was little evidence of low-energy emission with only NGC 6752 having 3.4σ flux point below below 100 MeV. I also demonstrated that there is a correlation between GCs which are gamma-ray emitters and those that exhibit diffuse X-ray emission and proposed that this could be due to either an unresolved source population of gamma-ray emitters which are also X-ray emitters or synchrotron X-ray emission arising from relativistic electrons provided by the MSPs residing in the GCs. I also highlighted that additional spectral models, such as simple, hard power laws and broken power-law models, can be fitted to GC spectra. These are not compatible with power-law with super-exponential cut-off spectral models of MSPs and hint at an alternative source population.

A *Fermi*-LAT analysis is made of all 157 GCs in the Harris Catalogue in the recent paper [94]. Here 9 years of PASS8 event data were analysed in the energy range 100 MeV$-$100 GeV with the 3FGL catalog as the source model and further confirmed that GCs exhibit no variability on 3 month timescales nor have significant extension. The analysis of [94] detected NGC 7078 only at the 3σ level and so did not class this as a significant detection in tension with the detection for the 4FGL catalog and the works above. [94] also examined the relationship between GC gamma-ray luminosity and the encounter rate per binary, Λ, as Eqn. 3.1, with ρ_0 being the central luminosity density of the GC and r_c being the cluster core radius.

$$\Lambda \propto \sqrt{\rho_0}/r_c \tag{3.1}$$

They found that gamma-ray luminosity peaks for GCs at intermediate values of Λ, with GCs of low and high Λ values exhibiting a lesser gamma ray luminosity likely due to low and high values of Λ suppressing the formation of the binary systems necessary for MSP spin-up. [94] also shows that metallicity [Fe/H] is not important to MSP formation (as expected via increased magnetic braking and consequent Roche lobe overflow of a binary MSP companion) as the GC detections are not clustered by high metallicity and high encounter rate on a metallicity encounter rate plot. It is noteworthy that 8 of their 23 detected GCs emit in the 10-20 GeV range with 2 of these GCs, 2MS-GC01 and NGC 6440, also showing emission in the 20-30 GeV range. This is at odds with the traditional notion of MSP generated gamma-ray emission with energy cut-offs of a few GeV.

The *Fermi*-LAT detection of GCs with energies above 10 GeV is also evident in the 3FHL or "Third Catalog of Hard *Fermi*-LAT sources" [25] which analyses 7 years of PASS 8 data in the higher energy range (by LAT standards) of 10 GeV$-$2 TeV. This survey achieves sensitivities of 0.5% and 1% of the Crab nebula flux above 10 GeV for high latitude and in-plane sources respectively, equivalent to a photon flux sensitivity of $4.4-9.5 \times 10^{-11}$ cm^{-2} s^{-1}. The 3FHL lists just two GCs, 47 Tuc and Terzan 5.

Finally, the latest *Fermi*-LAT catalog, the 4FGL, contains the spectral models, fluxes and locations of 31 source associations with GCs and 2 source associations with gamma-ray bright pulsars, J1823-3021A and J1824-2452A which reside in the GCs NGC 6624 and NGC 6626 respectively. I list the names, 4FGL source IDs, along with equatorial and Galactic co-ordinates in Table 3.1 and detection significance with photon and energy fluxes in Table 3.2.

3.2.2 Globular Cluster Observations made with IACTs

Shortly after the initial *Fermi*-LAT detection of 47 Tuc demonstrated that GCs are sources of gamma-ray emission, the 3 *northerly* GCs NGCs 7078, 6205 and 5904 were selected for 6.5$-$15 h of VERITAS observations on the basis of their location, pulsar population and intensity of their central radiation field, but no significant detection was made. The UL energy fluxes determined for NGCs 7078, 6205 and 5904 were 1.6, 2.2 and 0.6% of the Crab flux respectively, for energies $>$ 600 GeV [195]. Thereafter, 90 h of H.E.S.S. I array observations at an optimum zenith angle of 20.4° detected Terzan 5 as an extended region of emission extending beyond the H.E.S.S. PSF of 0.07° [15]. The optical centre of the GC was detected with a significance of 5.3σ as part of the region of extended emission which had a higher significance of 7.5σ offset from the GC core. The probability of this detection overlapping with another very high energy (VHE) counterpart such as a young pulsar wind nebula was estimated by [15] to be 10^{-4} by considering the known distribution

Name	4FGL Source ID	RA (Degrees)	Dec (Degrees)	l (Degrees)	b (Degrees)
NGC 6341	4FGL J1716.8+4310	259.20	43.17	68.38	34.92
NGC 6838	4FGL J1953.6+1846	298.42	18.78	56.73	-4.54
NGC 7078	4FGL J2129.9+1208	322.48	12.14	64.99	-27.32
NGC 5904	4FGL J1518.8+0203	229.70	2.05	3.89	46.73
GLIMPSE C01	4FGL J1848.7-0129	282.20	-1.50	31.30	-0.10
NGC 6218	4FGL J1647.2-0154	251.81	-1.91	15.75	26.33
NGC 6402	4FGL J1737.5-0313	264.39	-3.22	21.34	14.83
GLIMPSE C02	4FGL J1818.5-1656	274.65	-16.94	14.17	-0.65
2MS-GC01	4FGL J1808.8-1949c	272.21	-19.83	10.53	0.00
NGC 6440	4FGL J1748.9-2021	267.23	-20.36	7.74	3.79
NGC 6717	4FGL J1855.1-2243	283.78	-22.72	12.86	-10.91
NGC 6093	4FGL J1616.9-2257	244.24	-22.96	352.68	19.49
NGC 6656	4FGL J1836.8-2354	279.21	-23.91	9.94	-7.64
NGC 1904	4FGL J0524.4-2413	81.10	-24.22	226.92	-29.20
Terzan 5	4FGL J1748.0-2446	267.02	-24.77	3.85	1.69
PSR J1824-2452A NGC 6626	4FGL J1824.6-2452	276.16	-24.87	7.81	-5.60
NGC 6316	4FGL J1716.7-2808	259.18	-28.15	357.18	5.74
NGC 6304	4FGL J1714.2-2928	258.57	-29.48	355.78	5.41
NGC 6528	4FGL J1804.9-3001	271.24	-30.03	1.18	-4.19
NGC 6266	4FGL J1701.2-3006	255.30	-30.11	353.58	7.32
PSR J1823-3021A NGC 6624	4FGL J1823.5-3020	275.89	-30.35	2.79	-7.89
Terzan 1	4FGL J1735.7-3026	263.94	-30.44	357.59	1.02
Terzan 2	4FGL J1727.6-3050	261.91	-30.85	356.30	2.26
NGC 6652	4FGL J1835.7-3258	278.94	-32.97	1.55	-11.37
NGC 6441	4FGL J1750.3-3702	267.58	-37.05	353.55	-5.02
NGC 6139	4FGL J1627.6-3852	246.91	-38.87	342.34	6.92
NGC 6541	4FGL J1807.8-4340	271.96	-43.67	349.31	-11.14
NGC 6388	4FGL J1736.2-4443	264.06	-44.72	345.56	-6.73
NGC 5139	4FGL J1326.6-4729	201.67	-47.49	309.08	14.96
NGC 6397	4FGL J1741.1-5341	265.29	-53.68	338.19	-12.02
NGC 6752	4FGL J1910.8-6001	287.72	-60.02	336.45	-25.64
NGC 2808	4FGL J0912.1-6449	138.05	-64.82	282.17	-11.22
47 Tuc	4FGL J0024.0-7204	6.01	-72.08	305.90	-44.89

Table 3.1 The 33 sources of the 4FGL (listed in RA order) which are associated with GCs with name, 4FGL source ID, Catalog Co-ordinates RA/DEC and Galactic l and b. NGC 6624 and NGC 6626 are classified as pulsars in the catalog due to the emission predominantly coming from a pulsar (PSR) source.

Name	4FGL Source ID	Detection Significance	Photon Flux 10^{-8} cm^{-2} s^{-1}	Energy Flux 10^{-11} erg cm^{-2} s^{-1}
2MS-GC01	4FGL J1808.8-1949c	4.1	0.16 ± 0.03	2.44 ± 0.68
NGC 1904	4FGL J0524.4-2413	4.8	0.01 ± 0.00	0.28 ± 0.05
NGC 6304	4FGL J1714.2-2928	5.3	0.04 ± 0.01	0.62 ± 0.13
NGC 6397	4FGL J1741.1-5341	5.4	0.03 ± 0.01	0.46 ± 0.10
NGC 6341	4FGL J1716.8+4310	6.0	0.02 ± 0.00	0.23 ± 0.05
NGC 6528	4FGL J1804.9-3001	6.0	0.06 ± 0.01	0.54 ± 0.14
NGC 7078	4FGL J2129.9+1208	6.6	0.02 ± 0.00	0.38 ± 0.06
NGC 6218	4FGL J1647.2-0154	6.7	0.02 ± 0.00	0.14 ± 0.03
NGC 5904	4FGL J1518.8+0203	6.7	0.03 ± 0.01	0.15 ± 0.03
NGC 6838	4FGL J1953.6+1846	6.9	0.04 ± 0.01	0.41 ± 0.10
NGC 6402	4FGL J1737.5-0313	7.1	0.06 ± 0.01	0.27 ± 0.05
NGC 6139	4FGL J1627.6-3852	7.2	0.06 ± 0.01	0.68 ± 0.12
Terzan 2	4FGL J1727.6-3050	7.5	0.11 ± 0.02	0.58 ± 0.11
NGC 6717	4FGL J1855.1-2243	7.7	0.04 ± 0.01	0.53 ± 0.09
NGC 6656	4FGL J1836.8-2354	8.4	0.07 ± 0.01	0.41 ± 0.08
Terzan 1	4FGL J1735.7-3026	9.0	0.17 ± 0.02	0.73 ± 0.09
NGC 6541	4FGL J1807.8-4340	10.1	0.06 ± 0.01	0.38 ± 0.07
NGC 2808	4FGL J0912.1-6449	10.3	0.05 ± 0.01	0.32 ± 0.06
GLIMPSE C02	4FGL J1818.5-1656	10.6	0.34 ± 0.03	3.13 ± 0.63
NGC 6093	4FGL J1616.9-2257	10.7	0.07 ± 0.01	0.43 ± 0.09
NGC 6652	4FGL J1835.7-3258	11.6	0.08 ± 0.01	0.47 ± 0.06
NGC 6316	4FGL J1716.7-2808	15.4	0.16 ± 0.01	0.90 ± 0.10
NGC 6752	4FGL J1910.8-6001	15.4	0.07 ± 0.01	0.33 ± 0.04
NGC 6440	4FGL J1748.9-2021	16.5	0.21 ± 0.02	1.64 ± 0.22
GLIMPSE C01	4FGL J1848.7-0129	18.7	0.78 ± 0.06	3.88 ± 0.53
NGC 6441	4FGL J1750.3-3702	20.8	0.20 ± 0.01	1.48 ± 0.13
NGC 5139	4FGL J1326.6-4729	24.0	0.21 ± 0.01	1.10 ± 0.09
PSR J1823-3021A NGC 6624	4FGL J1823.5-3020	26.9	0.21 ± 0.01	1.41 ± 0.08
PSR J1824-2452A NGC 6626	4FGL J1824.6-2452	28.0	0.30 ± 0.01	2.22 ± 0.12
NGC 6266	4FGL J1701.2-3006	33.8	0.32 ± 0.01	1.84 ± 0.11
NGC 6388	4FGL J1736.2-4443	33.8	0.31 ± 0.01	1.87 ± 0.11
Terzan 5	4FGL J1748.0-2446	58.3	1.26 ± 0.03	7.67 ± 0.36
47 Tuc	4FGL J0024.0-7204	77.6	0.44 ± 0.01	2.61 ± 0.08

Table 3.2 The 33 sources of the 4FGL associated with GCs ordered by detection significance with name, 4FGL source ID, detection significance (in σ units), photon and energy fluxes.

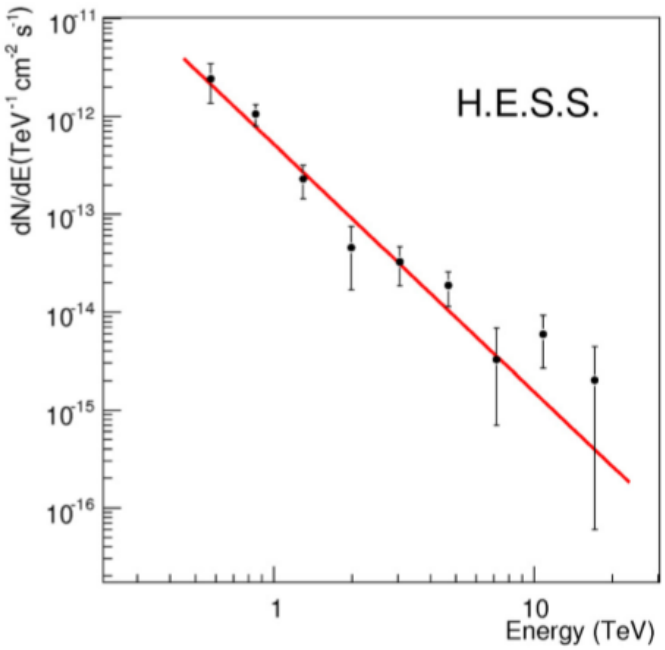

Fig. 3.2 The H.E.S.S. gamma-ray spectrum of Terzan 5 fitted with a soft power law (spectral index $\Gamma = 2.5$). Figure taken from [15].

of VHE sources with Galactic latitude *b* in [76]. The Terzan 5 spectrum is fitted with a soft power law (Fig. 3.2, spectral index $\Gamma = 2.5$) while its photon flux is 1.5% of the Crab flux in the 0.44−24 TeV range, just above the 1% Crab flux sensitivity of the instrument for 25 h of observations. The detection of Terzan 5 remains the first and only detection of a GC with an IACT. Subsequently, H.E.S.S. I attempted to detect VHE emission of energies $>$ 100 GeV for 15 GCs at zenith angles of 11.8°−49.8° with observation times of 4.2h−46.7h [16]. Of these 15 GCs, curiously only 3 are recognised *Fermi*-LAT gamma-ray emitters; 47 Tuc, NGC 6388 and NGC 7078. No detection was made of any GC in the sample, either as point sources or as areas of extended emission. The UL photon fluxes of the 15 GCs were $(0.53-4.5)\times10^{-12}$ cm^{-2} s^{-1} for energy thresholds of (0.16−0.72) TeV.

The most intensively observed GC, using an IACT, is NGC 7078 with 165 h of MAGIC observations [17]. This GC was chosen for observation because it is observable at optimum zenith angles from the MAGIC site in La Palma (culminating at a minimum zenith of 16°). However NGC 7078 was undetected and has an UL photon flux for energies $>$ 300 GeV of 3.2×10^{-13}cm^{-2} s^{-1}. MAGIC has also observed the GC NGC 6205 at low zenith angles (8°−31°) obtaining an UL of 5.1×10^{-12} cm^{-2} s^{-1} for energies of 200 GeV and above.

Finally it is worth noting that H.E.S.S. I has also conducted a survey of the Galactic plane [4] with 2700 h of observations in the energy range 0.2−100 TeV for Galactic longitudes

$l = 250°-65°$ and latitudes $|b| \leq 3°$, hereafter the "HGPS". The HGPS achieves worst case sensitivities of 1.5% of the Crab flux for point like sources and while no new GCs are detected, it re-confirms the detection of Terzan 5. The sensitivity of the survey allows me to set a VHE UL constraint on GCs in the Galactic plane, source confusion not withstanding, by comparing the l and b range used in the HGPS with the Harris Online Catalog of Globular clusters[1] for GCs at helio distance $\leq$ 12.9 kpc (this distance is chosen because it is the distance to furthest gamma-ray emitting GC in the 4FGL catalog: NGC 1904 at 12.9 kpc). This identifies 22 GCs within the Galactic l and b range surveyed in the HGPS which likely have no VHE emission above 1.5% of the Crab flux. A comparison of these GCs with the the 4FGL identifies 5 of these GCs as gamma-ray emitting sources. I list these 22 GCs in Table 3.3 along with their heliocentric distance and co-ordinates and the 4FGL source identifier of the 5 GCs detected with *Fermi*-LAT.

3.2.3 Modelling Globular Cluster Emission

In [281] the gamma-ray emission of 47 Tuc and Terzan 5 is modelled using a pair-starved polar cap model for their MSPs where primary electrons are accelerated out towards the light cylinder radius (where the electric and magnetic space influenced by the MSP co-rotates at the speed of light) without significant pair-production. The spectral energy distribution of the 2 GCs is then predicted as a combination of direct magnetospheric gamma-ray emission from the MSP and the inverse Compton scattering of the GC photon field by relativistic leptons. This model reproduces the spectral shapes and differential fluxes of the *Fermi*-LAT observations of 47 Tuc and Terzan 5. The model also predicts the correct flux level for the $E >1$ TeV H.E.S.S observations of Terzan 5 but not the spectral shape, with the spectrum predicted to peak at $\gtrapprox$ 1 TeV when in fact a reasonably flat spectrum (within errors) is observed in the $1-100$ TeV range. The same model also predicts a similar very high energy peak for 47 Tuc (as yet unobserved) which the authors indicate should be detectable with 50 h of CTA observations (Fig. 3.3).

The broadband X-ray to gamma-ray spectral energy distribution of Terzan 5 is also modelled in [162]. Here the model comprises a transport equation, a power law lepton injection spectrum and an estimation of the GC soft-photon field. The model is used to determine radiation losses due to inverse Compton upscattering of soft ambient photons in the GC along with X-ray emission produced by synchrotron processes and to integrate the resulting flux along the line of sight. This model fits the *Fermi*-LAT and H.E.S.S spectral energy distributions well but is at odds with the *Chandra* X-ray observations of Terzan 5

[1] Harris Online Catalog of 157 Globular Clusters 2010 version accessed 1st May 2020 https://heasarc.gsfc.nasa.gov/W3Browse/all/globclust.html

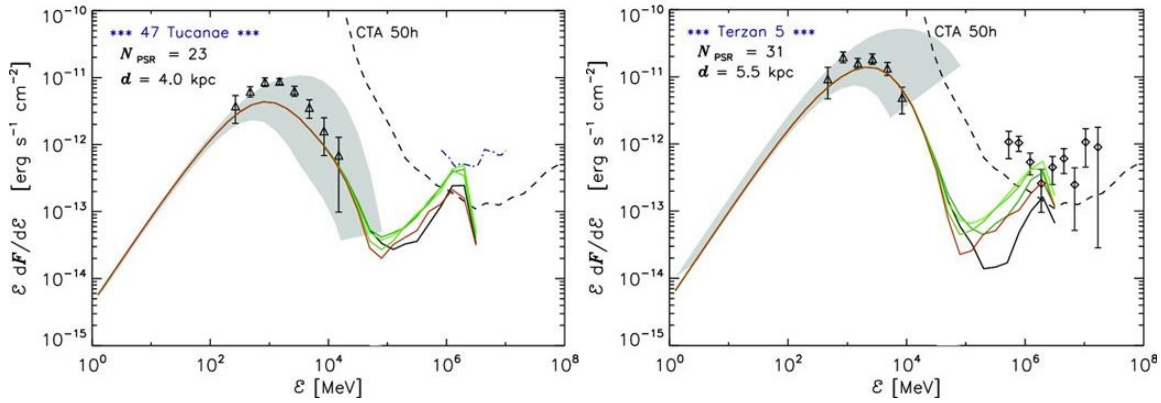

Fig. 3.3 The predicted total (magnetospheric and inverse Compton scattering gamma-ray emission, grey band is uncertainty), from 47 Tuc and Terzan 5 with black, green, brown lines indicating GC B field from 0.3 to 30 μG, assuming distances and number of MSPs as caption. Triangles are *Fermi*-LAT observations from [10], for Terzan 5 diamonds are H.E.S.S. observations in the TeV range from [15]. 47 Tuc blue dotted line in TeV range is an UL from [23]. CTA 50h sensitivity curve also shown. Figure taken from [281].

[104] as it predicts a cut-off spectrum in the $1-10$ keV band whereas in [162] an increasing X-ray flux is derived from the counts spectrum of [104]. The authors of [162] indicate that additional physical processes apart from X-ray synchrotron radiation should be considered to account for this, and model this as an additional high energy synchrotron radiation component in [206]. This model is then re-applied by the same group in [205] with an emission model which employs MSPs as the source of relativistic particles which again upscatter the soft photons of the modelled GCs and produce X-rays via synchrotron process. This model is again able to reproduce the VHE component in Terzan 5 observed using H.E.S.S. but the predicted X-ray flux remains at odds with *Chandra* observations as described above although the observed X-ray flux is used as a UL constraint in the model. The authors of [205] also do not choose to constrain or compare their model to *Fermi*-LAT observations on the grounds that MSP emission due to curvature radiation is not included. For this reason I consider the GeV flux predictions of this model to be an under estimate and I will re-examine this point further in Chapter 5. The authors also use the model to predict the spectral energy distributions of the 15 GCs observed using H.E.S.S. in [16] (of which only Terzan 5 was detected) and conclude that of these 15 the GCs 47 Tuc and NGC 6388 should be observable with H.E.S.S. in 100 h of observations and that 47 Tuc, NGC 6388, Terzan 5 , Djorg 2 and Terzan 10 are the most promising for future detection using CTA.

The offset gamma-ray emission of Terzan 5 is considered in [54] where it is proposed that stellar and MSP winds mix and interact with the Galactic medium to form a bow-shock

nebula which is presumed to be populated with relativistic leptons. Gamma-ray emission then arises from the shock front due to inverse Compton up-scattering of optical, infra-red and microwave background photons by the relativistic lepton population in the shock. It is predicted that the morphology of gamma-ray emission will reflect that of the shock front. For low latitude GCs such as Terzan 5, which are within a denser Galactic medium, an offset bow shock relatively close to the GC centre is predicted, whereas for GCs at higher latitudes, in lower density regions of the Galactic medium, spherically-shaped emission is predicted, centered on the GC core and at a greater distance from it than the low latitude case. I will examine in this work whether *Fermi*-LAT observations support this hypothesis. One of the authors of [54] also applies similar shock front arguments to individual MSPs [53], which I refer to subsequently. Finally, Terzan 5 is currently undetected with the HAWC observatory in the latest 2HWC catalogue [14].

Name	4FGL Source ID	heliocentric distance (kpc)	RA (degrees)	Dec (degrees)	l (degrees)	b (degrees)
NGC 6544		3.0	271.84	-25.00	5.84	-2.20
2MS-GC01	4FGL J1808.8-1949c	3.6	272.09	-19.83	10.47	0.10
GLIMPSE01	4FGL J1848.7-0129	4.2	282.21	-1.50	31.30	-0.10
Terzan 12		4.8	273.07	-22.74	8.36	-2.10
2MS-GC02		4.9	272.40	-20.78	9.78	-0.62
GLIMPSE02	4FGL J1818.5-1656	5.5	274.63	-16.98	14.13	-0.65
Terzan 10		5.8	270.90	-26.07	4.49	-1.99
Pal 6		5.8	265.93	-26.22	2.09	1.78
Pal 10		5.9	289.51	18.57	52.44	2.72
Djorg 2		6.3	270.45	-27.83	2.76	-2.51
Terzan 1	4FGL J1735.7-3026	6.7	263.95	-30.47	357.57	1.00
Terzan 6		6.8	267.69	-31.28	358.57	-2.16
Terzan 5	4FGL J1748.0-2446	6.9	267.02	-24.78	3.84	1.69
Terzan 9		7.1	270.41	-26.84	3.60	-1.99
Terzan 4		7.2	262.66	-31.60	356.02	1.31
Terzan 2	4FGL J1727.6-3050	7.5	261.89	-30.80	356.32	2.30
UKS 1		7.8	268.61	-24.15	5.13	0.76
NGC 6749		7.9	286.31	1.90	36.20	-2.20
Lynga 7		8.0	242.77	-55.32	328.77	-2.80
Liller 1		8.2	263.35	-33.39	354.84	-0.16
HP 1		8.2	262.77	-29.98	357.43	2.12
FSR 1735		9.8	253.04	-47.06	339.19	-1.85

Table 3.3 The 22 GC with a heliocentric distance $\leq$ 12.9 kpc (the distance to the furthest 4FGL GC NGC 1904) which could be expected to have an UL flux of 1.5% of the Crab in the energy range 0.2$-$100 TeV on the basis of the HGPS. The celestial and Galactic co-ordinates for each GC are listed. The 4FGL source ID is also shown for those GCs which are recognised gamma-ray emitters in the 4FGL.

3.3 Gamma-ray emission from Millisecond Pulsars

3.3.1 Observations of Gamma-Ray Emission from Millisecond Pulsars

In 2009 the *Fermi*-LAT established 8 MSPs as pulsed gamma-ray emitters using just 8 months of observations combined with radio timing data [6] and also confirmed the tentative detection of the MSP J0218+4232 with the EGRET experiment on the *Compton Gamma-Ray Observatory* [164]. The initial discoveries of [6] showed that the peaks of radio and gamma-ray emission in MSPs need not be co-incident, favoring different emission regions for radio and gamma-rays and supporting the prevailing slot-gap and outer gap models of gamma-ray emission. The most recent published catalogue of gamma-ray pulsars is "The Second *Fermi* Large Area Telescope Catalog of Gamma-Ray Pulsars" or 2PC, compiled by the *Fermi*-LAT collaboration [11] (with the 3PC in preparation at the time of writing [179]). This catalogue uses 3 yr of *Fermi*-LAT observations to identify 40 MSPs above 0.1 GeV by three search methods which mitigate the problem of sparse gamma-ray observations where an MSP may emit a *detectable* gamma-ray photon only once in a few million rotations. Firstly, the known MSP rotation ephemerides obtained by X-ray or in most cases radio, timing, are used as a basis to phase-fold the gamma-ray data to look for gamma-ray peaks. Alternatively, a blind periodicity search can be used with targets drawn from the 2FGL catalog which are identified as candidate pulsars by long-term stability and spectra that can be fitted by an exponential cut-off in the GeV band. This helps to identify MSPs which may have been missed due to their being in a binary system where Doppler shifts from orbital motion can smear the X-ray and radio signal. Finally, radio pulsar discoveries can lead to gamma-ray pulsar discoveries where unassociated LAT sources are searched for evidence of radio pulsations, an ephemeris is derived and the gamma-ray data phase-folded as in the first method above. This last strategy has detected 20 of the 40 MSPs listed in the 2PC. The 40 MSPs have short periods, P,$<$ 6 ms and spin-down slowly compared to young pulsars with period derivatives, $\dot{P}$, of 10^{-20} ss^{-1} and spin-down power, $\dot{E}$, of $10^{33}-10^{34}$ erg s^{-1}. Their observed photon fluxes are $(0.2-9.2)\times10^{-8}$ cm^{-2} s^{-1} and energy fluxes $(0.3-11)\times10^{-11}$ erg cm^{-2} s^{-1}. The phase-folded light curves of the MSPs most commonly exhibit 1 or 2 peaks (13 and 24 MSPs respectively) but 3 peaks occur in 3 MSPs. The energy cut-off of the exponential power law used to fit the spectra is 1.2$-$5.3 GeV. A typical exponential power law fit of an MSP is shown in Fig. 3.4.

The gamma-ray luminosities L_γ are $10^{32}-10^{34}$ erg s^{-1} which, by comparison with the higher and more restrictive range of $\dot{E}$, indicates a typical efficiency of conversion of spin-down power to gamma-ray luminosity of $\eta < 1$, with $\eta = L_\gamma/\dot{E}$. In the 2PC, η is typically 0.1 (or 10%) for MSPs but can be much higher, with one lower-luminosity MSP J0610-2100 ($L_\gamma = 10^{33}$ erg s^{-1}) having $\eta = 10$, although this is uncommon. In a more recent study

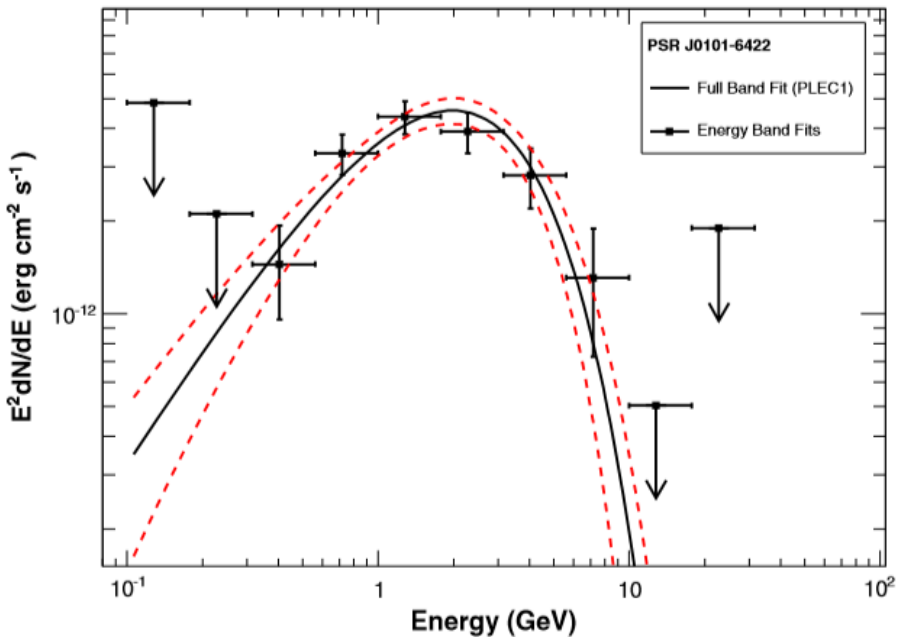

Fig. 3.4 The gamma-ray spectrum of a typical MSP J0101-6422 fitted with a power law with an exponential cut-off (PLEC1) . Figure taken from the 2PC [11].

than the 2PC, an analysis of 19 MSPs with 7 years of PASS 8 *Fermi-LAT* event data in the range 0.1−300 GeV shows that the empirical MSP death-line (or $\dot{E}$ below which gamma-ray emission cannot be detected) is 8×10^{32} erg s^{-1} [117]. This analysis also demonstrates that L_γ is uncorrelated with $\dot{E}$, showing a nearly 2 orders of magnitude of scatter for MSPs with an $\dot{E}$ of 10^{34} erg s^{-1}. For $\dot{E} > 5\times10^{34}$ erg s^{-1}, L_γ is directly proportional to $\sqrt{\dot{E}}$. The MSP death-line below which individual MSPs cannot be detected could potentially allow an observationally unconstrained population of lower-luminosity MSPs to contribute to overall GC emission whilst we remain ignorant of the true extent of such a contribution. Similarly the wide variation of the relationship between η, L_γ and $\dot{E}$ makes it difficult to deduce gamma-ray luminosities *a priori* from MSP timing information alone.

At higher energies of 10 GeV−2 TeV the 3FHL catalog identifies 15 MSPs at Galactic latitude $|b| \geq 10°$ with 13 previously identified as pulsed gamma-ray emitters using the LAT whilst the remaining 2 are radio pulsars previously undetected in gamma-rays.

Above the energies observable with *Fermi*-LAT, there are also hints for the production of TeV halos around MSPs as are clearly seen in HAWC results from the young Geminga and Monogem pulsars. The authors of [137] examined 24 MSPs in HAWC's field of view selected on the basis of higher spin-down fluxes (defined as $\dot{E}/d^2 > 5\times10^{33}$ erg kpc^{-2} s^{-1}). Using a public access tool provided by the HAWC collaboration they obtained a weak indication of an extended TeV halo in 4 MSPs of 2.1−2.6 σ. They cited the overall significance of

the TeV halo detection to be 3.1 σ for the stacked analysis on the basis of the significance distribution.

Finally, the detection of pulsed gamma-ray emission at 5.4 σ and 7 σ significance using *Fermi*-LAT from the MSPs B1821-24 [151] and J1823-3021A [109] located in the GCs NGC 6626 and NGC 6624 respectively provides the most direct observational link between MSP gamma-ray emission and GCs. It is striking that NGC 6624 is not detected in gamma-rays in the off-pulse phase of J1823-3021A and so J1823-3021A must account for nearly all the gamma-ray emission of this GC [109].

3.3.2 Modelling Millisecond Pulsar Emission

One site of gamma-ray production was once presumed to be the polar cap of the pulsar [208, 121, 87] but observations using *Fermi*-LAT have shown this not to be the case as the expected very *sharp* super exponential cut-off due to magnetic absorption at the polar surface is not seen [248, 11] and in addition the phase-folded peaks of polar emitted radio and gamma-ray emission are not co-incident, hinting at a different emission region for gamma-rays [152].

The literature consensus emission model of MSPs is that of an electric field, $E_{||}$, parallel to the magnetic field lines of the star which accelerates leptons to ultra-relativistic energies in gap structures bounded by the magnetic field lines [265]. The leptons emit gamma-rays via synchro-curvature and inverse Compton processes and at the same time the gamma-rays themselves can convert to electron/positron pairs and be further accelerated and further emit gamma-rays so the process continues in a cascading fashion [265]. The gaps themselves can either be placed high in the magnetosphere in the "slot gap" model (SG) [202, 203] or in the "outer gap" (OG) where the gap is placed only in the outer magnetosphere [78]. A newer alternative to the gap models is the stripped wind (SW) [74] or equatorial current sheet models [73, 260] although as yet there is insufficient modelling or observation to prefer these over the SG and OG models [75].

I summarise the schematic elements of the pulsar system in Fig. 3.5. I restrict my discussion of MSP models to those that either attempt to account for existing *Fermi*-LAT observations of MSPs, specifically the phase-folded light curves and fluxes, or make specific predictions of very high energy emission that can be tested with existing and future IACTs.

The state of the art of simulating gamma-ray emission from MSPs are three dimensional global kinetic magnetosphere models where the lepton trajectories and the corresponding electromagnetic fields are treated self-consistently using a particle-in-cell (PIC) [73, 77, 72, 220] code as exemplified in [153] Here, the self-consistent treatment arises from integrating time-dependent Maxwell's equations using the current generated during the lepton's motion.

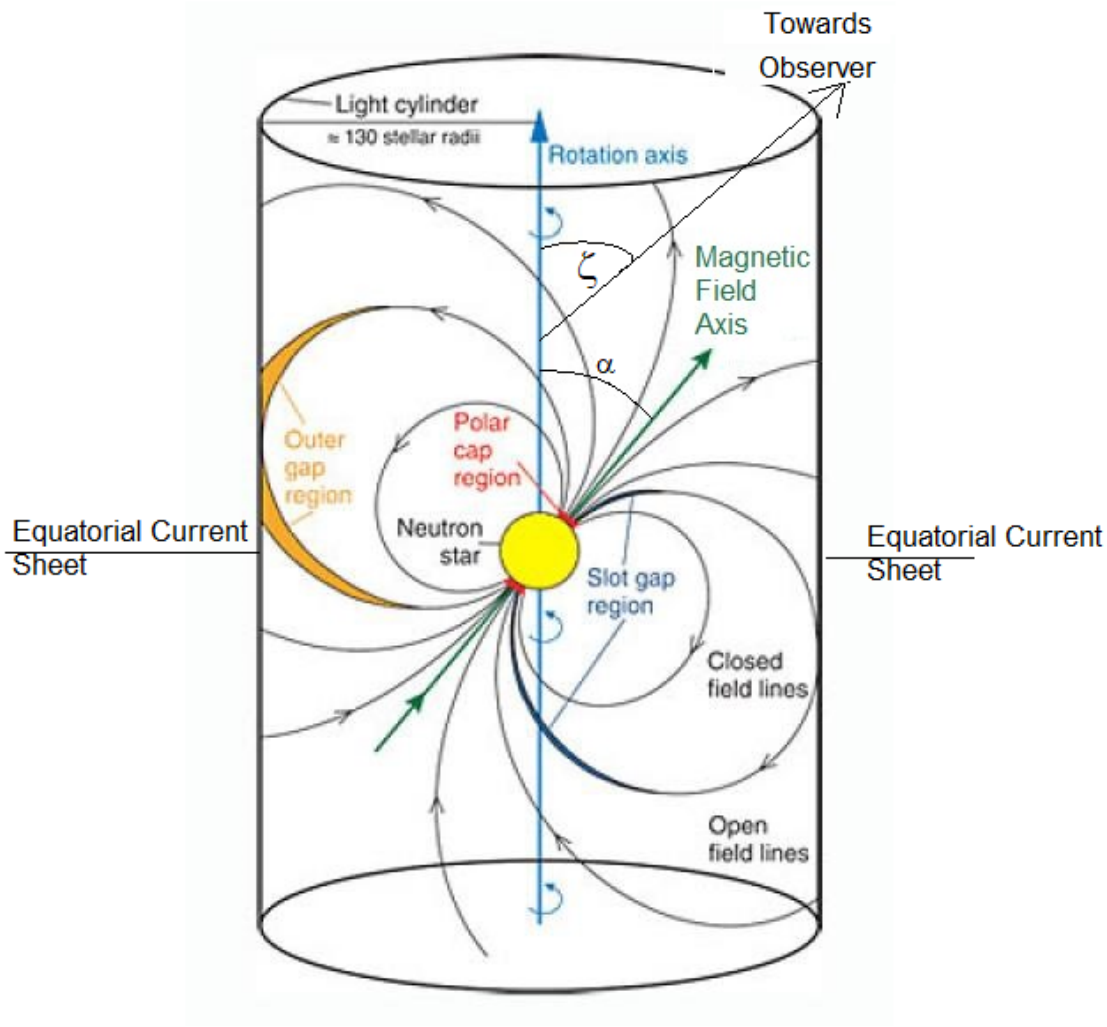

Fig. 3.5 The schematic elements of the pulsar system which shows the offset between rotational and magnetic axes and the position of the polar cap, SG and OG regions and the light cyclinder with equatorial current sheets beyond it. Also shown are the magnetic field lines and angles between the magnetic axis , observer line of sight and the rotation axis of the star (α and ζ respectively). Figure adapted from [29].

The equations of motion are then integrated over the same time step as the motion whilst allowing for the magnetosphere field structure; this is done repeatedly for all particles while varying the lepton injection rate F. These simulations are able to reproduce the observed gamma-ray luminosity proportionality to $\dot{E}$ and $\sqrt{\dot{E}}$ for lower and higher $\dot{E}$ values respectively and the range of energy cut-off (E_c) values observed in MSPs with *Fermi*-LAT. It is seen that increasing F decreases E_c and that E_c is directly proportional to $\dot{E}$. For $\dot{E}$ $\leq 10^{32}$ erg s^{-1} the E_c values generated are smaller than those observed with *Fermi* and are close to the detection threshold. This highlights that a knowledge of MSP $\dot{E}$s and hence the expected range of $\dot{E}$ given by the luminosity function of MSPs is crucial in determining the spectra expected from MSPs either singly or en-masse in GCs.

MSP emission models which rely on a small number of free physical parameters with a wider set of values set to notional fiducial parameters are also able to reproduce the spectral characteristics of MSPs. This is exemplified in [266] where the modelled spectrum arising from synchro-curvature radiation generated by leptons moving along magnetic field lines, matches the phase averaged spectra of 22 MSPs in the 2PC. This relatively simple model is able to exclude gamma-ray emission close the surface of the star by varying just 3 parameters, the parallel electric field component, $E_{||}$, in the gap, the length scale over which photons are emitted, X_0, and a normalisation, N_0, which reflects the number of leptons moving along field lines.

In [75], the two emission models of OG and SW are considered. A Markov chain Monte Carlo method is able to pick best-fitting model parameters for both OG and SW models and to reproduce well the *individual* phase-folded light curves, fluxes and cut-off energy of 22 MSPs listed in the 2PC [11] which exhibit double peak structures in their gamma-ray light curves. However, the authors note that the preferred model remains unknown as both can yield satisfactory fits, with the OG model requiring a large magnetic obliquity, α (defined as the angle between the rotation axis of the pulsar and the magnetic dipole axis passing through the magnetic North and South pole of the star) and small viewing angle (defined as the difference beween spin axis and the observer line of sight), ζ, while in the SW model the converse is true. As α and ζ are not precisely constrained observationally a preferred model cannot be chosen on the basis of these angles alone.

Different modelling with a vacuum-retarded dipole model (where the magnetic field is assumed to be in the inertial frame) allows the simultaneous fitting of simulated radio and gamma-ray data to the phase-folded radio and gamma ray lightcurves of 40 MSPs [152] and this places α in the range $10°-90°$ while ζ is $70°-90°$.

In [219] modelling of pulsar gamma-ray emission is based on the radiation reaction limit where ultra-relativistic leptons in the magnetosphere follow a velocity field set by the local

electro-magnetic field alone. Using just the simple parameters of P, $\dot{P}$ (both constrained by timing observations), a fiducial B field deduced at the equator, and a range of obliquities (as this quantity is not usually known), the radiation spectra of young and millisecond pulsars can be computed and the expected power law with exponential cut off spectral shape (with a cut-off at several GeV), as in the 2PC, can be recreated. Moreover, they show that millisecond pulsars can produce fluxes around 100 GeV assuming a B field of 4.4 $\times 10^9$ G and that this flux should be detectable with 50 h of CTA-S observations.

MSPs have also been proposed as sites of higher energy emission via inverse Compton scattering processes. The authors of [53] considered the case of B1957+20, the prototype black widow MSP (defined as a binary MSP system where the companion is degenerate and of low mass < 0.03 $M_\odot$), with a bow shock nebula previously detected by $H\alpha$ emission in [167]. In the [53] model, relativistic electrons are produced either as a pulsar wind or from or from the nebula shock front directly. These relativistic electrons are collimated by the shock front and exit away from the direction of motion of the MSP. The relativistic electrons then up-scatter microwave background and infra-red photons to produce VHE gamma-ray emission predicted to peak at 1 TeV with a differential flux of 5.6×10^{-13} ergs cm^{-2} s^{-1} which the authors indicate is detectable with CTA and potentially detectable with MAGIC using 100 h of observations. As an aside, by considering differential flux sensitivity, I note that this predicted emission should be detectable with either CTA-N or CTA-S in 50 h of observations but would not be detectable using the *Fermi*-LAT at these energies. A subsequent observation of this system using MAGIC (66.5 h) [24] detects no emission and instead sets an UL of 8.0×10^{-13} ergs cm^{-2} s^{-1}, just above the shock front flux predicted above.

An alternative means of producing emission above 10 GeV is the synchrotron self-Compton (SSC) process modelled in [122] for the Crab pulsar and the bright pulsar B1821-24 in the GC NGC 6626. In the SSC process, the radiating particles are accelerated primary electrons and a spectrum of electron-positron pairs is produced in cascades near the polar cap. These particles follow paths in the slot gap using a 3D force-free magnetic field geometry (where the global field is assumed to be unchanged) and gain pitch angles through resonant absorption of radio photons. These particles then produce synchroton emission high in the magnetosphere across the light cylinder. This model can reproduce the expected fluxes and spectra of the Crab in the optical and X-ray bands, as well as VHE emission > 50 GeV as observed with MAGIC and VERITAS. The same model applied to MSP B1821-24 suggests there should be a flux peak of 1.1×10^{-12} erg cm^{-2} s^{-1} at 50 GeV. I note that this flux is only slightly below CTA-N and CTA-S sensitivity (3×10^{-12} erg cm^{-2} s^{-1} at 50 GeV for a 50 h observation).

3.4 Conclusion

Millisecond pulsars (MSPs) have long been proposed as potential sources of gamma-ray emission in globular clusters (GCs).

Longstanding observations using *Fermi*-LAT show that globular clusters are indeed gamma-ray sources with 30 such sources associated with GCs in the 4FGL catalog. GCs exhibit no evidence of gamma-ray variability on week-to-month timescales or emission extension and are consistent with point sources. The similar spectral shapes of MSPs and GCs observed with *Fermi*-LAT, with cut-offs in the $1-4$ GeV range, suggest that MSPs are sources of gamma-ray emission in GCs.

In the high-energy domain, above 10 GeV, only the GCs 47 Tuc and Terzan 5 are listed in the 3FHL catalog. Observations of GCs using IACTs have been relatively few and yielded only 1 detection (Terzan 5) which exhibits a curiously offset emission morphology, perhaps due to bow-shock emission process. The H.E.S.S. Galactic plane survey allows me to set an UL constraint of 1.5 % of Crab Flux on 22 GCs in the plane. Models of cumulative MSP magnetospheric emission and inverse Compton up-scattering of ambient photons can reproduce the spectral shape of GeV gamma-ray emission in 47 Tuc and Terzan 5 but the TeV band of Terzan 5 is only poorly fitted by such models.

In my published work I draw a link between GCs which are gamma-ray emitters and those exhibiting diffuse X-ray emission and note that the spectral shape of many GCs is at odds with the exponential cut-off shapes of MSPs which are the presumed sources of gamma-ray emission in GCs.

The *Fermi*-LAT observations also established MSPs as a population of gamma-ray sources with spectral characteristics and phase-folded light curves of 40 MSPs listed in the 2PC catalog. This allows the testing of models of MSP emission against the 2PC spectra and light-curves with simple outer and slot gap models able to reproduce the observed emission well with few free parameters. The relationship between gamma-ray luminosity and MSP spin-down power is not well defined and exhibits considerable scatter below an empirical death-line of 10^{34} erg s^{-1}, and MSPs are undetected in gamma-rays for spin-down power $< 8\times10^{32}$ erg s^{-1}. These uncertainties and detection thresholds make it difficult to assess the gamma-ray contribution of unresolved MSPs in GCs which may be otherwise well-characterised by radio or X-ray timing methods. The pulsed gamma-ray emission of single MSPs in the GCs NGC 6626 and 6624 is direct observational evidence for MSP sources of gamma-ray emission in GCs and shows that such MSPs can account for a large proportion or even the entire GC emission.

In the HE domain the 3FHL lists 15 MSPs of which 2 are radio pulsars without previously recognised gamma-ray emission. There is tentative evidence for TeV halos around MSPs using a stacked analysis of HAWC observations.

I will expand greatly on the work of my paper [181], by re-analysing 111 GCs in the energy range 100 MeV to 100 GeV using 10.5 yr of PASS 8 event data with the 4FGL catalog and present the results in Chapter 5 of this work. First, I shall analyse 47 Tuc to demonstrate my standard *Fermi*-LAT analysis technique in Chapter 4.

Chapter 4

Fermi-LAT Analysis of the Globular Cluster 47 Tuc

4.1 Introduction

The globular cluster 47 Tuc was the first GC detected at gamma-ray energies, with around 8 months of *Fermi*-LAT (large area telescope) observations providing a detection with a significance of 17 σ [7]. Later *Fermi*-LAT observations show that 47 Tuc exhibits an exponential cutoff power law spectrum between 200 MeV and 10 GeV [7, 10]. However, the previous analyses of 47 Tuc were performed using just the 2 years of *Fermi*-LAT PASS 6 data then available. Thus, the published SED for 47 Tuc is coarsely binned at 4 bins per decade of energy [10] and the analysis only extends down to 100 MeV. The latest PASS 8 data release and tools of the *Fermi*-LAT, now allow spectral analysis in the 60 - 100 MeV range, and the re-analysis described in this chapter with a further 6.5 years of photon events allows the spectral form to be refined while also serving as an exemplar of my gamma-ray analysis method for a point source. The photon event selection criteria and gamma-ray analysis method described here have previously been used in my study of 30 high Galactic latitude globular clusters wherein a spectral fit and analysis was produced for 47 Tuc [181] and the analysis presented here is a further refined and extended analysis of the 47 Tuc spectrum.

In Section 4.2 I describe my data selection and analysis method. In Section 4.3 I provide a spectral model, a spectral energy distribution (SED), light curve and flux determinations for 47 Tuc along with a test statistic (TS) map. Finally in Section 4.4, I summarise my findings.

Name	Helio Distance /kpc	Metallicity	lii	bii	M_V	Core radius	Central surface brightness	Mass x 10^5 $M_\odot$	Gamma Source Ref
47 Tuc	4.5	-0.72	305.89	-44.89	-9.42	0.36	14.38	7.0 [49]	[10]

Table 4.1 47 Tuc characteristics: helio distance (distance from Sun) in kpc and metallicity defined as [Fe/H]. lii and bii are Galactic longitude and latitude respectively in degrees, M_V is absolute visual magnitude, core radius is the radius of the GC core in arc mins and GC central surface brightness is in V Magnitudes/square arc sec from Harris 1996 (2010 Edition) [124]. GC mass and previous identification as a gamma-ray source is from the reference listed in the table.

4.2 Overview of the Gamma-ray Analysis Method

4.2.1 Photon Event Data Selection

The event data in this analysis were collected by *Fermi*-LAT between 4th Aug 2008 to 28th December 2016 (Mission Elapsed Time (MET) 2395574147[s] to 504661408[s]). I consider all PASS 8 events which are *source* class photons (evclass=128), both Front and Back converting events (evtype=3), spanning the energy range 60 MeV to 300 GeV. I choose *source* class photons because this is the recommended photon class for general analysis of non-transient sources, and Front and Back converting events because I wish to consider all valid events and have no requirement to optimise PSF by selecting a more stringent event type (such as just Front events or the PSF3 event type) which would have the disadvantage of reducing the photon events available for analysis. The energy range starts at 60 MeV, which is the practical minimum where the Background Emission Models produced by *Fermi* are considered to be valid and ends at 300 GeV as most sources have few detectable *Fermi* events above 100 GeV and emission above this is considered unlikely.

Throughout my analysis, the FERMIPY software package[1] with version V10R0P5 of the *Fermi Science Tools* is used, in conjunction with the P8R2_SOURCE_V6 instrument response functions. I apply the standard PASS 8 cuts to the data, including a zenith angle 90° cut to exclude contaminating photons from the Earth limb and good-time-interval cuts of DATA_QUAL > 0 and LAT_CONFIG = 1 which identify when the LAT is in correct data taking mode and not within the South Atlantic Anomaly which could cause unreliable events to be recorded. The energy binning used is 8 bins per decade in energy as 47 Tuc is a bright source and I expect each energy bin to have a flux value. The spatial binning is 0.1° per image pixel which is of the order of the best PSF (0.2° for 68% containment at 10 GeV) expected across the analysis range and is a standard FSSC recommendation in general.

[1] FERMIPY change log version 0.12.0 ([275])

4.2.2 Analysis Method

In my analysis method I search for significant gamma-ray emitters in a 25° width source region of interest (ROI) centred on the nominal co-ordinates for 47 Tuc in the energy range 60 MeV to 300 GeV but allow for sources out to a 40 ° source ROI width. These are derived from extrapolation of the FSSC recommended ROI and ROI source width increase for that of a 1 GeV analysis going to 100 MeV (15°/20° to 20°/30° respectively), as the worsening of the PSF from 100 MeV to 60 MeV is comparable to that between 1 GeV and 100 MeV. For front and back events combined, the 95 percent containment angle PSFs for energies of 1 GeV, 100 MeV and 60 MeV are 3°, 11° and 20° respectively.

The model I use in my likelihood analysis consists of a point source population seeded from the *Fermi*-LAT's third point source catalog (3FGL), diffuse gamma-ray emission and extended gamma-ray sources. The diffuse emission detected by the *Fermi*-LAT consists of two components: the Galactic diffuse flux, and the isotropic diffuse flux. The Galactic component is modelled with *Fermi*-LAT's gll_iem_v06.fit spatial map with the normalisation left free to vary. The isotropic diffuse emission is defined by *Fermi's* iso_P8R2_SOURCE_V6.txt tabulated spectral data. The normalisation of the isotropic emission is also left free to vary. I include all 3FGL model sources within a wider region (the source ROI) of 40° width to allow for the emission of gamma-ray sources outside the ROI which must be considered due to the PSF of the LAT in the subsequent likelihood model fit.

Initially, I run the FERMIPY *setup* and *optimize* methods to create count and photon exposure maps and to compute the TS values of all 3FGL sources in the model.

The *optimize*[2] method loops over all model components in the ROI and fits their normalization and spectral shape parameters whilst computing the TS of all sources in the ROI. The behaviour of the *Optimize* method is to use an iterative strategy. Firstly it simultaneously fits and frees the normalisation of all the sources in the model in order of the highest predicted photon count contribution to 95 percent of the predicted total photon counts for the model as a whole. It then fits the normalisation of all sources not included in this first step in order of their predicted photon counts. Finally, the *optimize* method individually fits the shape (spectral parameters) and normalisation parameters of all sources with a TS > 25.

After this initial likelihood fit, I remove all point sources with a TS < 4, or with a predicted number of photons, *npred*, < 4 from the model as they are of no significance to the overall fit. This is done using the FERMIPY *delete_source* command. I then conduct a secondary BINNED likelihood analysis again using the *optimize* method, with the normalisation of all point sources within 10° of 47 Tuc being left free, whereas point sources between 10° to 25° from 47 Tuc are frozen to their 3FGL values. The spectral parameters of 47 Tuc and its

[2]Described at https://fermipy.readthedocs.io/en/latest/fitting.html accessed on 12th March 2020

normalisation are also explicitly freed at this point. During the secondary likelihood fit the spectral shape and normalisation of all TS > 25 sources are individually fitted.

The best-fit model from this secondary likelihood fit is used with the *Fermi Science Tool* GTTSMAP, to search for new point sources in the data that were not accounted for by the 3FGL. This is necessary because we use nearly twice the integration time of event data as that used to produce the 3FGL catalog and so additional sources may now be detectable (due to increased statistics) over above those used to compile the 3FGL. In particular, I do this by running FERMIPY's *find_sources* method to detect all sources above 3σ significance. *Find_sources* is a peak detection algorithm which analyses the test statistic (TS) map to find new sources over and above those defined in the 3FGL model by placing a test point source, defined as a power law (PL) with spectral index 2.0, at *each* pixel on the TS map and recomputing likelihood. I then perform a final likelihood fit using the *fit* method with just the normalisation of all sources within 10° of 47 Tuc being left free, whereas 47 Tuc has both its normalisation and spectral parameters left free. *fit* is a likelihood optimisation method which executes a fit of all parameters that are currently free in the model and updates the TS and predicted count (*npred*) values of all sources. An excerpt of the ROI made with the *print_roi* command can be seen in Fig. 4.2 which shows the sources within 5° of 47 Tuc (3FGL J0023.9-7203 in the 3FGL catalog) which have names, spatial models (point or extended sources) and spectrum types drawn from the 3FGL along with TS values (with $\sqrt{TS}$ approximately indicating significance in σ units) and a predicted photon count (*npred*) for each source. A new source found by *Find_sources* and not included in the 3FGL catalog is PS J0000.3-7355 which is fitted with a PL spectrum by default. This listing of the ROI is used primarily to show that I have identified my main source of interest, 3FGL J0023.9-7203[3], as it has a very small angular offset from the GC optical co-ordinates of 47 Tuc which are used to set the centre of the ROI. A visual indication of quality of model fit is provided by the FERMIPY *residmap* command which convolves the smoothed data of the final model produced by my analysis with a test model. I use *residmap* to convolve the final model with a PL point source of index 2.0 (Fig. 4.1). In Fig. 4.1, the residual significance map shows that the final best-fit model produced by the analysis is a good description of the event data within 5° of 47 Tuc with mostly small $\pm 1\sigma$ residuals. Some broad 3σ residual contours are present outside this area but these likely represent fluctuations due to imperfections in the *Fermi* background model rather than un-modelled bright point sources. I next run the FERMIPY *localize* and *extension* commands to determine the best fit source position and

[3]The 4FGL name has format 4FGL JHHMM.m+DDMM with the "J" denoting, that the co-ordinate system is based on the J2000 Earth Inertial Frame, while HHMM.m is right ascension in hours, minutes and decimal minutes and DDMM is declination in degrees and minutes, signed positive or negative. The 4FGL name can be suffixed with "e" to indicate an extended source as seen in Fig. 4.2.

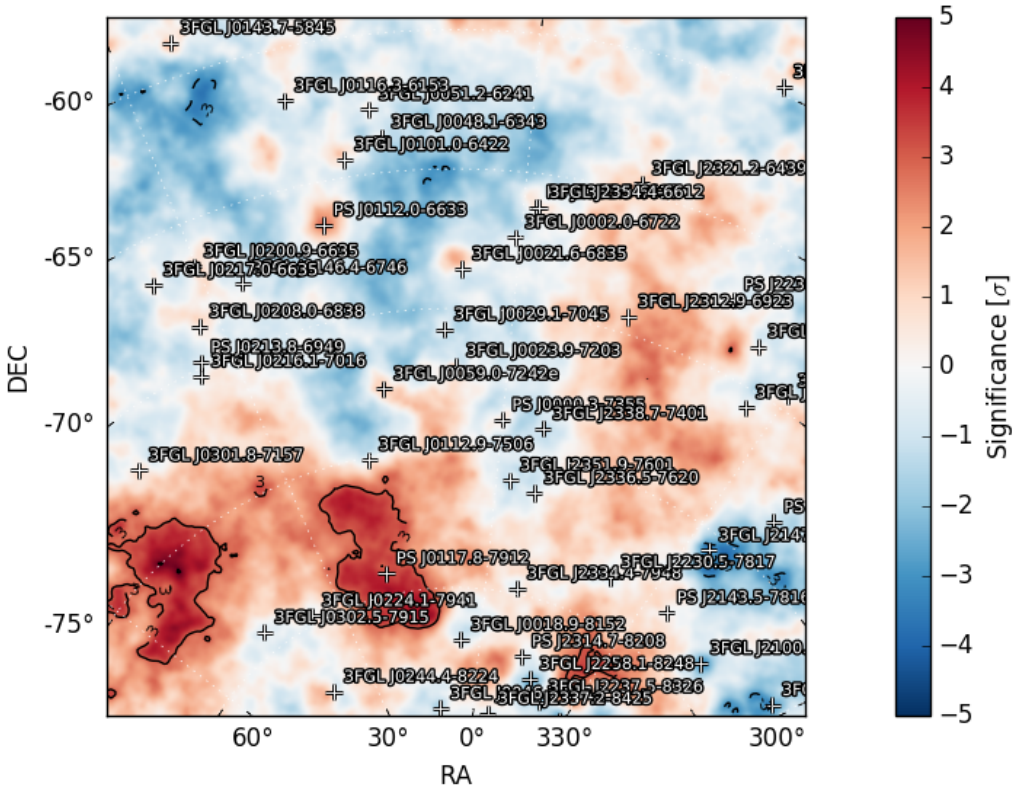

Fig. 4.1 A residual significance map with 47 Tuc (source 3FGL J0023.9-7203) in centre. The final analysis model is convolved with a point test source model, index 2.0. The final best-fit model produced by the analysis is a good description of the event data within 5° of 47 Tuc with mostly small $\pm 1\sigma$ residuals. Some broad 3σ residual contours are present outside this area but these likely represent broad fluctuations in the background model rather than undetected bright point sources.

tsmap excluding 47 Tuc so that a test statistic map is produced of the contribution from 47 Tuc alone.

Finally, I use the *sed* method to generate a spectral energy distribution for 47 Tuc, with any additional energy dispersion correction disabled. This would normally correct for the finite energy resolution of the LAT at low energies but because 47 Tuc is a known 3FGL source, this correction has already been applied in the 3FGL catalog creation and does not need to be applied again (in line with FSSC recommendations). The *sed* performs an independent fit on the normalisation of the source in each energy bin with the energy bin energy span matching that of the original analysis by default. The normalisation of each bin is fitted using a power law spectral parameterisation with a spectral index of 2.0 by default and flux upper limits are determined at the 95 percent confidence level (2σ) by default. The

name	SpatialModel	SpectrumType	offset	ts	npred
3FGL J0023.9-7203	PointSource	LogParabola	0.021	5229.51	4387.9
3FGL J0029.1-7045	PointSource	PowerLaw	1.386	280.52	2345.7
PS J0000.3-7355	PointSource	PowerLaw	2.525	113.51	3403.0
3FGL J0059.0-7242e	SpatialMap	PowerLaw	2.709	1578.50	11325.1
3FGL J0021.6-6835	PointSource	PowerLaw	3.496	58.69	2237.9
3FGL J2338.7-7401	PointSource	PowerLaw	3.822	192.61	761.3
3FGL J2351.9-7601	PointSource	PowerLaw	4.516	191.40	675.0
3FGL J0112.9-7506	PointSource	PowerLaw	4.574	126.50	828.4
3FGL J0002.0-6722	PointSource	PowerLaw	5.077	80.06	323.7

Fig. 4.2 An excerpt of the ROI listing produced at the end of the analysis within 5° of 47 Tuc (3FGL J0023.9-7203) with sources ordered by offset in degrees from the centre of the ROI. The spatial model indicates whether the source is defined as a point source or an area of extended emission as a spatial map. The spectrum types or functional form of the sources are set to their catalog values whereas one source found during the *find_sources* step is classed as a power law source by default and given a positional identifier name starting with 'PS' (PS J0000.3-7355) . At the end of the analysis the sources have a test statistic value indicating the significance of detection and a predicted number of photon counts or *npred* value.

sed method also outputs a dictionary file (in the NUMPY file format) which I use for custom plotting, for comparison of the SED with stacked MSP spectral models and in subsequent chapters for my own stacking of MSP emission.

The results of this analysis are also used for the variability (Section 4.2.3), GC extension (Section 5.3.4) and source localisation analyses.

4.2.3 Variability

I use the analysis output from 8.4.2 to construct a light curve for 47 Tuc by running the FERMIPY *lightcurve* method. *lightcurve* fits the flux in a sequence of time bins by repeating the analysis steps of 8.4.2 for each time bin whilst freeing all spectral parameters of the GC and freezing all other source parameters. An empirically chosen bin size of 6 months is used so that there are sufficient photon statistics to perform a good fit and a baseline time selection of several years to ensure the best characterisation of sources in the ROI in line with FERMIPY recommendations.

4.2.4 Spatial Extension

I also use the analysis output from 8.4.2 to check for source extension by running the FERMIPY *extension* method. *extension* replaces the GC point source spatial model with an azimuthally symmetric 2D Gaussian model. It then profiles likelihood with respect to spatial extension in a 1-dimensional scan to determine the likelihood of extension.

4.3 Results

4.3.1 GC position, Emission and Model Parameters

The localised source position, luminosity, energy flux, photon flux and spectral model parameters of 47 Tuc are listed in Table 4.3. All values reported are for the analysis between 60 MeV and 300 GeV with 8 bins per decade in energy for 47 Tuc.

4.3.2 Spectral Model

The differential flux, *dN/dE*, (photon flux per energy bin) of 47 Tuc is described through a log parabola (Eqn. 4.1) spectral model[4].

$$\frac{dN}{dE} = N_0 \left(\frac{E}{E_\mathrm{b}}\right)^{-(\alpha+\beta\log(E/E_\mathrm{b}))} \tag{4.1}$$

where *norm* = N_0, *alpha* = α, *beta* = β and E_b is a *scale* parameter.

4.3.3 47 Tuc Significance and Spectrum

Over the 8.3 year integration, 47 Tuc is detected with an overall significance of 72 σ (TS 5229). 47 Tuc is associated with an existing 3FGL catalog source 3FGL J0023.9-7203 which has a log parabola spectral model. Due to the longer exposure of my analysis, the gamma-ray spectrum of 47 Tuc (Fig. 4.4) is refined at high and low energies compared to [7] and [10]. The spectral parameters of this best-fit log parabola model (Eqn. 5.2), are listed in Table 4.3. Interestingly, Fig. 4.4 shows tension between the observed spectrum and the best-fit model, particularly at low energies where some evidence of a spectral softening is present. It can be seen that there is no significant emission below 100 MeV. Although there is evidence of emission above 10 GeV, it of lesser significance (less than 3 σ for each flux point). Above 40 GeV there is no detected emission and the upper limits shown effectively track the sensitivity of the *Fermi*-LAT.

The TS map shows the detected source to be within the tidal radius of 47 Tuc (Fig. 4.3)

4.3.4 Spatial Extension

There is no evidence for spatial extension of gamma-ray emission in 47 Tuc and it is consistent with a point-like gamma-ray emission source.

[4] As described in the FSSC source model [1]

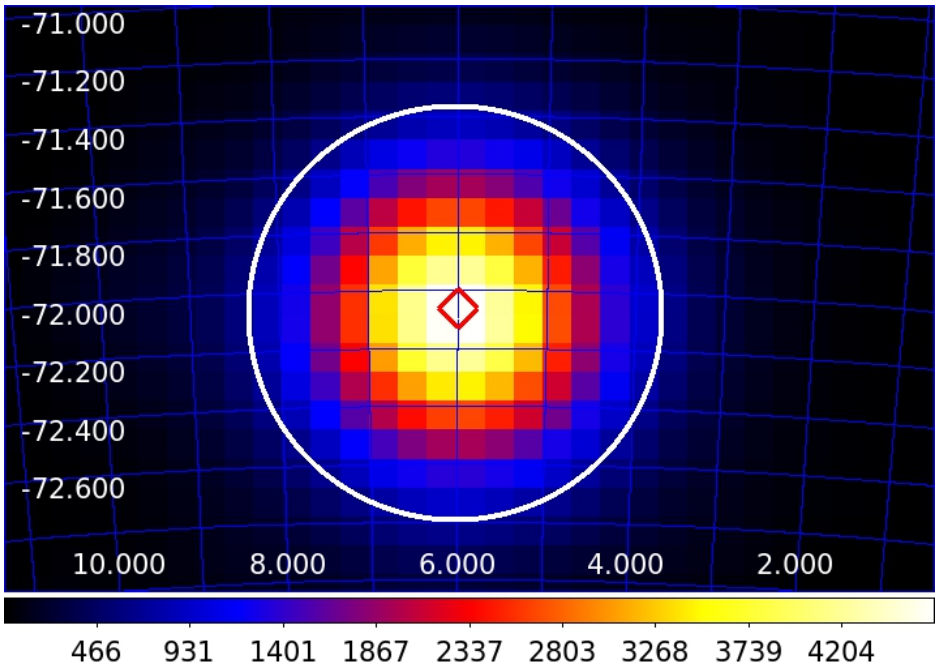

Fig. 4.3 TS map of 47 Tuc with tidal radius 0.715° (white circle) and gamma-ray detection location (red diamond) marked. Graduated color bar (bottom) shows the TS value. RA and DEC are horizontal and vertical axes respectively on the white interior scale.

4.3.5 Variability

A light curve is generated for 47 Tuc in the range between 60 MeV to 300 GeV and is binned in time bins of 6 months (Fig. 4.5). The light curve for 47 Tuc has energy flux determinations in each bin as opposed to upper limits indicating that the optimisation and fitting process has converged to an acceptable solution for each bin. A χ^2 statistic is generated for a model comparing the observed fluxes in the 6 month bins against the average flux across all bins (Table 4.2). The χ^2 statistic for 47 Tuc is less than the critical value indicating no significant variability over a 6 month timescale at a probability of p=0.95.

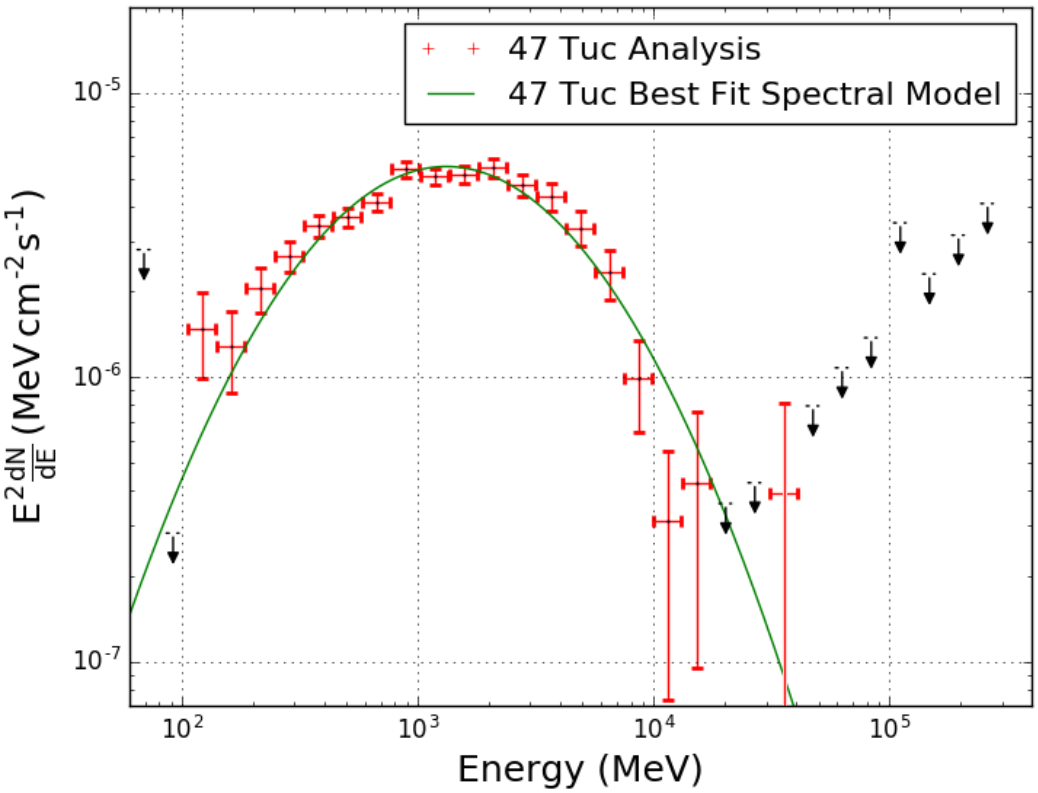

Fig. 4.4 47 Tuc SED which I plot using the dictionary produced by the FERMIPY software *sed* method. - The best fit (green line) is a log parabola as described in the FSSC source model, Eqn. 4.1, [1] with spectral parameters *norm* (7.0 $\pm$ 0.2) x 10^{-12}, *alpha* 1.67 $\pm$ 0.04, *beta* 0.38 $\pm$ 0.03 and Eb 856.5. There is no significant emission below 100 MeV or above the 40 GeV bin, where the increasing ULs effectively track the sensitivity of the instrument. The ULs are determined at the 95% confidence level.

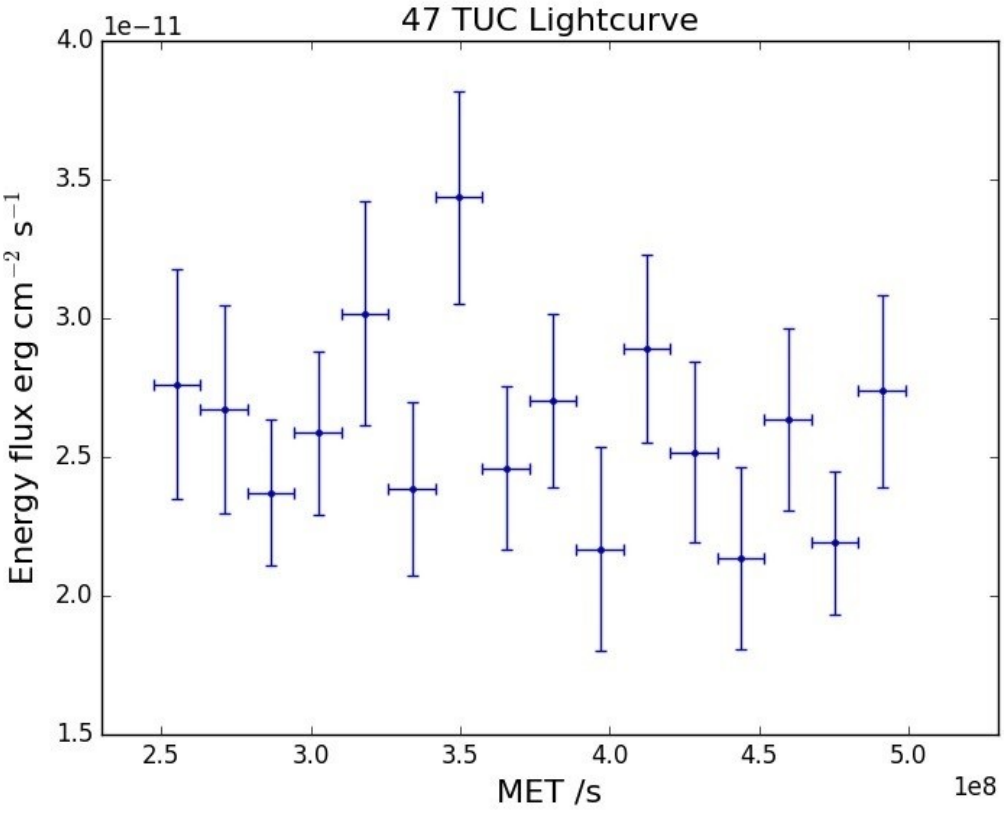

Fig. 4.5 Lightcurve for 47 Tuc which exhibits no variability on 6 month timescales at the 2 σ level. This allows exclusion of sources variable on 6-month timescales (e.g. active galactic nucleii) as a significant source of emission within the ROI of 47 Tuc.

Globular Cluster	χ^2	Degrees of freedom	Upper Critical Value p=0.95
47 Tuc	14.17	15	24.996

Table 4.2 47 Tuc χ^2 value for a model comparing variable flux with average of variable flux across all bins. The critical value is not exceeded at p=0.95 and thus there is no evidence for variability on a 6 month time scale

Globular Cluster	Source RA Degree	Source DEC Degree	Luminosity 10^{34} erg s^{-1}	Energy Flux 10^{-11} erg cm^{-2} s^{-1}	Photon Flux 10^{-8} cm^{-2} s^{-1}	*norm* 10^{-12}	α	β	Eb
47 Tuc	6.01 $\pm$ 0.01	-72.08 $\pm$ 0.01	6.29 $\pm$ 0.19	2.60 $\pm$ 0.08	2.45 $\pm$ 0.15	7.0 $\pm$ 0.2	1.67 $\pm$ 0.04	0.38$\pm$0.03	856.5

Table 4.3 Detected GC 47 Tuc with positions (RA, DEC),luminosity, energy and photon flux and LP spectral model parameters of best fit on SED. Luminosity calculated assuming the distance in Table A.1.

4.4 Conclusion

In this chapter, I describe my *Fermi*-LAT analysis of the globular cluster 47 Tuc detecting it with very high significance (TS 5229). I refine the gamma-ray spectrum of the globular cluster 47 Tuc and re-confirm that its is a point source with no variability on 6 month timescales or evidence of extension. The ROI listing, TS Map and residual significance map show no other sources to account for the emission of 47 Tuc. The spectral energy distribution is well described by a log-parabola spectral model but has a softer spectrum at the lowest energies, which is in tension with this model. I now apply this analysis method to a larger sample of 111 GCs in Chapter 5.

Chapter 5

Globular Cluster Analysis

5.1 Introduction

In this chapter I analyse 111 globular clusters (GCs) out to the distance limit of the furthest *Fermi*-LAT source associated with a GC in the 4FGL (NGC 1904 at 12.9 kpc). I perform this analysis in two distinct energy bands: $0.1-10$ GeV, where the bulk of emission occurs, and at $10-100$ GeV to identify any GCs displaying high energy (HE) emission. The analysis of $0.1-10$ GeV is used to characterise the spectral functional form of the GCs, their spectral energy distribution and to produce test statistic (TS) maps to demonstrate the morphology of the sources. The analysis of $10-100$ GeV is used to produce counts maps for the GCs 47 Tuc and Terzan 5, to probe the symmetry of any emission and to identify whether the morphological features of a bow shock nebula may be present as introduced in Chapter 3.

I then examine to what extent millisecond-pulsars (MSPs) account for gamma-ray emission in globular clusters (GCs), to first order, by considering the link between GC luminosity and MSP related GC characteristics. I derive the relationships between GC gamma-ray luminosity and characteristics relevant to MSP formation, namely the stellar encounter rate, GC metallicity and a new quantity, derived in this thesis, the mass encounter rate product (MERP). Finally, I show how diffuse X-ray emission in GCs is positively correlated with gamma-ray emission and consider some explanations for this connection.

This chapter expands and updates the discussion and results of my MNRAS paper, in which I considered 30 high latitude Galactic globular clusters in the 3FGL catalog [181], detecting NGC 6254 for the first time and demonstrating the X-ray / gamma-ray connection.

5.2 Globular Cluster Selection

My selection of 111 GCs (listed in Appendix Table A.1) is based on the selection of all GCs in the Harris catalogue (2010 version) [124] out to a maximum heliocentric distance of 12.9 kpc for NGC 1904, as this is the furthest GC identified as a gamma-ray source in the 4FGL catalog.

5.3 Analysis

5.3.1 Initial Photon Event Data Selection

The data in this analysis were collected by *Fermi*-LAT between 4th Aug 2008 (15:43 h) to 7th March 2019 (00:45 h), (Mission Elapsed Time (MET) 2395574147[s] to 573612309[s]). I select all PASS 8 events which are *source* class photons (evclass=128), both Front and Back converting events (evtype=3), spanning the energy range 60 MeV to 300 GeV. Throughout my analysis, the *Fermipy* software package[1] with version V11R0P4 of the *Fermi Science Tools* is used, in conjunction with the P8R3_SOURCE_V2 instrument response functions. I apply the standard PASS8 cuts to the data, including a zenith angle 90° cut to exclude photons from the Earth limb and good-time-interval cuts of DATA_QUAL > 0 and LAT_CONFIG = 1. The energy binning used is 4 bins per decade in energy and spatial binning is 0.1° per image pixel.

5.3.2 Initial Detection of GC gamma-ray Emitters

Initially I search for significant gamma-ray emitters from my list of 111 GC targets (Table A.1) using a narrow radius of interest for reasons of efficiency. This entails using a 12° Radius of Interest (ROI) centred on the nominal GC co-ordinates and a 20 ° Source Radius of Interest (SROI) for each GC target. The model I use in my likelihood analysis consists of a point source population seeded from the *Fermi*-LAT's fourth point source catalog (4FGL), extended gamma-ray sources and diffuse gamma-ray emission. The diffuse emission detected by the *Fermi*-LAT consists of two components: the Galactic diffuse flux, and the isotropic diffuse flux. The Galactic component is modelled with *Fermi*-LAT's gll_iem_v07.fit spatial map with the normalisation free to vary. The isotropic diffuse emission is defined by *Fermi's* iso_P8R3_SOURCE_V2_v1.txt tabulated spectral data. The normalisation of the isotropic emission is left free to vary.

[1] *Fermipy* change log version 0.17.4 ([275])

I conduct an initial BINNED likelihood analysis, with both the normalisation of all point sources within 12° of each GC target and the spectral shape of all TS > 25 sources being left free. Point sources within 12° to 20° from each GC target are frozen to their 4FGL values. I run the *optimize* method which loops over all model components in the ROI and fits their normalization and spectral shape parameters. It also computes the TS of all sources in the ROI. The best-fit model from this likelihood fit is used with the *Fermi Science Tool* GTTSMAP, to search for new point sources in the data that were not accounted for by the 4FGL. In particular, FERMIPY's *'find_sources'* method is then run twice to detect all sources above 3σ significance. *Find_sources* is a peak detection algorithm which analyses the test statistic (TS) map to find new sources over and above those defined in the 4FGL model by placing a test point source, defined as a power law (PL) with spectral index 2.0, at each pixel on the TS map and recomputing likelihood.

5.3.3 Refining the Spectral Energy Distributions of Detected GCs

Sources which lie within the tidal radius of the of the GC co-ordinates which are either unattributed point source detections or are a recognised GC with a 4FGL identifier are analysed again in the energy range $0.1-10$, $10-100$ and $0.1-100$ GeV with a new likelihood fit with an expanded 25° ROI and 40° source region width. The steps of this analysis are described in detail in the analysis of 47 Tuc in Chapter 4 and are summarised briefly here. Initially, the *setup* and *optimize* methods are run to create count and photon exposure maps and to compute the TS values of all 4FGL sources in the model. The *fit* method is then run. *fit* is a likelihood optimisation method which executes a fit of all parameters that are currently free in the the model and updates the TS and predicted count ($Npred$) values of all sources. The normalisation of all sources within 10° of the GC are freed using the *free_source* method to allow for the Point Spread Function (PSF) of front and back converting events down to 100 MeV. The source nearest to the GC centre had *prefactor* and *index* spectral parameters (Eqn. 8.12) freed for power law sources, *prefactor*, *index1*, and *beta* spectral parameters (Eqn. 5.2) freed for a log parabola source and *prefactor*, *index1* and *expfactor* freed for a PLSuperExpCutoff2 source (Eqn. 5.3). The shape and normalisation parameters of all sources with a TS > 25 are then individually fitted using the *optimize* method. From this fit, all point sources with a TS < 4, or with a predicted number of photons, $Npred$, < 4 are removed from the model[2]. Finally, the *fit* method is run twice more with an intervening *find_sources* step. The *sed* method generates a spectral energy distribution, with energy

[2]To exclude a systematic effect I re-analyse 47 Tuc omitting this step and show that the spectral model and energy flux obtained is consistent with the original analysis within error and that the spectral energy distributions are identical.

dispersion disabled for GCs which are known 4FGL sources, and a 5σ confidence limit on the determination of instrument upper limits.

5.3.4 Spatial Extension

The analysis output from 5.3.3 is used to check for source extension for each detected GC by running the GTAnalysis *extension* method, which replaces the GC point source spatial model with an azimuthally symmetric 2D Gaussian model. It then profiles likelihood with respect to spatial extension in a 1 dimensional scan to determine the likelihood of extension.

5.3.5 Determination of GC Upper Limits

I determine gamma-ray emission upper limits (UL) for undetected GCs by repeating the $0.1-10$ GeV analysis of 5.3.3 above and adding GC PL test point sources with *index* 2.0, *scale* 100 MeV and *prefactor* = 1 x 10 $^{-11}$ at the GC nominal co-ordinates after the *setup* analysis step and before any subsequent likelihood fit steps.

5.3.6 Spectral Models

The differential flux, *dN/dE*, (photon flux per energy bin) of the detected GCs is described through a power law (Eqn. 8.12) or log parabola (Eqn. 5.2) spectral model[3].

$$\frac{dN}{dE} = N_0 \Big(\frac{E}{E_0}\Big)^{\gamma} \tag{5.1}$$

where *prefactor* = N_0, *index* = γ and *scale* = E_0.

$$\frac{dN}{dE} = N_0 \Big(\frac{E}{E_\mathrm{b}}\Big)^{-(\alpha+\beta\log(E/E_\mathrm{b}))} \tag{5.2}$$

where *norm* = N_0, *alpha* = α, *beta* = β and E_b is a *scale* parameter.

The differential flux spectrum of millisecond pulsars (MSPs), (as in the case of NGC 6626 and NGC 6624 where the emission is dominated by single bright MSPs) is described by an exponential cut-off power law 2 (Eqn. 5.3)

$$\frac{dN}{dE} = N_0 \Big(\frac{E}{E_0}\Big)^{\gamma_1} \exp\Big(-aE^{\gamma_2}\Big) \tag{5.3}$$

where *normalisation* (also known as *prefactor*) = N_0, *index1* = γ_1, E_0 is the scale, a is the exponential factor and *index2* = γ_2.

[3] As described in the FSSC source model [1]

In addition, all known sources take their 4FGL spectral shape.

5.4 Results

5.4.1 GC Analysis Results in the Energy Range 0.1−10 GeV

The 0.1−10 GeV, Front and Back, gamma-ray analyses confirm the 4FGL catalogue GC associations yielding significant detections, with the results shown in Table 5.1. Nearly all GCs have 4FGL catalogue positions co-incident with their optical centre with the exceptions of NGC 6528, NGC 6254, NGC 6656 and 2MS-GC01, which are nonetheless still within the GC tidal radius. I therefore classify the sources 4FGL J1804.9-3001, 4FGL J1656.4-0410, 4FGL J1836.8-2354 and 4FGL J1808.8-1949 as associated with the GCs NGC 6528, NGC 6254, NGC 6656 and 2MS-GC01 respectively. The association of 4FGL J1656.4-0410 with NGC 6254 is a new association as the 4FGL does not classify this source, whereas 4FGL J1836.8-2354 has an alternative association with NGC 6656 listed in 4FGL, with a prior association, the source 3FGL J1837.3-2403, classified as the millisecond pulsar J1836-2354A. However, the reported positional uncertainty of 4FGL J1836.8-2354 is consistent with NGC 6656 but not J1836-2354A [31].

The refined source position and error obtained with the *localize* command, luminosity, energy flux, photon flux and spectral model parameters of the detected GCs are listed in Tables 5.3, 5.4 and 5.5.

I show the TS maps of each detected GC in Figs. A.1 to A.5 with their tidal radii, best fit localisation position of the gamma-ray source and the localisation error shown as a 95% containment circle. This again shows that nearly all the gamma-ray emission from GCs is within their tidal radii. The exception is GLIMPSE02 where the best fit localisation containment overlaps the tidal radius of the GC.

The best fit spectral models of the GCs are plotted on spectral energy distributions in Figs. A.7 to A.13. These individual plots show that the best fit spectral models produced by FERMIPY are of varying quality with deviations from the SEDs, especially at lower energies (< 250 MeV), and where constrained by SED ULs. The spectral model fit to the SED can be assessed by determining the χ^2 test statistic.

The null hypothesis is that energy fluxes on the SED are the same as the energy fluxes predicted from the spectral model for every bin with a flux observation (as opposed to an UL). A test statistic above the critical value indicates that the null hypothesis can be rejected at a given significance level. At the α=0.05 significance level, the null hypothesis cannot be rejected for 16 GCs, rising to 25 GCs for the α=0.001 significance level as listed in Table 5.2.

Globular Cluster	Catalogue Source ID	TS	Offset (Degrees)	Tidal Radius (Degrees)	Offset As % of Tidal Radius	Tidal Ref
NGC 6304	4FGL J1714.2-2928	25	0.19	0.27	70	[200]
NGC 6218	4FGL J1647.2-0154	28	0.05	0.27	19	[92]
NGC 5904	4FGL J1518.8+0203	47	0.06	0.44	14	[92]
NGC 6838	4FGL J1953.6+1846	54	0.06	0.42	14	[200]
NGC 6139	4FGL J1627.6-3852	55	0.01	0.14	7	[92]
NGC 6397	4FGL J1741.1-5341	57	0.05	0.84	6	[92]
NGC 1904	4FGL J0524.4-2413	58	0.35	0.48	73	[92]
Terzan 2	4FGL J1727.6-3050	58	0.08	0.17	47	Harris 2003
NGC 6341	4FGL J1716.8+4310	60	0.06	0.31	19	[92]
2MS-GC01	4FGL J1808.8-1949	61	0.02	0.13	15	Harris 2003
Terzan 1	4FGL J1735.7-3026	65	0.09	0.18	50	Harris 2003
NGC 6254	4FGL J1656.4-0410	66	0.2	0.38	53	[92]
NGC 6528	4FGL J1804.9-3001	67	0.12	0.28	43	[200]
NGC 7078	4FGL J2129.9+1208	75	0.24	0.38	63	[92]
NGC 6402	4FGL J1737.5-0313	77	0.04	0.23	17	[92]
NGC 6717	4FGL J1855.1-2243	86	0.06	0.1	60	[92]
NGC 6656	4FGL J1836.8-2354	123	0.11	0.59	19	[92]
NGC 6093	4FGL J1616.9-2257	128	0.03	0.08	38	[92]
NGC 2808	4FGL J0912.1-6449	130	0.06	0.39	15	[200]
NGC 6541	4FGL J1807.8-4340	159	0.1	0.27	37	[92]
NGC 6652	4FGL J1835.7-3258	184	0	0.05	0	[92]
NGC 6752	4FGL J1910.8-6001	219	0.03	0.5	6	[92]
NGC 6316	4FGL J1716.7-2808	295	0.03	0.11	27	[200]
NGC 6440	4FGL J1748.9-2021	473	0.05	0.11	45	Harris 2003
GLIMPSE02	4FGL J1818.5-1656	485	0.32	0.25	128	[168]
NGC 6441	4FGL J1750.3-3702	620	0	0.13	0	Harris 2003
GLIMPSE01	4FGL J1848.7-0129	739	0.04	0.13	31	Harris 2003
NGC 6624	4FGL J1823.5-3020	809	0.02	0.05	40	[92]
NGC 5139	4FGL J1326.6-4729	964	0.01	1.07	1	[92]
NGC 6626	4FGL J1824.6-2452	1107	0.04	0.2	20	[92]
NGC 6388	4FGL J1736.2-4443	1368	0.01	0.08	13	[92]
NGC 6266	4FGL J1701.2-3006	1432	0.01	0.16	6	[92]
Terzan 5	4FGL J1748.0-2446	4955	0.01	0.08	13	[169]
47 Tuc	4FGL J0024.0-7204	7023	0.01	0.73	1	[92]

Table 5.1 Detected GCs in the energy range 100 MeV−10 GeV, in order of increasing detection significance (TS). The offset of most gamma-ray GC sources from the optical center is small <0.1 ° and in nearly all cases is within the GC tidal radius with the exception of GLIMPSE02 which is just outside. The Harris 2003 GC catalog with tidal radii is accessible at http://www.naic.edu/ pulsar/catalogs/mwgc.txt.

Globular Cluster	χ^2 Test Statistic	D.o.f	Critical Value $\alpha = 0.05$	Model Accepted at $\alpha = 0.05$	Critical Value $\alpha = 0.001$	Model Accepted at $\alpha = 0.001$
NGC 1904	1.4	3.0	7.815	Yes	16.266	Yes
NGC 2808	0.2	3.0	7.815	Yes	16.266	Yes
NGC 5139	8.0	4.0	9.488	Yes	18.467	Yes
NGC 5904	2.7	1.0	3.841	Yes	10.828	Yes
NGC 6254	5.9	2.0	5.991	Yes	13.816	Yes
NGC 6266	7.5	4.0	9.488	Yes	18.467	Yes
NGC 6304	5.3	2.0	5.991	Yes	13.816	Yes
NGC 6316	8.3	4.0	9.488	Yes	18.467	Yes
NGC 6341	1.3	3.0	7.815	Yes	16.266	Yes
NGC 6388	4.0	4.0	9.488	Yes	18.467	Yes
NGC 6528	1.5	2.0	5.991	Yes	13.816	Yes
NGC 6541	5.2	4.0	9.488	Yes	18.467	Yes
NGC 6624	1.5	4.0	9.488	Yes	18.467	Yes
NGC 6652	5.6	3.0	7.815	Yes	16.266	Yes
NGC 6656	5.6	3.0	7.815	Yes	16.266	Yes
NGC 6752	3.2	2.0	5.991	Yes	13.816	Yes
Terzan 2	13.6	2.0	5.991	No	13.816	Yes
NGC 7078	10.0	2.0	5.991	No	13.816	Yes
NGC 6717	17.9	4.0	9.488	No	18.467	Yes
NGC 6626	12.2	4.0	9.488	No	18.467	Yes
NGC 6441	10.0	4.0	9.488	No	18.467	Yes
NGC 6402	8.2	3.0	7.815	No	16.266	Yes
NGC 6397	8.9	3.0	7.815	No	16.266	Yes
NGC 6139	14.9	4.0	9.488	No	18.467	Yes
NGC 6093	12.4	4.0	9.488	No	18.467	Yes
47 Tuc	12.2	5.0	11.070	No	20.515	Yes
Terzan 5	41.7	4.0	9.488	No	18.467	No
NGC 6838	24.3	2.0	5.991	No	13.816	No
NGC 6440	26.9	4.0	9.488	No	18.467	No
GLIMPSE02	29.8	4.0	9.488	No	18.467	No
GLIMPSE01	67.7	4.0	9.488	No	18.467	No
2MS-GC01	45.0	2.0	5.991	No	13.816	No

Table 5.2 Testing the goodness-of-fit of GC spectral models to spectral energy distributions(SEDs, 100 MeV$-$10 GeV) using the χ^2 test statistic. The number of GCs having spectral models consistent with their SEDs ($\chi^2 <$ critical value), are 16 and 25, at significance level $\alpha = 0.05$ and $\alpha = 0.001$ respectively. NGC 6218 and Terzan 1 are excluded as they have $<$1 degree of freedom (d.o.f).

There are only weak indications for extension in the detected GCs with just 4 GCs (NGC 6541, 2MS-GC01, NGC 1904 and GLIMPSE02) showing extensions of $0.3-0.6^{\circ}$ with extension TS values in the range $9.2-15.7$. This suggests that GCs, in the main, are point like gamma-ray sources.

5.4.2 GC Analysis Results in the Energy Range 10−100 GeV

Using Front and Back converting events in the $10-100$ GeV energy range, only Terzan 5 (TS 66.8) and 47 Tuc (TS 45.8) are detected significantly, with a weak indication of detection for NGC 6440 (TS 13.8) and NGC 6441 (TS 10.7).

As I wish to produce counts maps at the best spatial pixel resolution (to determine the symmetry of the emission), I also re-analyse with an event type of PSF3 (to make use of the best quartile direction reconstruction and resulting superior PSF). This yields reduced TS values of 11.7 and 38.4 for 47 Tuc and Terzan 5 respectively. There are also weak indications of detection for NGC 6624 (TS 14.3), NGC 6139 (TS 9.4) and NGC 6440 (TS 14). The GCs have no indication for extension with either the PSF3 or Front and Back event types with the exception of NGC 6440 (Front and Back) which has weak indication of a 0.48 ° extension (TS 11.3).

In order to probe the morphology of significant HE emission, I plot the predicted counts for both 47 Tuc and Terzan 5, for Front and Back and PSF3 event types in Figs. 5.1 and 5.2 respectively. The spatial bin size used in the analysis is 0.1° and 0.04° for Front and Back and PSF3 event types respectively which sets the resolution of the TS maps. The predicted count emission extends beyond the 68 % containment PSF for both Front and Back and PSF3 events in both GCs. The emission also extends beyond the compact tidal radius of Terzan 5 but is contained within the $\sim 10\times$ larger tidal radius of 47 Tuc. The predicted emission is centered on both GCs with no indication of any strong asymmetry.

In [54], and as previously referred to in Chapter 3, the bow shock nebula, proposed to be formed by an MSP relativistic particle wind interacting with the denser Galactic medium at low latitudes is expected to produce offset emission for Terzan 5, as compared to the high latitude GC, 47 Tuc, where a radially symmetric emission centered on the GC is expected due to the less dense inter-Galactic medium. The lack of expected asymmetry in the gamma-ray emission for Terzan 5 would seem to exclude any such bow shock nebula mechanism.

5.4.3 Upper Limits

The energy flux and photon flux upper limits for the 77 GCs in our sample which were not detected are presented in Appendix Table A.2.

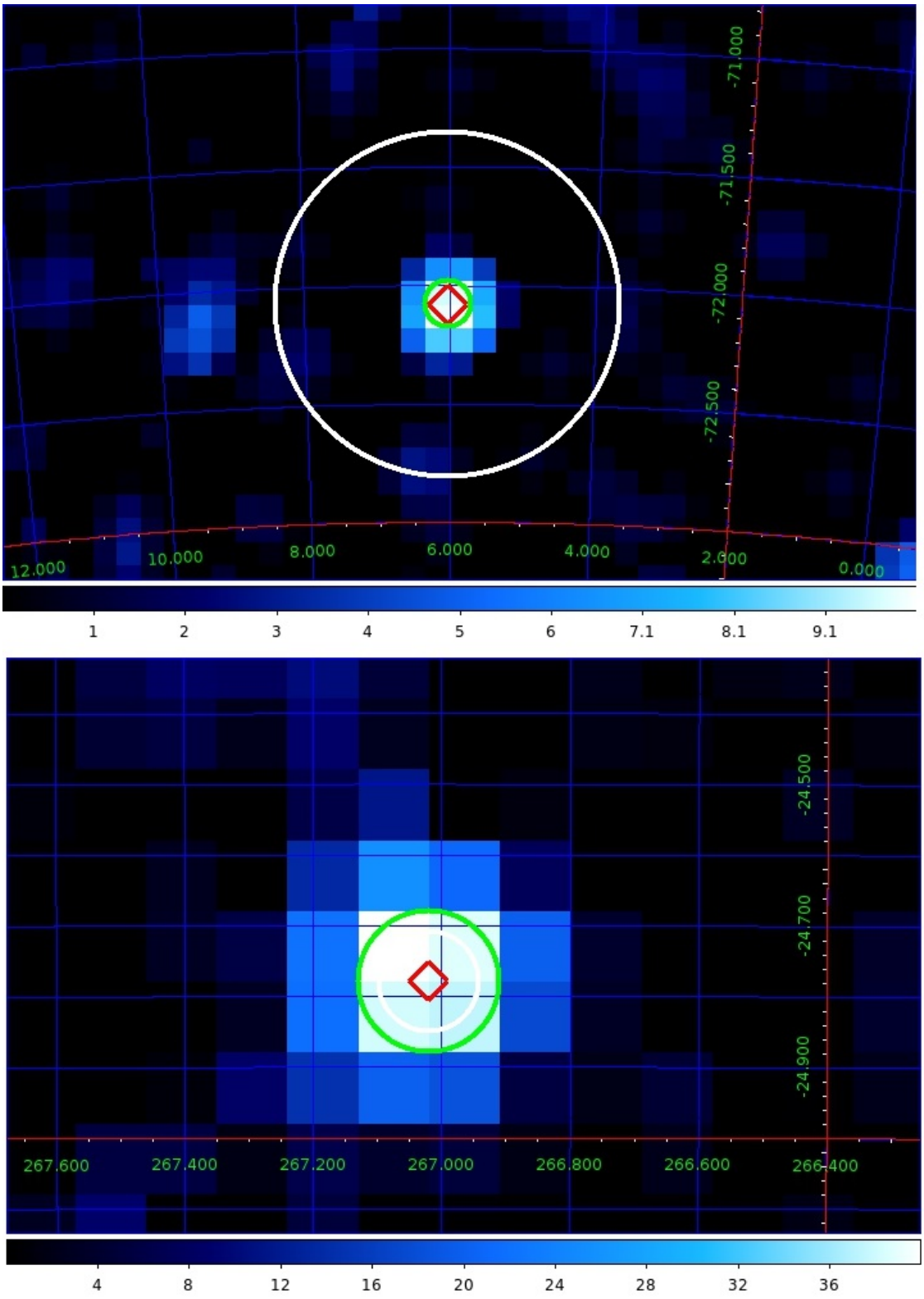

Fig. 5.1 A predicted counts map of 47 Tuc (top panel) and Terzan 5 (lower panel) obtained using the Front and Back $10-100$ GeV analysis. The optical centre of GCs from the Harris Catalogue is indicated by the red diamond and the tidal radius and PSF is indicated by the white and green circles respectively. The emission extends beyond the 68 % containment PSF in both GCs and also beyond the tidal radius of Terzan 5 but is contained within the tidal radius of 47 Tuc. The horizontal graduated scale is predicted counts.

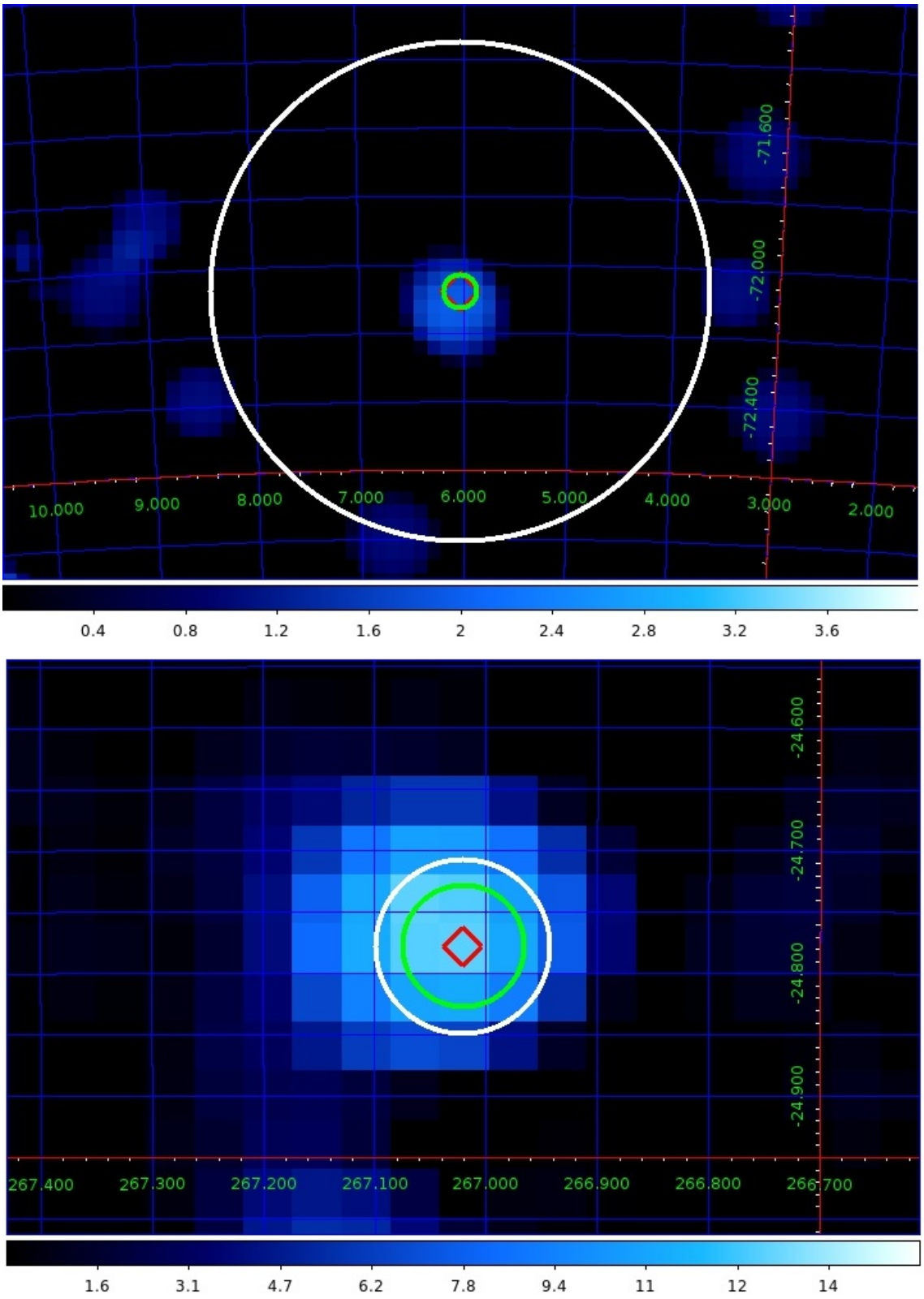

Fig. 5.2 A predicted counts map of 47 Tuc (top panel) and Terzan 5 (lower panel) obtained using the PSF3 10−100 GeV analysis. The optical centre of GCs from the Harris Catalogue is indicated by the red diamond and the tidal radius and PSF is indicated by the white and green circles respectively. The emission extends beyond the 68 % containment PSF in both GCs and also beyond the tidal radius of Terzan 5 but is contained within the tidal radius of 47 Tuc. The horizontal graduated scale is predicted counts.

Globular Cluster	Source RA Degree	Source DEC Degree	Luminosity 10^{34} erg s^{-1}	Energy Flux 10^{-11} erg cm^{-2} $^{-1}$	Photon Flux 10^{-8} cm^{-2} s^{-1}	*norm* 10^{-12}	α	β	Eb
47 Tuc	6.00 ± 0.01	-72.08 ± 0.01	6.51 ± 0.17	2.69 ± 0.07	2.53 ± 0.13	5.71 ± 0.16	1.84 ± 0.03	0.26 ± 0.03	956.16
GLIMPSE01	282.17 ± 0.03	-1.50 ± 0.03	9.52 ± 0.45	4.51 ± 0.22	4.18 ± 0.44	1.55 ± 0.07	2.37 ± 0.07	0.30 ± 0.04	2328.37
GLIMPSE02	274.35 ± 0.05	-16.80 ± 0.03	14.34 ± 0.77	3.96 ± 0.21	6.83 ± 0.52	0.78 ± 0.22	4.01 ± 0.45	0.69 ± 0.15	1897.51
NGC 2808	138.03 ± 0.02	-64.81 ± 0.02	3.71 ± 0.50	0.34 ± 0.05	0.34 ± 0.11	0.43 ± 0.07	2.15 ± 0.15	0.35 ± 0.18	1300.38
NGC 5139	201.68 ± 0.01	-47.48 ± 0.01	3.51 ± 0.23	1.08 ± 0.07	0.86 ± 0.13	0.93 ± 0.06	2.22 ± 0.07	0.45 ± 0.07	1662.42
NGC 5904	229.68 ± 0.04	2.05 ± 0.03	0.95 ± 0.22	0.14 ± 0.03	0.11 ± 0.06	0.16 ± 0.03	2.10 ± 0.29	0.46 ± 0.27	1472.78
NGC 6093	244.24 ± 0.02	-22.96 ± 0.02	5.54 ± 0.78	0.46 ± 0.07	0.53 ± 0.15	0.24 ± 0.03	2.19 ± 0.15	0.17 ± 0.08	1814.19
NGC 6218	251.83 ± 0.03	-1.91 ± 0.04	0.23 ± 0.07	0.08 ± 0.02	0.01 ± 0.01	0.02 ± 0.01	1.50 ± 0.76	1.35 ± 1.08	4291.26
NGC 6254	254.11 ± 0.03	-4.19 ± 0.04	0.52 ± 0.11	0.22 ± 0.05	0.13 ± 0.08	0.06 ± 0.01	2.62 ± 0.35	0.54 ± 0.31	3010.87
NGC 6266	255.30 ± 0.12	-30.11 ± 0.01	10.85 ± 0.46	1.96 ± 0.08	1.93 ± 0.18	2.69 ± 0.12	2.07 ± 0.05	0.32 ± 0.04	1242.89
NGC 6316	259.21 ± 0.02	-28.15 ± 0.02	13.27 ± 0.93	1.03 ± 0.07	1.05 ± 0.14	0.88 ± 0.06	2.23 ± 0.10	0.31 ± 0.00	1535.93
NGC 6388	264.08 ± 0.01	-44.74 ± 0.01	20.95 ± 0.94	1.79 ± 0.08	1.56 ± 0.16	2.95 ± 0.14	1.99 ± 0.06	0.40 ± 0.05	1186.21
NGC 6402	264.37 ± 0.03	-3.26 ± 0.03	3.77 ± 0.58	0.36 ± 0.06	0.38 ± 0.11	0.35 ± 0.06	2.44 ± 0.39	0.45 ± 0.24	1506.97
NGC 6440	267.26 ± 0.02	-20.40 ± 0.02	15.93 ± 0.97	1.84 ± 0.11	2.66 ± 0.29	1.00 ± 0.07	2.88 ± 0.12	0.42 ± 0.06	1672.21
NGC 6441	267.58 ± 0.01	-37.04 ± 0.01	26.29 ± 1.55	1.63 ± 0.10	2.25 ± 0.26	1.67 ± 0.10	2.41 ± 0.07	0.28 ± 0.05	1324.22
NGC 6528	271.34 ± 0.08	-30.01 ± 0.08	4.41 ± 0.57	0.59 ± 0.08	0.88 ± 0.11	1.30 ± 0.17	2.52	0.44	986.50
NGC 6541	271.92 ± 0.03	-43.64 ± 0.02	2.89 ± 0.34	0.43 ± 0.05	0.42 ± 0.10	0.82 ± 0.10	2.08 ± 0.14	0.43 ± 0.12	1114.51
NGC 6652	278.94 ± 0.02	-32.99 ± 0.02	5.44 ± 0.56	0.45 ± 0.05	0.40 ± 0.08	0.60 ± 0.06	2.23 ± 0.15	0.51 ± 0.12	1372.67
NGC 6656	279.20 ± 0.03	-23.96 ± 0.04	0.59 ± 0.06	0.48 ± 0.05	0.47 ± 0.05	0.79 ± 0.08	2.27	0.53	1241.12
NGC 6752	287.76 ± 0.02	-60.00 ± 0.02	0.65 ± 0.08	0.34 ± 0.04	0.29 ± 0.08	0.57 ± 0.06	2.20 ± 0.15	0.58 ± 0.18	1255.56
NGC 6838	298.49 ± 0.05	18.74 ± 0.05	0.72 ± 0.11	0.37 ± 0.06	0.59 ± 0.09	0.61 ± 0.09	2.48	0.31	1068.39
Terzan 1	263.94 ± 0.02	-30.38 ± 0.03	2.70 ± 0.64	0.50 ± 0.12	0.12 ± 0.02	0.32 ± 0.07	1.77 ± 0.42	2.00 ± 0.00	2816.27
Terzan 2	261.90 ± 0.04	-30.89 ± 0.06	4.68 ± 0.76	0.70 ± 0.11	0.82 ± 0.26	0.26 ± 0.04	2.32 ± 0.18	0.20 ± 0.00	2067.05
Terzan 5	267.03 ± 0.004	-24.78 ± 0.005	43.52 ± 0.98	7.64 ± 0.17	7.94 ± 0.40	6.59 ± 0.15	2.21 ± 0.03	0.29 ± 0.02	1515.64

Table 5.3 Detected GCs with positions (RA, DEC),luminosity, energy and photon flux and LP spectral model parameters of best fit on SED. Luminosity calculated assuming the distances in Table A.1. In some cases the analysis was unable to determine an uncertainty value and this is indicated by gaps in the table.

Globular Cluster	Source RA Degree	Source DEC Degree	Luminosity 10^{34} erg s^{-1}	Energy Flux 10^{-11} erg cm^{-2} s^{-1}	Photon Flux 10^{-8} cm^{-2} s^{-1}	*prefactor* 10^{-14}	*index*	*scale*
NGC 1904	80.84 ± 0.16	-24.48 ± 0.16	5.48 ± 0.88	0.28 ± 0.04	0.80 ± 0.16	271.7 ± 43.8	-(2.84 ± 0.16)	408
NGC 6139	246.92 ± 0.03	-38.86 ± 0.04	6.24 ± 0.92	0.51 ± 0.08	1.01 ± 0.15	8.1 ± 1.2	-2.33	2413
NGC 6304	258.44 ± 0.00	-29.54 ± 0.73	1.68 ± 0.35	0.40 ± 0.08	0.91 ± 0.19	18.8 ± 3.9	-2.47	1430
NGC 6341	259.16 ± 0.04	43.22 ± 0.06	1.67 ± 0.31	0.20 ± 0.04	0.40 ± 0.12	21.3 ± 3.4	-(2.33 ± 0.16)	1072
NGC 6397	265.22 ± 0.04	-53.71 ± 0.04	0.23 ± 0.04	0.37 ± 0.06	0.76 ± 0.16	23.9 ± 4.5	-(2.36 ± 0.13)	1305
NGC 6717	283.74 ± 0.03	-22.75 ± 0.03	2.38 ± 0.35	0.40 ± 0.06	0.54 ± 0.13	16.5 ± 2.2	-(2.02 ± 0.10)	1792
NGC 7078	322.28 ± 0.12	12.28 ± 0.07	4.68 ± 0.61	0.36 ± 0.05	0.86 ± 0.14	108.2 ± 14.2	-(2.53 ± 0.11)	666
2MS-GC01	272.08 ± 0.05	-19.81 ± 0.03	2.19 ± 0.29	1.41 ± 0.19	2.03 ± 0.37	28.3 ± 4.5	-(2.05 ± 0.09)	2540

Table 5.4 Detected GCs with positions (RA, DEC),luminosity, energy and photon flux and PL spectral model parameters of best fit on SED. Luminosities calculated assuming the distances in Table A.1. In some cases the analysis was unable to determine an uncertainty value and this is indicated by gaps in the table.

Globular Cluster	Source RA Degree	Source DEC Degree	Luminosity 10^{34} erg s^{-1}	Energy Flux 10^{-11} erg cm^{-2} $^{-1}$	Photon Flux 10^{-8} cm^{-2} s^{-1}	*prefactor* 10^{-14}	*index1*	*Scale*	*expfactor* 10^{-3}	*index2*
NGC 6624	275.91 ± 0.001	-30.34 ± 0.001	9.54 ± 1.52	1.28 ± 0.20	1.19 ± 0.12	192 ± 39	-(1.24 ± 0.12)	1969	6.99	0.67
NGC 6626	276.19 ± 0.01	-24.87 ± 0.01	7.57 ± 0.29	2.09 ± 0.08	2.76 ± 0.10	521 ± 20	-1.38	1610	9.38	0.67

Table 5.5 Detected GCs with positions (RA, DEC),luminosity, energy and photon flux and PLSuperExpCutoff2 spectral model parameters of best fit on SED. Luminosity calculated assuming the distance in Table A.1. In some cases the analysis was unable to determine an uncertainty value and this is indicated by gaps in the table.

5.4.4 Gamma-ray Luminosity and the Evidence for MSPs in GCs

If the gamma-ray emission for globular clusters derives exclusively or even primarily from MSPs, one would expect the gamma-ray luminosity to be correlated with the numbers of MSPs in the GCs in question. This presents its own problems, as the total number of MSPs in a given cluster is rarely (if ever) known.

[10] estimated the number of MSPs, N_{MSP}, in 10 GCs from observed GC gamma-ray luminosity divided by expected emission for a canonical MSP (product of average $\dot{E}$ (1.8 x 10^{34} erg s^{-1}) and gamma-ray efficiency (0.08). They then derived a stellar encounter rate Γ_e = $\rho_0{}^{1.5} r_c{}^2$ for each GC, where ρ_0 is central cluster density in units of solar luminosity per pc^3 and r_c is cluster core radius in units of pc. The relationship between N_{MSP} and Γ_e was fitted by the linear relation $N_{MSP}=(0.5\pm0.2)\Gamma_e +(18\pm9)$. I determine N_{MSP} as [10] but use stellar encounter rates from [41] which are derived using luminosity density profiles and velocity dispersion. It should be noted that encounter rate data are available for only 31 of my 34 detections and just 59 UL GCs in [41]. I normalise the stellar encounter rates to the values of [10] (to allow direct comparison), and plot N_{MSP} vs stellar encounter rate in Fig. 5.3 to yield the linear relationship $N_{MSP}=(1.14\pm0.01)\Gamma_e +(3.92\pm0.20)$. Therefore, the proportionality of the expected number of MSPs, and hence gamma-ray luminosity, to encounter rate in this work is twice that of [10].

The χ^2 statistic for the best fit line $N_{MSP}=(1.14\pm0.01)\Gamma_e +(3.92\pm0.20)$ (Green line of Fig. 5.3), is 12212 / 28 d.o.f), exceeding the critical value (56.892 α=0.001), indicating that the fit is not good but nonetheless preferred to a line of average N_{MSP} (χ^2 statistic 64363 / 29 d.o.f).

Terzan 5 and NGC 7078 are outliers to this relationship, both being less luminous than predicted. My result re-affirms the connection between GC stellar encounter rate (which is presumed related to the number of MSPs) and gamma-ray luminosity. However, the detection of Terzan 1, NGC 6218 and NGC 6254, shown more clearly in Fig. 5.4, all having low encounter rates, (0.292, 13.0 and 31.4 respectively in [41]), and therefore presumably few, if any, MSPs, demonstrates that gamma-ray luminosity in GCs is not entirely related to the number of MSPs. This view is reinforced by the cases of NGC 6752, with luminosity below the best fit line despite an encounter rate of 401, (almost half the 47 Tuc value), in [41]) and the non-detection ULs of NGC 7089 and NGC 362 despite their even larger encounter rates of 518 and 735.

[143] investigated the fundamental plane relations of gamma-ray globular clusters and determined a postive correlation between log of gamma-ray luminosity L_γ and increasing metallicity [Fe/H] for 15 GCs including the 8 GC detections of [10]. This linear relationship had the form $L_\gamma=(0.59\pm0.15)$[Fe/H] + $(35.56\pm0.15$). This correlation was ascribed to the

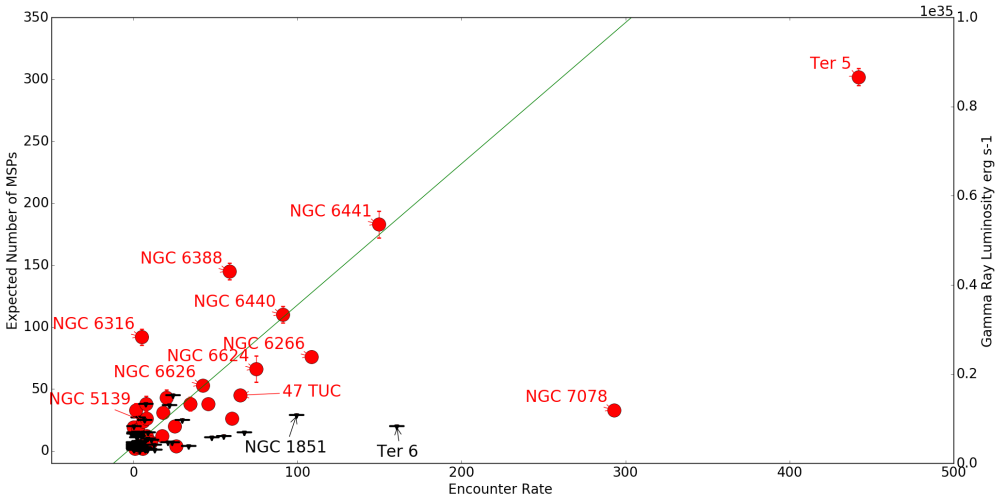

Fig. 5.3 Plot of inferred MSP count vs Encounter Rate Γ_e from [41] which I renormalise assuming 47 Tuc encounter rate is 65 to allow comparison with [10]. Outlying selected GCs are labelled (red captions) and upper limits are indicated by black symbols. The line of best fit (ignoring upper limit values) is shown in green and has the functional form $N_{MSP}=(1.14\pm0.01)\Gamma_e$ $+(3.92\pm0.20)$. Terzan 5 and NGC 7078 are outliers, with lesser luminosity than might be expected on the basis of Γ_e.

increased likelihood of Roche-lobe overflow and MSP recycling due to increased magnetic breaking in higher metallicity stellar systems as proposed by [145]. I plot L_γ vs metallicity for the detected and undetected GCs in my study but do not see an immediate correlation (Fig 5.5). The wide scatter of this plot with GCs of high and low metallicity sharing similar luminosities reinforces the view that non MSP related sources of gamma-ray emission exist in GCs.

I also plot gamma-ray luminosity against *detected* MSPs for the GCs in our study which have been the subject of sustained radio observations (Fig 5.6) and see that there is no correlation between detected MSP count and luminosity. For example, NGC 6093 and NGC 6218, with no detected MSPs, have comparable luminosity to 47 Tuc (25 MSPs) and NGC 6752 (5 MSPs) respectively. Of the 34 detected GCs in this study, 18 have no known pulsars[4]. 50 GCs were imaged by the MAVERIC radio survey [258] using the Karl G. Jansky Very Large Array and the Australia Telescope Compact Array, to determine if putative central IMBHs were actively accreting. Although no active IMBHs were found, 8 of the 18 GCs with no known MSPs above were imaged, and a possible pulsar candidate was found in just

[4]From the list of currently known pulsars in GCs is maintained at http://www.naic.edu/~pfreire/GCpsr.html, accessed 26/7/2020

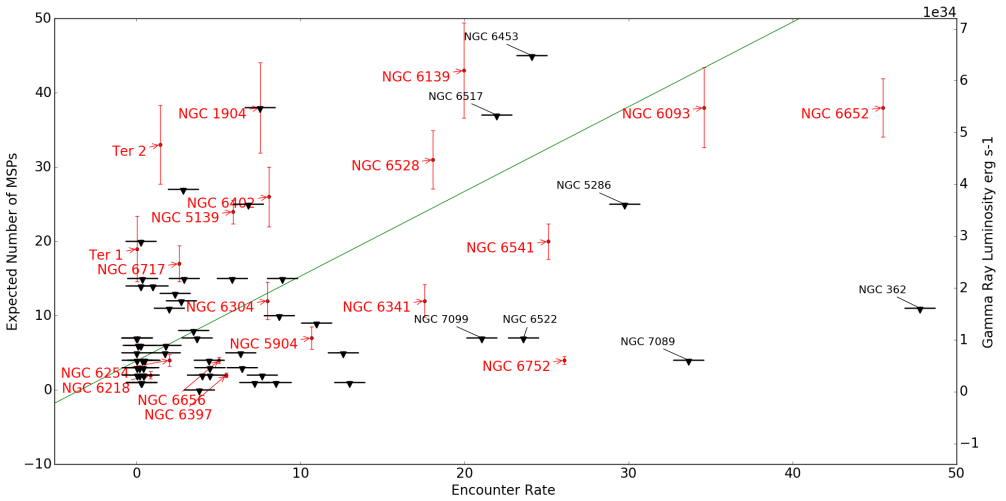

Fig. 5.4 An expanded view of inferred MSP count vs renormalised Encounter Rate Γ_e ,for lower encounter Rates and expected number of MSPs <50. There is considerable scatter around the fit line (green), for example Terzan 1 on the left of the figure has a higher luminosity, despite its low encounter rate, than GCs of comparable encounter rate, NGC 6254 and 6218 which are closer to the best fit line. NGC 6752 has luminosity below the best fit line despite its higher encounter rate. Only ULs with encounter rate >20 are labelled to avoid clutter.

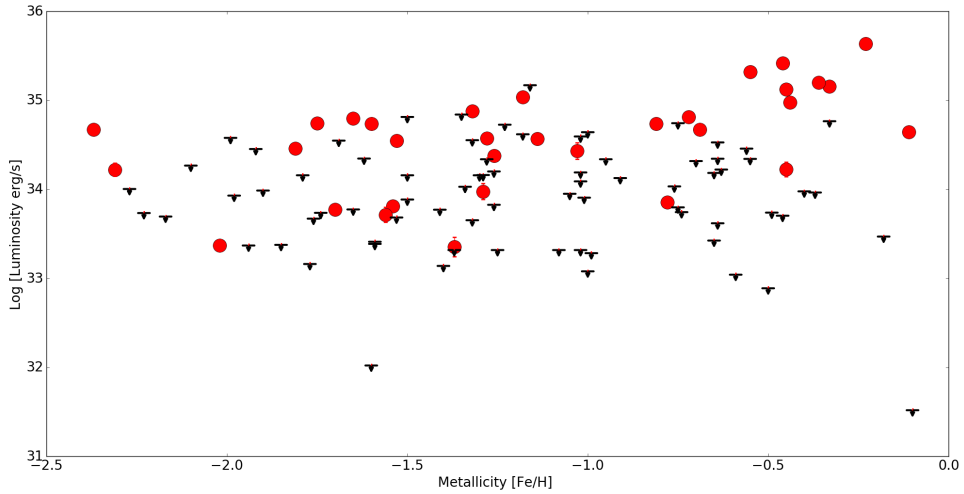

Fig. 5.5 Plot of log gamma-ray luminosity vs Metallicity [Fe/H] for GCs with heliocentric distance of 10.4 kpc or less. Detected GCs are captioned in red whilst undetected GCs are captioned in black and shown as upper limits. There is no apparent correlation between luminosity and metallicity for the GCs in this study.

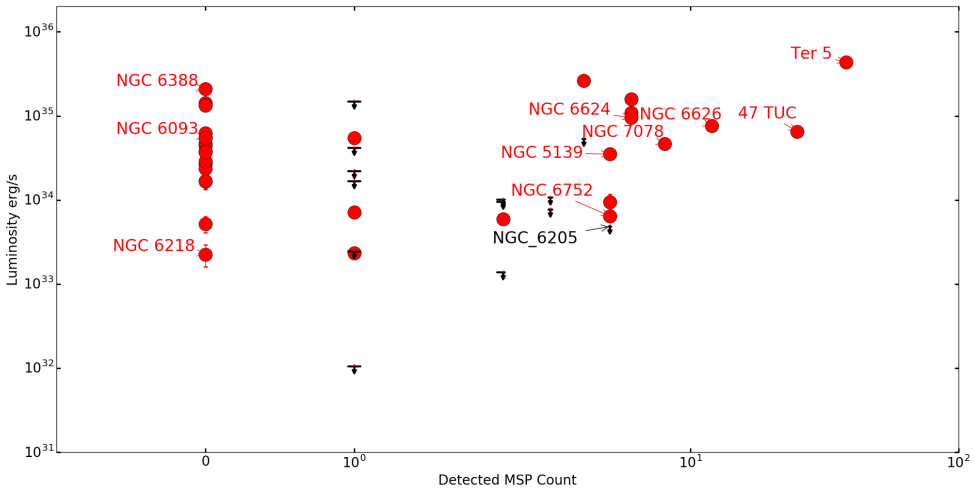

Fig. 5.6 Log Plot of gamma-ray luminosity vs number of known MSPs in each GC. I show GCs which are detected in this study (in red) and undetected GCs (in black) with known MSPs. For undetected GCs an upper luminosity limit is shown. For reasons of clarity, not all GCs are labelled.

two, Terzan 1 and NGC 6388. 22 GCs were also surveyed using the Arecibo radio telescope at $\sim$ 1.4 GHz but this did not include the 18 GCs lacking MSPs [131].

To first order the number of MSPs in GCs is proportional to the encounter rate and stellar number density, and thus to the GC mass. Terzan 5 and NGC 7078 do not fit the MSP encounter rate relation well on Fig. 5.3, which leads me to consider the effect of GC mass in addition to encounter rate. Therefore, to investigate further the connection between presumed binary-system creation and resulting MSPs and gamma-ray luminosity for the detected GCs in my sample, I define a mass encounter rate product (MERP) derived from GC mass x GC normalised encounter rates (listed in [41]). I take MERP as a proxy for the prevalence of binary system creation and MSP recycling and plot it against GC luminosity on Fig. 5.7. On this plot Terzan 5 and NGC 7078 are no longer outliers, although Terzan 1 is, due to its very low encounter rate of 0.292.

A line of best fit for Fig. 5.7 determined by minimising χ^2 yields a tentative relationship between GC gamma-ray luminosity (L_γ) and MERP (Eqn 5.4) which I plot on Fig. 5.7. Although the best-fit straight line (ignoring the outlier Terzan 1) of:

$$L_\gamma = 0.36 \log\left(Mass * Encounter\,Rate\right) + 33.48 \tag{5.4}$$

is also not compelling (χ^2 = 3247 / 25 d.o.f.), it is preferred over a fit to constant average luminosity (χ^2 = 79174 / 26 d.o.f.)

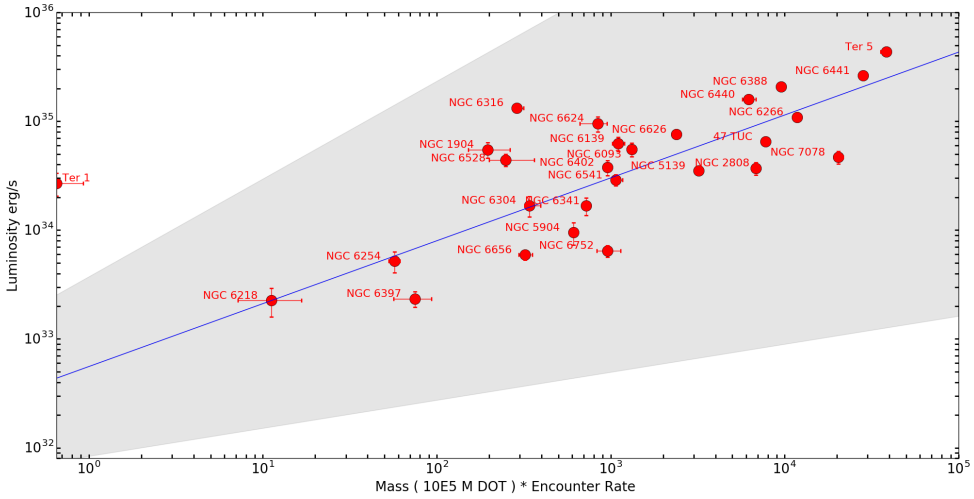

Fig. 5.7 Log plot of gamma-ray luminosity vs MERP (the product of cluster mass in units of 10^5 $M_\odot$ and a normalised encounter rate from [41]) for GCs detected in this study. In [41] the encounter rate of 47 Tuc is set to an arbitrary value of 1000 and the encounter rate of other GCs are determined relative to that of 47 Tuc. The line of best fit determined by a weighted least squares method (ignoring upper limit values) is shown in blue and has functional form Log (L_γ)=(0.578 $\pm$ 0.320) Log (Mass*Encounter Rate) + (32.75 $\pm$ 0.824) with the error on the best fit line indicated by grey shading. Terzan 1 (left) with its very low encounter rate of 0.292 is a clear outlier.

There is therefore a weak correlation between gamma-ray luminosity and MERP for the GCs in my sample. This once again suggests that, while MSPs have a role to play in the gamma-ray emission from GCs, they are not necessarily the only source of the emission. The Terzan 1 outlier with its very low encounter rate, yet a luminosity of 2.7×10^{34} erg s^{-1}, provides some support for this view. I also note that mass alone appears unimportant; NGC 6093, which has a relatively low mass of 3.37 x 10^5 $M_\odot$ and a distance of 10 kpc, is detected, whereas the larger clusters NGC 6205 and NGC 5272 (both of mass 5.00 x 10^5 $M_\odot$ at distances of 7.1 kpc and 10.2 kpc respectively) are not.

5.4.5 Diffuse Emission and Unresolved Point Sources

The non MSP-like spectra of some of my detected GCs coupled with the relatively poor correlation of gamma-ray luminosity with metallicity or observed numbers of MSPs leads me to consider other sources of gamma-ray emission. It is possible that the gamma-ray emission originates from as-yet unresolved point sources or has a more diffuse origin. I therefore explore the gamma-ray emission of GCs through its correlation with any diffuse

X-ray emission excess, which is defined as the X-ray emission remaining after subtraction of all resolved X-ray point sources in a GC. The spatial distribution of this diffuse emission is, however, complex, and may be split into two, largely separate, components: extended and core. The angular resolution of *Fermi* is such that it is not possible to distinguish with which component the gamma-ray emission may be associated by positional coincidence.

Extended X-ray Emission

In [211], the *Chandra*-ACIS (Advanced CCD Imaging Spectrometer), was used to examine 12 GCs and after subtraction of known X-ray point sources, detected extended diffuse X-ray emission (0.5−4.5 keV) in 6 objects, offset 1'-6' from the GC centre and extending to a few arc minutes, beyond the half-mass radius. For 5 GCs (47 Tuc, NGC 6752, 5904, 6093 and 6266) this emission was ascribed to the GC motion through the Galactic halo and shock heating of internal gas interacting with halo plasma, whereas in the case of GC Omega Centauri (NGC 5139), a background cluster of galaxies was the likely X-ray source. Subsequently [280], using *Suzaku*-XIS (X-ray Imaging Spectrometer), ascribed the putative 47 Tuc extended diffuse X-ray emission (0.5−6 keV) to a background cluster of galaxies with redshift z=0.34.

In contrast, [103] conducted a search for extended X-ray emission, using the *Chandra*-ACIS (0.5−7 keV), in 6 *Fermi*-LAT detected GCs (NGC 6266, 6388, 6541, 6626, 6093 and 6139) in concentric zones between half to 4 times the GC half-mass radius. They concluded that there was no evidence for diffuse emission above the level of the Galactic diffuse background in these GCs. The lack of extended X-ray emission in NGC 6093 and NGC 6266 is at odds with the above detections of [211]. This is likely due to the different methods used by the authors to determine and account for the Galactic diffuse X-ray background. [103] model the Galactic diffuse X-ray background by scaling the flux measurements of [102] using expected X-ray emission and absorption arising from the GC interstellar medium. In contrast, [211] subtract an exposure-corrected observational background, a few arc-minutes from the aim point.

Core X-ray Emission

The authors of [142] examined the unresolved core X-ray emission (0.3−8 keV) of 10 MSP-hosting GCs through subtraction of known X-ray point sources detected with the *Chandra* X-ray observatory ACIS instrument. Diffuse X-ray core emission was detected in 4 GCs (NGC 6626, 6440, 6266 and 6752), which was then fitted with power law (PL) and thermal Bremsstrahlung (BREMSS) models. They linked this unresolved X-ray emission to the

cumulative contribution of CVs and faint MSPs. In [276], again using *Chandra*, diffuse X-ray emission ($0.5-7$ keV) from 47 Tuc was identified, consisting of 2 components, one a non-thermal component correlated with the GC stellar density profile, and the other a uniform thermal component offset from the GC. They interpreted the non-thermal X-ray emission from the core as resulting from shock fronts of stellar winds and inverse-Compton scattering of relic photons by pulsar winds. In [211], which largely concentrated on extended emission, it was noted that NGC 5904 (M5) showed evidence for two X-ray components: a pair of soft, wing-like regions and harder emission associated with the core. The latter was also interpreted as arising from an ensemble of faint point sources. However, in the case of Terzan 5, the authors of [104] note that the contribution of unresolved sources to the centrally-peaked X-ray emission which they identify in *Chandra* data is likely to be negligible.

X-ray and γ-ray Emission

I summarise this information, for GCs from this study and others for which information is available regarding their diffuse X-ray emission, in Table 5.6. In so far as there is an association between diffuse X-ray emission and gamma-ray detection, it appears that the objects with core X-ray emission are more likely to be gamma-ray emitters than not, and that the presence of extended X-ray emission is not as important. It therefore seems likely that the gamma-ray emission arises from the cores of the globular clusters rather than any extended region. NGC 6397 and NGC 6838 are marginal cases, with low gamma-ray luminosity and low X-ray UL / no diffuse X-ray emission respectively.

The question then arises as to the source(s) of the gamma-ray emission. I have noted there appears to be no strong connection with the number of MSPs known to exist in the objects, although there does appear to be some correlation with the mass $\times$ normalised encounter rate of the GCs. Assuming there is a connection to the core X-ray emission, it is not clear whether this arises from several unresolved point sources or genuinely diffuse emission.

If the gamma-ray emission comes from unresolved point sources other than MSPs, the obvious candidates are cataclysmic variables (CVs) and X-ray binaries (XRBs), both of which are expected to exist within GCs due to the high stellar encounter rates. While gamma-ray emission has been detected from cataclysmic variables [9], the emission is transient in nature, with gamma-ray emission only observed on the timescales of days after the nova event. Furthermore, only CVs in our local Galactic neighbourhood have been observed to be gamma-ray bright, which suggests that their gamma-ray emission is detected primarily because of their proximity [201]. In addition, the detection rate of CVs by *Fermi*-LAT is modest (compared to that of MSPs) at < 1 per yr, with only 6 of 75 optical novae being

detected in gamma-rays [108], suggesting that, to first order, that they are less significant gamma-ray emitters than MSPs. X-ray binaries are a less likely prospect, as XRBs in GCs will be low-mass systems, whereas nearly all the known gamma-ray emitting XRBs are wind-driven, high-mass systems, the one possible exception being XSS J12270-4859 [93].

One potential source of the diffuse X-ray emission in these objects is relativistic electrons provided by the MSP population, which can produce X-ray emission via synchrotron radiation. As both [211] and [104] have pointed out, assuming a typical Galactic magnetic field of a few μG, the electrons would require an energy of $\sim 10^{14}$ eV to produce emission at keV energies. Associated TeV gamma rays produced via inverse Compton radiation would be diagnostic of the existence of relativistic electrons and a low magnetic field. In this context, I note that Terzan 5 has been detected at TeV energies with the H.E.S.S. telescopes [129], but that this seems to be a unique object, with only TeV upper limits being obtained for several other GCs, including 47 Tuc and NGC 7078 [130].

GC Name and L_γ Ref	L_γ 10^{34} erg s^{-1}	Core Diffuse X-ray emission	Core PL L_x 0.3-8.0 keV 10^{32} erg s^{-1}	Core BREMSS L_x 0.3-8.0 keV 10^{32} erg s^{-1}	Extended Diffuse X-ray emission	Shock Front L_x 0.5-4.5 keV 10^{32} erg s^{-1}
GC detected in γ-ray showing diffuse X-ray:						
47 TUC	6.51 ± 0.17	Yes [276]	$2.36^{+0.50}_{-0.48}$	-	Yes [276]	$1.26^{+0.07}_{-0.08}$
NGC 6093	5.54 ± 0.78	-	-	-	Yes [211]	0.36±0.24
NGC 6752	0.65 ± 0.08	Yes [142]	$0.15^{+0.08}_{-0.04}$	$0.12^{+0.11}_{-0.06}$	Yes [211]	6.0±0.3
NGC 5139	3.51 ± 0.23	-	-	-	Yes - Galaxy cluster source [211]	-
NGC 5904	0.95 ± 0.22	No [142] / Yes [211]	M5C 0.8±0.2	-	Yes [211]	M5W 0.1±0.03
NGC 6266	10.85 ± 0.46	Yes [142]	$1.5^{+0.62}_{-0.36}$	$1.41^{+0.26}_{-0.27}$	Yes [211]	0.6±0.2
NGC 6440	15.93 ± 0.97	Yes [142]	$2.00^{+1.71}_{-0.76}$	$1.57^{+1.51}_{-0.74}$	No [211]	<0.19
NGC 6626	7.57± 0.29	Yes [142]	$2.54^{+1.27}_{-0.62}$	$1.67^{+0.99}_{-0.62}$	No [211]	<0.51
Terzan 5	43.52± 0.98	Yes [104]	20±3 (1-7 keV)	-	-	-
GC detected in γ-ray **lacking diffuse X-ray**						
NGC 6397	0.23 ± 0.04	-	-	-	No [211]	<0.13
NGC 6838	0.72± 0.11	No [142]	-	-	-	-
GC undetected in γ-ray this work:						
NGC 5272	<0.77	No [142]	-	-	-	-
NGC 6121	<14.8	No [142]	-	-	No [211]	<0.04
NGC 6205	<0.48	No [142]	-	-	-	-
NGC 6366	<0.11	-	-	-	No [211]	<0.62
NGC 7099	<1.01	-	-	-	No [211]	<0.21
GC undetected in γ-ray previous work:						
NGC 5024	<4.04 [181]	No [142]	-	-	-	-

Table 5.6 Correspondence of detected diffuse X-ray and gamma-ray emission for GCs. GC's 47 Tuc−Terzan 5 have diffuse X-ray emission and are detected in gamma-ray (top panel) whereas GCs 5272−NGC 5024 lack diffuse X-ray emission and are not detected in gamma-ray (lower two panels). NGC 6397 and NGC 6838 are marginal cases both with low gamma-ray luminosity and low X-ray UL / no diffuse X-ray emission respectively (middle panel). Core X-ray emission is determined either as power law (PL) or thermal Bremsstrahlung component (BREMSS) and GCs for which the diffuse X-ray emission is undetermined are indicated with a "-" NGC 5904 has two distinct X-ray emitting regions M5C (core) and M5W (wing) both observed between 0.5-4.5 keV. Gamma-ray and X-ray luminosities are from references listed in table. X-ray energy bands as indicated in table except for 47 Tuc observed between 0.5-7 keV

5.5 Conclusion

I analyse 111 GCs and identify 34 as gamma-ray sources in the energy range $0.1-10$ GeV. I produce spectral energy distributions (SEDs) and, through plotting the spectral models of each GC over the SED and using the χ^2 statistic, show that these sources are in many cases well described by the functional form (log parabola, power law or power law super exponential with a cut-off) produced by the analysis. I also produce test statistic (TS) maps and show that the sources are point like and co-incident with their optical centres in most cases. There is no significant evidence of extended emission. High energy emission (> 10 GeV) is significantly detected in 47 Tuc and Terzan 5 and counts maps for these sources show that the emission is symmetric and centred on the GC, in tension with the predictions of a shock-front model which predicts offset emission in Terzan 5.

The importance of MSPs as sources of GC gamma-ray emission can be considered by examining proxies such as metallicity and stellar encounter rate which are thought to be positively correlated with MSP formation. I show that the magnitude of GC gamma-ray luminosity is correlated with encounter rate $\sim$ a factor of 2 more than previously reported but that there are significant outliers, with Terzan 5 and NGC 7078 having lower luminosity than expected and some GCs detected despite very low encounter rates, such as NGC 6254, NGC 6218 and Terzan 1. In order to account for the effect of GC mass, I define a new quantity in this thesis, the mass encounter rate product (MERP), which again is positively correlated (albeit weakly) with luminosity and resolves the encounter rate outliers, Terzan 5 and NGC 7078, suggesting that MSPs are still the main emission source in these objects. On the other hand, GC luminosity appears uncorrelated with GC metallicity or detected MSPs which weakens the MSP case.

I demonstrate a link between GC core diffuse X-ray emission and GC gamma-ray emission which potentially explains why some GCs are undetected despite being predicted as strong candidates for gamma-ray emission (e.g NGC 6205). The core diffuse X-ray emission could be due to either unresolved point sources such as MSPs or to relativistic electrons produced by MSPs in the GCs. In the latter case, one might expect TeV emission from the GCs due to inverse Compton radiation, and observations with ground-based gamma-ray telescopes such as CTA could resolve this issue. The link between core diffuse X-ray emission and gamma-ray emission is tentative, largely because there are relatively few gamma-ray emitting GCs for which X-ray observations are available. Further X-ray observations of GCs would be helpful in this regard.

The connection between gamma-ray luminosity, diffuse X-ray emission and MERP has been very useful in re-affirming a connection (albeit a complex one) between the gamma-ray emission of GCs and their MSPs. A detailed spectral comparison is now necessary to proceed

further. In Chapter 6 I will construct my own stacked model of Galactic field MSPs, in order to further probe the connection between MSPs and GC emission at the level of individual spectral bins.

Chapter 6

A General Spectral Model for Millisecond Pulsars

6.1 Introduction

In this chapter, I seek to construct a general spectral model for millisecond pulsars (MSPs) which can be then compared to the spectra of globular clusters (GCs) in Chapter 7. In doing this, I will use a larger sample of 103 MSPs, rather than the 39 MSPs of the 2PC [11] used by the previous stacked MSP analyses of Xing and Wang [278] and McCann [194]. I will show some representative MSP spectra and determine to a first order if the emission of the MSPs is comparable in each spectral bin, as a pre-requisite to stacking and summation. I will then show that a general spectral model can be derived from the stacked summed spectra of detected MSPs, and I assess the goodness-of-fit of this general model to the stacked spectrum using the χ^2 statistic.

6.2 MSP Selection

I select 103 MSPs (defined as any pulsar with period $\leq$ 30 ms) from the Public List of LAT Detected Gamma-Ray Pulsars[1] and list their co-ordinates, periods and $\dot{E}$ values in Table C.1. My selection includes the MSPs J1824-2452A and J1823-3021A, in NGC 6626 and NGC 6624, respectively.

[1] https://confluence.slac.stanford.edu/display/GLAMCOG/Public+List+of+LAT-Detected+Gamma-Ray+Pulsars, accessed on 2nd April 2019

6.3 Analysis Method

6.3.1 Initial Photon Event Data Selection

The data in this analysis were collected by *Fermi*-LAT between 4th Aug 2008 (15:43 h) to 7th March 2019 (00:45 h), (Mission Elapsed Time (MET) 2395574147[s] to 573612309[s]). I select all PASS 8 events which are *source* class photons (evclass = 128), and PSF3 events with the best quartile direction reconstruction, (evtype = 32), spanning the energy range 50 MeV to 300 GeV. Throughout my analysis, the *Fermipy* software package[2] with version V11R0P4 of the *Fermi Science Tools* is used, in conjunction with the P8R3_SOURCE_V2 instrument response functions. I apply the standard PASS8 cuts to the data, including a zenith angle 90° cut to exclude photons from the Earth limb and good-time-interval cuts of DATA_QUAL > 0 and LAT_CONFIG = 1. The energy binning used is 4 bins per decade in energy and spatial binning is 0.1° per image pixel.

6.3.2 MSP Likelihood Analysis

I perform a full likelihood analysis on all 103 MSP targets (Table C.1) using a 25° Radius of Interest (ROI) centred on the nominal MSP co-ordinates and a 40° Source Radius of Interest (SROI) for each MSP target. The model I use in my likelihood analysis consists of a point source population seeded from the *Fermi*-LAT's fourth point source catalog (4FGL), extended gamma-ray sources and diffuse gamma-ray emission. The diffuse emission detected by the *Fermi*-LAT consists of two components: the Galactic diffuse flux, and the isotropic diffuse flux. The Galactic component is modelled with *Fermi*-LAT's gll_iem_v07.fit spatial map with the normalisation free to vary. The isotropic diffuse emission is defined by *Fermi's* iso_P8R3_SOURCE_V2_v1.txt tabulated spectral data. The normalisation of the isotropic emission is left free to vary. The MSPs are analysed separately in the energy range $0.1-10$ and $10-100$ GeV and the steps of this analysis are described in detail in the analysis of 47 Tuc in Chapter 4[3]

[2] *Fermipy* change log version 0.17.4 ([275])

[3] To exclude a systematic effect due to the removal of low significance sources with a TS < 4, or with a predicted number of photons, $Npred < 4$, I re-analyse one MSP: J1939+2134, omitting source removal showing that the spectral model and energy flux obtained is consistent with the original analysis within error and that the spectral energy distributions are identical.

6.4 Analysis Results

I detect 98 of the 103 catalogue MSPs in the energy range 100 MeV−10 GeV whilst 5 MSPs, J0636+5129, J0737-3039A, J1327-0755, J1909-3744 and J1946+3417 are undetected. The non detection of these MSPs is unsurprising as they have been only previously detected by *Fermi*-LAT through their pulsed emission, as opposed to a likelihood analysis [243, 116, 244]. I list the detection significance (TS), offset from catalogue co-ordinates, and fluxes in Tables C.2 and C.3. I include all detections of significance $> 3\sigma$, rather than $> 5\sigma$, because the pulsars are all associated with known 4FGL sources, and in nearly all cases have very small offsets ($< 0.09°$) from the catalogue pulsar co-ordinates

I also list the best fit spectral models for MSPs with a PLSuperExpCutoff2 spectral model or PL model, in Tables C.4 and C.5, respectively. The average energy flux is $1.55 \pm 0.18 \times 10^{-11}$ erg cm^{-2} s^{-1}.

In the energy range, 10 GeV−100 GeV, I detect 32 MSPs and list their detection significance (TS), offset from catalogue co-ordinates and fluxes in Table C.6. The average energy flux is $0.11 \pm 0.03 \times 10^{-11}$ erg cm^{-2} s^{-1}.

I next determine the average flux per bin and the standard error of the mean, in the range 100 MeV−100 GeV, for the detected MSPs to assess if the distribution of fluxes might be skewed by a few flux dominant MSPs in the population. The flux error for bins between 133 MeV − 13.3 GeV are $\sim$ one order of magnitude less than the mean flux, suggesting that the flux distribution in each bin is not skewed by the high flux of a few dominant MSPs (Table 6.1).

In Fig. 6.1, I show selected spectral energy distributions (SEDs) from the 100 MeV−10 GeV MSP analysis, across the range of significant TS values, for PLSuperExpCutOff2 and PL models. The PLSuperExpCutOff2 SEDs show the cut-off at a few GeV, which is characteristic of MSPs, and also a softening of flux at low energies.

6.5 Deriving a Stacked MSP Model

In order to derive a model for an ensemble of Galactic field MSPs, I sum the fluxes in each bin (ignoring ULs) between 100 MeV−100 GeV for MSPs detected in the energy range 100 MeV−10 GeV and 10−100 GeV. These are listed in Table 6.2. There is no significant flux for any MSP in the highest energy bin between 56.2 and 100 GeV. I also plot the flux summation in Fig. 6.2 which yields a spectral shape with low fluxes at lower energies and an energy cut-off above 10 GeV. The summation includes two Globular Cluster MSPs, J1824-2452A and J1823-3021A in NGC 6626 and 6624, respectively, but although they are not part of the

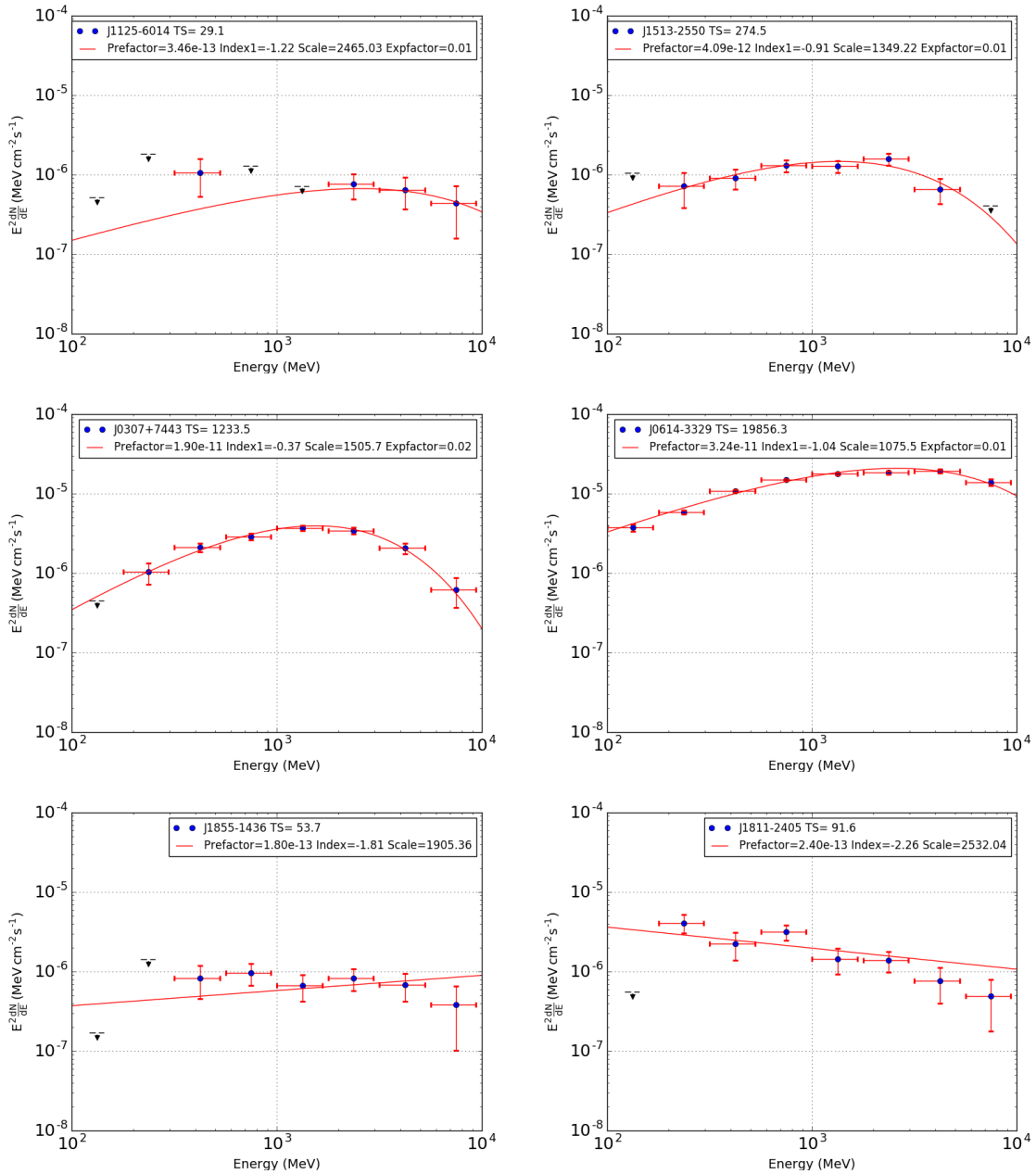

Fig. 6.1 A selection of representative spectral energy distributions from the MSP 100 MeV−10 GeV analysis, including both PLSuperExpCutoff2 (Top and middle panels) and PL models (bottom panel), across the full range of significant TS values.

Bin Center MeV	Count of Significant Flux Points	Mean Energy Flux 10^{-6} MeV cm^{-2} cm^{-1}
133	26	2.56 ± 0.39
237	70	2.42 ± 0.24
422	88	2.59 ± 0.26
750	92	2.85 ± 0.32
1334	95	3.00 ± 0.35
2371	95	2.71 ± 0.33
4217	92	2.23 ± 0.32
7499	72	1.44 ± 0.26
13335	24	1.29 ± 0.30
23714	11	0.86 ± 0.29
42170	3	0.82 ± 0.22

Table 6.1 The count of significant flux points and mean flux for each bin with error from the standard error of the mean. The flux errors for bins between 133 MeV − 13.3 GeV are $\sim$ one order of magnitude less than the mean flux, suggesting that the flux distribution in each bin is not skewed by the high flux of a few dominant MSPs.

field population, their flux contribution is not excessive, being just 0.9 and 1% of the total flux in the energy range 100 MeV−10 GeV.

I then use GAMMAPY version 0.18[4] software to fit the flux summation of 98 MSPs in the range 100 MeV−10 GeV. I choose to fit in this more restricted range because few GCs have detectable emission above 10 GeV, and the comparison of the MSP models to GCs will be in the 100 MeV−10 GeV energy range. I define an initial exponential cut-off power law model spectral model as Eqn. 5.3 with *index1* = -1.8, *index1*, *Normalisation* = 2×10^{-12} cm^{-2} s^{-1} TeV^{-1} and *exponential factor* = 1×10^{-4} TeV^{-1}. The parameters *index1*, *Normalisation* and *exponential factor* are left free. The *scale* and *index2* parameters are frozen to 1×10^{-3} TeV and 1 respectively. I then use the GAMMAPY *Fit* command to perform a likelihood fit of this initial model to the summed fluxes of the 98 MSPs. The GAMMAPY fit fails to determine parameter errors directly, so I estimate these by re-fitting the 98 MSPs assuming fluxes values at the extremes of the maximal flux error and obtaining the spectral parameter differences as compared to the original fit. My best fit spectral model, "Lloyd" in the chapters that follow, is *index1* = -1.332±0.012, *Normalisation* = $(4.029\pm0.056)\times10^{-4}$ cm^{-2} s^{-1} TeV^{-1} and exponential factor = $(3.914\pm0.085)\times10^{2}$ TeV (Eqn. 6.1, Energy E in units of TeV). It can be seen that my model fits all $\frac{dN}{dE}$ flux values of the 98 summed MSPs within error (Fig. 6.3).

[4] Available from https://docs.gammapy.org/dev/overview.html

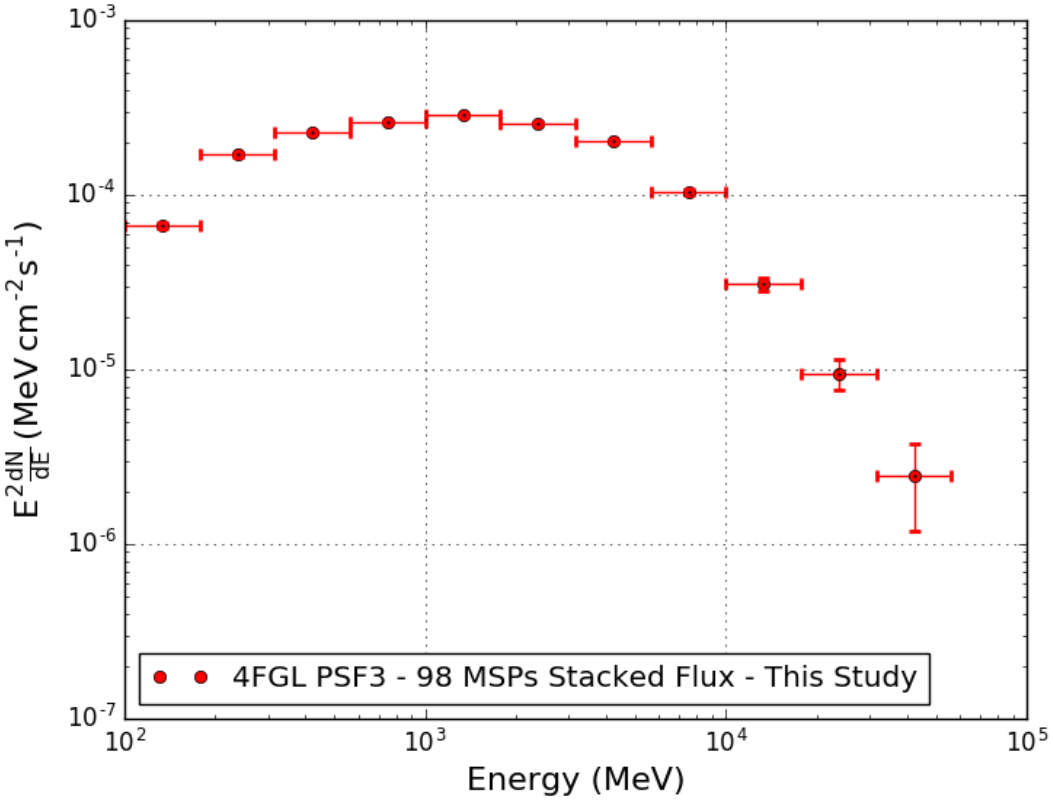

Fig. 6.2 The stacked emission of all significant fluxes for MSPs detected in the energy range 100 MeV−10 GeV and 10−100 GeV.

Bin Center MeV	Lower Bin Energy MeV	Upper Bin Energy MeV	Sum of significant flux 10^{-6} MeV cm^{-2} cm^{-1}
133	100	177	66.49±2.33
237	177	316	169.7±3.95
421	316	562	227.81±3.48
749	562	1000	262.59±3.12
1333	1000	1778	284.74±3.19
2371	1778	3162	257.28±3.46
4216	3162	5623	204.79±3.89
7498	5623	10000	104.01±3.6
13335	10000	17782	30.86±2.57
23713	17782	31622	9.46±1.87
42169	31622	56234	2.46±1.27
74989	56234	100000	-

Table 6.2 The sum of significant fluxes in the energy range 100 MeV−100 GeV for each energy bin. The minimum and maximum extent of each energy bin is also listed. There is no significant flux in the 75 GeV bin.

$$\frac{dN}{dE} = (4.029 \pm 0.056) \times 10^{-4} \left(\frac{E}{1 \times 10^{-3}} \right)^{-1.332 \pm 0.012} \exp\left(-(3.914 \pm 0.085) \times 10^{2} E \right) \tag{6.1}$$

6.6 Stacked Models of MSP Emission

In this discussion I re-summarise the Second *Fermi* Large Area Telescope catalog of Gamma-Ray pulsars [11] (the 2PC) from which the MSP sample was drawn to construct stacked models of MSP emission spectra by Xing and Wang [278] and McCann [194].

The Second *Fermi* Large Area Telescope Catalog of Gamma-Ray pulsars [11] (hereafter the 2PC), although compiled in 2013, remains the most complete published survey of pulsars observed by *Fermi*-LAT to date. The survey uses 3 years of PASS 7 event data in the energy range between 100 MeV and 100 GeV with the 2FGL source catalog as a source model and lists the spectral models and fluxes of 117 pulsars evenly divided between MSPs, young radio-quiet and young radio-loud pulsars. The survey uses three search strategies for pulsar detection to overcome the difficulty of only one photon being detected in a few million pulsar rotations. Firstly, the known rotation ephemerides of pulsars, obtained mostly through radio and in some cases X-ray observations, are used to fit a timing model with TEMPO/TEMPO2 software, to tag the gamma-ray event data with a pulsar phase. The gamma-ray data are then

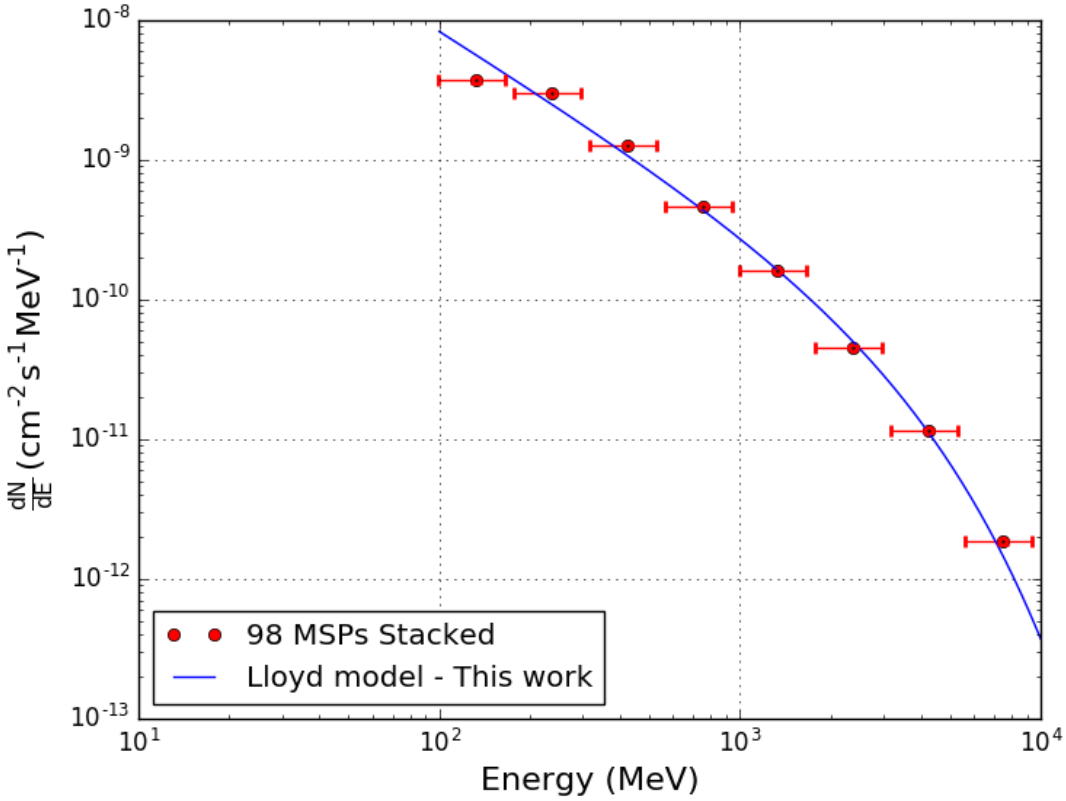

Fig. 6.3 A plot of summed photon flux per energy for the 98 MSPs. My model, an exponential cut-off power law spectral model (blue line) passes through all flux points within error.

phase-folded to identify any emission peaks. Secondly, blind periodicity searches are used on unassociated sources classed as candidate pulsars because they show no variability and have spectra that can be fitted by an exponential cut-off in the GeV band. This method is challenging because the event data are sparse with only a few photons detected per hour and in addition pulsars may have been missed by being in binary systems, which tends to smear the signal through Doppler shifts arising from orbital motion. Finally, the detection of pulsed radio emission in unassociated sources and the construction of timing models can lead to the detection of gamma-ray pulsations through phase folding methods as above. The 2PC lists 40 MSPs, 20 of which have been detected using this final method. The 2PC increased the then known MSP sample from 8 to 40 MSPs with heliocentric distances up to 2 kpc and a uniform distribution in the sky. The MSPs exhibit between $1-3$ gamma-ray peaks and their differential flux spectrum, *dN/dE*, (photon flux per energy bin) is an exponential cut-off power law as described by Eqn. 6.2 where normalisation = k, photon index at low energy = Γ and $E_{\rm cut}$ is the cut-off energy. E_0 is the pivot energy of the spectrum (or 1 GeV where no pivot energy is given for the spectrum) and b controls the sharpness of the exponential cut-off.

$$\frac{dN}{dE} = k\Big(\frac{E}{E_0}\Big)^{-\Gamma} \exp\Big(-\frac{E}{E_{\rm cut}}\Big)^{\rm b} \tag{6.2}$$

The MSPs listed in the 2PC also provide a pulsar sample to use in determining models of stacked gamma-ray emission. Xing and Wang [278] re-analyse 39 of the 40 MSPs in the 2PC (excluding one, J1939+2134, whose detection significance is $\simeq 3\sigma$) using 7.5 years of PASS 8 event data in the energy range 100 MeV$-$300 GeV in 15 energy bins using the 3FGL as a source catalog model. In the 3FGL, 33 MSPs are described by an exponential cut-off power law model (Eqn. 6.2), whereas 6 MSPs are best fitted with a simple power law (PL) (Eqn. 6.3) where prefactor = N_0 and index = γ). However, in their analysis they find that an exponential cut-off can be detected in the 6 PL MSPs at > 3 σ significance. They therefore use an exponential cut-off power law model throughout their analysis. They then stack all flux points from the 39 MSPs with a TS > 9 (equivalent to > 3 σ significance) to obtain a functional form described by an exponential cut-off power law as Eqn. 6.2 with $\Gamma = 1.54^{+0.10}_{-0.11}$ and $E_{\rm cut} = 3.70^{+0.95}_{-0.70}$ but with E_0 and b equal to 1 (hereafter the "Xing and Wang" model). Finally, they recommend that this functional form can be used as a model to find candidate MSPs in unidentified Fermi-LAT sources at high Galactic latitudes.

$$\frac{dN}{dE} = N_0 E^{-\Gamma} \tag{6.3}$$

In contrast, McCann [194] constructs a stacked MSP gamma-ray spectrum using an aperture photometry (AP) method rather than likelihood analysis. The AP approach has the advantage over the likelihood approach in that it is model independent and less computationally intensive. However, it does require timing information for the pulsars analysed. McCann chooses 39 MSPs from the 2PC (excluding a different one, J2215+5135 because its off-phase, where emission is at a minimum, is undefined) and consider 4.2 years of PASS 7 event data per MSP in the energy range 100 MeV$-$1 TeV binned at 4 bins per decade of energy. McCann then uses the TEMPO 2 software to barycentre the photon events and phase fold them. McCann then obtains the energy excess counts of all events outside the off-phase (i.e the on-phase), distributed by energy. McCann next corrects for exposure and produces a spectral energy distribution from the stacked fluxes. Finally he fits the differential flux $E^2\frac{dN}{dE}$ (as opposed $\frac{dN}{dE}$ alone) with an exponential cut-off power law, with a functional form as Eqn. 6.2. This exponential cut-off power law has $\Gamma = 0.54 \pm 0.05$, $E_{\rm cut} = 3.60 \pm 0.21$ GeV and $b = 0.7 \pm 0.15$ (hereafter the "McCann" model). McCann also makes a check on the performance of the AP method vs the likelihood method of the 2PC by defining a flux ratio for the MSPs of $\frac{APflux}{2PCflux}$ which varies between 0.8 and 0.9 for energies of 250 MeV$-$8 GeV.

In Fig. 6.4, I show my model in comparison to the McCann and Xing and Wang MSP models by normalising all 3 models to the summed MSP flux at 1.3 GeV. The McCann model appears to fit the stacked 98 MSPs less well above 2 GeV than my model and Xing and Wang.

The preferred MSP model can be determined more rigorously using the minimum value of the Akaike Information Criterion (AIC) statistic [26], (Eqn. 6.4). The AIC ranks how well a model fits a data set (compared to other models) and penalises the over-fitting which results from the model having more free parameters. The AIC is a relative measure in that it allows a set of models to be compared with the model exhibiting the lowest AIC score considered superior in that set but it does not allow a determination of whether any model is best in an absolute sense. The AIC is defined in Eqn. 6.4 where k is the number of free model parameters and ℓ is the likelihood of the best fit model.

$$AIC = 2k - 2\ln(\ell) \tag{6.4}$$

For the purposes of spectral model comparison a more convenient definition of AIC is Eqn. 6.5 where n is the number of flux data points or energy bins and RSS is the residual sum of squares as defined in Eqn. 6.6 with y_i being the observed flux and $f(x_i)$ the flux predicted by the model for at an energy x_i for an energy bin i.

$$AIC = 2k + n\ln\left(\frac{RSS}{n}\right) \tag{6.5}$$

Bin Center MeV	Lower Bin Energy MeV	Upper Bin Energy MeV	χ^2 Statistic
133	100	177	42.94
237	177	316	4.00
421	316	562	11.39
749	562	1000	0.000128
1333	1000	1778	0.000000
2371	1778	3162	0.000001
4216	3162	5623	0.000033
7498	5623	10000	0.000009

Table 6.3 A breakdown of χ^2 test statistic by energy bin for my model fitted to the 98 MSP stacked flux. Above 177 MeV, my model is a good fit to the 98 MSP stack at the $\alpha = 0.001$ significance level with total χ^2 = 15.39, which is less than the critical value 20.515 for 5 degrees of freedom.

$$RSS = \sum_{i=1}^{n} (y_i - f(x_i))^2 \tag{6.6}$$

In cases where the number of free parameters is comparable to the number of predicted points, the corrected AIC (AICc) can also be used (Eqn. 6.7) and this corrects for the over selection of models with more free parameters in this case and I shall use this subsequently in Chapter 7.

$$AICc = AIC + \frac{2k^2 + 2k}{n - k - 1} \tag{6.7}$$

The AIC statistic for the fit of my model, and the models of Xing and Wang and McCann to the stacked MSPs between 100 MeV−10 GeV, is -163.70, -161.87 and -147.97 respectively. Therefore, my model, having the minimum AIC statistic, is the preferred model.

The goodness-of-fit of my model to the stacked MSPs can be determined by the χ^2 statistic. The fit of my model to the 98 stacked MSPs has a χ^2 statistic of 58.33 (5 degrees of freedom) and exceeds the critical value of 11.070 and 20.515 at the $\alpha = 0.05$ and $\alpha = 0.001$ significance level, respectively, and thus, overall is not a good fit. However, a breakdown of the χ^2 statistic per bin (Table 6.3), shows that my model is a very good fit between 562 MeV and 10 GeV with χ^2 values of $10^{-5}-10^{-6}$ and only a poor fit at low energies, with χ^2 = 42.9 for the 133 MeV bin. From 177 MeV to 10 GeV, my model is a good fit to the 98 MSP stack at the $\alpha = 0.001$ significance level with total χ^2 = 15.39, which is less than the critical value 20.515 for 5 degrees of freedom. Therefore, I judge my model to be an acceptable fit to the stacked spectrum of 98 MSPs.

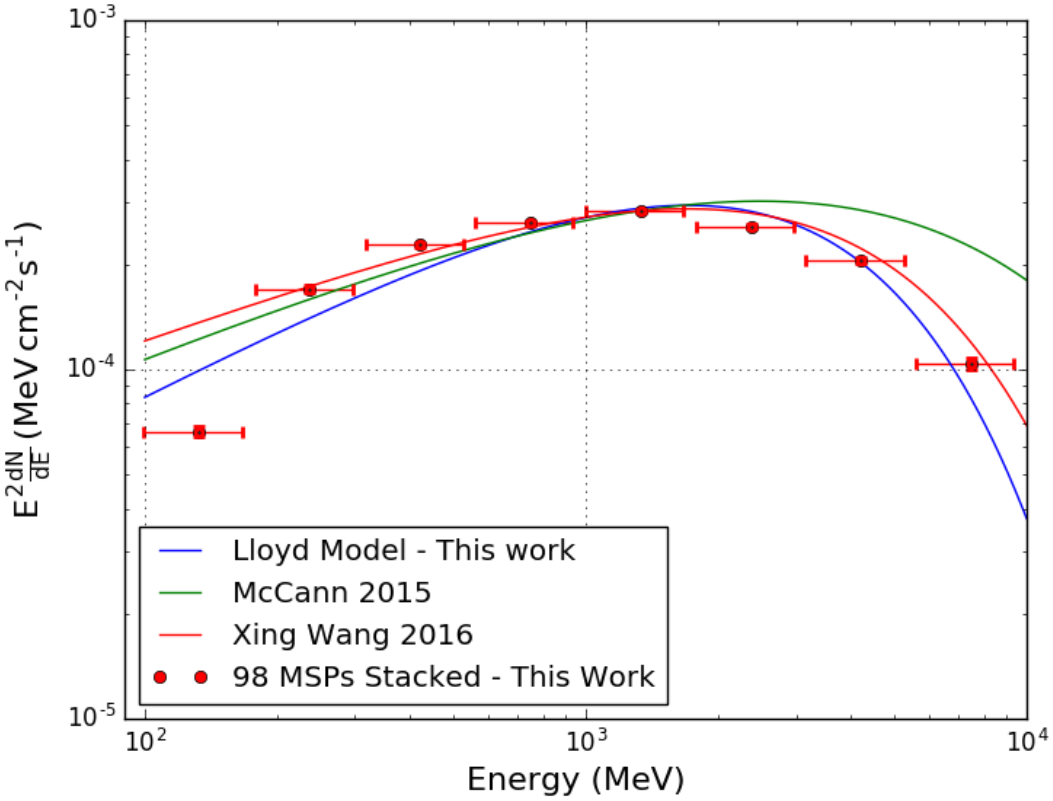

Fig. 6.4 My MSP model (Lloyd), McCann and Xing and Wang MSP models compared to the summed flux of 98 MSPs by normalising model flux to that of the summed flux at 1.3 GeV. The McCann model is a poorer fit to the summed flux above 1.3 GeV than Lloyd or Xing and Wang.

6.7 Conclusion

I select 103 MSPs from the Public List of LAT Detected Gamma-Ray Pulsars and detect 98 MSPs in the range 100 MeV−10 GeV, and 32 MSPs in the range 10 GeV−100 GeV with no emission detected above 56 GeV. I show that the emission for the ensemble of MSPs, in each bin, is probably not dominated by a few bright pulsars. I sum the 100 MeV−10 GeV fluxes and fit the resulting spectral energy distribution with an exponential cut-off power law to produce my own stacked MSP model. I show that this model is a good fit (using the χ^2 statistic) to the 98 MSPs in the energy range 177 MeV−10 GeV at the $\alpha = 0.001$ significance level, but a poorer fit when flux below 177 MeV is also considered. I also show that my model and Xing and Wang models are a good description of the stacked 98 MSP spectrum but that the McCann model only fits between 100 MeV and 1.8 GeV, diverging from the 98 MSP spectrum at higher energies. Using the minimum AIC statistic, I show that my model is the preferred model in comparison to the models of Xing and Wang and McCann, when fitted to the 98 MSPs. Therefore, my MSP model is a good general spectral model for MSPs and I will now use it in Chapter 7 to assess to what extent components of GC spectra result from MSP emission .

Chapter 7

Spectral Analysis of Globular Cluster Gamma-ray Emission

7.1 Introduction

In this chapter, I examine to what extent millisecond-pulsars (MSPs) account for gamma-ray emission in globular clusters (GCs). I consider selected GCs to determine if they have known gamma-ray sources and whether their spectra are consistent with MSP emission.

I discuss to what extent the gamma-ray emission of 47 Tuc can be accounted for by the predicted gamma-ray emission of its radio resolved Millisecond Pulsars (MSPs) using a gamma-ray/X-ray flux relationship for MSPs in a model independent way. I use this predicted gamma-ray emission to normalise the Xing and Wang and McCann models of stacked MSP emission and show how this compares to the observed spectral energy distribution of 47 Tuc.

I use the AIC statistic to show that my own stacked model of MSP emission, hereafter, "Lloyd", is preferred over the stacked MSP models of Xing and Wang and McCann, as a model of GC emission. The goodness-of-fit of the Lloyd model to the GC spectral models and SED is tested using the χ^2 statistic to identify two populations of GCs, those which are well-fitted and those that are not. Using the Kolmogorov-Smirnov test, I compare these two populations to see if they have a different distribution of characteristics relevant to MSP formation, which provides indirect evidence as to whether MSPs are the main source of gamma-ray emission or not. I then turn to a more detailed examination of the low- and medium-energy spectral characteristics of the GCs and MSPs, by defining colour bands, which are a measure of how sharply emission rises and falls at low and medium energies respectively. I compare these GC colours against GC metallicity, binary encounter rate, MERP and GC gamma-ray luminosity to see if those characteristics relevant to MSP

formation exert any influence on GC spectral characteristics. I also see if these colours are related to the $\dot{E}$ of individual MSPs which if correlated would allow constraints to be placed on the GC MSP population. I examine the higher energy GC and MSP results above 10 GeV and the spectra of the sole HE detection, Terzan 5.

Finally, I show that while my *Fermi*-LAT analysis can constrain model of MSP emission at higher energies, CTA will be required to improve these constraints further. I determine whether GCs will be detectable by CTA by analysing the 30 sources of the 4FGL catalogue identified with GCs in the energy range $0.1-100$ GeV to produce GC spectral models which are then input into the CTA analysis package, CTOOLS to yield a detection significance.

7.1.1 Millisecond Pulsars and Globular Clusters: Spectral Characteristics

Before the launch of *Fermi*, [52] modeled the GC gamma-ray emission arising from the Comptonisation of stellar and CMB photons due to energetic leptons accelerated by millisecond pulsar wind shockwaves or from the magnetosphere. The spectra derived from this model predicted rising gamma-ray flux between 1-10 GeV and a hardening of the spectrum for 47 Tuc, NGC 7078 and NGC 6205, with the best candidates for gamma-ray detection predicted to be 47 Tuc and NGC 6205 (the latter being undetected in this study). The authors of [123] predicted that curvature radiation (CR) (where relativistic electron / positron pairs are constrained to move along magnetic field lines) would produce gamma-ray emission peaking at 1-10 GeV from MSPs, while [263] noted that the single particle CR spectrum of [123] with its super exponential cut-off, would be reflected in the total phase-averaged spectrum of an MSP with the cut-off arising from radiation reaction limited acceleration, in which the acceleration rate of relativistic electrons equals the loss rate. This predicted spectral cut-off in MSPs was confirmed by [6] who first observed gamma-ray pulsations from 8 MSPs (5 of which were in binary systems). They found that the gamma-ray spectrum of these MSPs was well described by a exponential cut-off power law (Eqn. 5.3) with a hard spectral index ($\Gamma < 2$) and cut-off energy E_c in the range 1-4 GeV. These spectral characteristics were found to hold more generally for a larger selection of 40 MSPs (10 isolated and 30 binary) in the second catalogue of *Fermi*-LAT pulsars [11]. Later, a stacked MSP spectrum was constructed from 39 of these 40 MSPs (10 isolated and 29 binary MSP systems), by McCann [194], who demonstrated a spectral cut-off at 5 GeV.

These average spectral characteristics of MSPs were used to identify the first gamma-ray emitting GCs. [10] classified 5 gamma-ray sources as *plausible* GC candidates on the basis of their spectral signature being MSP-like and matching that of the magnetospheric emission

from an individual MSP with a spectral index < 2 and an exponential cut-off in the range 1.0-2.6 GeV. In contrast 3 sources were classed as *possible* GCs because whilst they had a hard spectral index, they lacked evidence for an exponential cut-off in their spectra.

Observational evidence for the existence of individual MSPs (as opposed to an ensemble) within GCs may be found from radio observations. To date 150 pulsars have been detected and timed in 28 GCs, with the vast majority being MSPs[1]. Phase-resolved, pulsed gamma-ray emission from GCs is very rare, with pulses detected from a single gamma-ray bright MSP in only two GCs: NGC 6626 [277] and NGC 6624 [109]. This provides an important link between GCs and gamma-ray emitting MSPs, albeit that these particular objects are unusually bright. MSP J1823-3021A in NGC 6624 has a gamma-ray luminosity of 8.4 x 10^{34} erg s^{-1} which can potentially account for the entire GC emission ([109]) and MSP B1821-24 in NGC 6626 can account for 25 % of the GC emission [277]. The gamma-ray spectra of these GC are fitted with a PL exponential model and have the spectral cut-offs characteristic of MSPs (1.5 GeV for NGC 6624 and 1-2.6 GeV for NGC 6626 respectively [249],[10]). This confirms the view that the gamma-ray spectra of GCs, even when dominated by a small number of very bright MSPs, should exhibit spectral cut-offs and provides indirect support for the argument that an ensemble of MSPs in GCs should also exhibit a spectral cutoff.

From the above I draw the following conclusions: the spectral characteristics of single MSPs are broadly predictive of the ensemble gamma-ray emission of MSPs in GCs in general, and the stacked spectrum of MSPs exhibits similar characteristics to the single MSP case. Furthermore, this stacked spectrum exhibits a spectral cut-off even when there is a mix of isolated and binary pulsar systems, as shown by [11] and [194], where in fact binary systems were in the majority. Therefore, I take the characteristic spectral cut-off of single or stacked MSPs to be indicative of the expected spectra from MSPs in GCs.

7.2 GC Spectral Shape and Potential Gamma-Ray sources

I now select a representative sample of the detected GCs to discuss in more detail, on the basis that their gamma-ray emission has been previously well modelled or that they have been observed in sufficient detail to suggest counterpart sources of gamma-ray emission.

[1] A list of currently known pulsars in GCs is maintained at http://www.naic.edu/~pfreire/GCpsr.html, accessed 2/7/2018

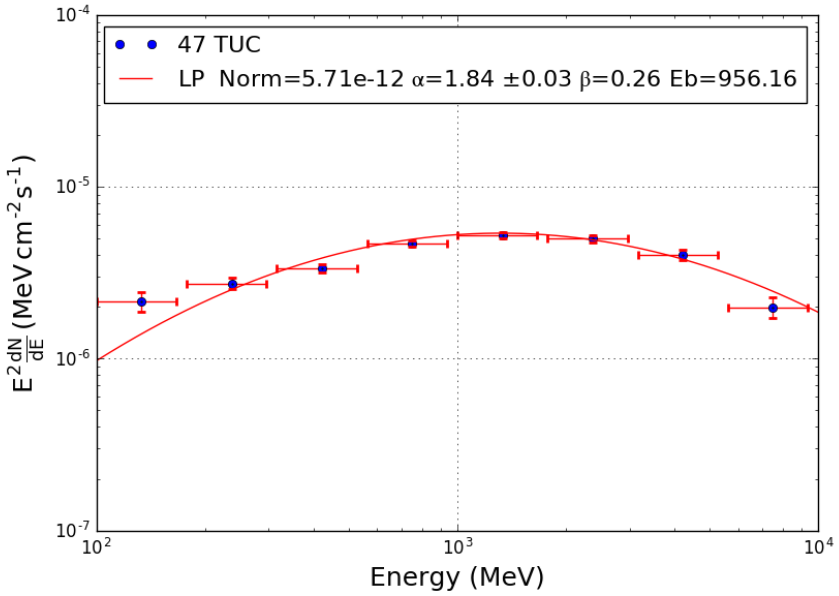

Fig. 7.1 The spectral energy distribution of 47 Tuc, showing the tension between the best-fit model and the observed spectrum at the lowest and highest energies energies.

7.2.1 47 Tuc

The spectrum of 47 Tuc is well described by a log-parabola model (Fig. 7.1), which is binned at 4 bins per decade in energy for consistency with the analysis of the other 110 GCs. However, there is tension between this best-fit model and the observed spectrum at the lowest and highest energies energies considered in this analysis, even more clearly seen, when binned at 8 bins per decade in energy (Fig 4.4). This tension may suggest that there are multiple emission sources within 47 Tuc. With 25 phase resolved MSPs, 47 Tuc has the second largest MSP population after that of Terzan 5 [225]. However, kinematic data has recently revealed possible evidence of an IMBH in 47 Tuc [159]. The presence of an IMBH within 47 Tuc raises the interestingly possibility of gamma-ray emission from DM annihilation [139]. In order to investigate this possibility, as a co-author to [63], hereafter "Brown", I provided a gamma-ray spectral fit analysis of 47 Tuc, hereafter "Lloyd 47 Tuc", (using the 3FGL catalogue, energy range 100 MeV$-$100 GeV, binned at 5 bins per decade of energy with 9 yr of front and back event data) and a separate model of the MSPs in 47 Tuc (as described in Section 7.3 below). A spectral study of Lloyd 47 Tuc combined with the MSP model by the co-authors (Brown and Lacroix), found that the gamma-ray emission from 47 Tuc is best described by a two-source population model consisting of MSPs and

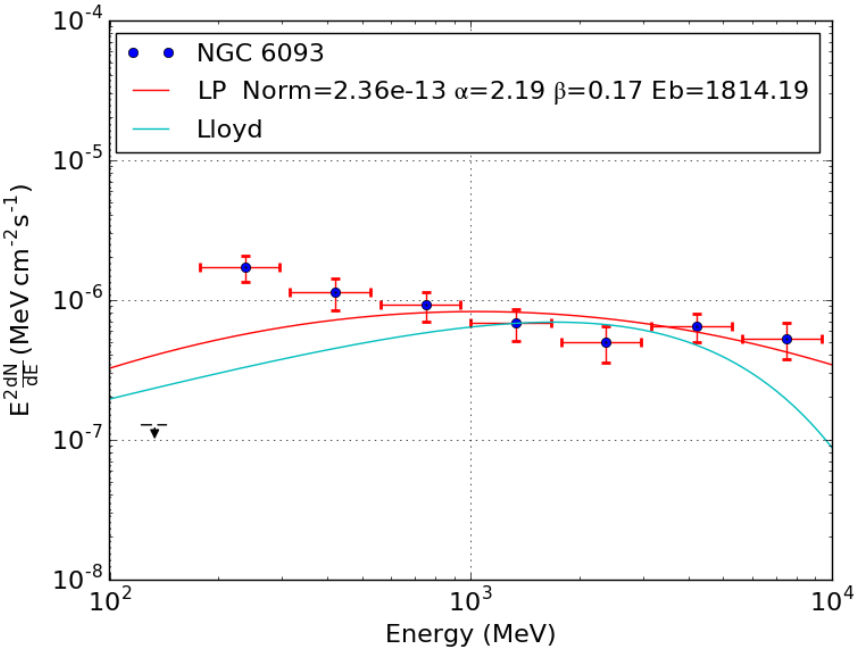

Fig. 7.2 The spectral energy distribution of NGC 6093 is hard and is in tension with the Lloyd model below 1 GeV and above 5.6 GeV.

annihilating DM around the putative central IMBH via the $b\bar{b}$ channel, when compared to a MSP-only explanation [63].

7.2.2 NGC 6093 and 6218

The spectra of both NGC 6093 (Fig. 7.2) and NGC 6218 (Fig. 7.3) are hard, with NGC 6093 having a flat spectrum and NGC 6218 exhibiting increasing emission beyond $\sim$ 1.8 GeV, whilst lacking detected flux below 1.8 GeV, which is unusual. These GCs are not known to contain any MSPs (Fig 5.6), and it is perhaps not surprising that the spectra in both objects are in tension with the typical stacked spectra of MSPs presented in Lloyd [194] with NGC 6218 showing increasing emission above 1.8 GeV and NGC 6093 showing increasing emission below 1 GeV and above 5.6 GeV. NGC 6218 shows some evidence for variability (Fig. 7.4), which may point to a contribution from e.g. a background AGN. An X-ray study of NGC 6218 [185], showed that there are several sources in the field of view, one of which, CX3, may indeed be an AGN. However, the gamma-ray AGN catalogue is dominated by blazars - indeed, 98% of the 3FGL AGN are this class of object [19]. There is no evidence that CX3 is a blazar, and given that blazars constitute only $\sim$ 3% of known AGN, the chance that it is a blazar is small. An X-ray study of NGC 6093 shows that it contains 5 CVs [127],

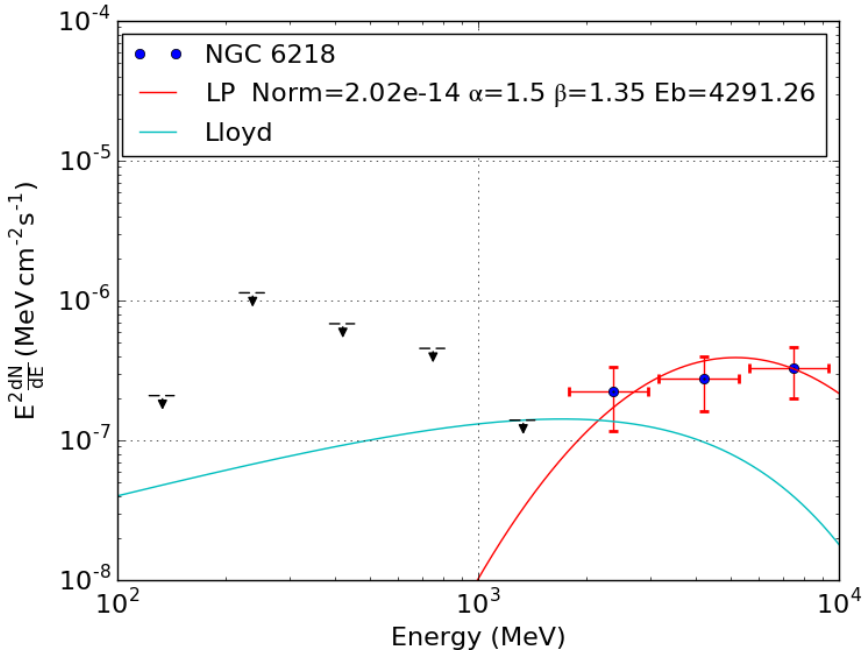

Fig. 7.3 The spectral energy distribution of NGC 6218 showing no emission below 1.8 GeV, and increasing emission above 1.8 GeV which is in tension with the Lloyd model up to 10 GeV.

but these are unlikely to be significant gamma-ray sources as NGC 6093 has no indication of gamma-ray variability (Fig. 7.4).

7.2.3 NGC 6752

NGC 6752 has a hard, flat spectrum between 400 MeV and 6 GeV (Fig. 7.5), but indications of a cut-off above 6 GeV. This object is known to contain 5 MSPs and the presence of this cut-off suggests that these are likely important contributors to the gamma-ray emission. In addition, there are 39 X-ray sources within the 1' 9" half-mass radius of NGC 6752, of which 16 are likely cataclysmic variables (CVs) and 3 are background AGN [186]. Three dwarf novae (CX1, CX4 and CX7) within this GC have been seen in outburst, over the last twenty years, using B band photometry and far UV/Hα observations [154], [253], [186]. Some of these objects could be sources of gamma-ray emission, but the lack of gamma-ray variability on timescales of 6 months suggests this contribution is minor (Fig. 7.4).

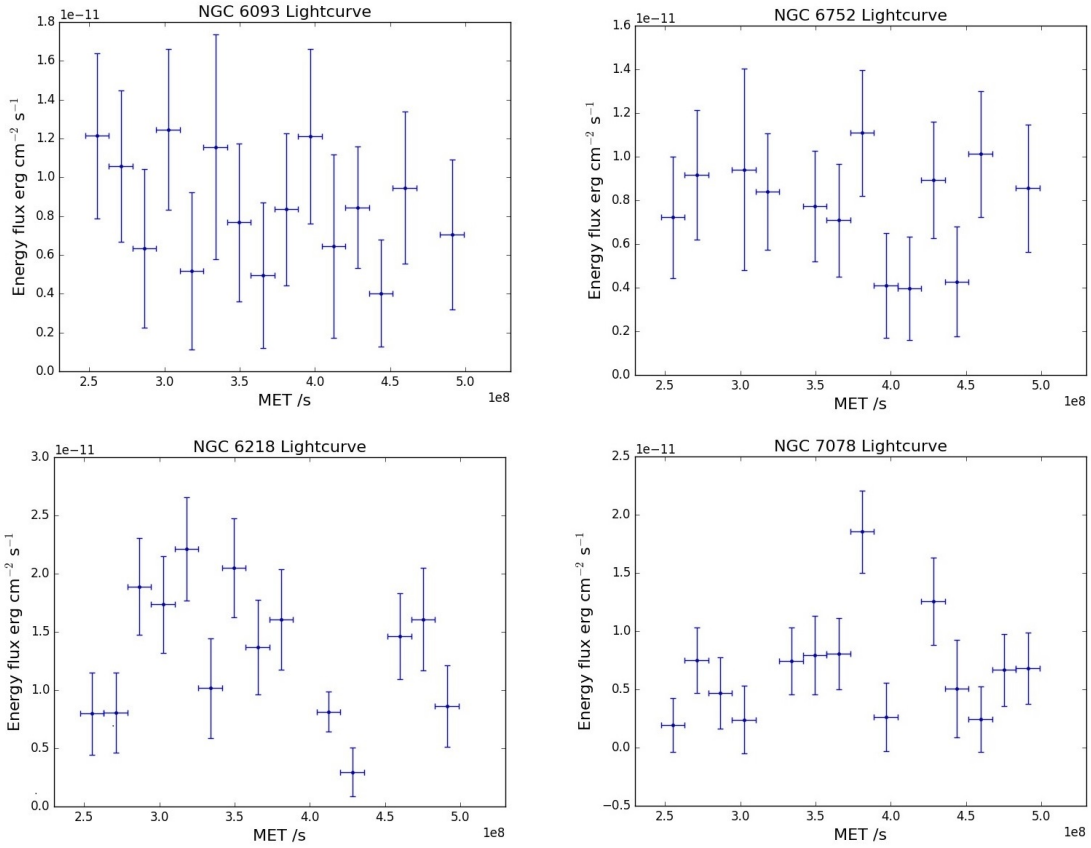

Fig. 7.4 The light-curves of NGCs 6093, 6752, 6218 and 7078, in the energy range 100 MeV−10 GeV, binned at 6 monthly intervals, from Aug 2008 to March 2016. NGC 6093 and 6752 show no indication for variability, whereas NGC 6218 and 7078 show 3 and 2σ indications for variability respectively. Taken from my 3FGL GC study [181].

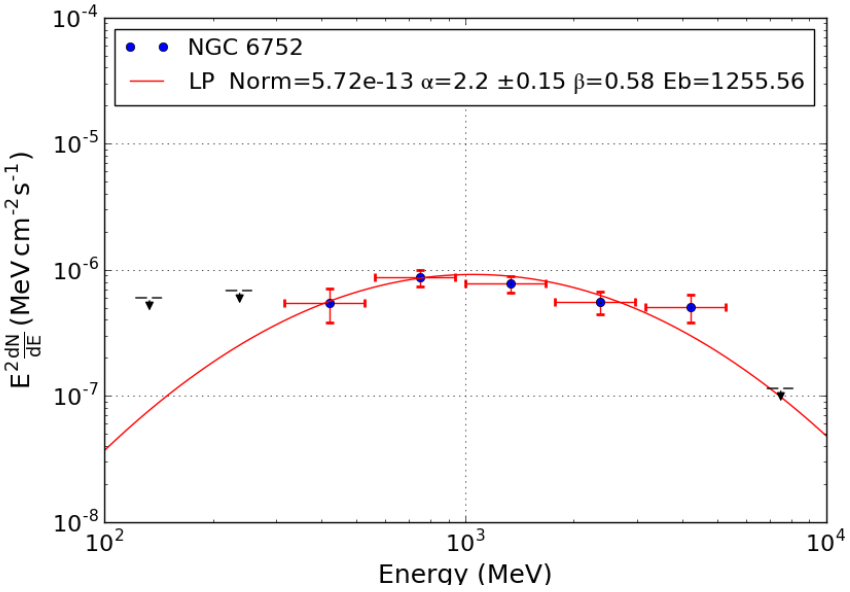

Fig. 7.5 The spectral energy distribution of NGC 6752 has a hard, flat spectrum between 400 MeV and 6 GeV, with indications of a cut-off above 6 GeV.

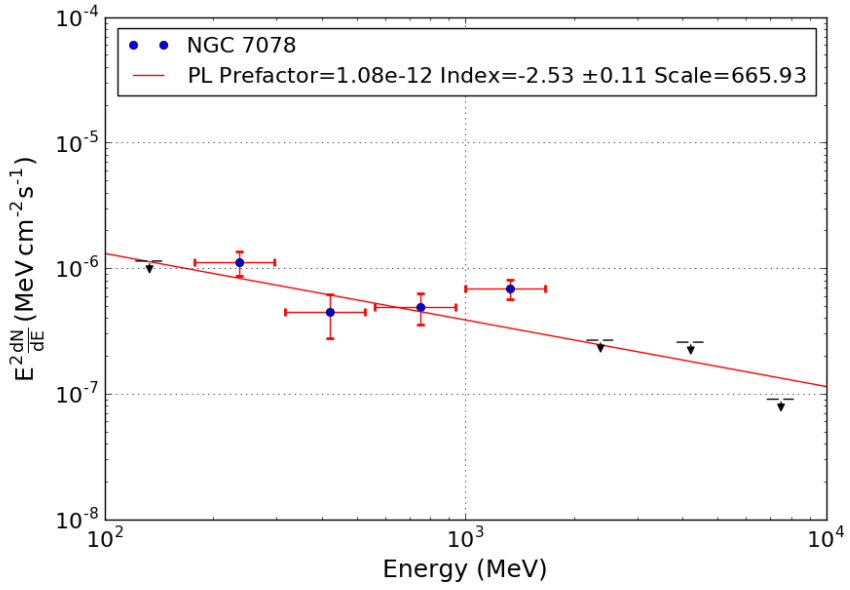

Fig. 7.6 The spectral energy distribution of NGC 7078 has a soft power law spectrum, which is less typical of the detected GCs, being shared only by NGCs 6304, 6341 and 1904.

7.2.4 NGC 7078

NGC 7078 (Fig. 7.6) has a soft power law spectrum, which is atypical of the detected GCs, being shared only by NGCs 6304, 6341 and 1904 (Figs. 7.14 and A.8). The core of NGC 7078 was previously the target of a very long baseline interferometry radio study, (Fig. 7.7) which constrained the mass of a putative central IMBH [158] to $< 500\ M_{\odot}$. This found no evidence of central IMBH variability over a timescale of 2 months to 2 years, but did locate a strong radio source within 1.5 arc min of the GC centre. It was suggested that this radio source, S1, could be a background quasar. Similarly to NGC 6218, in the absence of a blazar classification (unlikely on population grounds), there is no evidence that S1 is the source of the gamma-ray emission. There are two further objects in the field of view of NGC 7078, AC211 and S2, both of which are low-mass X-ray binaries. None of this class of object is a confirmed gamma-ray source, so these also seem unlikely candidates for the gamma-ray emission. NGC 7078 has only a weak 2σ indication of variability (Fig. 7.4), which again suggests that a background AGN is unlikely to be the source of gamma-ray emission. In the absence of any other plausible candidates, the working hypothesis is that the globular cluster is the source of the gamma-ray emission. The asymmetric TS map of Fig. 7.8, (with significant emission skewed towards direction of S1), suggests that NGC 7078 could be comprised of multiple point sources. Attempting to resolve NGC 7078 into two point sources in my previous 3FGL analysis [181], with an additional point source placed at a second significant point on the TS map (RA 322.20° and Dec 12.65°) does not yield a significant detection of the additional point source.

Conclusion

The globular clusters 47 Tuc and NGC 6752 both show evidence of a spectral cut-off which could plausibly be explained by MSPs. However in the case of 47 Tuc, a more finely binned analysis with tension between the observed spectrum and the best fit at lowest and highest energy suggests that other sources may contribute. The flat, hard spectra of NGC 6093 and 6218, which do not display a cut-off below 10 GeV are harder to explain by MSP emission, particularly given the absence of radio-detected MSPs in these objects. NGC 6218's unusual spectrum is accompanied by evidence for variability at the $\sim 3\sigma$ level, which may point to a contribution from a variable source in the field of view, although a suitable candidate object appears lacking. NGC 7078, along with NGCs 6341, 1904 and 6304, has a soft power law spectrum, not typical of MSPs. I now consider in more detail the MSP gamma-ray emission in the GC 47 Tuc, which is a special case being the most significantly detected gamma-rays emitting GC with 25 resolved MSPs.

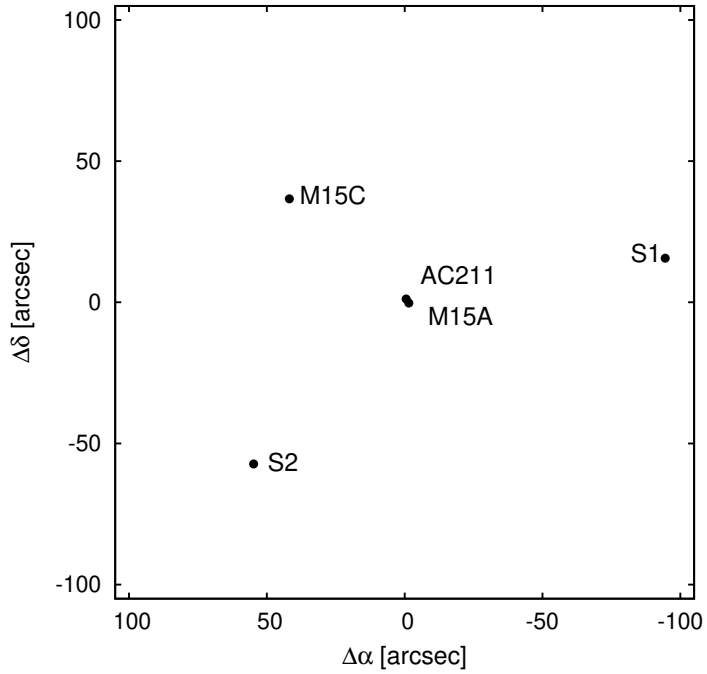

Fig. 7.7 Radio detected sources in NGC 7078 using VLBI at 1.6 GHz with offset from the pointing centre, taken from [158], S1 is an extra-galactic object, S2 is a probable foreground LMXB (distance 2.2 kpc), AC211 is an LMXB and M15A and M15C are pulsars (periods 110 and 30.5 ms respectively).

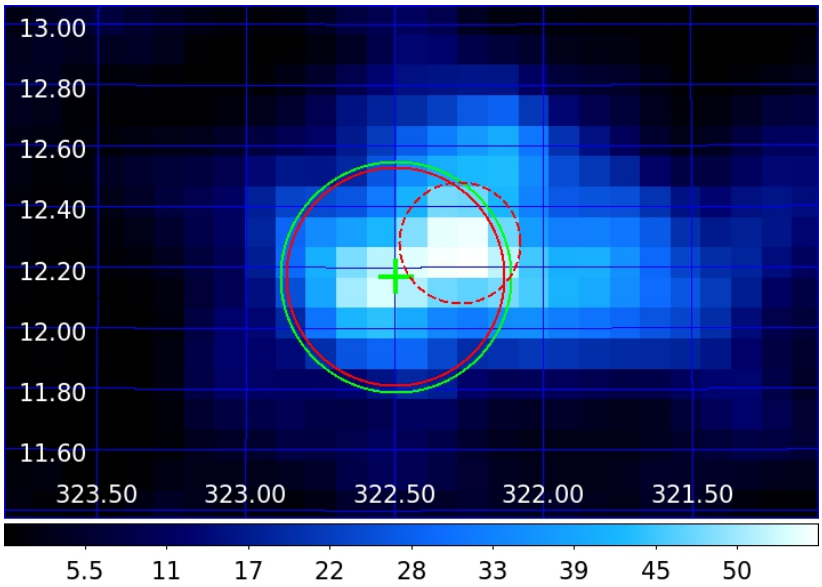

Fig. 7.8 Test statistic map of NGC 7078 showing offset emission at the best localisation position with 95 percent containment (red dashed circle) . The tidal radii are Harris 2003 GC catalogue at http://www.naic.edu/ pulsar/catalogs/mwgc.txt (red circle) and more recent determination from [92] (green circle). The GC catalogue co-ordinate is indicated with a green cross. Graduated color bar shows the TS value. RA and Dec are horizontal and vertical axes respectively on the white interior scale. Spatial bin size is 0.1°.

7.3 Estimating MSP Emission in 47 Tuc

Although the MSPs in 47 Tuc are unresolved at gamma-ray energies it is possible to estimate their gamma-ray contribution through measurements of X-ray emission. The 2PC provides a broad relationship between the integral energy flux between 100 MeV−100 GeV (G_{100}) and non-thermal X-ray flux between 0.3−10 keV (F_X), in Fig. 18 of [11]) for all pulsars. For 12 MSPs with sufficient X-ray counts, the non-thermal X-ray spectrum is well characterised by *Chandra*-ACIS, XMM-Newton, *Swift*-XRT and *Suzaku* and this provides a relationship between gamma-ray and X-ray flux (Eqn. 7.1, hereafter the "Abdo Ratio" (AR), taken from the caption of Fig. 18 of [11]). Although $\frac{G_{100}}{F_X}$ can span a thirty-fold range for the same $\dot{E}$ value (Fig. 18 of [11]) and hence is a somewhat poorly constrained relation, the Abdo Ratio does provide a way to infer broadly the expected gamma-ray emission for radio-resolved MSPs, as yet unresolved in the gamma-ray but for which non-thermal X-ray measurements are available.

$$AR = \log_{10}\left(\frac{G_{100}}{F_{\rm X}}\right) = 2.3 \pm 0.5 \tag{7.1}$$

I now examine to what extent the Abdo Ratio can predict the contribution made by known MSPs to the gamma-ray emission of 47 Tuc. In [60], 19 precisely-localised MSPs in 47 Tuc are analysed using four 65 ks *Chandra* X-ray observations in the $0.3-8$ keV energy range as seen by the ACIS-S instrument. The majority of these MSPs exhibit soft X-ray emission which is well-described by a thermal blackbody (BB) or neutron star hydrogen atmosphere spectrum (NSA). Three of the MSPs (47 Tuc J, O and W) have an X-ray spectrum which also shows a significant non-thermal power law (PL) component, in addition to the BB emission, which the authors of [60] ascribe to an intra-binary shock interaction between the relativistic pulsar wind and matter from the binary stellar companion. They then define 3 X-ray colour bands; a soft band ($0.3-0.6$ keV), a medium band ($0.6-1.5$ keV) and a hard band ($1.5-4$ keV). The authors then plot the hardness ratios of each MSP using these bands on an X-ray colour-colour diagram (which I show in Fig. 7.9) of (medium counts)/(soft counts) vs (hard counts)/(medium counts) in an attempt to discriminate between the thermal or non-thermal PL model cases in the MSP population.

Fig. 7.9 shows that 3 MSPs (47 Tuc M U and L) fall in the BB color space, whereas 47 Tuc W falls in the non-thermal PL space. The remaining 15 MSPs fall between the PL non-thermal model and the BB model which they suggest implies a more complex MSP spectrum of a composite thermal and non-thermal PL or a multi-temperature thermal spectrum. I interpret Fig. 7.9 as meaning that for most of the MSPs in [60]) a BB or non-thermal PL model cannot be chosen on colours and hence X-ray photon counts alone. I therefore make the simplifying assumption that the X-ray emission of all 19 MSPs is non-thermal and that the application of the Abdo ratio is valid for the MSPs in 47 Tuc.

The X-ray analysis of the 19 MSPs is re-visted by one of the co-authors of [60] in the archive only posting of [51]. Though not published in a refereed journal, it can be considered a valid update of the determinations in [60] and a continuation of the same work, with most fluxes consistent between the two to within a factor of a few. The 19 MSPs above are re-analysed using the same publicly available *Chandra* observations quoted in [60] with a further fifteen 50 ks *Chandra* High Resolution Camera-S observations from $0.1-10$ keV. This re-analysis confirms that the 19 MSPs have a soft X-ray spectrum and are consistent with [60]. However the author makes the point that the X-ray photon statistics are so poor that one cannot distinguish between BB and PL spectral models of X-ray emission, which is consistent with my comments about the colour plot above. I use the X-ray luminosities of the 19 MSPs quoted in [51] to derive X-ray energy fluxes in the energy band $0.3-8$ keV which I list in Table 7.1. I also include an X-ray flux value for another 47 Tuc MSP, J0024-7204

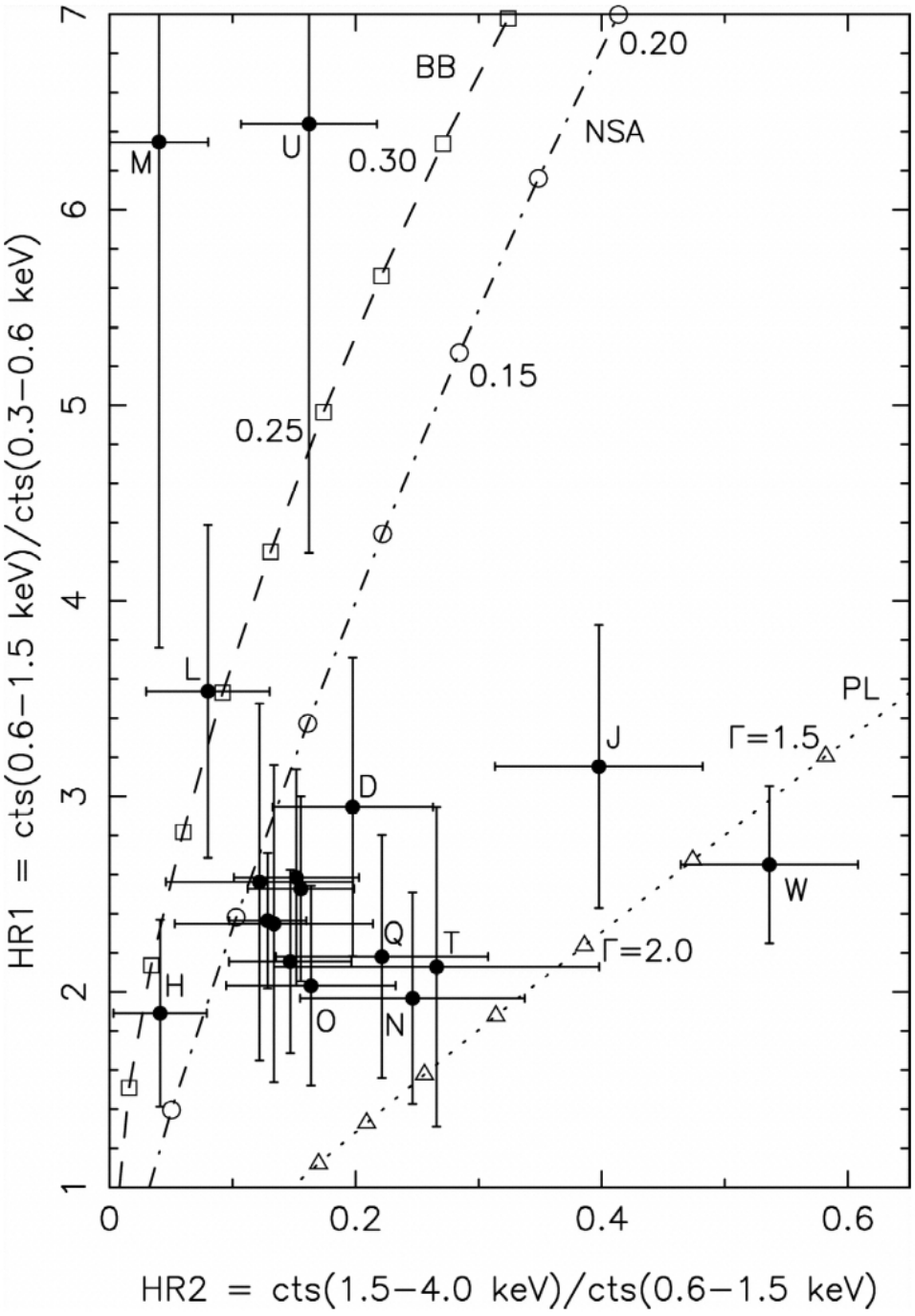

Fig. 7.9 X-ray colour-colour diagram for the MSPs in 47 Tuc. The lines represent model tracks for absorbed (non-thermal) power law (PL-dotted line), blackbody (BB-dashed line) and neutron star atmosphere (dot-dashed line) spectra convolved with the *Chandra* ACIS-S instrument response. Fifteen MSPs fall between the BB and PL cases suggesting a composite thermal and non-thermal spectrum. Figure taken from [60].

X, from [233] in which it is noted that limited photon statistics preclude detection of a non-thermal component.

I then straightforwardly use the Abdo Ratio (Eqn. 7.1) to calculate the gamma-ray flux G_{100} as Eqn. 7.2 for each MSP using 3 values of the Abdo Ratio (2.3 ± 0.5 from the 2PC) and I again list this predicted gamma-ray flux for each MSP in Table 7.1.

$$G_{100} = F_{\mathrm{X}} 10^{AR} = F_{\mathrm{X}} 10^{2.3\pm0.5} \tag{7.2}$$

It can be seen that for an Abdo Ratio of 1.8 the 20 MSPs cannot account for the total gamma-ray energy flux from 47 Tuc, whereas an Abdo Ratio of 2.3 might account for between an half and the total emission (within error). An extreme Abdo Ratio of 2.8 allows the 20 MSPs to account for all the gamma-ray emission in 47 Tuc.

I do not offer a single final percentage contribution with error (as might be obtained using error propagation rules which consider the X-ray flux errors in quadrature combined with the error on the Abdo Ratio), because in order to be trusted, this calculation requires that the upper and lower error bounds on any measurement are symmetric [46] which does not hold in the X-ray flux case (column 1 and 2 of Table 7.1) and that the error on any quantity is sufficiently "small" which does not hold for the Abdo Ratio when used as an exponent.

It therefore appears from all of the above that while 20 MSPs could account for the observed gamma-ray emission from 47 Tuc (which is known to host 25 confirmed MSPs[2]), it is also possible that up to half of the gamma-ray emission from 47 Tuc could be from another source.

Finally, the 6 month variability light-curve for 47 Tuc (Fig. 4.5), which exhibits no variability at the 2 σ level, allows me to exclude any additional sources of gamma-ray emission in the ROI with variability on this scale such as active galactic nuclei [228, 21].

[2]http://www.naic.edu/~pfreire/GCpsr.html Pulsars in Globular Clusters accessed 15th May 2020

Pulsar	X-ray Luminosity 0.3-8 keV 10^{30} erg s^{-1}	F_X X-ray Flux 0.3-8 keV 10^{-15} erg cm^{-2} s^{-1}	G_{100} Abdo Ratio=1.8 10^{-12} erg cm^{-2} s^{-1}	G_{100} Abdo Ratio=2.3 10^{-12} erg cm^{-2} s^{-1}	G_{100} Abdo Ratio=2.8 10^{-12} erg cm^{-2} s^{-1}
J0024-7204C	$1.58^{+0.36}_{-0.38}$	$0.65^{+0.15}_{-0.16}$	$0.04^{+0.01}_{-0.01}$	$0.13^{+0.03}_{-0.03}$	$0.41^{+0.10}_{-0.10}$
J0024-7204D	$2.51^{+0.88}_{-0.69}$	$1.04^{+0.36}_{-0.29}$	$0.07^{+0.02}_{-0.02}$	$0.21^{+0.07}_{-0.06}$	$0.65^{+0.23}_{-0.18}$
J0024-7204E	$3.63^{+0.94}_{-0.75}$	$1.50^{+0.39}_{-0.31}$	$0.09^{+0.02}_{-0.02}$	$0.30^{+0.08}_{-0.06}$	$0.95^{+0.24}_{-0.19}$
J0024-7204F	$7.41^{+1.71}_{-1.25}$	$3.06^{+0.70}_{-0.51}$	$0.19^{+0.04}_{-0.03}$	$0.61^{+0.14}_{-0.10}$	$1.93^{+0.44}_{-0.32}$
J0024-7204S	$7.41^{+1.71}_{-1.25}$	$3.06^{+0.70}_{-0.51}$	$0.19^{+0.04}_{-0.03}$	$0.61^{+0.14}_{-0.10}$	$1.93^{+0.44}_{-0.32}$
J0024-7204G	$4.57^{+1.89}_{-1.10}$	$1.89^{+0.78}_{-0.46}$	$0.12^{+0.05}_{-0.03}$	$0.38^{+0.16}_{-0.09}$	$1.19^{+0.49}_{-0.29}$
J0024-7204I	$4.57^{+1.89}_{-1.10}$	$1.89^{+0.78}_{-0.46}$	$0.12^{+0.05}_{-0.03}$	$0.38^{+0.16}_{-0.09}$	$1.19^{+0.49}_{-0.29}$
J0024-7204H	$2.04^{+1.27}_{-0.66}$	$0.84^{+0.52}_{-0.27}$	$0.05^{+0.03}_{-0.02}$	$0.17^{+0.10}_{-0.05}$	$0.53^{+0.33}_{-0.17}$
J0024-7204J	$11.48^{+9.90}_{-5.02}$	$4.74^{+4.09}_{-2.07}$	$0.30^{+0.26}_{-0.13}$	$0.95^{+0.82}_{-0.41}$	$2.99^{+2.58}_{-1.31}$
J0024-7204L	$39.81^{+36.05}_{-15.26}$	$16.43^{+14.88}_{-6.30}$	$1.04^{+0.94}_{-0.40}$	$3.28^{+2.97}_{-1.26}$	$10.37^{+9.39}_{-3.97}$
J0024-7204M	$3.09^{+1.18}_{-0.69}$	$1.28^{+0.49}_{-0.29}$	$0.08^{+0.03}_{-0.02}$	$0.25^{+0.10}_{-0.06}$	$0.80^{+0.31}_{-0.18}$
J0024-7204N	$2.09^{+1.00}_{-0.80}$	$0.86^{+0.41}_{-0.33}$	$0.05^{+0.03}_{-0.02}$	$0.17^{+0.08}_{-0.07}$	$0.54^{+0.26}_{-0.21}$
J0024-7204O	$21.88^{+22.79}_{-9.57}$	$9.03^{+9.41}_{-3.95}$	$0.57^{+0.59}_{-0.25}$	$1.80^{+1.88}_{-0.79}$	$5.70^{+5.93}_{-2.49}$
J0024-7204Q	$1.38^{+0.66}_{-0.36}$	$0.57^{+0.27}_{-0.15}$	$0.04^{+0.02}_{-0.01}$	$0.11^{+0.05}_{-0.03}$	$0.36^{+0.17}_{-0.09}$
J0024-7204R	$27.54^{+23.74}_{-14.05}$	$11.37^{+9.80}_{-5.80}$	$0.72^{+0.62}_{-0.37}$	$2.27^{+1.96}_{-1.16}$	$7.17^{+6.18}_{-3.66}$
J0024-7204T	$1.51^{+0.53}_{-0.44}$	$0.62^{+0.22}_{-0.18}$	$0.04^{+0.01}_{-0.01}$	$0.12^{+0.04}_{-0.04}$	$0.39^{+0.14}_{-0.12}$
J0024-7204U	$2.29^{+0.46}_{-0.59}$	$0.95^{+0.19}_{-0.24}$	$0.06^{+0.01}_{-0.02}$	$0.19^{+0.04}_{-0.05}$	$0.60^{+0.12}_{-0.15}$
J0024-7204W	$24.55^{+7.81}_{-6.35}$	$10.13^{+3.22}_{-2.62}$	$0.64^{+0.20}_{-0.17}$	$2.02^{+0.64}_{-0.52}$	$6.39^{+2.03}_{-1.65}$
J0024-7204Y	$2.19^{+0.97}_{-0.64}$	$0.90^{+0.40}_{-0.26}$	$0.06^{+0.03}_{-0.02}$	$0.18^{+0.08}_{-0.05}$	$0.57^{+0.25}_{-0.17}$
J0024-7204X	$2.00^{+0.60}_{-0.60}$	$0.83^{+0.25}_{-0.25}$	$0.05^{+0.02}_{-0.02}$	$0.16^{+0.05}_{-0.05}$	$0.52^{+0.16}_{-0.16}$
Total	173.55	71.63	4.52	14.29	45.19
Predicted MSP gamma-ray flux as a percentage of observed 47 Tuc flux:			17^{+12}_{-6}	55^{+37}_{-20}	174^{+116}_{-62}

Table 7.1 A table of 20 MSPs in 47 Tuc with X-ray luminosities and fluxes for J0024-7204C to J0024-7204Y and J0024-7204X taken from [51] and [233] respectively. The gamma-ray flux G_{100} is determined for Abdo Ratios of 1.8, 2.3 and 2.8 (i.e. 2.3 ± 0.5).Finally the total predicted gamma-ray flux is quoted as a percentage of the observed 47 Tuc gamma-ray luminosity of 2.60 x 10^{-11} erg cm^{-2} s^{-1}. An Abdo Ratio of 2.3 accounts for only half the emission of 47 Tuc (excepting error).

7.4 Selecting the Best MSP Model for 47 Tuc

In assuming that the gamma-ray emission of 47 Tuc results from the combined emission of a population of gamma-ray emitting MSPs it is useful to compare the Lloyd, McCann and Xing and Wang stacked models of gamma-ray emission with the finely binned SED of 47 Tuc obtained using the 3FGL analysis in Chapter 4. To do this I normalise all models so that their differential flux is consistent with the observed flux of 47 Tuc at 1182 MeV (the centre of the first bin above 1 GeV). I extract the dictionary output of the *Fermipy sed* method from above to obtain the differential energy flux points of the SED analysis and their error and I plot this with the normalised models and the best likelihood fit spectral model using my own Python code (Fig. 7.10). On inspection it appears that Lloyd fits the flux points best, followed by the *Fermi* analysis spectral model. The next best model is Xing and Wang which fits the SED well for energies above 10 GeV but somewhat less well below 500 MeV, whereas the McCann model appears to fit least well both at high and low energies whilst being a good description of the 47 Tuc spectrum between 700 MeV and 2 GeV in common with the other models. This ranking of models as fitted to 47 Tuc is confirmed by the ranking of χ^2 statistic for each model in Table 7.2 with Lloyd fitting 47 Tuc well at both the $\alpha = 0.001$ and $\alpha = 0.05$ significance level whereas the *Fermi* fit is only acceptable at $\alpha = 0.001$. The Xing and Wang and McCann models are not good fits to the emission of 47 Tuc.

The preferred model can also be selected through the AIC statistic as previously described. (Eqn. 6.4). Lloyd has 3 free parameters (*index1*, *Normalisation* and *exponential factor*), as does the best fit *Fermi* spectral model (*norm*, *alpha*, *beta*) and Xing and Wang (*norm*, Γ, E_{cut}), while McCann has 4 (*norm*, Γ, E_{cut} and b). I determine the AIC and AICc for each spectral model considered in this chapter, using my own Python code as Eqn. 6.5 and Eqn. 6.7 and list them in Table 7.3. As expected from the χ^2 fit the Lloyd model has the lowest AIC and AICc and is superior in describing the gamma-ray spectrum of 47 Tuc, with the *Fermi* analysis best fit spectral model, the next best, followed by Xing and Wang model and McCann. There is virtually no difference between AIC and AICc for the models considered implying that no AICc correction is required for the small number of predicted flux points compared to the number of free parameters in the model.

Finally, I consider whether the two source population model (above) comprised of an ensemble of MSPs and annihilating dark matter (DM) as in [63], hereafter Brown, is a better model of the gamma-ray emission of 47 Tuc than an ensemble of MSPs alone. I extract the DM gamma-ray spectrum from Brown and combine this with the Lloyd model, which I normalise so that the Lloyd flux at 330 MeV is the same as the DM flux, to set the relative flux contribution of DM and MSPs to be similar to Brown. I then normalise the Lloyd plus DM model so that the differential flux is consistent with the observed flux of 47 Tuc

Model	χ^2 Test Statistic	D.o.f	Critical Value $\alpha = 0.05$	Model Accepted at $\alpha = 0.05$	Critical Value $\alpha = 0.001$	Model Accepted at $\alpha = 0.001$
Lloyd	11.7	15	24.996	Yes	37.697	Yes
Lloyd+DM	12.2	14	23.685	Yes	36.123	Yes
47 Tuc *Fermi* fit	26.3	15	24.996	No	37.697	Yes
Xing and Wang	46.8	15	24.996	No	37.697	No
McCann	267.3	14	23.685	No	36.123	No

Table 7.2 Testing the goodness-of-fit of emission models to 47 Tuc using the χ^2 test statistic. Both the Lloyd model alone and the Lloyd model plus a dark matter (DM) component fits 47 Tuc well at both $\alpha = 0.001$ and $\alpha = 0.05$ whereas the *Fermi* fit is only acceptable at the $\alpha = 0.001$ significance level. The Xing and Wang and McCann models are not good fits to the emission of 47 Tuc.

at 1182 MeV. I show the individual DM and MSP components along with the Lloyd MSP and DM plus MSP models with the spectrum of 47 Tuc (Fig. 7.11). The Lloyd plus DM model exhibits a softer spectrum than the Lloyd model below 600 MeV but both models are equivalent with that of 47 Tuc within flux error at higher energies. The ranking of the χ^2 statistic demonstrates that the Lloyd plus DM model is only marginally less preferred than the Lloyd MSP model and, like the Lloyd model, is an acceptable fit at the $\alpha = 0.001$ and $\alpha = 0.05$ significance level (Table 7.2). Therefore the spectrum of 47 Tuc can equally be accounted for by using the Lloyd model alone, where MSPs account for all emission, or a Lloyd plus DM model, where the differential flux arising from MSPs is *less* than that from DM above energies of 330 MeV.

As a check, I perform a likelihood analysis to determine the significance of the Lloyd plus DM model vs that of Lloyd (if any). I do this by allowing the normalisation of both the Lloyd and the Lloyd plus DM model to vary and determine for each normalisation the residual for each energy bin which is the difference between the 47 Tuc flux and the model flux evaluated at the centre of each energy bin in the spectrum. I sum the log of the absolute value of each bin residual to obtain a set of log likelihood values, one for each normalisation. I then determine a minimum log likelihood value of -261.16 and -260.45 for the Lloyd plus DM, and the Lloyd model respectively from the set of log likelihood values. Using Eqn. 2.4 and the minimum log likelihood value of each model, I calculate a test statistic of 1.4 for the preference of the Lloyd model over that of the Lloyd plus DM model which is too low to be statistically significant. Thus, each model can equally well account for the emission from 47 Tuc and neither are significantly preferred, in agreement with the χ^2 result above.

Model	AIC	AICc
Lloyd	-910.15	-910.15
47 Tuc *Fermi* fit	-886.46	-886.46
Xing and Wang	-853.02	-853.02
McCann	-816.22	-815.22

Table 7.3 A comparison of AIC and AICc for the different emission models as compared to the observed flux of 47 Tuc. AICc is a version of the statistic which corrects for a small number of data points or in this case flux points. The AIC and AICc corrected statistic is essentially the same in all cases implying that AIC correction for the small number of predicted flux points is not required. The models are listed in order of relative merit from the best to the worst with the Lloyd MSP model being the best description of the gamma-ray emission of 47 Tuc.

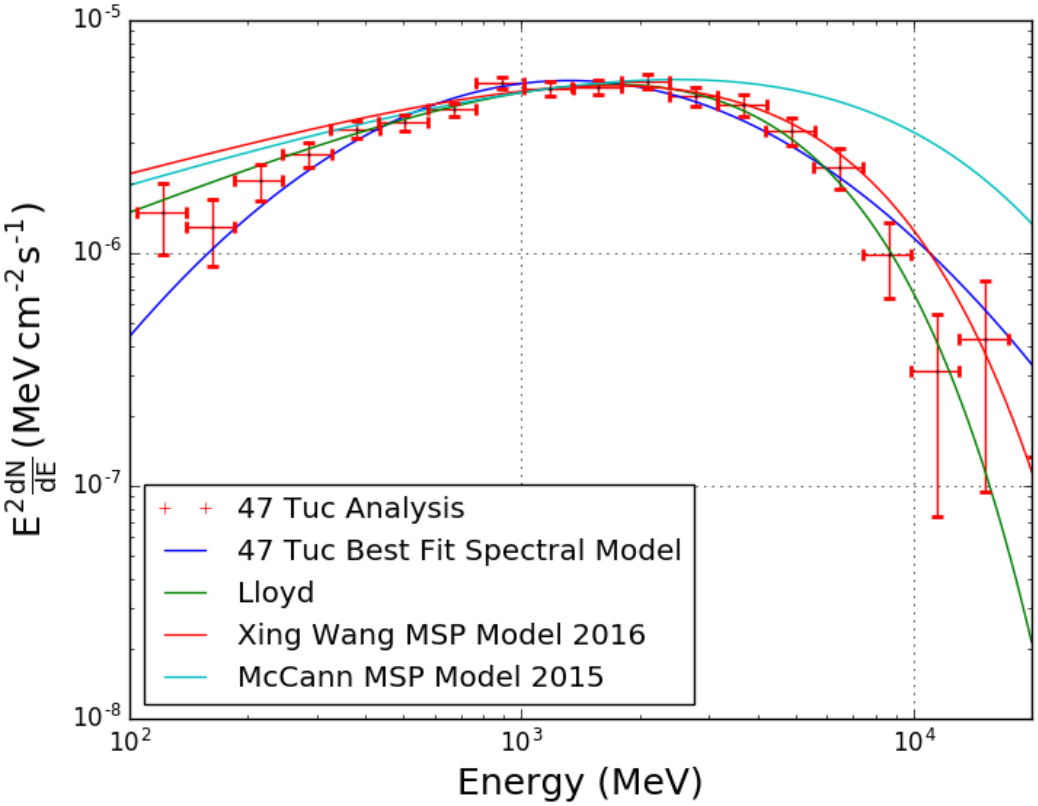

Fig. 7.10 Spectral energy distribution for 47 Tuc in the energy range 100 MeV to 20 GeV with spectral models for stacked MSP observations from my own model, McCann 2015 and Xing and Wang 2016. All MSP models are normalised to the 47 Tuc differential energy flux at 1 GeV. I extract the 47 Tuc fluxes from the *sed* method dictionary output and plot using my own Python code with pyplot. The best fit spectral model from the *Fermi*-LAT analysis is also shown.

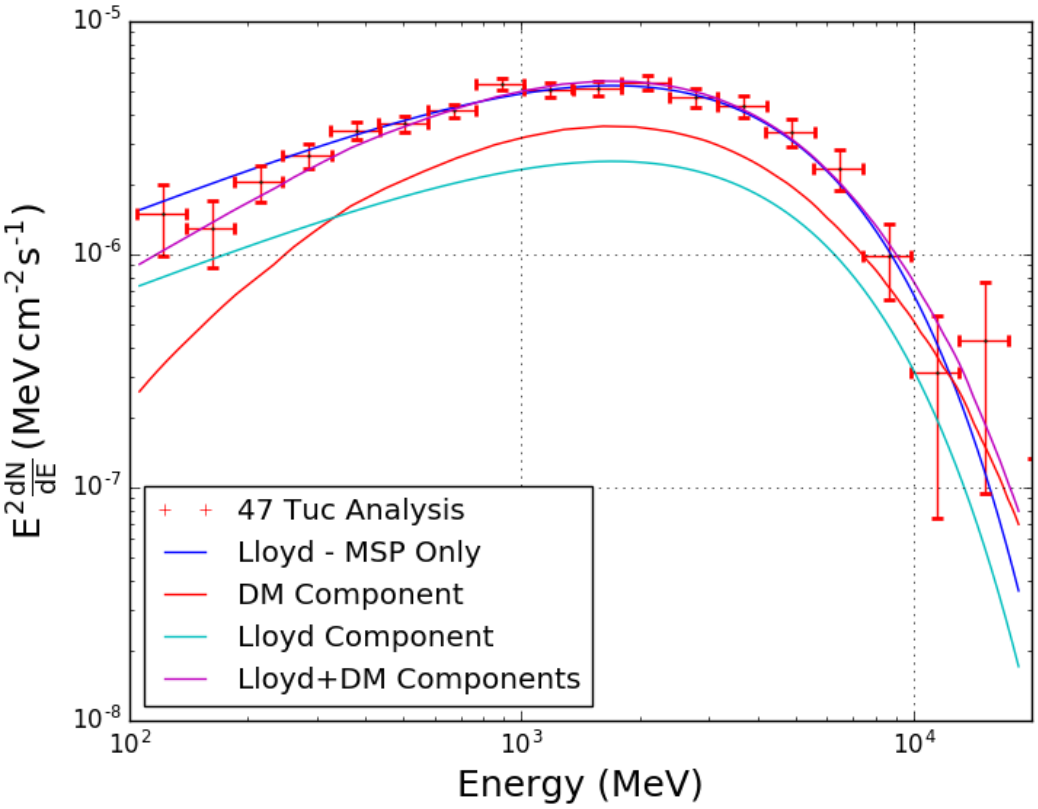

Fig. 7.11 Spectral energy distribution for 47 Tuc in the energy range 100 MeV to 20 GeV with spectral models for stacked MSP observations from my own model (Lloyd) and the Lloyd model as a component combined with a dark matter (DM) component as in [63] with equal flux at 330 MeV. The models are then normalised to the 47 Tuc spectrum at 1 GeV. Both the Lloyd MSP model and the Lloyd + DM model are a good fit to the 47 Tuc spectrum.

7.4.1 Confirming Best MSP model for Individual GCs

I now move from considering 47 Tuc to determining how well, stacked MSP spectral models describe the emission of all gamma-ray bright GCs. I use the AIC statistic to select the best fitting MSP model for the 34 detected GCs. The minimum AIC statistic indicates the optimum MSP model for each GC spectral model as listed in Table 7.4. The Lloyd MSP model is preferred for 21 GCs, followed by Xing and Wang (8 GCs) and McCann (5 GCs).This further confirms that the Lloyd MSP model is preferred for individual GCs over that of Xing and Wang, or McCann.

7.4.2 MSP Model to Globular Cluster Goodness-of-Fit Using χ^2

I then compare the Lloyd model goodness-of-fit against the GC SEDs, in the energy range 100 MeV$-$10 GeV, using the χ^2 method, employing all non UL flux points and the SED flux 1σ error. I normalise the Lloyd model, so that its flux at 1.33 GeV is the same as the GC SED flux point with a bin centre energy of 1.33 GeV. The number of GCs where the Lloyd model is consistent with the SEDs ($\chi^2 <$ critical value), is 11 and 20, at significance level[3] $\alpha = 0.05$ and $\alpha = 0.001$ respectively (Table 7.5). This is comparable with the goodness-of-fit of the individual *Fermi*-LAT spectral models to each GC SED in Chapter 5 (16 and 25 GCs, at significance level $\alpha = 0.05$ and $\alpha = 0.001$ respectively).

Next, I compare the Lloyd model to the GC spectral models and their maximal error, in the energy range 100 MeV$-$10 GeV at intervals of 10 MeV, again using the χ^2 method. I normalise the Lloyd model, so that the flux of Lloyd at 1.33 GeV is the same as the GC model flux at 1.33 GeV. The number of GCs where the Lloyd model is consistent with the GC spectral model ($\chi^2 <$ critical value), is 18 and 21, at significance level $\alpha = 0.05$ and $\alpha = 0.001$ respectively (Table 7.6).

On the other hand, my MSP model is not a good fit for 12,21 GC SEDs, and 13,16 GC *Fermi* analysis spectral models, for significance levels $\alpha = 0.05$ and $\alpha = 0.001$, respectively. The failure to fit between a third and two-thirds of GCs with the MSP model challenges the assumption that the totality of GC emission arises solely from MSPs.

7.4.3 The Effect of GC Characteristics on GC Spectra

I now attempt to determine if there is a characteristic difference, relevant to MSP formation, between the GCs which are well fitted by the Lloyd model and those that are not. The

[3]Here, the significance level α is the probability of a Type-I error, falsely rejecting the null hypothesis, which is that both the Lloyd model and the SED are the same, when in fact they actually are the same.

Globular Cluster	Best Model	AIC	AIC Δ Best to Intermediate	AIC Δ Best to Worst	Intermediate Model	AIC	Worst Model	AIC
NGC 5904	Lloyd	-33752	-900	-2715	XW	-32852	McCann	-31037
NGC 6254	Lloyd	-33520	-640	-2868	XW	-32880	McCann	-30652
NGC 2808	Lloyd	-31685	-627	-2303	XW	-31058	McCann	-29382
NGC 1904	Lloyd	-31150	-15	-444	XW	-31135	McCann	-30706
NGC 6541	Lloyd	-30375	-533	-1904	XW	-29842	McCann	-28471
NGC 6402	Lloyd	-30278	-446	-1665	XW	-29832	McCann	-28613
NGC 6838	Lloyd	-30191	-290	-1329	XW	-29901	McCann	-28862
NGC 6752	Lloyd	-30077	-453	-1615	XW	-29624	McCann	-28462
NGC 6652	Lloyd	-29999	-538	-1849	XW	-29461	McCann	-28150
NGC 6316	Lloyd	-29900	-594	-2476	XW	-29306	McCann	-27424
NGC 5139	Lloyd	-29674	-878	-2681	XW	-28796	McCann	-26993
NGC 6656	Lloyd	-29396	-427	-1574	XW	-28969	McCann	-27822
NGC 6266	Lloyd	-28808	-613	-2608	XW	-28195	McCann	-26200
NGC 6528	Lloyd	-28745	-265	-1184	XW	-28480	McCann	-27561
NGC 6388	Lloyd	-28618	-773	-2557	XW	-27845	McCann	-26061
NGC 6626	Lloyd	-28480	-651	-2408	XW	-27829	McCann	-26072
NGC 6441	Lloyd	-27821	-373	-1655	XW	-27448	McCann	-26166
GLIMPSE01	Lloyd	-27587	-95	-2649	XW	-27492	McCann	-24938
NGC 6440	Lloyd	-26617	-288	-1257	XW	-26329	McCann	-25360
Terzan 5	Lloyd	-26106	-502	-2513	XW	-25604	McCann	-23593
GLIMPSE02	Lloyd	-24576	-171	-884	XW	-24405	McCann	-23692
NGC 6341	XW	-32821	-311	-867	Lloyd	-32510	McCann	-31954
NGC 6093	XW	-32370	-1018	-2165	Lloyd	-31352	McCann	-30205
NGC 6397	XW	-31539	-234	-888	Lloyd	-31305	McCann	-30651
Terzan 2	XW	-31118	-249	-2248	Lloyd	-30869	McCann	-28870
NGC 7078	XW	-31096	-28	-757	Lloyd	-31068	McCann	-30339
NGC 6304	XW	-31043	-74	-826	Lloyd	-30969	McCann	-30217
NGC 6139	XW	-30991	-312	-866	Lloyd	-30679	McCann	-30125
47 TUC	XW	-29245	-1022	-2838	Lloyd	-28223	McCann	-26407
NGC 6717	McCann	-32259	-1779	-2209	XW	-30480	Lloyd	-30050
NGC 6218	McCann	-29920	-19	-25	XW	-29901	Lloyd	-29895
2MS-GC01	McCann	-29777	-1603	-2074	XW	-28174	Lloyd	-27703
NGC 6624	McCann	-29674	-300	-1155	XW	-29374	Lloyd	-28519
Terzan 1	McCann	-27080	-62	-77	XW	-27018	Lloyd	-27003

Table 7.4 Best fit stacked MSP models for each GC spectral model, ranked by minimum AIC statistic which indicates the preferred model, in the energy range 100 MeV−10 GeV. The model from this work, the Lloyd model, is preferred for 21 GCs, followed by Xing and Wang (XW), (8 GCs) and McCann (5 GCs). The AIC delta difference beween the best and intermediate, and the best and worst models is also shown.

Globular Cluster	χ^2 Test Statistic	D.o.f	Critical Value $\alpha = 0.05$	Model Accepted at $\alpha = 0.05$	Critical Value $\alpha = 0.001$	Model Accepted at $\alpha = 0.001$
GC 2808	0.8	3	7.815	Yes	16.266	Yes
NGC 5904	2.6	1	3.841	Yes	10.828	Yes
NGC 6752	3.1	2	5.991	Yes	13.816	Yes
NGC 6388	3.8	4	9.488	Yes	18.467	Yes
NGC 6254	3.8	2	5.991	Yes	13.816	Yes
NGC 6656	5.5	3	7.815	Yes	16.266	Yes
NGC 6717	5.9	3	7.815	Yes	16.266	Yes
NGC 6541	6.4	4	9.488	Yes	18.467	Yes
NGC 6624	6.9	4	9.488	Yes	18.467	Yes
NGC 6441	7.1	4	9.488	Yes	18.467	Yes
47 Tuc	8.8	5	11.070	Yes	20.515	Yes
NGC 6341	6.6	2	5.991	No	13.816	Yes
NGC 6304	7.7	1	3.841	No	10.828	Yes
NGC 6652	8.3	3	7.815	No	16.266	Yes
NGC 7078	9.4	1	3.841	No	10.828	Yes
NGC 6266	9.5	4	9.488	No	18.467	Yes
NGC 5139	10.7	4	9.488	No	18.467	Yes
NGC 6528	11.3	2	5.991	No	13.816	Yes
NGC 6402	11.5	3	7.815	No	16.266	Yes
NGC 6316	13.0	4	9.488	No	18.467	Yes
Terzan 2	17.3	2	5.991	No	13.816	No
NGC 6397	19.5	2	5.991	No	13.816	No
NGC 6093	23.8	4	9.488	No	18.467	No
NGC 6626	28.8	4	9.488	No	18.467	No
2MS-GC01	28.8	1	3.841	No	10.828	No
NGC 1904	28.9	2	5.991	No	13.816	No
NGC 6139	29.2	3	7.815	No	16.266	No
Terzan 5	42.4	4	9.488	No	18.467	No
NGC 6838	47.1	2	5.991	No	13.816	No
GLIMPSE01	72.3	4	9.488	No	18.467	No
NGC 6440	91.0	4	9.488	No	18.467	No
GLIMPSE02	183.2	4	9.488	No	18.467	No

Table 7.5 Testing the goodness-of-fit of Lloyd to GC spectral energy distributions (SEDs, 100 MeV$-$10 GeV) using the χ^2 test statistic. The number of GCs where Lloyd is consistent with the SEDs ($\chi^2 <$ critical value), is 11 and 20, at significance level $\alpha = 0.05$ and $\alpha = 0.001$ respectively. NGC 6218 and Terzan 1 are excluded as they have $<$1 degree of freedom (d.o.f).

Globular Cluster	χ^2 Test Statistic	D.o.f	Critical Value $\alpha = 0.05$	Model Accepted at $\alpha = 0.05$	Critical Value $\alpha = 0.001$	Model Accepted at $\alpha = 0.001$
NGC 6254	0.1	5	11.070	Yes	20.515	Yes
NGC 5904	0.3	5	11.070	Yes	20.515	Yes
NGC 2808	0.7	5	11.070	Yes	20.515	Yes
NGC 6093	1.2	5	11.070	Yes	20.515	Yes
NGC 6402	1.3	5	11.070	Yes	20.515	Yes
Terzan 2	1.8	5	11.070	Yes	20.515	Yes
NGC 6624	2.3	5	11.070	Yes	20.515	Yes
NGC 6541	2.6	5	11.070	Yes	20.515	Yes
NGC 6316	5.8	5	11.070	Yes	20.515	Yes
NGC 6652	6.2	5	11.070	Yes	20.515	Yes
NGC 6752	6.2	5	11.070	Yes	20.515	Yes
GLIMPSE01	7.3	5	11.070	Yes	20.515	Yes
NGC 6266	7.4	5	11.070	Yes	20.515	Yes
NGC 6397	9.3	6	12.592	Yes	22.458	Yes
NGC 6341	9.5	6	12.592	Yes	22.458	Yes
NGC 6218	9.7	5	11.070	Yes	20.515	Yes
47 Tuc	10.9	5	11.070	Yes	20.515	Yes
NGC 6717	12.4	6	12.592	Yes	22.458	Yes
2MS-GC01	12.7	6	12.592	No	22.458	Yes
NGC 5139	13.0	5	11.070	No	20.515	Yes
NGC 6388	13.5	5	11.070	No	20.515	Yes
NGC 6441	28.0	5	11.070	No	20.515	No
Terzan 5	34.2	5	11.070	No	20.515	No
NGC 7078	36.5	6	12.592	No	22.458	No
NGC 1904	43.0	6	12.592	No	22.458	No
NGC 6304	48.8	6	12.592	No	22.458	No
NGC 6139	87.4	6	12.592	No	22.458	No
NGC 6440	135.9	5	11.070	No	20.515	No
NGC 6838	177.0	5	11.070	No	20.515	No
GLIMPSE02	288.0	5	11.070	No	20.515	No
NGC 6626	359.8	5	11.070	No	20.515	No
NGC 6656	579.1	5	11.070	No	20.515	No
NGC 6528	927.6	5	11.070	No	20.515	No
Terzan 1	4.44E+13	5	11.070	No	20.515	No

Table 7.6 Testing the goodness-of-fit of the Lloyd model to GC spectral models (100 MeV−10 GeV) using the χ^2 test statistic. The number of GCs where the Lloyd model is consistent with the GC spectral model ($\chi^2 <$ critical value), is 18 and 21, at significance level $\alpha = 0.05$ and $\alpha = 0.001$ respectively. Terzan 1's very high χ^2 arises from the very narrow energy range of its log parabola spectral model and consequent sharp cut-offs which generates fluxes far below those of Lloyd.

population of GCs which have SEDs and spectral models well fitted by the Lloyd model (in Tables 7.5 and 7.6), can be compared to those that do not, with the Kolmogorov-Smirnov (KS) test, by individually considering GC characteristics which are expected to influence the formation of MSPs in those GCs such as encounter rate, Γ, metallicity [Fe/H], GC mass, MERP and binary encounter rate (BER), Λ, (which I determine using Eqn. 3.1 from [264] and list in Table A.4). I compare the distribution of these characteristics using the KS test, with the null hypothesis, H_0, being that the two GC populations have the same distribution of characteristics. All characteristics for all GCs are compared with the exception of 2MS-GC01 and GLIMPSE01 which are compared only on the basis of mass, GLIMPSE02 compared on metallicity alone and NGC 6838, which is compared on all characteristics except Γ and MERP, due to some characteristics being undefined in the literature. I obtain the KS test statistic[4] (D). In all cases, both for Lloyd model fit to the SED and GC spectral model, and not, D is less than the critical value at the 95% confidence level (CL), and thus H_0 cannot be rejected at the 95% CL (Table 7.7).

Therefore, the GC characteristics relevant to MSP formation are distributed similarly whether GCs are well fitted by the Lloyd model or not. It might be expected that the MSP populations derived from similarly distributed GC characteristics are similar and, as an ensemble, should have similar MSP like spectra, equally well fitted by Lloyd. I take this as further indirect support for another source of gamma-ray emission in GCs, apart from MSPs, which prevents GCs being well fitted by the Lloyd MSP model in some cases.

In relating the GC SEDs to any proposed source model of emission or characteristic of the GC, it is necessary to look for diagnostic features in the SED which can be compared quantitatively with the proposed source model or range of GC characteristics relevant to that model. Half of the detected GCs have a relatively flat spectra in the range 562 MeV$-$3.16 GeV, spanning the middle 3 energy bins of the SED, and lack distinctive spectral features for quantitative comparison. As such it is useful to use other spectral features for comparison outside this range, in the lower and higher energy bins where the flux differences between bins are more readily apparent, and the lever arm is greater.

In this regard, the GC SEDs can be grouped by whether fluxes are detected in the lowest and medium energy bins, hereafter, LEB and MEB respectively. The LEB spans 100$-$177 MeV centered on 133 MeV and the MEB spans 5.6$-$10 GeV centered on 7.5 GeV. NGC 6624 and NGC 6626 are GCs where the emission is presumed be largely due to a single dominant MSP. Both NGC 6624 and NGC 6626 have an UL in the LEB which is markedly lower than the energy flux of the next bin and have fluxes in all bins up to and including the

[4] D = max(|F(x)$_1$-F(x)$_2$|) where F(x)$_{1,2}$ is proportion of x values less than current x for populations 1 and 2 being compared

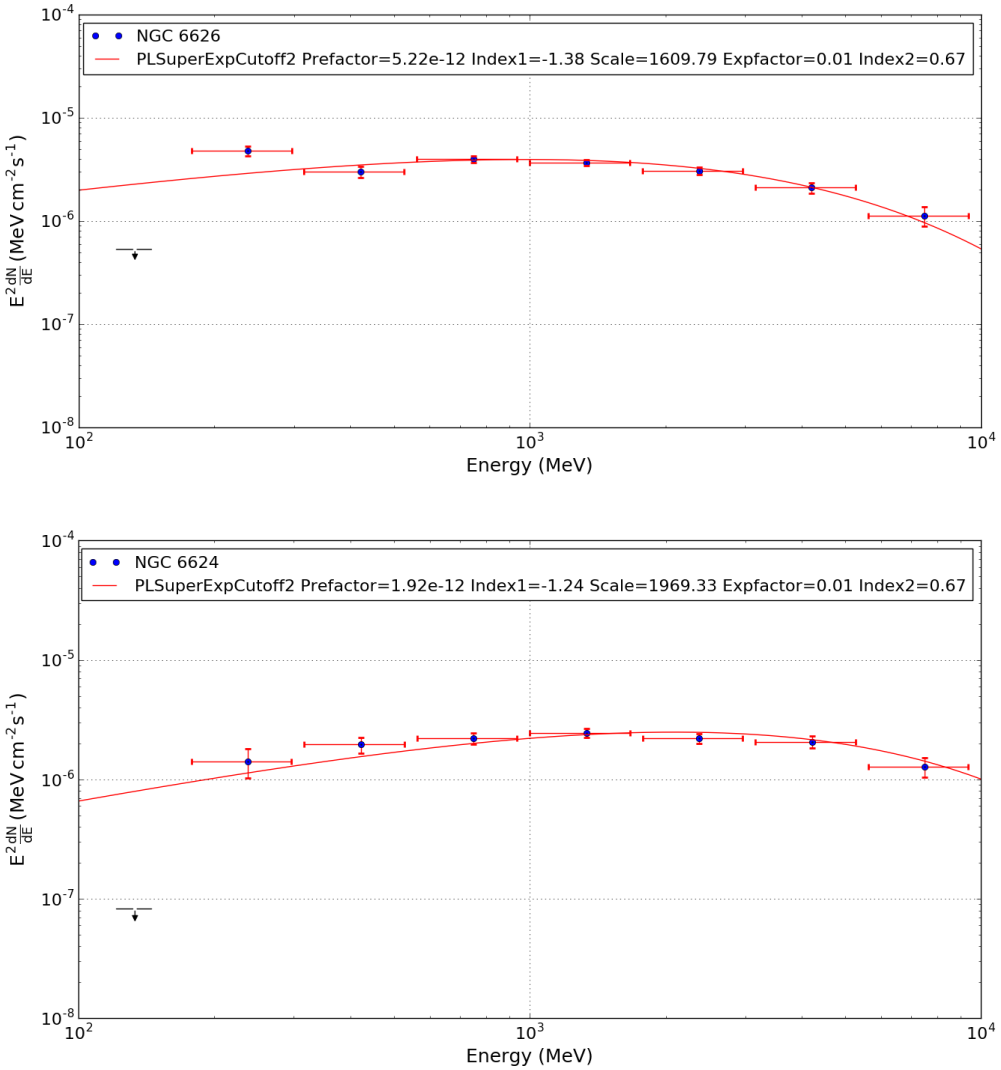

Fig. 7.12 The spectral energy distributions of NGC 6626 and NGC 6624 showing PL super exponential spectra with a cut-off and flux in all bins except at 133 MeV which has an UL markedly lower than the best fit model.

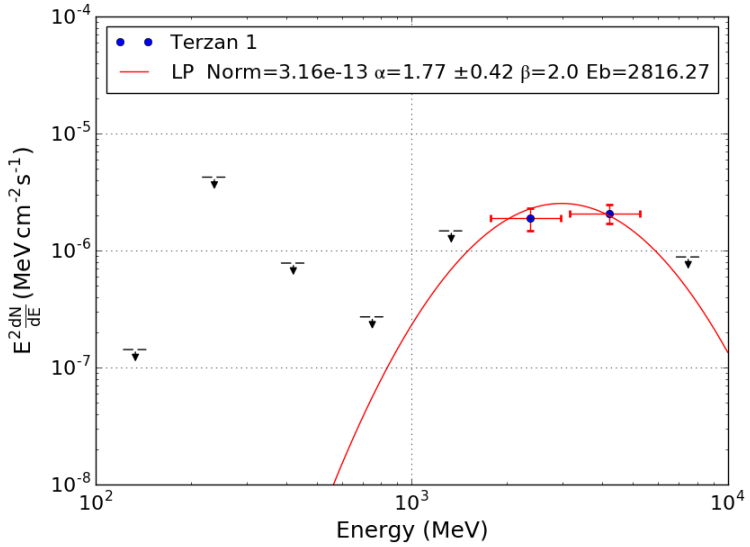

Fig. 7.13 The spectral energy distributions of Terzan 1 has few flux points and only ULs below 1 GeV.

MEB (Fig. 7.12). The SEDs of 17 other GCs share these same features of a much lower UL in the LEB and a flux point in the MEB. A further 10 GCs have ULs in the LEB and MEB. Only 3 GC have a flux in the LEB instead of an UL, 47 Tuc, NGC 6341 and NGC 1904. The SEDs of NGC 6341 and NGC 1904 (Fig. 7.14) show the clearest examples of a soft PL spectrum in the detected GCs, which is in tension with the PL super exponential spectra, characteristic of MSPs, as seen in NGC 6626 and NGC 6624. A further 2 GCs, Terzan 1 (Fig. 7.13) and NGC 6218 have SEDs with noticeably fewer flux points and only ULs below 1 GeV.

I now consider the individual binned fluxes of the best quality (in terms of having few ULs) GC SEDs in more detail to determine if there are spectral characteristics correlated with either systematic effects or GC characteristics of relevance to MSP formation.

The sharp UL observed in the lowest energy bin (centered on 133 MeV and spanning 100−177 MeV), in the majority of GC SEDs (with the exception of 47 Tuc, NGC 6341 and NGC 1904) is also worthy of comment. These GC LE ULs are in tension with the Lloyd model, where 26 of the 98 MSPs have mean flux of $(2.56 \pm 0.39) \times 10^{-6}$ MeV cm^{-2} s^{-1}, rather than an UL in the 133 MeV bin. The mean flux in the 1.3 GeV bin (which is usually co-incident with the peak flux) is $(5.68 \pm 1.02) \times 10^{-6}$ MeV cm^{-2} s^{-1} for MSPs with a flux in the 133 MeV bin as compared to $(1.99 \pm 0.20) \times 10^{-6}$ MeV cm^{-2} s^{-1} for MSPs with an UL in the 133 MeV bin. This suggests that the 133 MeV UL in MSP SEDs is an instrument sensitivity effect arising from including MSPs with lower peak flux. As such it might be

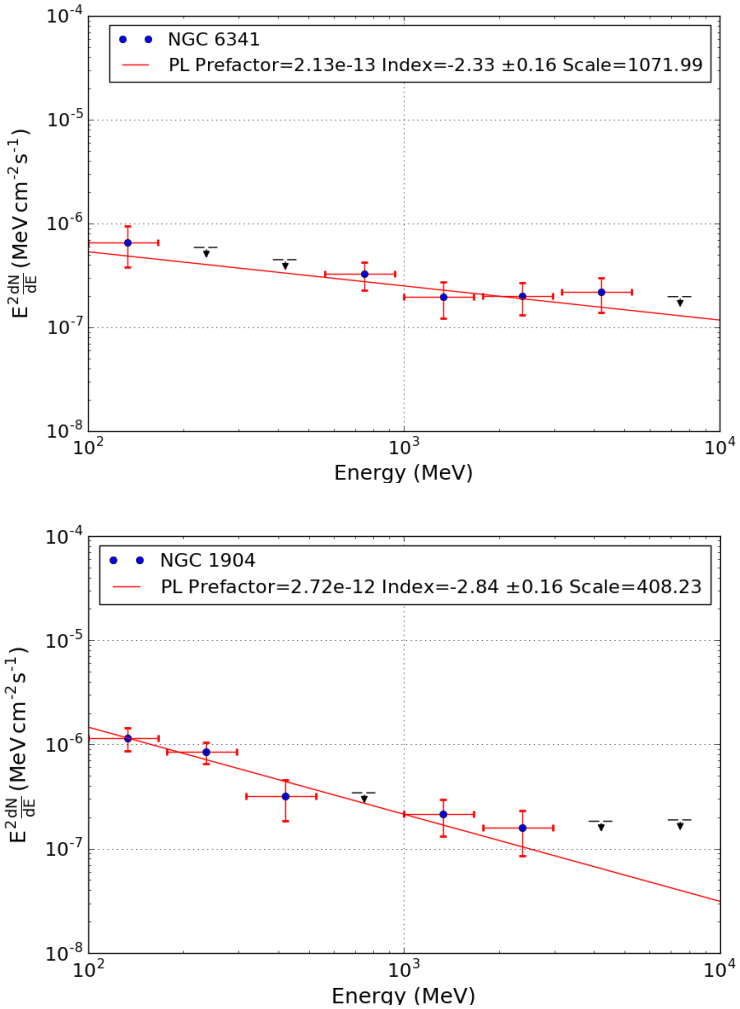

Fig. 7.14 The spectral energy distributions of NGC 6341 and NGC 1904 are best fit with soft PL spectra and have flux at 133 MeV rather than an UL.

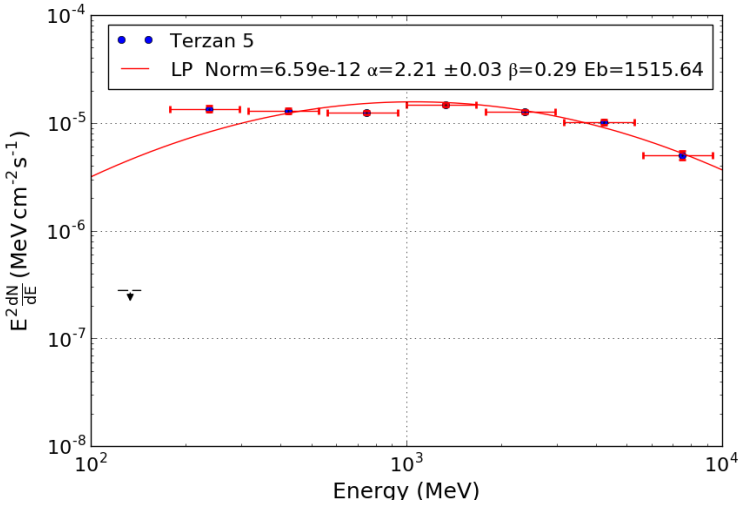

Fig. 7.15 The spectral energy distribution of Terzan 5 with a high flux of $\sim 10^{-5}$ MeV cm^{-2} s^{-1} in bins from 177 MeV to 4 GeV but a markedly lower UL below 177 MeV.

expected that if detectable GC emission arises from an ensemble of MSPs, then the combined sub UL emission at 133 MeV should be seen as a flux points in GCs with high observed fluxes such as Terzan 5 (which has $\sim 10^{-5}$ MeV cm^{-2} s^{-1} in bins from 177 MeV to 4 GeV, with an UL below 177 MeV), when in fact, an UL is nearly always observed. On the other hand, the magnitude of the difference in flux between the UL in the 133 MeV bin and the flux value in the following 237 MeV bin seems to be influenced by the systematic effect of the Galactic latitude as can be seen in Fig. 7.16. The flux difference tends to increase at lower Galactic latitudes suggesting the presence of a systematic effect of the gamma-ray background in the Galactic plane. It also noteworthy that the three GCs with a flux in the 133 MeV bin are at higher Galactic latitudes (i.e. NGC 1904, NGC 6341 and 47 Tuc have latitudes of -29.35, 34.86 and -44.89 degrees respectively). NGC 7078 at a Galactic latitude of 44.89 degrees is a transitional case with an UL in the 133 MeV bin just above the flux of the 237 MeV bin.

Similarly, towards higher energies, in the top 2 bins, some GCs have ULs in the bin centered on 7498 MeV (spanning 5623 MeV−10 GeV) and fluxes in the proceeding bin centered on 4216 MeV (spanning 3162 MeV−5623 MeV), whereas in the Lloyd model, 71 of the 98 MSPs have fluxes in both bins.

In order to further investigate if the ULs in the GC bins at 133 MeV and 7498 MeV are related to systematic effects or related to the MSP population in the GC, I define two colour bands, low energy, LE and medium energy, ME, with the LE band defined as the flux in 133 MeV bin / flux in 237 MeV bin and the ME band defined as flux in 4216 MeV bin /

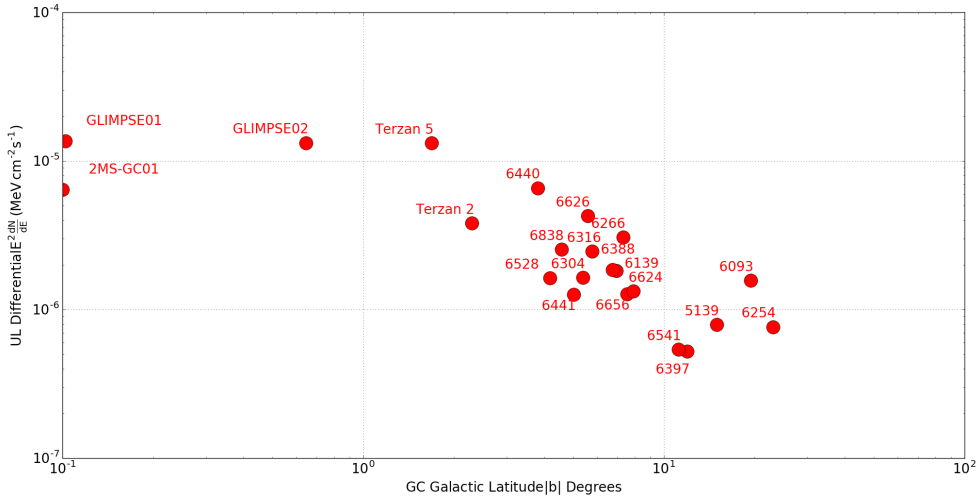

Fig. 7.16 The flux difference between the UL in the 133 MeV bin and the flux in the following 237 MeV bin for 22 GCs against the absolute value of GC Galactic latitude. The flux difference tends to increase at lower Galactic latitudes suggesting the presence of a systematic effect of the gamma-ray background.

flux in 7498 MeV bin. Where an UL is present at 133 MeV or 7498 MeV, then the LE and ME colours represent upper and low limits respectively. The LE and ME colours for the Lloyd model are 0.39±0.02 and 1.97±0.07 respectively. I plot the individual GC colours against GC heliocentric distance, Galactic latitude, and gamma-ray luminosity between 100 MeV−10 GeV, to determine if there are systematic background or sensitivity effects, and metallicity, binary encounter rate and MERP to determine if factors relevant to MSP formation are correlated with the colour distribution in Fig. 7.17. It can be seen that the GC LE colour UL falls below the Lloyd model in nearly all cases implying that the 133 MeV GC bin has a much lower UL cut than predicted. In addition, the distribution of the LE UL colour ratio exhibits no correlation with any characteristics plotted. It is noteworthy that there are only two LE flux colours in the figure (47 Tuc and NGC 1904) and that a LE UL persists across the full range of gamma-ray luminosity. Similarly, the GC ME UL and flux colours mostly fall on or below the Lloyd model implying that the 7498 MeV flux is higher in proportion to the 4216 MeV flux. The distribution of ME colour is again insensitive to all characteristics with the exception of gamma-ray luminosity where higher GC luminosity ($L_\gamma > 2\times 10^{34}$ erg s^{-1}) seems to favour a flux point in the 7498 MeV bin as opposed to a UL

in the SED, leading to flux colours rather than flux colour lower[5] limits, on the colour plot, at higher luminosities.

The colour difference between GC spectra and the Lloyd model could be explained by an additional source of gamma-ray emission, apart from MSPs, which increases the flux between $177-316$ MeV and $5.6-10$ GeV or, less likely, by GC MSPs having spectral differences which, in aggregate, favour emission in these bands, although there is no evidence for such a MSP population in GCs.

It is useful to ask whether there is a MSP sub-population of the 98 MSPs in Lloyd which have spectral characteristics functionally related to a pulsar observable such as $\dot{E}$. If such a population were to exist then a blend of MSPs spectral characteristics could be derived from the known $\dot{E}$s of the MSP population in well studied GCs such as 47 Tuc and Terzan 5. This could allow the determination of additional GC spectral components superimposed on the GC MSP gamma-ray emission. I now consider if there are any such sub-populations within the Galactic field MSP population, which could be used to infer the emission properties of the ensemble MSP population in GCs.

The Lloyd model is a summation of an ensemble of MSPs and their fluxes, and that within Lloyd, 21 MSPs have a UL at 7498 MeV (average ME colour $\geq 1.92 \pm 0.32$) and 45 MSPs have an UL at 133 MeV (average LE colour $\leq 0.63 \pm 0.08$). It may be possible, therefore, that the GC MSP population is more characteristic of these MSPs in the Lloyd model displaying ULs in the LE and ME bins, rather than fluxes, as low and upper limits predominate in the GC colour ratio plots of Fig. 7.17.

The MSP gamma-ray luminosity and the spectral index (*Index1*) parameter of the *PLSuperExpCutoff2* spectral model for MSPs are positively correlated with MSP $\dot{E}$ as shown in the 2PC [11]. It therefore seems reasonable to suppose that $\dot{E}$ could affect spectral features and hence colour ratios. Thus, I consider whether there is a MSP $\dot{E}$ to colour relationship which favours ULs in 133 MeV and 7498 MeV bins, as this could be used to determine the GC MSP population characteristics. However, a plot of MSP spectral colours against $\dot{E}$, indicates that there is no apparent correlation between these quantities, with LE and ME colours scattered evenly above and below the Lloyd model colours (Fig. 7.18).

The discussion of sub-populations of MSPs, also prompts the question of whether the gamma-ray luminosity function (i.e. the expected distribution of MSP luminosities as a count binned by luminosity) is similar in the Galactic field population used to construct the Lloyd model and in GCs, because if the MSP luminosity and by implication the $\dot{E}$ is greater, than the positive spectral index vs $\dot{E}$ relation would skew the spectral shape of the SED, increasing

[5] A colour ratio lower limit arises from dividing an SED flux point by an UL flux in the next SED bin and as such the maximum of the colour ratio is unconstrained.

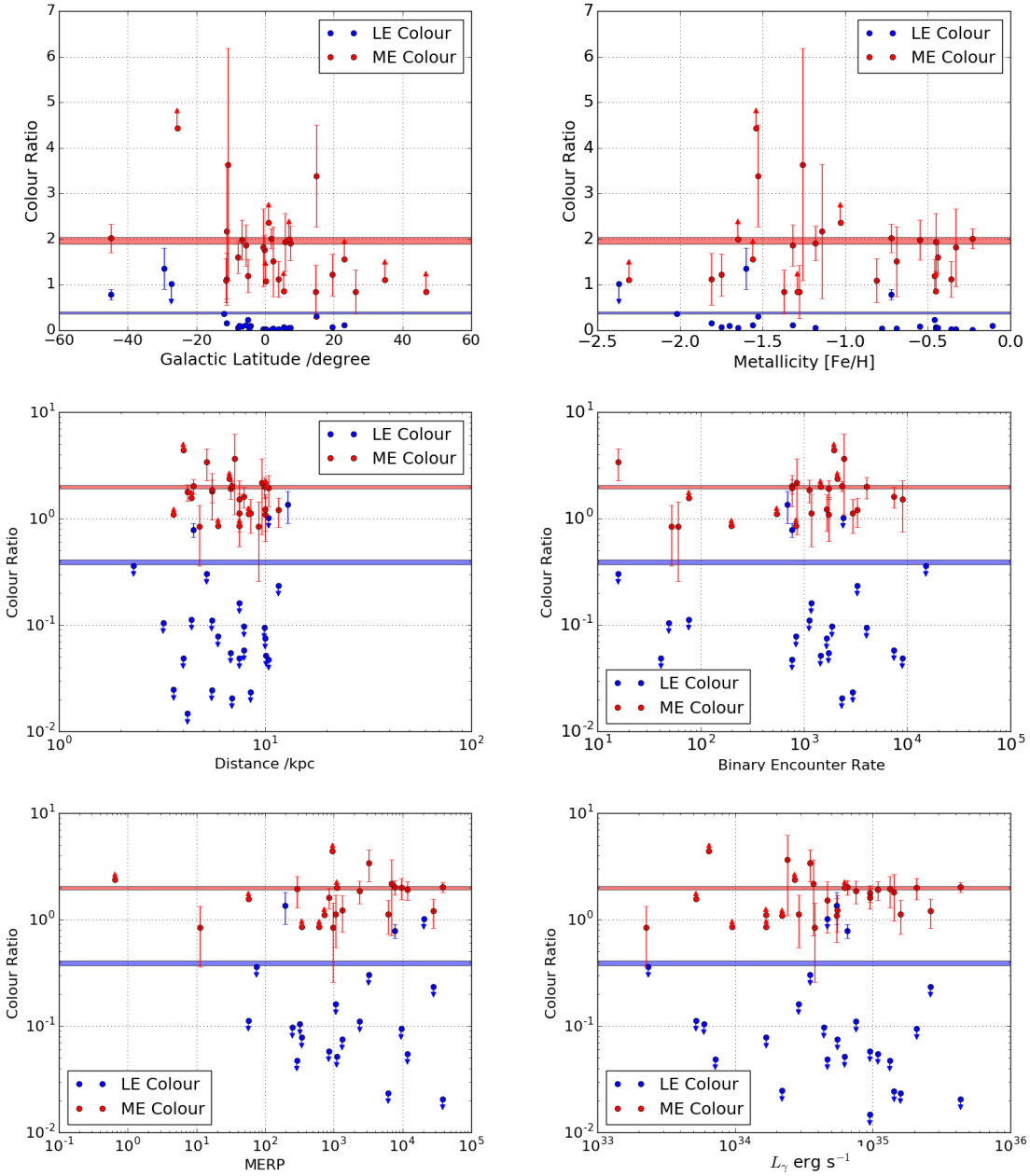

Fig. 7.17 The low energy (LE, 133/237 MeV, blue points) and Medium Energy (ME, 4216/7498 MeV, red points) colour bands of detected GCs plotted against characteristics to exclude systematic effects (Distance, Galactic latitude, b) and effects relevant to MSP formation (Metallicity, Binary Encounter Rate (BER), and MERP). Red and blue bands are ME and LE colour ranges from the Lloyd model stacked MSP spectrum of this work. The colour offset of individual GCs from the colour bands of the Lloyd model appears uncorrelated with distance / b systematics or by MSP formation related to metallicity or BER or MERP. There is a preference for higher luminosity GCs, $>2\times10^{34}$ erg s^{-1}, to have fluxes in the 7498 MeV bin rather than ULs, leading to defined ME colours at higher luminosity rather than lower limits (bottom right panel). The LE colour distribution is insensitive to all characteristics.

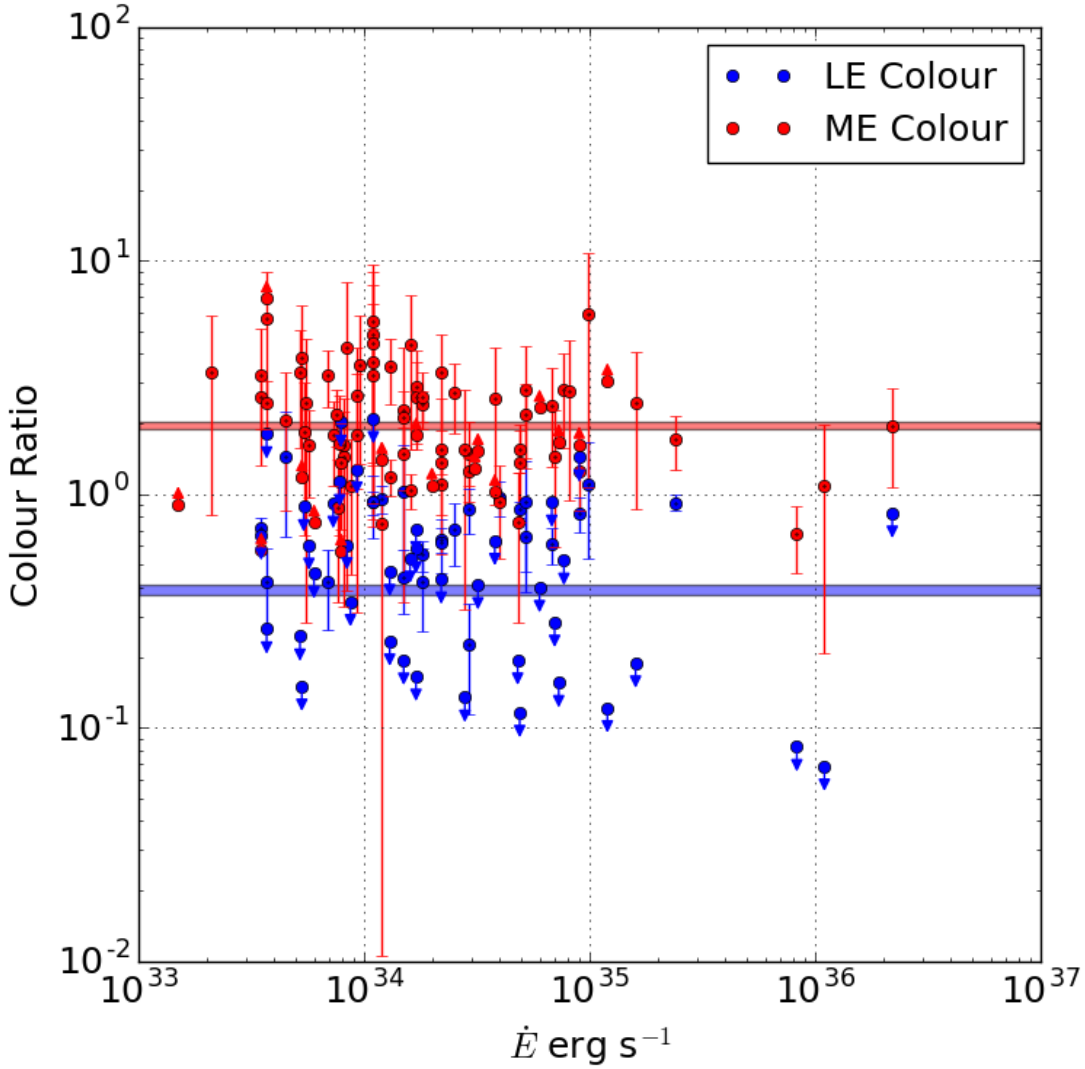

Fig. 7.18 The LE and ME colours for the MSPs in the Lloyd model plotted against their $\dot{E}$ values. There is no apparent correlation, with LE and ME colours distributed evenly above and below the Lloyd average colour values (red and blue bands).

the flux in higher energy bins with increasing positive index while decreasing the flux in lower energy bins.

The MSP luminosity function has been examined in a population study [138], constrained by the spatial distribution of *Fermi*-LAT observations of MSPs from the 2PC. The authors of [138] obtain a central value luminosity of 4.7×10^{32} erg s^{-1} for field MSPs and predict that the MSP luminosity function should be similar for both the GC and Galactic field MSP population for L_γ in the range $10^{32} - 10^{34}$ erg s^{-1}. They also constrain the incidence of high luminosity MSPs in GCs by considering MSP J1823-3021A in NGC 6624 with an L_γ of 7.0×10^{34} erg s^{-1}. They note that this luminosity is 10% of the gamma-ray emission of 16 other GCs which they predict to have a population of 2000 MSPs, by their modelled luminosity function, and from this they predict that the *remaining* GCs will have ~ 0.04 MSPs with $L_\gamma > 10^{34}$ erg s^{-1}. A similar study [111] using three different MSP emission models (two pole caustic slot gap, outer gap and pair starved polar cap emission) predicts an average L_γ of 8.0×10^{32} erg s^{-1} for the MSPs in 47 Tuc and yields an estimated number of MSPs of 43 ± 6, in broad agreement with the original estimate of *Fermi*-LAT collaboration, 33 ± 15 [10]. Assuming a gamma-ray efficiency of $\sim 10\%$, this places the average GC MSP $\dot{E}$ at $\sim 10^{34}$ erg s^{-1}, within the centre of the range of most $\dot{E}$ values in the Lloyd model (Fig. 7.18). This allows me to conclude that for the most part GC MSPs are not unusually bright and so my comparison of the MSPs in the Lloyd model with those of the GC MSP population remains valid.

I now turn to energies above 10 GeV (HE). In the Lloyd model, HE emission is rarer, with only 20, 12 and 3 MSPs having significant emission in the bins centered on 13.3 GeV, 23.7 GeV and 42.2 GeV respectively. In addition, the energy flux at 23.7 GeV and 42.2 is a factor of 10 and 43 times less than at 7498 MeV. This implies that detectable HE emission from MSPs in GCs should be rarer, consistent with the detection of just 2 GCs (47 Tuc and Terzan 5) at HE. On the other hand, the HE spectrum of Terzan 5 is flat with significant flux up to 100 GeV which appears at odds with an MSP interpretation (Fig. 7.19). As previously discussed in Chapter 3, there are weak indications for TeV emission in a stacked analysis of MSPs using HAWC [137]. The proposed mechanism is that MSP leptons are accelerated across the voltage drop of the pulsar wind nebulae termination shock, to generate gamma-ray emission through the inverse Compton process along with radio emission via the Synchrotron process. Although the detection indication is weak, the modelling of [137] also suggests a flat spectrum up to TeV energies can be generated by MSPs. However, at the time of writing, Terzan 5 remains undetected by HAWC at TeV energies [14], so direct evidence for this mechanism in GCs is lacking.

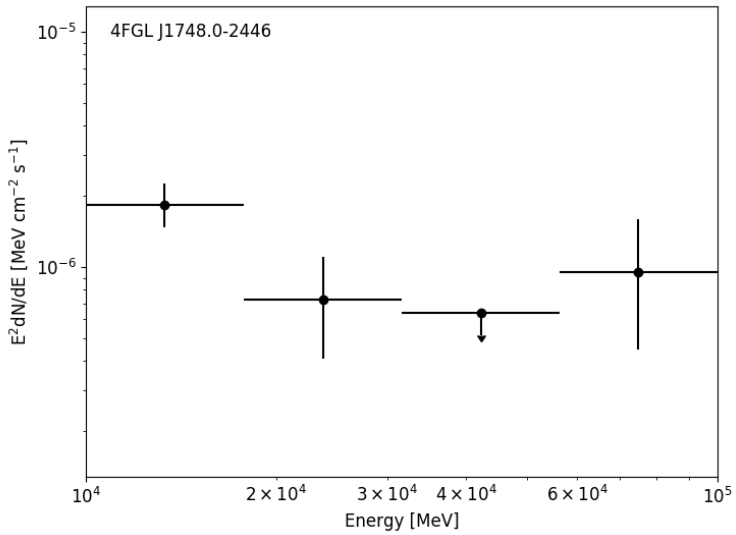

Fig. 7.19 The spectral energy distribution of Terzan 5 between 10 and 100 GeV from this work. The spectrum is flat with significant flux up to 100 GeV.

The gamma-ray spectrum (1 GeV$-$1 TeV) is predicted for 3 GCs, NGC 6624, NGC 6626 and NGC 7078 [55], by modelling the inverse Compton scattering of infra-red, optical and microwave-background photons by MSP leptons which are advected in MSP and stellar winds and emitted by MSPs offset from the GC centre. The model predicts increasing gamma-ray flux up to $\sim$ 100 GeV where a spectral turn-over occurs. However, the predicted fluxes at 10 GeV are at odds with those observed in this work, with the predicted flux of NGC 6624 and 6626 being only 16 and 50% of the actually observed flux, respectively. In contrast, at 10 GeV, NGC 7078 has an UL a factor of 3 higher than the predicted flux and as such the model of [55] cannot be excluded for this GC based on my observations.

The model of [55] is tested against 165 h of observations of NGC 7078 using MAGIC in [17]. However NGC 7078 remains undetected using MAGIC (contrary to expectation) and this is used to set constraints on relativistic lepton injection rate by MSPs into the GC. The authors of [17] conclude that the injection rate must be lower than from classical pulsars or that leptons are removed more efficiently by MSP winds in the GC than expected.

7.4.4 Simulating the Detectability of 4FGL GCs with CTA

CTA is expected to improve on *Fermi* by providing increasing sensitivity above 60 GeV, ($\sim$ an order of magnitude improvement for CTA at 1 TeV as compared to the sensitivity of *Fermi*-LAT at 10 GeV), and superior angular resolution above $\sim$ 200 GeV (0.05°, 68%

Model and GC Characteristic	KS Test Statistic D	KS Critical Value at the 95% CL
Lloyd to GC SED ($\alpha = 0.05$)		
Encounter Rate, Γ	0.22	0.53
Metallicity	0.22	0.52
Mass	0.26	0.51
MERP	0.19	0.53
BER, Λ	0.20	0.52
Lloyd to GC SED ($\alpha = 0.001$)		
Encounter Rate, Γ	0.15	0.57
Metallicity	0.25	0.53
Mass	0.37	0.51
MERP	0.28	0.57
BER, Λ	0.28	0.55
Lloyd to GC model ($\alpha = 0.05$)		
Encounter Rate, Γ	0.25	0.50
Metallicity	0.35	0.48
Mass	0.34	0.48
MERP	0.38	0.50
BER, Λ	0.21	0.49
Lloyd to GC model ($\alpha = 0.001$)		
Encounter Rate, Γ	0.31	0.52
Metallicity	0.36	0.49
Mass	0.32	0.49
MERP	0.27	0.52
BER, Λ	0.21	0.50

Table 7.7 Comparing the GC characteristics relevant to MSP formation between the population of GCs which are well fitted by the Lloyd model, and those that are not, using the KS test. All models and characteristics have a KS test statistic D less than the KS critical value and so the null hypothesis that the characteristic distributions are the same, between GCs fitted and not fitted by the Lloyd model, cannot be rejected at the 95% CL.

containment for CTA-S at 1 TeV, rising to 0.03°at 20 TeV, vs 0.1°of *Fermi*-LAT PASS 8 at 20 GeV). These improvements will be important to distinguish between different spectral models of MSP emission whilst simultaneously allowing the morphology of any emission to be probed to distinguish between emission arising from sources in the GC core and shock-front emission.

Therefore, I consider to what extent the 30 GC sources (listed in Table A.3) identified as associated with a GC in the 4FGL are detectable using CTA-N and CTA-S using its publicly-released prod3b-v1 instrument response functions (IRFs),[6] and the CTOOLS analysis suite [160]. I first determine the maximum altitude that the GCs can attain when observed from the CTA-N and CTA-S using my own Python code employing the ASTROPLAN package (version 0.4)[7]. ASTROPLAN is built on the well known package ASTROPY and allows the definition of observatories and targets for observing. For GCs which attain an altitude $>$ 60° I use the CTA IRFs applicable to a zenith angle of 20° whereas for lower altitudes I use the zenith 40° IRFs, both averaged over the azimuth angle. I use the spectral models obtained from the $0.1-100$ GeV analysis above of 30 4FGL GCs and simulate events using CTOOLS, version 1.6.1, (with my simulation chain previously described in Chapter 2) for times of 5h and 50h for a single GC source in the energy range $0.03-50$ TeV over a selection radius of 3° from a 5° simulated region. For each GC, I perform 880 simulations[8] using random number seeds of $1-880$. The analysis output is a results file with a detection TS value calculated for each GC. Although the bulk of emission will usually be in the $0.1-10$ GeV band, I use the spectral model produced by the $0.1-100$ GeV analysis as this allows the spectral model to be fitted and constrained by events above 10 GeV. In Table 7.8, I list all GCs which achieve a significant detection (TS$\geq$25) along with the percentage number of runs with a simulated significant detection. The simulation predicts that 2MS-GC01 will be detectable with just 5 h of observations, and NGC 6717, 6218, 6139 and Terzan 1 should be reliably detected in 50 h of observations as $\geq 98\%$ of simulations result in a significant detection. I also plot histograms of the simulated distribution of TS values obtained for all GCs where $\geq 98\%$ of simulation runs have a detection significance of TS$\geq$25 in Fig. 7.22. In 50 h of CTA-N observations, Terzan 1 and NGC 6218 are expected to be detected with a peak TS of $\sim$ 310 and 300, respectively. In 50 h of CTA-S observations, NGC 6139, NGC 6717 and 2MS-GC01 can expect to be detected with a greater peak significance of $\sim$ 1100, 1300 and 5800, respectively. The high significance predicted detection of NGC 6139, 6717 and 2MS-GC01 (Fig. 7.22) is as expected from their hard PL spectral fits with predicted

[6] Available from http://cta.irap.omp.eu/ctools/users/user_manual/irf_cta.html?highlight=prod3b

[7] Available from https://astroplan.readthedocs.io/en/latest/what-is-astroplan

[8] I use 880 runs, instead of my preferred 1000, as this is the highest common number of simulations successfully performed, for all GCs, as due to run time errors some simulations were restarted.

fluxes $> 2 \times 10^{-7}$ MeV cm^{-2} s^{-1} at 100 GeV (Fig. 7.20), while their higher significance detection with CTA-S in comparison to CTA-N is expected from their southerly declinations (-38.8, -22.7 and -19.8° for NGC 6139, 6717 and 2MS-GC01 respectively). In contrast the other GCs have predicted fluxes at least an order of magnitude less than this at 100 GeV and so are are undetected in more simulations. The predicted detections of Terzan 1 and NGC 6218 are more difficult to account for, as they have a log parabola model and a sharp cut-off, with much lower fluxes of $\sim 2 \times 10^{-8}$ MeV cm^{-2} s^{-1} at 20 GeV. Further simulations will be required to probe this discrepancy. Based on the other predicted detections, I recommend the use of CTA-S in future observations of GCs.

It is useful to compare these results with the GCs predicted to be detected by CTA using the previously mentioned emission model of [205], which employs MSPs as the source of relativistic particles which up-scatter the soft photons of the modelled GCs to gamma-ray energies and produce X-rays via the synchrotron process. In [205] it is predicted that 5 GCs, (47 Tuc, NGC 6388, Terzan 5, Djorg 2 and Terzan 10, from a sample of 15 GCs previously observed by H.E.S.S.) are the most promising for future detection using CTA. However of these 5 favoured GCs only 47 Tuc, NGC 6388 and Terzan 5 are gamma-ray sources detected with *Fermi*-LAT and the CTOOLS simulation predicts that these GCs will not be detectable on the basis of their $0.1-100$ GeV spectral models alone.

The SEDs from X-ray to gamma-ray energies of 47 Tuc, Terzan 5 and NGC 6388 are also predicted in [205]. Their model uses MSPs as the relativistic particle source whilst solving transport equations to predict emission from inverse Compton scattering and synchrotron process for varying B field, lepton diffusion, lepton injection spectrum and maximum lepton energy. However the SED model used is conservative because it omits the pulsed curvature radiation produced by MSPs. It can be seen that the energy fluxes obtained from my *Fermi*-LAT analysis between $1-100$ GeV strongly constrain the gamma-ray emission models for 47 Tuc in [205] but are compatible with the models of Terzan 5 and NGC 6388 (Fig. 7.21), the unknown MSP pulsed emission notwithstanding. In Terzan 5, I may be detecting the start of the inverse Compton component while the NGC 6388 model predicts fluxes below my own and H.E.S.S. ULs and hence cannot be further constrained with current observations. Future observations with CTA will be very useful to select between these models and refine spectral features below the current ULs of both *Fermi*-LAT and H.E.S.S.

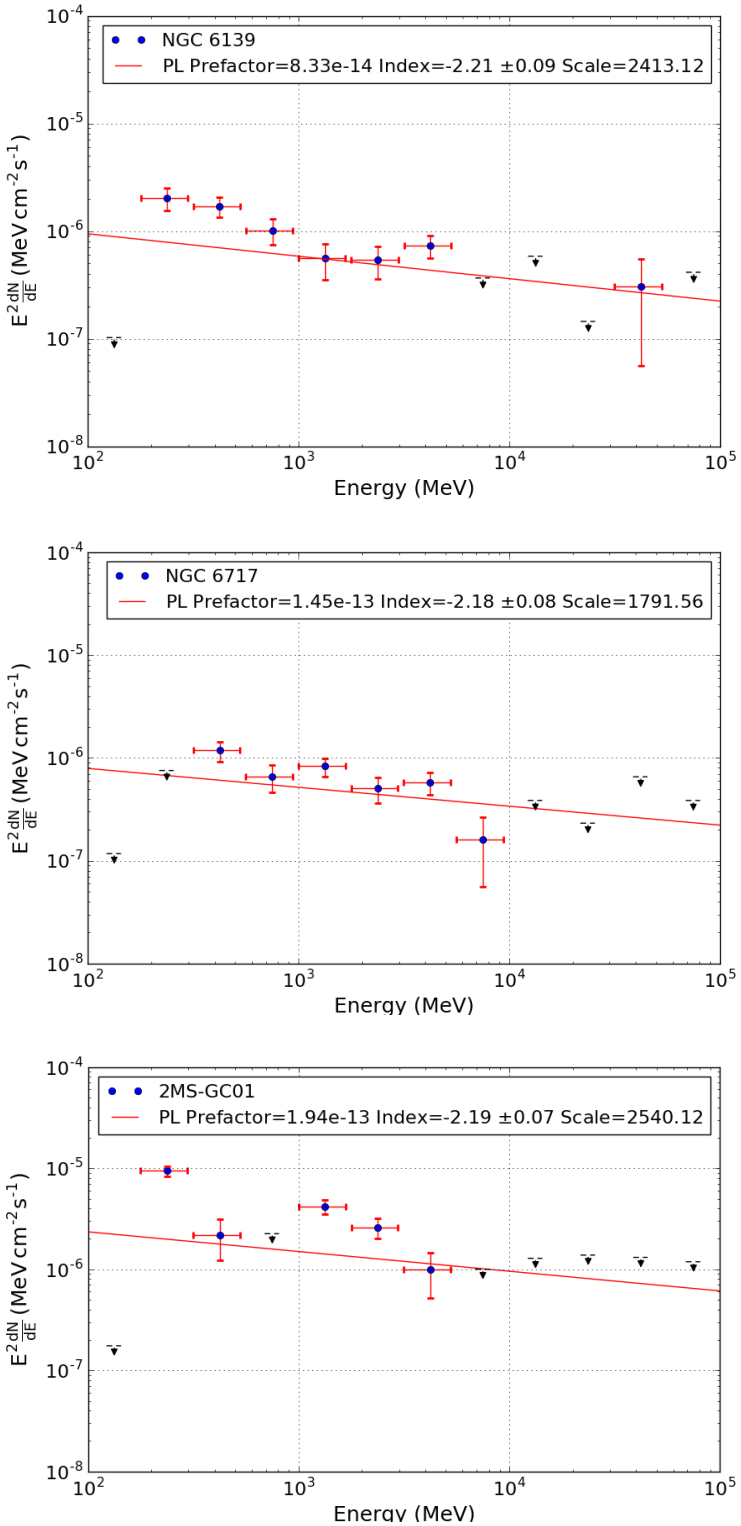

Fig. 7.20 The spectral energy distributions of NGC 6139, NGC 6717 and 2MS-GC01, for 100 MeV−100 GeV, showing a hard predicted spectra to 100 GeV which accounts for their predicted detection in most simulation runs using CTOOLS.

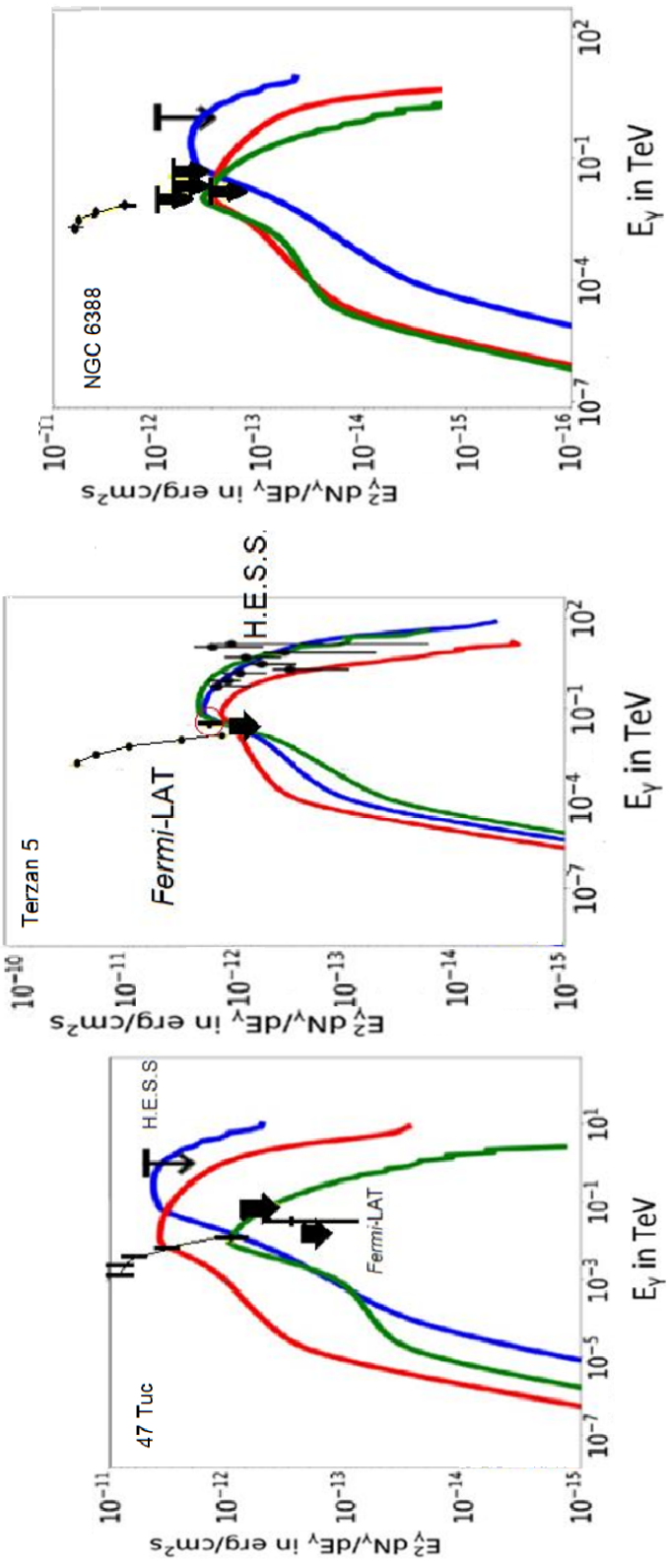

Fig. 7.21 The gamma-ray emission predicted for 3 GCs for 3 models of B field, lepton diffusion rate and lepton spectral index and initial energy, indicated by red, blue, green lines (adapted from [205]) with my *Fermi*-LAT observations between 1 – 100 GeV (ULs are broad black arrows and flux points by thin black lines). The *Fermi*-LAT ULs of my analysis in 47 Tuc(left panel) would seem to disfavour the predicted peak emission of all 3 models. The Terzan 5 models (centre panel) are all compatible with my *Fermi*-LAT observations and I may be detecting the start of the inverse Compton component (circled in red). The NGC 6388 SED is below my own and H.E.S.S. ULs and hence cannot be constrained. Future observations with CTA will be required to select between these models and refine spectral features below H.E.S.S ULs.

7.5 Conclusion

By using an X-ray gamma-ray relation in the 2PC, which I call the "Abdo Ratio", I estimate the gamma-ray flux contribution of 20 MSPs with published X-ray flux values in 47 Tuc (out of a resolved MSP total of 25 in that GC) and show that in a median case they likely account for only half the gamma-ray emission, but could account for the total emission at the extremes of uncertainty of both flux and the Abdo Ratio. The large log uncertainties on the Abdo ratio mean that standard error propagation rules cannot be used and so an overall propagated uncertainty cannot be calculated to limit this estimate further.

I consider whether the gamma-ray spectra of selected GCs can be accounted for by MSPs, through comparison with my stacked MSP model and by examining GC spectra. On an individual basis, the spectra of many GCs resemble those of MSPs with cut-offs a few GeV and this is likely the predominant emission mechanism in GCs, but there is certainly tension between the GC spectra and stacked models of MSP emission at low and medium energies which suggest other sources of emission. GCs are known to contain CVs and LMXBs and in some cases may have co-incident background AGN but there are unlikely to be predominant sources of emission, as gamma ray emitting CVs and background AGNs of the blazar class are rare, whereas LMXBs are rarely gamma-ray emitters. In addition the lack of GC reported variability on multi-month timescales would seem to exclude these sources as important emitters.

I show, using the minimum value of the AIC statistic, that my stacked model of 98 MSPs ("Lloyd") is the preferred model in the case of 47 Tuc, over that of the *Fermi*-LAT analysis spectral fit, the MSP models of Xing and Wang, and of McCann.

I show using a χ^2 statistic, that my stacked model of 98 MSPs is again a preferred model of individual GC spectral emission over that of the alternative models of McCann and Xing and Wang and a valid fit to $\sim$ third to a half of the GC SEDs depending on significance level chosen, (i.e. a valid fit in 11 and 20 GCs at α=0.05 and 0.001 respectively), and to the GC spectral models, (18 and 21 GCs at α=0.05 and 0.001 respectively). The fit of the Lloyd model to the GCs is slightly poorer than that of the *Fermi* analysis GC spectral models obtained in Chapter 5 (16 and 25 GCs at α=0.05 and 0.001 respectively). The fact that only a third to two-thirds of GCs are well fitted by the Lloyd MSP model, (depending on the significance level chosen) again shows the importance of MSP emission but hints at other sources of emission. This view is further supported by my analysis of those GCs well fitted by Lloyd, and those are not, which shows that the distribution of characteristics relevant to MSP formation in these populations, cannot be proved to be different.

A detailed GC spectral analysis considering the fluxes and colours of the first (LEB) and last two energy bins (MEB) is then used to draw comparisons with the Lloyd MSP emission

Globular Cluster	CTA Array	Zenith Angle (Degrees)	Observation Time (h)	Percentage of 880 runs with TS$\geq$ 25
NGC 6093	North	40	50	1
TERZAN 5	South	20	50	1
NGC 1904	North	40	50	2
TERZAN 2	North	40	5	3
GLIMPSE01	South	20	50	4
NGC 7078	South	40	50	5
TERZAN 2	South	20	50	6
NGC 6304	South	20	50	6
NGC 6397	South	20	50	13
NGC 6341	South	40	50	25
NGC 6717	North	40	5	75
NGC 6139	North	40	5	75
NGC 6304	North	40	50	76
NGC 6397	North	40	50	80
NGC 6717	South	20	5	82
NGC 6139	South	20	5	82
NGC 6218	North	40	5	85
TERZAN 1	North	40	5	86
2MS-GC01	North	40	5	98
NGC 6717	North	40	50	99
NGC 6717	South	20	50	99
2MS-GC01	South	20	5	99
NGC 6218	North	40	50	100
NGC 6139	South	20	50	100
2MS-GC01	North	40	50	100
NGC 6139	North	40	50	100
TERZAN 1	North	40	50	100
2MS-GC01	South	20	50	100

Table 7.8 GCs ordered by the percentage of 880 seeded CTOOLS runs which result in a TS $\geq$ 25 detection by either CTA-N or CTA-S for observation times of 5h and 50h. The spectral model assumed for each GC is that of my *Fermi*-LAT analysis from 0.1$-$100 GeV and the CTOOLS prod3b-v1 azimuth averaged IRFs are used throughout.

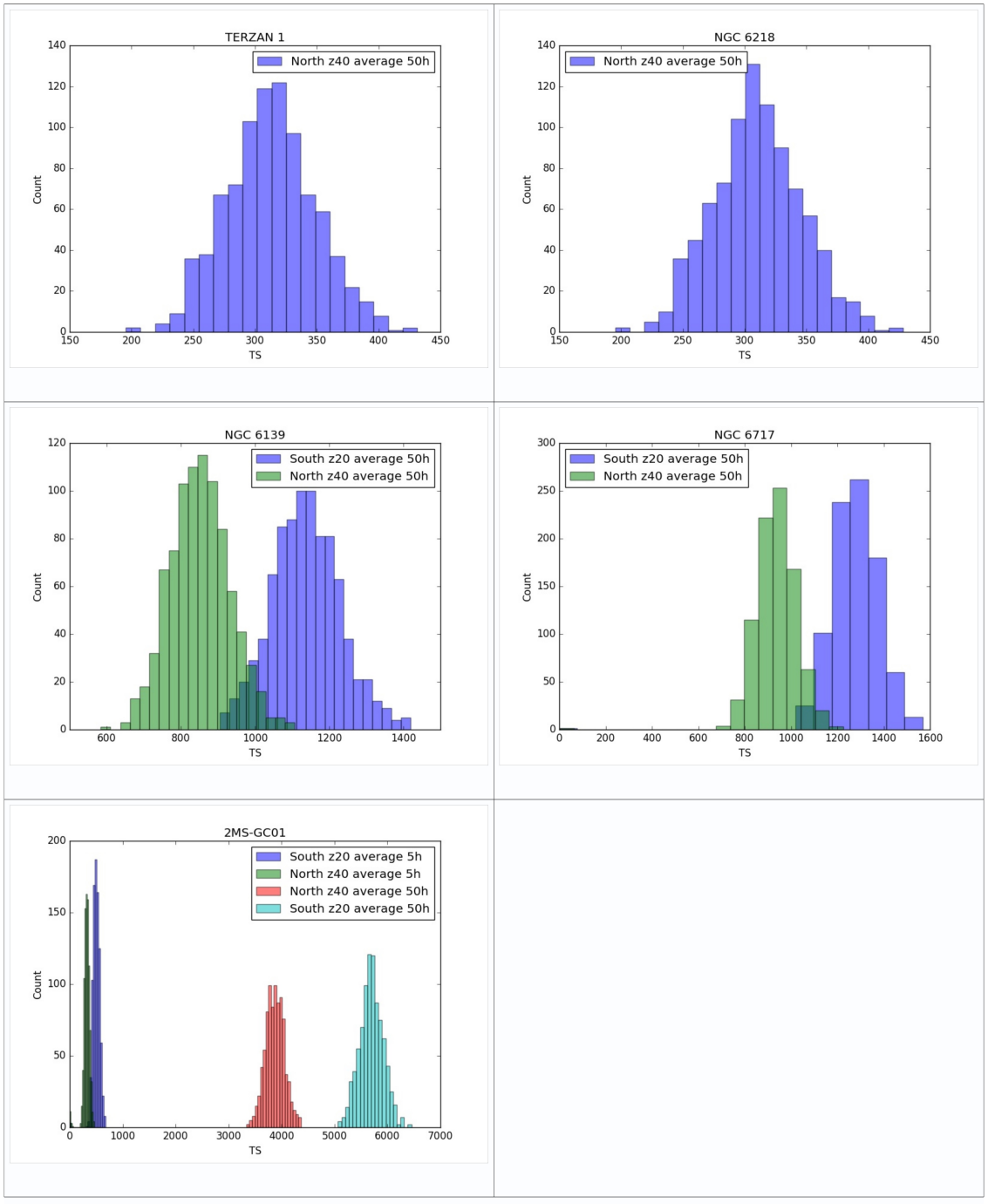

Fig. 7.22 TS distributions for GCs simulated with CTOOLS for CTA-N and S and observations of 5 and 50 h. For 50 h observations $\geq 98\%$ of simulation runs have TS ≥ 25. Plots are arranged in order of increasing maximum TS peak value. 2MS-GC01 is detectable by both CTA-N and CTA-S after 5 h of observations.

model. The presence of ULs in the majority of GC LEBs is in tension with Lloyd which suggests LEB fluxes should be seen, but this is likely due to systematic effects of Galactic background emission, as ULs increase with Galactic latitude, until, LEB fluxes are seen in the highest latitude GCs. An analysis of GC LEB and MEB colours shows that these are unaffected by factors relevant to MSP formation, and that the MEB is harder than that of the Lloyd MSP model, hinting at spectral components other than MSPs in these energy bins. It is possible that this harder component than that seen in Galactic field MSPs arises from the relativistic electron population generated by unresolved GC MSPs as discussed above. The LEB and MEB MSP colours appear unrelated to MSP $\dot{E}$, and so, cannot be used to infer the characteristics of an underlying MSP population in GCs.

Finally, I examine the higher energy GC and MSP results above 10 GeV. In my spectral model, HE emission occurs in far fewer MSPs and produces much reduced flux as compared to emission between $1-10$ GeV. This is consistent with the non-detection of most GCs at these energies. The spectra of the sole HE detection, Terzan 5 is relatively flat to 100 GeV and the tentative detection of TeV halos around MSPs using HAWC, may account for Terzan 5's HE spectrum. However, Terzan 5 is, as yet, undetected by HAWC.

A simulation of GC detectability by the proposed gamma-ray observatory CTA, using the spectral models produced by a $0.1-100$ GeV analysis, suggests at least 5 GCs should be detectable in 50 h of observations. I also show that my *Fermi*-LAT analysis of 47 Tuc can be used to constrain models where MSPs produce gamma-ray emission through inverse Compton scattering. Future observations with CTA will be able to constrain both MSP emission models and the morphology of GC high energy emission.

The presence of IMBHs in some GCs [159] could indicate a dark matter annihilation component to the emission in the more massive objects and could account for the emission seen in some objects such as 47 Tuc although the evidence for IMBHs in GCs more generally is not strong. I have also shown that both an MSP only emission model, and a model with a dark matter component and reduced MSP emission, can equally well account for the 47 Tuc spectrum, although a preferred model cannot be determined.

In conclusion, these results do not rule out MSPs being the major contributor of gamma-ray emission in GCs but the differences between the GC spectra and the Lloyd model coupled with the weak correlation of gamma-ray emission with characteristics relevant to MSP formation do suggest other important components of gamma-ray emission in GCs apart from that of MSPs. This view is re-enforced by the third to two-thirds of GCs (depending on the significance level chosen), which are not well fitted by my MSP model. The harder medium energy spectrum observed in some GCs combined with the GC diffuse X-ray / gamma-ray detection connection suggests that the relativistic electron population of unresolved MSPs is

a major additional component. More speculatively, the soft components of the GC spectrum could be due to a dark matter component, and as an exemplar of the constraints that can be placed on dark matter properties through the analysis of pulsars, I turn next in Chapter 8 to the case of a hypothetical dark matter particle, the axion, which may be produced in pulsar cores.

Chapter 8

Constraining the Axion Mass through Gamma-ray Observations of Pulsars

8.1 Introduction

The mass of the axion m_a can be constrained, in the main, either by astrophysical scenarios involving direct axion emission, acting as an energy loss channel, with the axions possibly converting to a photon flux, or by direct detection experiments which seek to measure the conversion of the axion flux impinging on the Earth to photons in a strong magnetic field. I do not consider here the further important case of spectral modulation arising from the conversion of photons from a bright source which, when travelling large distances in the weak Galactic magnetic field, can convert to axions, as these effects tend to result in small spectral features of low detection significance and hence are less compelling than other observations, yielding less restrictive limits than axion solar telescopes such as CAST [187].

The use of direct astrophysical axion emission scenarios to place limits on the axion mass has a long history. Shortly after the supernova event SN-1987A, the duration of its neutrino burst ($5-10$ s) was used to determine the cooling due to neutrino emission, and subsequently to calculate $m_a < 5 \times 10^{-3}$ eV [157] by assuming that the energy loss due to axion emission via nucleon-nucleon Bremsstrahlung was sub-dominant to that of the neutrino energy loss. This estimate was later refined to $m_a < 10^{-2}$ eV when fluctuating nucleon spin and collisional effects were included [149]. The energy loss due to axion emission is also expected to shorten the lifetime of He core burning stars on the horizontal branch (HB) as opposed to hydrogen shell burning stars on the red giant branch (RGB). This lowers the number ratio of HB stars to RGB stars from expectation, and direct observations of these counts in 39 globular clusters yields axion-photon couplings of $< 0.66 \times 10^{-10}$ GeV^{-1} [40],

corresponding to a limit of $m_a < 1$ eV. In [240] the authors have used cooling simulations, combined with surface temperature measurements of 4 thermal X-ray emitting pulsars (PSRs) including Cas A, to determine $m_a <$ (0.06-0.12 eV).

Axions can also be probed by direct detection experiments such as the Axion Dark Matter Experiment [236] where Galactic halo axions convert to microwave photons in a magnetic field, excluding m_a in the range (1.9-3.53) $\times$ 10^{-6} eV [37, 100, 118, 140, 99]. In [80] the CERN Axion Solar Telescope (CAST) has set constraints on the conversion of axions produced from the Sun into X-ray photons inside a 9 T magnet to produce axion-photon couplings of $< 0.66 \times 10^{-10}$ GeV^{-1} , the same as the determination from globular clusters above.

In the gamma-ray regime, the authors of a 2016 paper "Constraints on axions and axion like particles from *Fermi* large area telescope observations of neutron stars" [58], hereafter "BGM16", have used 5 years of PASS 7 *Fermi*-LAT gamma-ray observations of radiative axion decay in 4 nearby pulsars to constrain $m_a < 0.079$ eV. The work of BGM16, though innovative, can be improved upon by considering a larger sample of pulsars and using FERMIPY with its proven energy and photon flux upper limit calculation routines instead of a bespoke MINOS UL calculation.

The latest data release of the *Fermi*-LAT is now PASS 8, which incorporates improvements to further reduce gamma-ray background uncertainty, improve instrument effective area and point spread function (PSF) and to permit low-energy analysis down to 60 MeV. In this chapter, I refine the work of BGM16 to take advantage of the improved low-energy analysis in PASS 8, coupled with improved photon statistics (with 9 years of event data) and a larger sample of 17 pulsars which are undetected in gamma-rays. I then obtain improved gamma-ray ULs and a more robust determination of UL m_a than was possible previously.

The content of this chapter is as follows: in Section 8.2, I describe the phenomenology of the axion and its production in neutron stars. In Section 8.3, I list the criteria used to select pulsars for analysis. In Section 8.4, I describe the analysis method for the determination of gamma-ray upper limits from the pulsar sample. In Section 8.5, I present UL energy and photon flux determinations for the pulsar sample and from these is derived the axion mass upper limit m_a for two independent methods. In Section 8.6, I discuss the validity of the UL m_a determination with respect to pulsar core temperature. I then consider the determination of UL m_a in magnetars: In Section 8.7, I explain why magnetars are a good target for this work, In Sections 8.8 and 8.10 respectively, I discuss the core temperatures expected in magnetars and why their quiescent soft-gamma ray emission might be expected to be suppressed as a background signal. I present the UL m_a values obtained from magnetars in Section 8.9 and propose further observations with the *Fermi*-Gamma Ray Burst Monitor (GBM) in Section

8.12. Finally, in Section 8.13, I summarise my findings and make suggestions for future work.

It should be noted that my pulsar analysis and the resulting UL m_a determination and pulsar core temperature discussion have also been published in my paper [182] whereas my discussion of magnetar temperature, soft-gamma ray background and proposed *Fermi*-GBM observations have been published in my paper with Kuver Sinha and Huai-ke Guo [183], who used the legacy magnetar fluxes listed in this chapter to obtain the axion-photon coupling constraints which I discuss here. The listed UL m_a in this chapter, which I obtained from magnetars using an alternative model, has not yet been published.

8.2 Phenomenology

In the very early Universe, axions are created through the Peccei-Quinn (PQ) transition, when the temperature falls below the PQ symmetry breaking scale, $f_a \sim 10^8 - 10^9$ GeV. The PQ scalar field, Φ, settles to a potential minimum and the postulated $U(1)_{PQ}$ symmetry is broken, causing Φ to achieve a non-zero vacuum expectation value, which generates axions and an axion-string network which further decay to non-relativistic axions. Later, in a seperate transition, at a lower temperature, Λ_{QCD}, axions acquire a small mass, m_a, which is related to f_a through a scaling relation (Eqn. 8.1).

$$m_a \approx 6\mu\,\mathrm{eV}\left(\frac{f_a}{10^{12}\,\mathrm{GeV}}\right)^{-1} \tag{8.1}$$

In the more general case of axion-like-particles (ALP) this restriction is relaxed and an unconstrained mass is possible. The timing of the PQ transition is uncertain and could occur either before inflation or afterwards, the former leading to a wide range of possible $m_a < 1$ meV whilst the latter yields values of m_a in a narrow meV range as seen in Fig 1.7, with one theoretical value of m_a being $1-15$ meV [69].

Axions may also be produced in pulsar cores through the process of nucleon-nucleon Bremsstrahlung as depicted in the Feynman diagram of Fig. 8.1. The Bremsstrahlung process assumes a one pion exchange (OPE) approximation [146] and the nucleons involved are considered to be neutrons. Incoming nucleons N_1, N_2 and outgoing nucleons N_3, N_4 undergo one pion exchange to produce axions of energy ω via the Bremsstrahlung process. The axions then undergo radiative decay to gamma-ray photons.

The spin structure function $S_\sigma(\omega)$ (Eqn. 8.2) is a phase space integral corresponding to the Bremsstrahlung process depicted in Fig. 8.1. The phase space integral, shown in Eqn. 8.2, accounts for nucleon spin and the balanced energy ($E_{1,2,3,4}$) and momenta ($\mathbf{p_{1,2,3,4}}$) transfer between nucleons $N_{1,2,3,4}$ with conservation of momenta and energy provided by

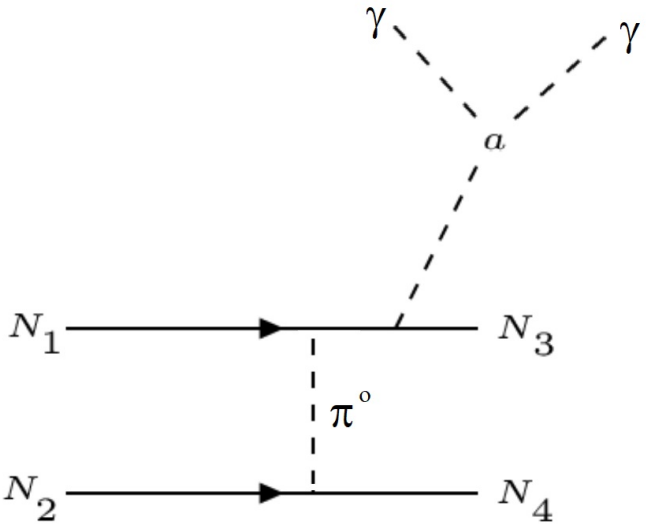

Fig. 8.1 Feynman diagram depicting the nucleon-nucleon Bremsstrahlung process which produces axions. Incoming nucleons $N_{1,2}$ undergo a one-pion exchange producing an axion a and outgoing nucleons $N_{3,4}$ with different energy and momenta from those of $N_{1,2}$. The axion undergoes radiative (conservative) decay to two gamma-ray photons.

Dirac δ functions. The momenta $\boldsymbol{p_i}$ have integration limits in the range $0 < \boldsymbol{p_i} < 2p_{Fn}$ where p_{Fn} is the neutron Fermi momentum. p_{Fn} is 300-400 MeV in supernova cores [147] and typically > 100 MeV in neutron stars [119]. $\mathscr{F}$ in Eqn. 8.2 is the product of thermodynamic functions as defined in Eqn. 8.3. $\mathscr{H}_{ij}$ is the hadronic tensor incorporating nucleon spin with value $10/\omega^2$. The rate of axion production can be determined independently of the OPE approximation using the soft-neutrino radiation rate which is proportional to the nucleon nucleon on-shell scattering amplitude. This soft-neutrino approximation (SNA) method gives an axion emission rate which is a factor of four smaller than that given by the OPE approximation [119]. It can be shown that a value of $\mathscr{H}_{ij} = 10/\omega^2$ largely includes the reduction in axion emission rate expected for the SNA by considering expressions for the scattering kernel of neutrinos produced by Bremsstrahlung in supernova cores as presented in [120] where the SNA has not been applied. I do this by taking the spin structure function $S_\sigma(\omega)$ (Eqn. 8.2) to be analogous to the neutrino scattering kernel $S_\sigma(\omega)$ of [120] and thus equate $\mathscr{H}_{ij}$ to the spatial trace, $\overline{M}$, in the neutrino scattering kernel expression of [120]. By combining the expressions presented in [120] for a generic scattering kernel, the spin fluctuation rate and an effective degeneracy parameter, I obtain a $\mathscr{H}_{ij}$ value of $30/\omega^2$. Thus, a value of $10/\omega^2$ for $\mathscr{H}_{ij}$ results in a factor of 3 reduction in axion emissivity which is comparable with the factor of 4 reduction expected from the SNA. The thermodynamic function (Eqn. 8.4) is the Fermi Dirac distribution in natural units ($k_B = 1$) for the nucleons

applicable to degenerate matter [62] incorporating energy E, temperature T and neutron star degeneracy μ. I take the value of μ/T = 10 as used in the analysis of BGM16.

$$\begin{aligned} S_\sigma(\omega) = \frac{1}{4}\int \Big[\prod_{i=1..4}\frac{d^3p_{\rm i}}{(2\pi)^3}\Big] \\ \times (2\pi)^4\delta^3(\mathbf{p_1}+\mathbf{p_2}-\mathbf{p_3}-\mathbf{p_4}) \\ \times \delta(E_1+E_2-E_3-E_4-\omega)\mathscr{F}\mathscr{H}_{\rm ij} \end{aligned} \tag{8.2}$$

$$\mathscr{F} = f(E_1)f(E_2)(1-f(E_3)(1-f(E_4)) \tag{8.3}$$

$$f(E) = 1/(1+\exp((E-\mu)/T)) \tag{8.4}$$

The axion emissivity or energy loss rate per volume in natural units (i.e. $\hbar = c = 1$), ε_a, is defined by Eqn. 8.5 as given in [119] where M_N is the nucleon mass of 938 MeV and $g_{\rm ann}$ is the axion-nucleon coupling with $g_{ann} = C_N M_N/f_a$. C_N encapsulates the vacuum expectation values for the Higgs u and d doublets with the doublets giving mass to the up and down quarks of the nucleons. The value of C_N depends on the coupling model considered with $0 < C_N < 2.93$ [193]; I take $C_N = 0.1$ as BGM16.

$$\varepsilon_a = \frac{g^2{}_{\rm ann}}{48\pi^2 M_N^2}\int \omega^4 S_\sigma(\omega)\,d\omega \tag{8.5}$$

The expected photon flux arising from axion decay for a photon of energy E is given by Eqn. 8.6 from BGM16 where d is the distance to the pulsar in parsecs and Δt is the timescale for the emission of axions from a neutron star with a core temperature of 20 MeV (Eqn. 8.7). I take the value of $S_\sigma(\omega)$ to be 2.4×10^7 MeV^2 and 6.25×10^4 MeV^2 for axion energies of 100 MeV and 200 MeV respectively from the values of $\omega^4 S_\sigma(\omega)$ in the axion emissivity versus energy plot of BGM16 for a pulsar of core temperature 20 MeV and μ/T = 10 (Shown as the green line on Fig. 8.3, reproduced from BGM16). I choose $S_\sigma(\omega)$ at ω = 100 MeV and ω = 200 MeV in my calculations because these represent reasonable extremes on the emissivity plot, with emissivity peaking and being less sensitive to energy near ω = 100 MeV and an emissivity cut-off at ω = 230 MeV.

$$\begin{aligned} E\frac{d\Phi}{dE} = 1.8\times10^{-2}\Big(\frac{m_a}{\rm eV}\Big)^5\Big(\frac{\Delta t}{23.2\,\rm s}\Big)\Big(\frac{100\,\rm pc}{d}\Big)^2 \\ \times\Big(\frac{2E}{100\,\rm MeV}\Big)^4\Big(\frac{S_\sigma(2E)}{10^7\,\rm MeV^2}\Big)\,\rm cm^{-2}\,s^{-1} \end{aligned} \tag{8.6}$$

$$\Delta t = 23.2\,s\Big(\frac{\rm eV}{m_a}\Big)^2 \tag{8.7}$$

By combining Eqn. 8.6 and Eqn. 8.7 the UL axion mass can be expressed in terms of the UL gamma-ray photon flux Φ of a pulsar (Eqn. 8.8).

$$\mathrm{UL}\, m_a = \Big[\mathrm{UL}\,\Phi \mathrm{cm}^{-2}\,\mathrm{s}^{-1} \times 55.5 \times \Big(\frac{d}{100\,\mathrm{pc}}\Big)^2 \times \Big(\frac{100\,\mathrm{MeV}}{2E}\Big)^4 \Big(\frac{10^7\,\mathrm{MeV}^2}{S_\sigma(2E)}\Big)\Big]^{\frac{1}{3}} \tag{8.8}$$

Alternatively, instead of using photon flux methods as described above, axion mass can be constrained using an expression for the energy lost from the pulsar as a result of axion production. The energy loss rate ${\varepsilon_a}^D$ for a given mass of neutron star material arising from the production of axions in the pulsar core (Eqn. 8.9) is as presented in [110] based on [146] and [62] with α_a as Eqn. 8.10. T_MeV is the neutron star core temperature in MeV and ρ_{15} is the neutron star mass density in units of 10^{15} g cm^{-3}. I include a further factor of 0.25 in Eqn. 8.9 to allow for the SNA reduction in axion emission rate.

$${\varepsilon_a}^D = 0.25 \times \alpha_a 1.74 \times 10^{31} \mathrm{erg\,g^{-1}\,s^{-1}}\, \rho_{15}^{-2/3} T_{MeV}^6 \tag{8.9}$$

$$\alpha_a \equiv \Big(\frac{C_N M_N}{f_a}\Big)^2 / 4\pi \tag{8.10}$$

The measured UL gamma-ray luminosity, L_γ can be equated to the expected gamma-ray luminosity arising from the axion energy loss rate for the total mass of the neutron star as L_γ=${\varepsilon_a}^D NS_{mass}\, P_{a\to\gamma}$, where NS_{mass} is the neutron star mass expressed in grams and $P_{a\to\gamma}$ is the axion to photon conversion probability $(0-1.0)$ in the pulsar B field. In the case of axion radiative decay where an axion decays to two gamma-ray photons, without conversion in the pulsar B field being required, I take $P_{a\to\gamma}$ to be 1.1×10^{-24} s^{-1}(m_a/1 eV)^5 [226]. From the above expression for L_γ and by combining Eqns. 8.1, 8.9 and 8.10, I obtain an expression for UL m_a, hereafter called the "alternative model" (Eqn. 8.11). The alternative model uses a canonical pulsar mass of 1.4 $\mathrm{M}_\odot$ or 2.786×10^{33} g and a density of 0.056×10^{15} g cm^{-3}.

$$\mathrm{UL}\, m_a = \frac{6.0 \times 10^{15}}{C_N M_N} \times \left(\frac{4\pi L_\gamma \mathrm{erg\,s^{-1}}}{0.435 \times 10^{31} \mathrm{erg\,g^{-1}\,s^{-1}}\, \rho_{15}^{-2/3} T_{MeV}^6 NS_\mathrm{mass} P_{a\to\gamma}}\right)^{\frac{1}{2}} \tag{8.11}$$

8.3 Pulsar Selection

I make the simple assumption that axions are emitted in a continuous isotropic fashion by the pulsar and are unaffected by pulsar rotation. In making my pulsar selection I want to maximise the probability of detecting isotropic gamma-ray emission arising solely from the decay of axions to gamma-rays. Thus I wish to exclude the pulsed gamma-ray emission arising from pulsar magnetospheric emission which would be unrelated to axion production and a background to the axion signal that I wish to measure. Therefore, my selection of 17 pulsars (Table 8.1) from version 1.57 of the Australia Telescope National Facility (ATNF) catalogue [190] [1] is based on the following criteria to minimise gamma-ray background and to select well-measured pulsars which are most likely to emit detectable gamma-rays solely through axion decay:

- Pulsars which are located off the Galactic plane ($|b|> 15°$) thus reducing the uncertainty arising from the Galactic gamma-ray background model of the Galactic disc
- Pulsars away from the Galactic centre with $l > 30°$ and $l < 330°$
- Nearby pulsars with a heliocentric distance of 0.5 kpc or less and possessing an $\dot{E} > 0$ in the ATNF catalogue
- Pulsars which are not known to have binary companions in the ATNF catalogue and have not been identified as prior sources of gamma-ray emission in either the Public List of LAT-Detected Gamma-Ray Pulsars[2] (which lists all publicly-announced gamma-ray pulsar detections whose significance exceeds 4σ) or in the Second *Fermi* Large Area Telescope Catalog of Gamma-Ray Pulsars [11].

[1] http://www.atnf.csiro.au/research/pulsar/psrcat/

[2] https://confluence.slac.stanford.edu/display/GLAMCOG/Public+List+of+LAT-Detected+Gamma-Ray+Pulsars, list last updated 19th Oct 2018, accessed on 14th Feb 2019

Name and Ref.		l (degree)	b (degree)	RA (degree)	Dec (degree)	Period (s) and Ref.	Distance (kpc)	B Surface 10^{10} (Gauss)	B Light Cylinder (Gauss)	$\dot{E}$ 10^{30} (erg s^{-1})	Spin Down Age (10^5 Yr)
J0736-6304	[66]	274.88	-19.15	114.08	-63.07	4.863 [150]	0.10	2750.00	2.24	52.1	5.07
J0711-6830	[43]	279.53	-23.28	107.98	-68.51	0.005 [231]	0.11	0.03	16400	3550	58400
J0536-7543	[188]	287.16	-30.82	84.13	-75.73	1.246 [242]	0.14	84.90	4.12	11.5	349
J0459-0210	[189]	201.44	-25.68	74.97	-2.17	1.133 [135]	0.16	127.00	8.21	37.9	128
J0837+0610	[221]	219.72	26.27	129.27	6.17	1.274 [135]	0.19	298.00	13.50	130.0	29.7
J0108-1431	[250]	140.93	-76.82	17.03	-14.53	0.808 [135]	0.21	25.20	4.49	5.8	1660
J0953+0755	[221]	228.91	43.70	148.29	7.93	0.253 [135]	0.26	24.40	141.00	560.0	175
J1116-4122	[188]	284.45	18.07	169.18	-41.38	0.943 [36]	0.28	277.00	31.00	374.0	18.8
J0630-2834	[170]	236.95	-16.76	97.71	-28.58	1.244 [135]	0.32	301.00	14.70	146.0	27.7
J0826+2637	[84]	196.96	31.74	126.71	26.62	0.531 [135]	0.32	96.40	60.50	452.0	49.2
J1136+1551	[221]	241.90	69.20	174.01	15.85	1.188 [135]	0.35	213.00	11.90	87.9	50.4
J0656-5449	[148]	264.80	-21.14	104.20	-54.82	0.183 [148]	0.37	7.74	118.00	205.0	909
J0709-5923	[148]	270.03	-20.90	107.39	-59.40	0.485 [148]	0.37	25.00	20.50	43.5	610
J0636-4549	[65]	254.55	-21.55	99.14	-45.83	1.985 [65]	0.38	254.00	3.05	16.0	99.1
J0452-1759	[261]	217.08	-34.09	73.14	-17.99	0.549 [135]	0.40	180.00	102.00	1370.0	15.1
J0814+7429	[79]	140.00	31.62	123.75	74.48	1.292 [135]	0.43	47.20	2.05	3.1	1220
J2307+2225	[68]	93.57	-34.46	346.92	22.43	0.536 [67]	0.49	6.91	4.21	2.2	9760

Table 8.1 My selection of 17 pulsars from the ATNF catalogue showing their Galactic longitude/latitude, RA and Dec co-ordinates, period, pulsar distance, magnetic field B at surface and light cylinder in Gauss, $\dot{E}$ and spin down age. Discovery and period are from the references listed.

8.4 Analysis

8.4.1 Photon Event Data Selection

The data in this analysis were collected by *Fermi*-LAT between 4th Aug 2008 to 18th October 2017 (Mission Elapsed Time (MET) 2395574147[s] to 530067438[s]). I consider all PASS 8 events which are *source* class photons (evclass=128), with Front converting events (evtype=1), spanning the energy range 60 to 500 MeV. I use Front[3] converting events because of the improved point spread function (PSF) of this event class with 95 per cent containment of 60 MeV photons at a containment angle of 13° as opposed to 20° for both Front and Back converting events. I select a conservative energy range of 60-500 MeV, as axion decay has previously been expected to produce gamma-rays in the range 60-200 MeV, with a cut-off by 200 MeV as determined in BGM16. Throughout my analysis, the FERMIPY software package[4][275] with version V10R0P5 of the *Fermi Science Tools* is used, in conjunction with the P8R2_SOURCE_V6 instrument response functions. I apply the standard PASS 8 cuts to the data, including a zenith angle 90° cut to exclude photons from the Earth limb and good-time-interval cuts of DATA_QUAL > 0 and LAT_CONFIG = 1. The energy binning used is 4 bins per decade in energy and spatial binning is 0.1° per image pixel.

8.4.2 Determining if Pulsars are Gamma-ray Emitters

I first determine if any of the pulsars in my selection are significant unpulsed gamma-ray emitters. For each pulsar I consider a 20° Radius of Interest (ROI) centred on the pulsar co-ordinates. I use an ROI of 20° as my analysis is made down to a low energy of 60 MeV and I wish to be certain to allow for the contribution of low energy sources given the PSF of 13° above.

I include known sources using a point source population derived from the *Fermi*-LAT's third point source catalog (3FGL), diffuse gamma-ray emission and extended gamma-ray sources. The diffuse gamma-ray emission consists of two components: the Galactic diffuse flux and the isotropic diffuse flux. The Galactic component is modelled with *Fermi*-LAT's gll_iem_v06.fit spatial map with the normalisation free to vary. The isotropic diffuse emission is defined by *Fermi's* iso_P8R2_SOURCE_V6.txt tabulated spectral data. The normalisation of the isotropic emission is also left free to vary. In addition, all known sources take their spectral shape as defined in the 3FGL catalogue.

[3] I have repeated the same analysis using the PSF3 event class which is the best quartile direction reconstruction. This does not change the determined m_a significantly considering all 17 PSRs. I therefore retain the Front analysis to allow direct comparison with BGM16.

[4] FERMIPY change log version 0.12.0

An energy dispersion correction is applied to the pulsar test source but disabled for all 3FGL sources in line with Fermi Science Support Centre recommendations for low energy analysis.

I perform an initial BINNED likelihood analysis using the *optimize* method with the normalisation of all point sources within 20° of the pulsar being left free.

From this initial likelihood fit, all point sources (with the exception of the target pulsar) with a TS < 4 or with a predicted number of photons, $Npred$, < 4 are removed from the model. Thereafter, I free the spectral shape of all TS > 25 sources in this refined model and undertake a further secondary likelihood fit using *optimize* and *fit* methods.

The best-fit model from this secondary likelihood fit is then used with the *Fermi Science Tool* GTTSMAP to search for new point sources that were not already present in the 3FGL. In particular, I run the FERMIPY *find_sources* method to detect all sources above 3σ significance. *Find_sources* is a peak detection algorithm which analyses the test statistic (TS) map to find new sources over and above those defined in the 3FGL model by placing a test point source, defined as a power law with spectral index 2.0, at each pixel on the TS map and recomputing likelihood. Lastly, I again run the *fit* method to perform a final likelihood fit, which fits all parameters that are currently free in the model and updates the TS and predicted count ($Npred$) values of all sources.

8.4.3 Pulsar Upper Limit Gamma-ray Emission

In order to determine PSR gamma-ray flux upper limits I repeat the analysis of Section 8.4.2 with a source model which includes a pulsar test source for each of the 17 pulsars. The differential flux, *dN/dE*, (photon flux per energy bin) of the test source for each pulsar is described as a power law [5] as defined in Eqn. 8.12 where *prefactor* = N_0, *index*=γ and *scale*=E_0. The test source has *index* of 2.0, a *scale* of 1 GeV and a *prefactor* = 1×10^{-11}. I leave the *prefactor* (normalisation) and *index* of the test source free to vary.

$$\frac{dN}{dE} = N_0 \left(\frac{E}{E_0}\right)^{\gamma} \tag{8.12}$$

I then obtain UL photon and energy fluxes integrated over the energy analysis range (at 2 σ significance, 95 percent confidence level) from the flux_ul95 and eflux_ul95 attributes respectively of the FERMIPY sources entry for each pulsar test source. The UL photon and energy fluxes are defined as the values where the likelihood function, 2ΔLog(L), which compares the likelihood of a model with the source and without, has decreased by 2.71 from its maximum value across the range of flux values arising from the analysis. In addition, I

[5] From the Fermi Science Support Centre at https //fermi.gsfc.nasa.gov/ssc/data/analysis/scitools/source_models.html

use a composite likelihood stacking technique to improve the UL photon flux determination by considering all test sources in the analysis together. I extract a likelihood profile of ΔLog(L) vs photon flux for each test source using the FERMIPY *profile_norm* method. Next I determine the functional form of this likelihood profile for each test source using *numpy polyfit* and *poly1d* and interpolate the likelihood profile with *numpy polyval* between the overall minimum and maximum photon flux value obtained by considering the UL photon flux of all test sources. I then sum the ΔLog(L) values of each interpolated likelihood profile to obtain a single stacked ΔLog(L) vs photon flux profile for the test sources as a whole. Finally, I determine the maximum photon flux where the stacked ΔLog(L) has decreased by 1.35 from its peak value to give the one-sided upper limit photon flux.

8.5 Results

8.5.1 Pulsar UL Gamma-ray Fluxes

I list the UL photon, energy fluxes and gamma-ray luminosities (assuming the distances in Table 8.1) for my sample of pulsars in Tables 8.2 and 8.3. The UL photon flux at 95 percent confidence obtained by likelihood stacking of all 17 pulsars is 7.8×10^{-10} cm^{-2} s^{-1}.

8.5.2 Upper Limit m_a Determination

I list my determination of UL m_a in Tables 8.2 and 8.3 for each pulsar derived from the UL photon flux and Eqn. 8.8 for axions of energy 100 MeV and 200 MeV. The average UL m_a considering all 17 pulsars is 9.6×10^{-3} eV and 3.21×10^{-2} eV for axions of energy 100 MeV and 200 MeV respectively. I obtain an average UL m_a for the 4 pulsars analysed in BGM16; J0108-1431, J0953+0755, J0630-2834 and J1136+1551 of 9.8×10^{-3} eV and 3.29×10^{-2} eV for axions of energy 100 MeV and 200 MeV respectively.

My determination of UL $m_a = 9.6 \times 10^{-3}$ eV is a factor of 8 improvement[6] on the result of BGM16 who determined an UL m_a of 7.9×10^{-2} eV.

Finally, I note that the UL m_a obtained by likelihood stacking is improved two-fold compared to the averaged result above, with UL m_a of 4.8×10^{-3} eV and 1.61×10^{-2} eV for axions of energy 100 MeV and 200 MeV respectively.

[6]My result is also published in the Particle Data Group Review of Particle Physics 2020 [114].

Pulsar	TS	UL Photon Flux (10^{-8} cm^{-2} s^{-1})	UL Energy Flux (10^{-12} erg cm^{-2} s^{-1})	UL γ Luminosity (10^{31} erg s^{-1})	UL m_a ω = 100 MeV (10^{-2} eV)	UL m_a ω = 200 MeV (10^{-2} eV)
J0711-6830	3	0.04	1.51	0.22	0.21	0.70
J0536-7543	0	0.22	0.53	0.12	0.43	1.45
J0837+0610	0	0.27	0.63	0.27	0.57	1.90
J0108-1431	0	0.18	0.41	0.21	0.52	1.75
J0953+0755	2	0.47	1.32	1.07	0.84	2.81
J1116-4122	1	0.90	1.73	1.62	1.09	3.66
J0826+2637	2	0.39	1.18	1.44	0.91	3.04
J1136+1551	0	0.50	1.16	1.70	1.04	3.49
J0656-5449	0	0.32	0.75	1.23	0.94	3.14
J0636-4549	3	1.31	2.08	3.60	1.52	5.08
J0452-1759	0	0.31	0.71	1.36	0.97	3.24
J0814+7429	0	0.23	0.54	1.19	0.93	3.10

Table 8.2 Test statistic, UL photon flux, UL energy flux, UL gamma luminosity and UL m_a for axion energies of 100 and 200 MeV for the 12 undetected pulsars.

Pulsar	TS	UL Photon Flux (10^{-8} cm^{-2} s^{-1})	UL Energy Flux (10^{-12} erg cm^{-2} s^{-1})	UL γ Luminosity (10^{31} erg s^{-1})	UL m_a ω = 100 MeV (10^{-2} eV)	UL m_a ω = 200 MeV (10^{-2} eV)
J0736-6304	33	2.68	4.87	0.58	0.79	2.65
J0459-0210	10	1.72	3.64	1.11	0.93	3.13
J0630-2834	19	1.89	3.59	4.40	1.53	5.12
J0709-5923	12	1.03	2.55	4.17	1.38	4.62
J2307+2225	14	1.12	2.87	8.25	1.71	5.72

Table 8.3 Test statistic, UL photon flux, UL energy flux, UL gamma luminosity and UL m_a for axion energies of 100 and 200 MeV for the 5 pulsars which are associated with areas of extended diffuse gamma-ray emission.

8.5.3 Pulsars Near Extended Emission

I note that the UL test sources for 5 pulsars are detected with a significance which exceeds 3 σ , namely J0736-6304 5.7 σ (TS 33), J0630-2834 4.4 σ (TS 19), J2307+2225 3.7 σ (TS 14), J0709-5923 3.5 σ (TS 12) and J0459-0210 3.2 σ (TS 10). However, the initial analysis which searches for point sources (whilst not introducing a pulsar test source), detects no point sources at the pulsar co-ordinates and thus I discount these apparent detections as true detections of the pulsars concerned. The lack of significant point source pulsar detections can also be seen on TS maps for the analysis (Fig. 8.2) where the pulsars are spatially coincident with regions of extended gamma-ray emission uncharacteristic of the point source emission expected from a pulsar.

I also check for source extension of the pulsars by running the GTAnalysis *extension* method. *extension* replaces the pulsar point source spatial model with an azimuthally symmetric 2D Gaussian model. It then profiles likelihood with respect to spatial extension in a 1 dimensional scan to determine the likelihood of extension. Only the J0736-6304 test source has some evidence of extension with an extension TS value of 14 (3.7 σ). The remaining 4 pulsars with significance $< 4.4\ \sigma$ are consistent with background and as expected have no significant extension.

I make the assumption that axion emission is isotropic and so the extended emission of J0736-6304, which is asymmetric and exhibits its highest significance offset from the pulsar, would seem to be inconsistent with an axion source. Instead, this emission is more likely to be consistent with variations in the Galactic diffuse gamma-ray background.

These 5 pulsars generally exhibit higher UL fluxes (Table 8.3) than the other 12 (Table 8.2) and so omitting these 5 pulsars from the determination of UL m_a yields an improved average UL m_a for the 12 remaining pulsars of 8.9×10^{-3} eV and 2.97×10^{-2} eV for axions of energy 100 MeV and 200 MeV respectively.

8.6 Discussion

8.6.1 Upper Limit Determination

In the BGM16 work, the authors analysed 4 pulsars (J0108-431, J0953+0755, J0630-2834 and J1136+1551) with an UNBINNED likelihood analysis using the 2FGL catalogue, 5 years of *Fermi*-LAT PASS 7 event data in the energy range $60-200$ MeV and employing front converting source photon events. They detected no gamma-ray emission and determined a 95 percent confidence UL photon flux for each of the 4 pulsars using the MINOS method of the *Fermi* Science Tools. In contrast, I analyse 17 pulsars (including the 4 pulsars of BGM16)

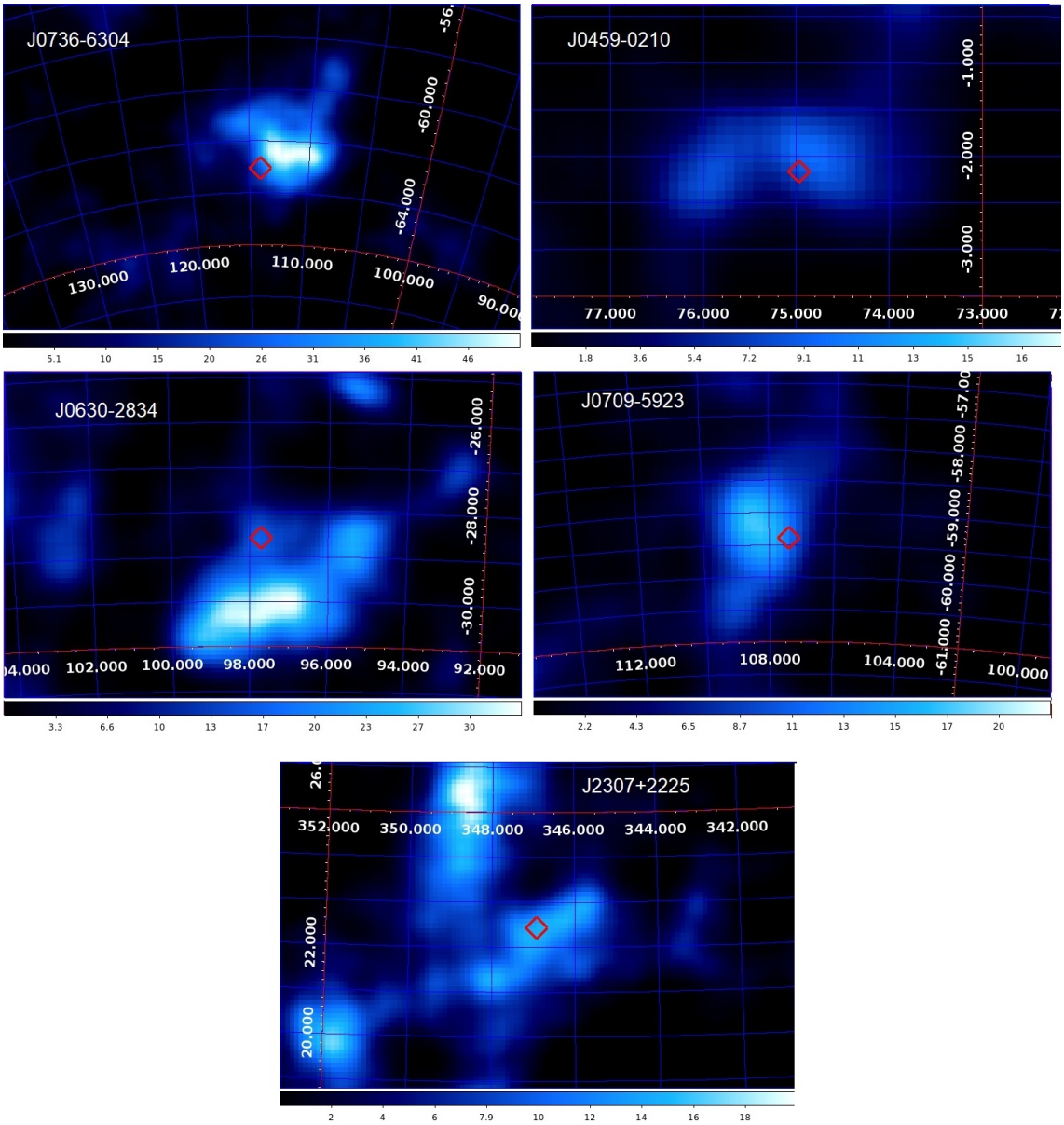

Fig. 8.2 TS maps for my gamma-ray analysis of the 5 pulsar test sources detected at > 3 σ significance (Table 8.3) showing that these sources are inconsistent with a point source detection, which is characteristic of pulsars, and part of extended diffuse features. The horizontal contour scale is the TS value, the red diamond is the pulsar position, horizontal axis is RA in decimal degrees, vertical axis is Dec in decimal degrees.

with a BINNED likelihood analysis using the 3FGL catalogue and 9 years of *Fermi*-LAT PASS 8 event data in the energy range 60−500 MeV, again using front converting events. I determine the UL photon flux using the FERMIPY flux_ul95 entry for each pulsar. Using this analysis I obtain UL photon fluxes (Table 8.5) comparable to BGM16 for the 4 pulsars they consider, which serves as a useful check of my gamma-ray analysis method, and do not detect any pulsars in my sample.

My method to determine UL m_a differs from BGM16 in that I use UL photon fluxes directly as input to Eqn. 8.8 whilst they fit a model of the spectral energy distribution (SED) of differential flux to a stacked likelihood analysis of the 4 pulsars using the *COMPOSITE2* module of the *Fermi* science tools and take the UL normalisation of this model to be UL $(m_a\ /\text{eV})^5$ from which they obtain UL m_a with all flux dependencies on astrophysical factors being accounted for in the SED model.

I can use the UL photon fluxes obtained by BGM16 to consider the improvement in UL m_a determination which arises from my UL m_a calculation method alone. The average UL m_a for the 4 pulsars using the BGM16 photon fluxes (Table 8.5) and my method (Eqn. 8.8) is 9.7 $\times$ 10^{-3} eV and 3.25 $\times$ 10^{-2} eV for axions of energy 100 MeV and 200 MeV, improving on the 7.9 $\times$ 10^{-2} eV determination of BGM16 by a factor of 2.4−8.1. Despite this improvement, I note that my determination of UL m_a is conservative because I assume that the integrated UL photon flux arises solely from a specific axion energy (100 MeV or 200 MeV) rather than the lower UL flux (and hence more constraining) UL m_a determination which would be expected if I could determine UL photon flux for each energy bin in the analysis energy range of 60−500 MeV.

I determine a very similar UL m_a in my sample of 17 pulsars of 9.6 $\times$ 10^{-3} eV and 3.21 $\times$ 10^{-2} eV for axions of energy 100 MeV and 200 MeV respectively. These results are also comparable with UL m_a values obtained by modelling the cooling of Cassiopeia A observed by *Chandra*. By assuming that the cooling results from both neutrino and axion emission and that a state of superfluidity exists in the star, an UL m_a of $(1.7 - 4.8) \times 10^{-2}$ eV is obtained for C_N = (0.14 − -0.05) [174].

As a final check to test whether the SED differential flux model used by BGM16 can be fitted individually to any of my 17 pulsars, I add a test source with the SED differential flux model from BGM16 implemented using the *FileFunction* spectral model (Eqn. 8.13) with flux values as Table 8.4 and re-analyse as Section 8.4 above. All 17 pulsars remain undetected with the differential flux model test source exhibiting a consistent normalisation of 10^{-5} for all pulsars which is equivalent to $m_a < 0.1$ eV.

$$\frac{dN}{dE} = N_0 \left(\frac{dN}{dE} \right) \Big|_{file} \tag{8.13}$$

Energy MeV	Differential Flux cm^{-2} s^{-1} MeV^{-1}
50	2×10^{-3}
60	8×10^{-4}
70	4×10^{-4}
80	1×10^{-4}
90	6×10^{-5}
100	2×10^{-5}
200	1×10^{-11}

Table 8.4 Definition of the FileFunction spectral model with differential flux at a given energy

8.6.2 The Effect of Pulsar Core Temperature

The emission rate for axions is strongly dependent on pulsar core temperature, T_c, being proportional to ${T_c}^6$ [62]. I therefore re-examine the applicable value of T_c for modeling axion emission and the effect of lowering T_c on that emission. In the BGM16 work the authors select T_c = 20 MeV on the basis of the range temperatures applicable to equation of state (EOS) simulations of pulsar degenerate matter [235, 241, 27], slower neutron star cooling due to super-fluidity [207, 171] and surface temperature observations of the pulsar J0953+0755 [213].

I now consider to what extent the works cited above explicitly support the choice of T_c = 20 MeV. In EOS modeling both [235] and [241] use T_c as a free model parameter (in the range $0-60$ MeV and $0-15$ MeV respectively) for the construction of phase diagrams but this does not indicate a preferential value for T_c. In [27], a specific Fermi temperature, T_F, of 20 MeV per nucleon is supported but no preferred value of T_c is indicated. The cooling of quark hybrid (QH) stars (a special case of a higher density neutron star where quarks experience deconfinement from nucleons) is considered in [207] with QH stars in fact cooling *more* quickly than hadron neutron stars unless a colour flavour locked (CFL) quark phase with a higher CFL gap parameter of 1 MeV is considered. However, by 10^5 yr all modelled QH stars again exhibit *greater* cooling than hadron neutron stars. As all neutron stars in my pulsar sample have age $> 10^5$ yr (Table 8.1), this QH star slow cooling regime will not result in a higher value for T_c in my sample than might be expected from normal cooling processes. The discussion of crustal heating arising from super fluidity in neutron stars also refutes T_c = 20 MeV, with one neutron star J0953+0755 (PSR 0950+08) analysed in BGM16 having an internal temperature of between 0.09 keV and 0.11 keV [171]. Although there is more recent evidence of internal heating of J0953+0755 from far UV HST observations (surface

temperature (ST) = $(1-3) \times 10^5$ K [214] vs 7×10^4 K of [213]), this would still only result in a maximum T_c of 1.34 keV assuming $T_c = 12 \times (\mathrm{ST}/10^6\ \mathrm{K})^{1.82}$ keV [171, 115].

The authors of [210] have modelled the cooling of neutron stars using a fully general relativistic stellar evolution code, without exotic cooling, allowing for inputs for equations of state and uncertainties in superfluidity along with a finite time scale of thermal conduction. They determine T_c to be initially 3.98×10^9 K (343 keV) when the neutron star is 9 hours old, decreasing to 1.99×10^9 K (171 keV) at 1 yr, 6.31×10^8 K (54 keV) at 1000 yr and 1.99×10^8 K (17 keV)) at 10^5 yr. This cooling trend agrees well with the modelling of pulsar cooling in [279] where the highest pulsar surface temperatures (in all scenarios) of 3.98×10^6 K at 1 yr and 1.99×10^6 K at 10^5 yr yield a T_c of 148 keV and 12 keV respectively using the ST to T_c conversion above. It should also be noted that *Chandra* observations of the very young pulsar Cas A (age $\approx$ 330 yr), yield an ST of 2.04×10^6 K [126] equivalent to T_c = 43.9 keV using the ST to T_c conversion above. Similarly, in their modeling of Cas A cooling using the observations of [126], the author of [174] determines the T_c of Cas A to be 7.2×10^8 K, equivalent to 62 keV.

I therefore consider $T_c = 20$ MeV to be a high temperature choice more consistent with the neutron star core just after the supernova event. In [247], EOS and hydrodynamic modeling is performed in the first second after the supernova core bounce and proto neutron star (PNS) creation. Here, at 150 ms post bounce, T_c can be 14 MeV at the core, falling to 10 MeV at a radius of 10 km, before rising to a peak of 32 MeV at radius 12 km. Other modeling work demonstrates that a peak PNS T_c of 30 to 43 MeV is possible, falling to 5 to 18 MeV within 50 s [222] due to efficient cooling by neutrino emission. A very short time later, at 120 s, the PNS T_c is 2.2 MeV [204]. This suggests that plausible values of T_c are much less than 20 MeV with $T_c = 1$ MeV being achieved within seconds [285].

I re-evaluate $\omega^4 S_\sigma(\omega)$, on which the axion emissivity depends (Eqn. 8.5), for $T_c < 20$ MeV. I use the analytic simplification for the phase space integral for $S_\sigma(\omega)$ from [120] and perform a 5 dimensional numeric Monte Carlo integration as described in the Appendix B. In order to check my method I first reproduce the $\omega^4 S_\sigma(\omega)$ plot from BGM16 (Fig. 8.3) using a T_c of $10-50$ MeV, $\mu/T_c = 9-11$ and $p_{Fn} = 300$ MeV in Fig. 8.4.

In Fig. 8.4, I obtain the essential features of the original plot from BGM16 (reproduced in Fig. 8.3) both in magnitude and in the following respects:

- Increasing the value of μ/T_c for fixed $T_c = 20$ MeV decreases amplitude of $\omega^4 S_\sigma(\omega)$
- $\omega^4 S_\sigma(\omega)$ for $T_c = 10$ MeV cuts-off at a lower value of $\omega = 100$ MeV than for $T_c = 20$ MeV

- The T_c = 50 MeV case has lower values of $\omega^4 S_\sigma(\omega)$ than the T_c = 20 MeV case, with $\omega^4 S_\sigma(\omega)$ remaining broadly flat across higher ω values of 100−300 MeV with no pronounced cut-off at 200−300 MeV
- The value of $\omega^4 S_\sigma(\omega)$ spans one order of magnitude for the 20 MeV case and varying $\mu/T_c = 9-11$

I then evaluate $\omega^4 S_\sigma(\omega)$, in a lower temperature regime, for p_{Fn} = 300 MeV, $\mu/T_c = 10$ and consider lower pulsar core temperatures with $T_c = 1-20$ MeV (Fig. 8.5). Lowering T_c from 20 MeV to a plausible PNS temperature of 4 MeV reduces axion emissivity and hence gamma-ray emission by a factor of 10^8 for axions of energy ω = 100 MeV. It therefore seems implausible that there would be detectable gamma-ray emission to allow the determination of m_a using the astrophysical model of gamma-ray emission from BGM16 (Eqn. 8.6), for realistic pulsar core temperatures. I note however that this model is based on a quite conservative assumption that gamma-ray emission arises solely from axion radiative decay as opposed to axion to gamma-ray photon conversion in the B field of the pulsar. It is therefore possible that an alternative model allowing axion to photon conversion could produce detectable gamma-ray emission.

The probable lack of detectable gamma-ray emission in the lower temperature regime leads us to derive values for UL m_a from an alternative model (Eqn. 8.11) based on the axion power equation which defines an energy loss rate due to axion production in the pulsar core (Eqn. 8.9). Using the UL gamma-ray luminosity (Table 8.2) I determine UL m_a from Eqn. 8.11 whilst varying T_c and the probability of axion to photon conversion in the pulsar B field. On Fig. 8.6 I show the range of UL m_a values that I obtain. The conversion of axions to gamma-ray photons via radiative decay results in the highest UL m_a (67.5 eV at 0.1 MeV, 9.4 eV at 1 MeV and 0.7 eV at 20 MeV, points A, B and C respectively) which is above the classic m_a search range of $10^{-2}-10^{-6}$ eV. Similarly by varying the axion to photon conversion probability from 0.001 to 1.0 (total conversion), I only obtain an UL m_a above the lower search bound of 10^{-6} eV for $T_c < 0.1$ MeV independent of the degree of axion to photon conversion or $T_c < 0.4$ MeV assuming a probability of ≤ 0.001 for axion to photon conversion (Points E and F of Fig. 8.6 respectively). At T_c = 1 keV the lowest UL m_a obtainable would be 3.0 eV assuming total conversion of axions to photons (Point D of Fig. 8.6). I do not offer a view on the degree of axion to photon conversion in the pulsar B field but simply present a range of conversion alternatives to give indicative values of the UL m_a.

The determination of a plausible and precise UL m_a from this alternative model thus requires both realistic lower values of T_c and a knowledge of the precise extent of the axion

to photon conversion in the pulsar B field. I have dealt with the value of T_c in the PNS and old pulsar cases above; however, whilst the authors of the BGM16 work consider there to be no axion to photon conversion in the pulsar B field (using vacuum bi-refringence arguments) there is no consensus on the extent of axion to gamma-ray photon conversion in pulsar B fields. More attention has been paid to axion to X-ray photon inter-conversion in pulsars [218] and in axion like particle (ALP) to X-ray conversion in the higher B field (20×10^{14} G) of magnetars by [107]. In this paper, $P_{a \rightarrow \gamma} = 0.225$ for $\omega = 3$ keV (the peak emission) and $P_{a \rightarrow \gamma} = 0.025$ for $\omega = 200$ keV when $T_c = 50-250$ keV. The lower B field of my sample notwithstanding (average $B = 2.78 \times 10^{12}$ G) such values of $P_{a \rightarrow \gamma}$ and T_c could yield constraints on m_a in the classic axion search range using the alternative model (Fig. 8.6).

The normalized axion energy spectrum $dN_a/d\omega$ peaks at $\omega/T_c = 2$ [110]. This implies that the photon energy spectrum would peak at energy T_c. Therefore for the values of T_c discussed above, in the 1 MeV range or below, the determination of an UL for unpulsed gamma-ray emission in my pulsar sample, or preferably younger pulsars with a potentially higher T_c, by future low-energy gamma-ray observatories such as the All-Sky Medium Energy Gamma-ray observatory (AMEGO) or e-ASTROGAM, with greater sensitivity than any current observatory in the $0.2-10$ MeV band [229], [33] may allow an improved determination on the UL m_a from pulsars presented in this work.

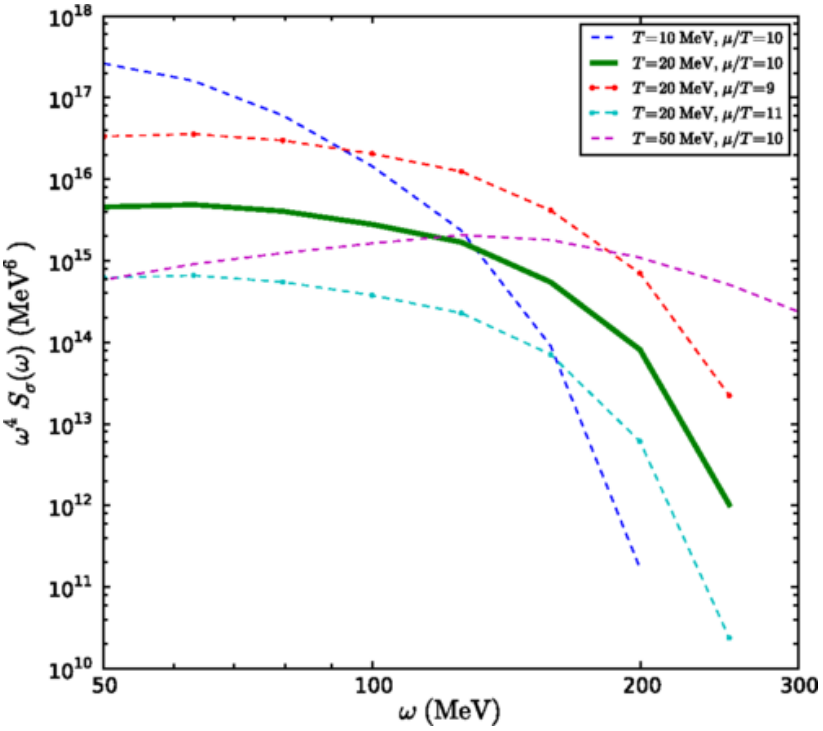

Fig. 8.3 The energy dependence of axion emissivity $\omega^4 S_\sigma(\omega)$ on axion energy ω for varying pulsar core temperature T_c and μ/T_c derived by Monte Carlo numerical integration of an analytic simplification of $S_\sigma(\omega)$, reproduced with permission from BGM16. The green line is the fiducial line in BGM16 from which I derive my values for the spin structure function at axion energies of 100 and 200 MeV.

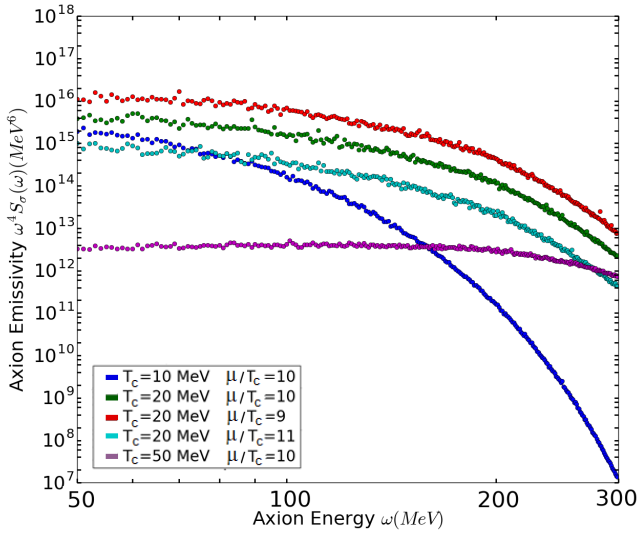

Fig. 8.4 The energy dependence of axion emissivity $\omega^4 S_\sigma(\omega)$ on axion energy ω for varying pulsar core temperature T_c and μ/T_c derived by Monte Carlo numerical integration of an analytic simplification of $S_\sigma(\omega)$.

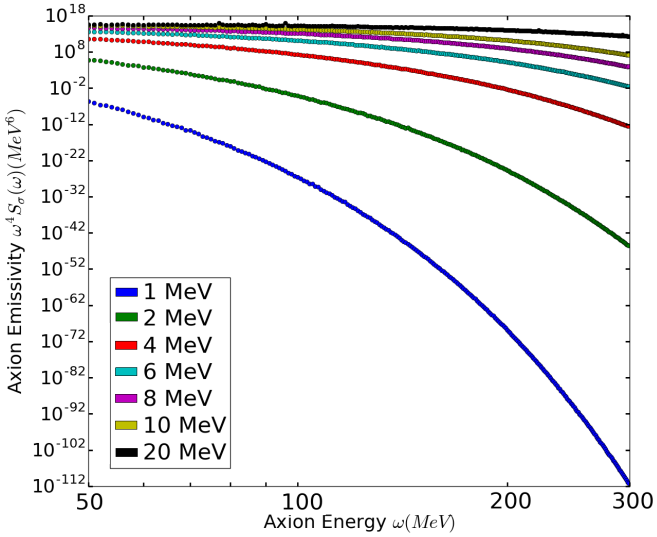

Fig. 8.5 The energy dependence of axion emissivity $\omega^4 S_\sigma(\omega)$ on axion energy ω for T_c = 1-20 MeV and μ/T_c = 10 derived by Monte Carlo numerical integration of an analytic simplification of $S_\sigma(\omega)$. Reducing T_c from 20 MeV to 4 MeV lowers emissivity by a factor of 10^8 at ω = 100 MeV.

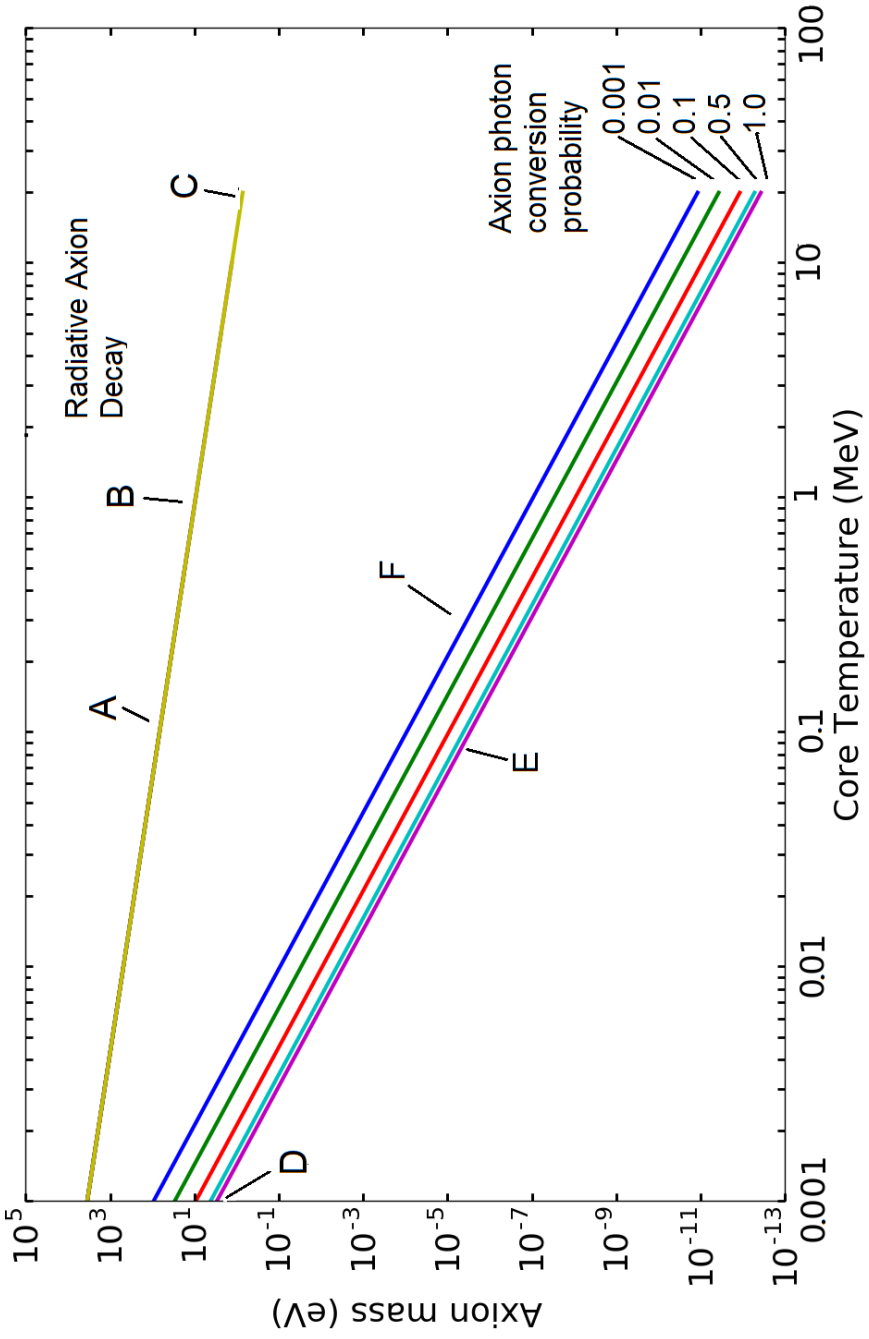

Fig. 8.6 Plot of axion mass with respect to T_c using an alternative energy loss rate model and varying axion to photon conversion probabilities from 0.001 to 1.00. Also shown is the more conservative axion radiative decay case (top). At realistic values of T_c of 0.1 and 1 MeV, radiative decay alone yields unrealistic values for UL m_a of 67.5 eV and 9.4 eV respectively (labelled A and B). At an unrealistic high value of 20 MeV for T_c the UL m_a is 0.7 eV (Labelled C) . At T_c = 1 keV, UL m_a is 3.0 eV, assuming total axion to photon conversion (labelled D). To keep UL $m_a > 10^{-6}$ eV, which is the classic axion search lower bound, requires $T_c < 0.1$ MeV (labelled E) or $T_c < 0.4$ MeV with a low axion to photon conversion probability of 0.001 (labelled F).

Pulsar	UL Photon Flux (60−200 MeV) (From BGM16) (10^{-9} cm^{-2} s^{-1})	UL Photon Flux (60−500 MeV) This analysis (10^{-9} cm^{-2} s^{-1})	UL m_a ω = 100 MeV (10^{-2} eV)	UL m_a ω = 200 MeV (10^{-2} eV)
J0108-1431	4.03	1.75	0.69	2.31
J0953+0755	7.40	4.75	0.97	3.26
J0630-2834	4.82	18.90	0.97	3.25
J1136+1551	8.52	5.01	1.25	4.17

Table 8.5 The UL photon flux for 4 pulsars from BGM16 (60−200 MeV) compared to my analysis (60−500 MeV) and UL m_a which I derive from the BGM16 fluxes for axions of energy 100 MeV and 200 MeV using Eqn. 8.8.

8.7 Magnetars

The determination of a plausible and precise UL m_a from the alternative model (Eqn. 8.11 and Fig. 8.6), thus requires both realistic lower values of T_c and a knowledge of the precise extent of the axion to photon conversion in the pulsar B field. I have dealt with the value of T_c in the PNS and old pulsar cases above; however, whilst the authors of BGM16 consider there to be no axion to photon conversion in the pulsar B field (using vacuum bi-refringence arguments) there is no consensus on the extent of axion to gamma-ray photon conversion in pulsar B fields. More attention has been paid to axion to X-ray photon inter-conversion in pulsars [218] and in axion like particle (ALP) to X-ray conversion in the higher B field (20 $\times$ 10^{14} G) of magnetars by [107]. In [107] the authors use coupled differential equations to calculate the ALP-to-photon conversion probability in the magnetosphere and its dependancy on ALP energy, mass, ALP-photon coupling, magnetar surface B field and the angle between the magnetic field and the direction of the ALP propagation. They find $P_{a\rightarrow\gamma}$ = 0.225 for ω = 3 keV (the peak emission) and $P_{a\rightarrow\gamma}$ = 0.025 for ω = 200 keV when T_c = 50−250 keV which they take as the likely range of T_c in magnetars. Such values of $P_{a\rightarrow\gamma}$ and T_c can yield constraints on m_a in the classic axion search range using the alternative model (Fig. 8.6) and flux observations in the soft gamma-ray regime. Furthermore such conversion could occur at several hundred NS radii (K. Sinha - personal communication), allowing bounds to be set on m_a if the quiescent emission of the magnetar itself could be discounted. I now go on to consider the likely range of T_c in magnetars and explain how their quiescent emission within a few NS radii in the soft gamma-ray band of 300 keV−1 MeV is likely to be suppressed.

8.8 Magnetar Heating and T_c

I now summarise the need for a magnetar heating mechanism over and above that found in conventional pulsars and discuss temperature modelling which supports my choice for the magnetar core temperature (T_c).

The quiescent X-ray luminosity of magnetars of $10^{34}-10^{35}$ erg s^{-1} exceeds the spin down luminosity of $10^{32}-10^{34}$ erg s^{-1}, thus excluding rotation spin down as the sole magnetar energy source. Furthermore, the lack of Doppler modulation in X-ray pulses arising from magnetars indicates a lack of binary companions, which combined with the slow periods of magnetars (2−12 s) excludes an accretion powered interpretation [106, 156].

In reference [155], the authors show the need for heating by theoretical cooling curves for neutron stars of mass 1.4 $M_\odot$, with and without proton superfluidity in the core, which yields effective surface temperatures below those observed in seven magnetars (including four which I will use in my selection below, namely: 1E 1841-045, 1RXS J170849.0-400910, 4U 0142+61 and 1E 2259+586). They then use a general relativistic cooling code which accounts for thermal losses from neutrino and photon emission and allows for thermal conduction to show that magnetars are hot inside with $T_c = 10^{8.4}$ K at age 1000 yr and temperatures of $10^{9.1}$ K in the crust, where the heat source should be located for efficient warming of the surface, to offset neutrino heat losses from the core.

The authors of [86] consider the case of magnetars born with initial periods of ≤ 3 ms combined with a strong internal toroidal B field of $\geq 3 \times 10^{16}$ G and an exterior dipole B field of $\leq 2 \times 10^{14}$ G. In this case, efficient heating of the core can occur via ambipolar diffusion which has a time-varying decay scale as a function of T_c and B field strength. As the core cools, an equilibrium is established between increasing B field decay and reducing neutrino emission, leading to reduced cooling which can keep T_c at $10^{8.9}$ K 2250 yr after magnetar creation.

The magnetar temperature modeling of [134] considers heating throughout the magnetar core arising from magnetic field decay and ambipolar diffusion, together with the cooling caused by the neutrino emission of the modified urca process (where an electron neutrino and a neutron is produced from a proton and an electron using the additional momentum from other nucleons via a pion) and Cooper pairing of nucleons. In this case, the authors find that strong core heating cannot account for the observed surface temperatures and conclude that, as in the case of [155], high surface temperatures require heating of the crust, rather than the core, with the crust and the core being thermally decoupled from one another. However the authors of [134] show that T_c at 10^4 yr can vary between 0.8×10^8 K with ***no*** heating of the superfluid core, 1.4×10^8 K with heating of the crust and 5×10^8 K with core heating. At 10^3 yr, with heating of the superfluid core, T_c can reach 7×10^8 K.

Instrument	Detector Material	Energy Range
ISGRI	Cadmium-Telluride	15 keV − 1 MeV [173]
SPI	Germanium	20 keV − 8 MeV [262]
COMPTEL	Liquid scintillator / Sodium Iodide	750 keV − 1 MeV [239]
Fermi-GBM	Sodium Iodide	$<$ 1 MeV
"	Bismuth Germanate	150 keV − 30 MeV [197]

Table 8.6 Soft gamma-ray detectors with detector material used, energy range measured and instrument description reference in brackets.

The strong B field of magnetars can produce strongly anisotropic thermal conductivity in the neutron star crust whilst also allowing the synchrotron neutrino process to become a predominant cooling mechanism while other contributions to the neutrino emissivity are far more weakly suppressed. These effects allow the temperature at the base of the crust (which acts as an insulating layer) to reach $10^{9.6}$ K while the surface temperature remains at 10^5 and $10^{6.7}$ K [224], for a B field parallel and radial to the neutron star surface respectively. This is compatible with the observed surface temperatures of $10^{6.5} - 10^{6.95}$ K for the seven magnetars in [155] and could allow T_c to exceed 10^9 K.

Finally, the quiescent luminosity of magnetars $10^{34}-10^{35}$ erg s^{-1} implies a T_c of $(2.7 - \geq 8.0) \times 10^8$ K for a magnetar with an accreted iron envelope and $(1.0 - 5.5) \times 10^8$ K for an accreted light element envelope [57].

Given the range of crust and core temperatures above, I therefore assume T_c to be 1×10^9 K (86.18 keV), which although at the upper limit of temperatures presented above, remains plausible.

8.9 Determination of UL m_a from Magnetars

I select the 6 magnetars which have published spectral energy distributions (SEDs) for differential energy fluxes in the soft gamma-ray band 300 keV to 1 MeV (Table 8.7). The SEDs are obtained from observations made by the *INTEGRAL* Soft Gamma-Ray imager (ISGRI) detector, on the angular resolution Image on Board instrument (IBIS) and *INTEGRAL* spectrometer (SPI), and from the non-contemporaneous observations of the COMPTEL instrument on the Compton Gamma-Ray Observatory *CGRO* and the *Fermi*-GBM. [97, 166, 251]. I summarise the detection materials employed and energy ranges observed for each of these instruments in Table 8.6.

I extract 2σ UL fluxes from the original spectral energy distributions of [97, 166], in a conservative manner, as the sum of *CGRO* COMPTEL determinations in range 0.3−1

MeV and adjacent *INTEGRAL* IBIS-ISGRI measurements in the 200-300 keV band. The flux obtained from the *Fermi*-GBM (using only the sodium iodide detectors) for 1E 1547.0-5408 [251], is a single pulsed flux in the 0.5-2 MeV band, however the overall detection significance of this magnetar is just 2.7σ and as such this flux point will have significance below 2σ. I therefore approximate this pulsed flux as an UL. I determine the UL luminosity in the 300 keV$-$1 MeV band for the summed UL fluxes and using the alternative model, with $P_{a\rightarrow\gamma} = 0.025$, calculate an UL m_a for each magnetar (Table 8.7) with the average UL m_a being 8.05×10^{-3} eV. This is in good agreement withe the UL axion m_a of 9.6×10^{-3} eV which I obtain above.

Magnetar	Distance kpc	Surface B Field 10^{14} G	Age kyr	UL Flux 300 keV - 1 MeV 10^{-10} erg cm^{-2} s^{-1}	UL Luminosity 300 keV - 1 MeV 10^{35} erg s^{-1}	UL m_a 10^{-2} eV
1E 2259+586	$3.2^{+0.2}_{-0.2}$ [163]	0.59	230	1.17 [166]	$1.43^{+0.18}_{-0.17}$	0.30
4U 0142+61	$3.6^{+0.4}_{-0.4}$ [101]	1.3	68	8.16 [97]	$12.65^{+2.97}_{-2.66}$	0.88
1RXS J170849.0-400910	$3.8^{+0.5}_{-0.5}$ [163]	4.7	9	1.92 [166]	$3.32^{+0.93}_{-0.82}$	0.45
1E 1547.0-5408	$4.5^{+0.5}_{-0.5}$ [257]	3.2	0.69	3.20 [251]	$7.75^{+1.82}_{-1.63}$	0.69
1E 1841-045	$8.5^{+1.3}_{-1.0}$ [254]	7	4.6	2.56 [166]	$22.13^{+7.28}_{-4.90}$	1.17
1E 1048.1-5937	$9.0^{+1.7}_{-1.7}$ [101]	3.9	4.5	3.04 [166]	$29.46^{+12.18}_{-10.07}$	1.34

Table 8.7 Magnetar sample with heliocentric distance in kpc, Surface magnetic field in Gauss, age in kyr, Sum of UL Flux in 300 keV$-$1 MeV band in erg cm^{-2} s^{-1}, UL luminosity in 300 keV$-$1 MeV band in erg s^{-1}. UL fluxes and distances are from the references shown, surface B field and age are from the online[48] version of the McGill magnetar catalog [212]. I extract UL fluxes from the original spectral energy distributions of [97, 166] in a conservative manner as the sum of *CGRO* COMPTEL determinations in range 0.3$-$1 MeV and adjacent *INTEGRAL* IBIS-ISGRI measurements in the 200$-$300 KeV band. The UL flux extracted from [251] is a pulsed UL in the 0.5$-$2 MeV band obtained from the *Fermi*-GBM. UL m_a is calculated using Eqn. 8.11 assuming $T_c = 10^9$ K. Average UL m_a using this method is 8.05 $\times 10^{-3} eV$.

8.10 Soft Gamma-ray Background

Magnetars exhibit thermal X-ray emission below 10 keV and a hard, pulsed, non-thermal X-ray emission with power law tails above 10 keV. This hard X-ray emission can extend to between $150 - 275$ keV [165, 112, 96] and appears to turn over above 275 keV on the basis of ULs obtained with INTEGRAL SPI ($20-1000$ keV) and CGRO COMPTEL ($0.75-30$ MeV) [97]. A spectral break above 1 MeV is also inferred by the non-detection of 20 magnetars using *Fermi*-LAT above 100 MeV [177]. The hard X-ray emission is most likely caused by resonant Compton upscattering (RCU) of surface thermal X-rays by non-thermal electrons moving along the magnetic field lines of the magnetosphere. The initial modeling of [45], using B field strengths typical of magnetars, at three times the quantum critical field strength, B_c, of 4.413×10^{13} G, produces flat differential flux spectra with sharp cut-offs at energies directly proportional to the electron Lorentz factor (γ_e) and places the maximum extent of the Compton resonasphere (the spherical volume around the star in which the RCU process takes place) within a few stellar radii of the magnetar surface.

In [282], Monte-Carlo models of the RCU of soft thermal photons, incorporating the relativistic QED resonant cross section, produces flat spectra up to 1 MeV for highly relativistic electrons ($\gamma_e = 22$), whilst mildly relativistic electrons ($\gamma_e = 1.7$) demonstrate spectral breaks at 316 keV. In [56], an analytic model of RCU, considering relativistic particle injection ($\gamma_e >> 10$) and deceleration within magnetic loops, predicts a spectral peak at ~ 1 MeV and a narrow annihilation line at 511 keV (both as yet unobserved). This model also places the active field loops emitting photons at $3-10$ stellar radii for a surface B field of $\sim 10^{15}$ G.

The analysis of [45] is recently extended in [268], allowing for a QED Compton cross scattering section which incorporates spin-dependent effects in stronger B fields. Electrons with energies $\lesssim 15$ MeV will emit most energy below 250 keV, which is consistent with the hard inferred X-ray turnover above. In [268], the maximum resonant cut-off energy can reach a peak of 810 keV for $\gamma_e = 10$ at some magnetar rotational phases and viewing angles. This violates COMPTEL ULs, however the model neglects the effects of Compton cooling and attenuation processes such as photon absorption due to magnetic pair creation ($\gamma \rightarrow e^+e^-$) and photon splitting ($\perp \rightarrow \parallel\parallel$). Also, the effect of electron Compton cooling is expected to steepen the cut-offs seen in the predicted hard X-ray spectral tails, which allows the models to be in agreement with the COMPTEL ULs. The emission region is placed at $4 - 15$ and $2.5-30$ stellar radii for γ_e values of 10 and 100 respectively.

The attenuation processes of magnetic pair creation and photon splitting, which act to suppress photon emission in RCU, are considered in detail in [141] for typical magnetar surface B fields of 10 B_c. In this case, the photon splitting opacity alone constrains the emission region of observed 250 keV emission in magnetars to be outside altitudes of 2-4

stellar radii and photons emitted from the magnetar surface at magnetic co-latitudes $< 20°$ can escape with energies > 1 MeV for typical magnetar surface B fields of 10 B_c. Also the emission of photons from field loops at < 2 stellar radii is suppressed, with photon escape energies of no greater then 287 keV. In contrast, emission regions at altitudes of > 5 stellar radii guarantee escape of 1 MeV photons at nearly all co-latitudes. The photon opacity caused by pair creation is shown to be much less restrictive and does not impact the < 1 MeV band. Finally, [141] determines the maximum energies produced by the resonant Compton process alongside the photon escape energies allowed by the photon splitting process (i.e. the maximum photon energies which can escape to an observer) as a function of magnetar rotational phase and obliqueness of rotation (which is the misalignment of the magnetic and rotational axis) and observer angle. It shows that photon emission > 1 MeV is permitted at some but not all rotational phases in the meridional case and that in most cases the RCU emission will vary with rotational phase in the 300 keV $-$ 1 MeV band.

Therefore, the RCU process *may* produce a background to the signal I wish to measure and this background might be expected to produce pulsed emission when photon opacity due to photon splitting is taken into account. On the other hand, a spectral turn over is possible if the electrons in the magnetosphere field loops are mildly relativistic. In addition, pulsed emission in magnetars has not been observed in the 300 keV $-$ 1 MeV band which would be suggestive of an RCU emission mechanism. I also note that photon splitting / pair creation opacity will not attenuate photon emission < 1 MeV at > 10 stellar radii [141]. As axion to photon conversion will occur at ~ 300 stellar radii, photon opacity processes can therefore be disregarded. In addition, the 440 magnetar bursts observed with the *Fermi*-Gamma Ray Burst Monitor (GBM), over 5 years, have been spectrally soft with typically no emission above 200 keV[82].

It is thus reasonable to assume that there is no RCU background and that all emission in the 300 keV $-$ 1 MeV band results from ALP-to-photon conversion. A more conservative approach is to require that any emission from ALP-photon conversion be *bounded* by the observed emission, which can then constrain m_a using the alternative model.

8.11 Constraints on ALP-photon coupling

The soft-gamma ray fluxes 5 of the 6 magnetars listed in Table 8.7 are also used to set constraints on the axion-photon coupling constant ($g_{a\gamma\gamma}$) by K. Sinha and H. Guo in our paper [183], using an energy resolved analysis. The magnetar 1E 1547.0-5408 [251] is excluded because the exact significance of its pulsed emission flux point is unknown and we wish all ULs to be at the same 2σ level to make a statistically valid comparison with CAST. In [183]

they model the case of relativistic ALPs produced by nucleon-nucleon Bremsstrahlung which convert to gamma-ray photons in the pulsar magnetosphere and provide expressions for the photon refractive indices in the strong and weak magnetic field regimes. They then solve the coupled ALP-photon propagation equations numerically using the appropriate refractive indices. By assuming that g_{aN} is such that ALP production from nucleon Bremsstrahlung in the core is just sub-dominant to neutrino production by modified urca processes, the calculated photon flux spectrum coming from ALP conversions is used to constrain $g_{a\gamma\gamma}$ by requiring that this flux be less than the observed soft-gamma-ray flux UL in the range 300 keV$-$1 MeV as taken from the same spectral energy distributions of [97, 166] as used above. The constraints on $g_{a\gamma\gamma}$ for $T_c = 10^9$ K are shown in Figure 8.7. It can be seen that for magnetars 1RXS J170849.0-400910 and 4U 0142+61, the limits on the ALP-photon coupling are better than the current CAST limits for ALP masses $m_a \lesssim 10^{-4}$ eV. The ULs on $g_{a\gamma\gamma}$ for the magnetars from my sample are listed in Table 8.8. For 1RXS J170849.0-400910 and 4U 0142+61, the ULs on $g_{a\gamma\gamma}$ are 6.16×10^{-11} GeV^{-1} and 4.39×10^{-11} GeV^{-1}, respectively. For 1E 2259+586, the UL is weaker, but still almost competitive with CAST limits.

The constraints become weak and taper off for $m_a \gtrsim 10^{-4}$ eV. This is because the ALP-photon mixing angle becomes small for large ALP masses and the probability of conversion becomes highly reduced.

Magnetar	$g_{a\gamma\gamma}$ (GeV^{-1})
1E 2259+586	8.21×10^{-11}
4U 0142+61	4.39×10^{-11}
1RXS J170849.0-400910	6.16×10^{-11}
1E 1841-045	1.31×10^{-10}
1E 1048.1-5937	1.69×10^{-10}

Table 8.8 Results: The 95% CL UL on the ALP-photon coupling $g_{a\gamma\gamma}$ obtained from conversions for the magnetars in our sample. The ALP mass is chosen to be 10^{-7} eV for all benchmarks shown in this table. The ALP-nucleon coupling is taken to be such that the ALP luminosity is just sub-dominant to the neutrino luminosity at a given temperature. The assumed core temperature is 10^9 K.

8.12 Proposed Magnetar Observations with the GBM

I now consider how further observations of magnetars with the GBM could provide further UL flux information which could improve the determination of UL m_a. The GBM is a non-imaging instrument with a wide field of view which is unable to assign gamma-ray fluxes to point sources by default. However, it is possible to assign detected events to pulsar

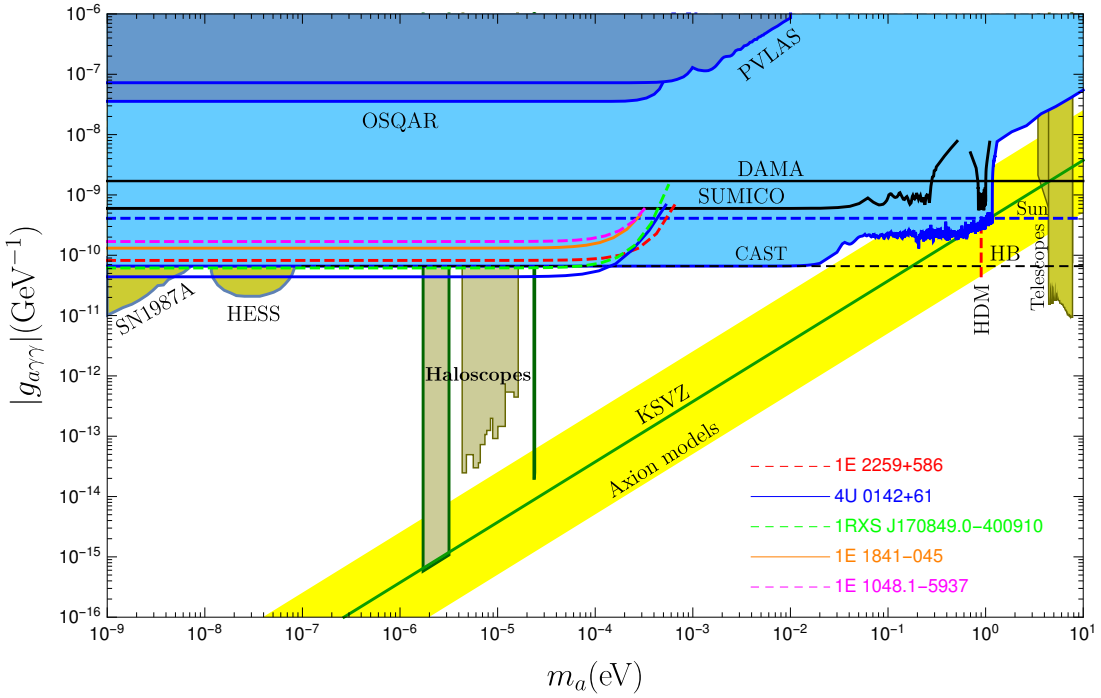

Fig. 8.7 The 95% CL upper limits on the ALP-photon coupling $g_{a\gamma\gamma}$ for the five magnetars in our sample, obtained for emissions in the energy range 300 keV$-$1 MeV, assuming $T_c = 10^9$K. The ALP-nucleon coupling g_{aN} is assumed to be such that the ALP luminosity is just sub-dominant to neutrino luminosity at a given temperature. All other constraints are taken from Fig. 6 of [32].

point sources with either a spatial event cut using the Earth Occultation Technique (EOT) or a temporal event cut using pulsar timing models. EOT uses a predefined catalogue of sources which exhibit step like changes in photon count rate as seen by the GBM when the sources are eclipsed by or rise above the Earth limb. Initially, 209 sources have been monitored using 3 years of data with 9 sources detected in the 100-300 keV energy band [274]. The *Fermi*-GBM Occultation project currently monitors 248 sources in the energy range 8 keV − 1 MeV with the majority of the signal being in 12-50 keV band[7].

The 53 day orbital precession period of *Fermi* can also be used to apply EOT without the use of a predefined source catalogue. Using the Imaging with a Differential Filter using the Earth Occultation Method (IDEOM), the Earth limb is projected onto the sky and used to determine count rates from 600,000 virtual sources with a 0.25° spacing, a technique which has identified 17 new sources [234]. This could also serve to process historical event data collected by the GBM since 2008 to recover legacy gamma-ray flux information if gamma-ray flares from magnetars and other bright sources were excluded.

In contrast, the author of [251] uses a pulsar timing method rather than an occultation technique. The CTIME data of the GBM are used to provide photon counts for 4 magnetars, 1RXS J170849.0-400910, 1E 1841-045, 4U 0142+61 and 1E 1547.0-5408, obtained with all 12 NaI detectors. The photon counts are attributed to the peak pulsed emission of each magnetar by epoch folding and the use of timing models (obtained with the Rossi X-ray Timing Explorer), which allow each event to be tagged by pulsar phase. This count rate is converted to an energy flux for 7 energy channels between 11 keV − 2 MeV by determining the GBM effective area as a function of photon direction, energy and probability of detection of a photon with a given energy. This yields pulsed ULs, a factor of just a few above those obtained by COMPTEL (which also serves as a useful check on the method) for the magnetars J170849.0-400910, 1E 1841-045 and 4U 0142+61. There are a further 7 magnetars (in addition to the 4 above) exhibiting a linear decrease in pulse frequency with time derived from X-ray observations in their glitch-free periods of between 100 to 6000 days [71]. This implies that these magnetars have a glitch-free timing model and so the method of [251] could be applied in 11 magnetars to GBM observations over the glitch -free period to determine soft-gamma ray UL fluxes and potentially place much tighter constraints on both m_a using the alternative model above (Eqn 8.11) and $g_{a\gamma\gamma}$ using the ALP-to-photon conversion model of [183].

The GBM is thus a very useful instrument, with a range of independent proven techniques, to determine the UL soft gamma-ray fluxes of the 23 confirmed magnetars[8] as listed in the

[7]https://gammaray.msfc.nasa.gov/gbm/science/earth_occ.html accessed on 25th November 2019

[8]http://www.physics.mcgill.ca/~pulsar/magnetar/main.html accessed on 25th November 2019

McGill Magnetar Catalog [212], most of which have no ULs defined in the 300 keV − 1 MeV band of interest in axion conversion.

8.13 Conclusion

I analyze 9 years of PASS 8 *Fermi*-LAT data in the 60−500 MeV range and determine flux upper limits (UL) for 17 gamma-ray dark pulsars as a probe of axions produced by nucleon-nucleon Bremsstrahlung in the pulsar core. Using a previously published axion decay gamma-ray photon flux model for pulsars which relies on an unrealistic high core temperature of 20 MeV, I improve the determination of the UL axion mass (m_a), at 95 percent confidence level, to 9.6×10^{-3} eV, which is a factor of 8 improvement on previous results. I show that the axion emissivity (energy loss rate per volume) at realistic lower pulsar core temperatures of 4 MeV or less is reduced to such an extent that axion emissivity and the gamma-ray signal becomes negligible. I then consider an alternative emission model based on energy loss rate per mass to allow m_a to be constrained with *Fermi*-LAT observations. This model yields a plausible UL m_a of 10^{-6} eV for pulsar core temperature < 0.1 MeV but knowledge of the extent of axion to photon conversion in the pulsar B field ($\approx 10^{12}$ G) would be required to make a precise UL axion mass determination. I show that the core temperatures of magnetars are sufficiently high to produce axions observable in the soft gamma-ray spectrum and that the quiescent emission of magnetars is relatively suppressed in this energy band, potentially mitigating the effect of background emission in the determination of UL m_a from these sources. I use literature soft gamma-ray flux observations of magnetars in the energy range 300 keV−1 MeV with an alternative emission model to determine an UL m_a for the ALP of 8.05×10^{-3} eV, in good agreement with the 9.6×10^{-3} eV value above. The same magnetar fluxes are used with ALP-to-photon propagation equations and the appropriate refractive indices to set limits on the ALP-photon coupling that are better than current CAST limits for 2 magnetars and for ALP masses $m_a \lesssim 10^{-4}$ eV.

The peak of axion flux is likely to produce gamma-rays in the ≤ 1 MeV energy range and so future observations with medium energy gamma-ray missions, such as AMEGO and e-ASTROGAM, will be vital to further constrain UL m_a. Specifically, I expect observations of magnetars with the *Fermi*-GBM to set improved constraints.

Chapter 9

Conclusion

9.1 Globular Cluster Gamma-Ray Emission

9.1.1 Basic Results

In this work, I analysed 111 globular clusters, (GCs), 75% of the known Galactic GC population, out to the distance of the furthest 4FGL catalogue detection, NGC 1904 at 12.9 kpc, using 10.5 yr of *Fermi*-LAT event data, in the energy range 100 MeV−10 GeV and 10−100 GeV. This is the most complete gamma-ray survey of these GCs to-date, as it uses the most event data (10.5 yr) and the 4FGL catalogue as a source model for the first time. In the energy range 100 MeV−10 GeV, I detected 34 GCs, all known sources in the 4FGL, producing their spectral energy distributions along with fitted models, test statistic maps and energy and photon fluxes. I showed that these GCs have no strong evidence for extension or emission beyond the GC tidal radius, indicating that emission is from sources in their cores. I reconfirmed my previous work that NGC 6254 is a gamma-ray source, associated with 4FGL J1656.4-0410, which is a new association not listed in the 4FGL. I reported flux upper-limits for the 77 remaining undetected GCs. I also demonstrated that Terzan 5 and 47 Tuc are the only GCs in the sample exhibiting significant gamma-ray emission in the energy range 10−100 GeV, in agreement with previous findings.

9.1.2 GC Millisecond Pulsar Gamma-Ray Connection

I next considered GC characteristics which influence millisecond pulsar (MSP) formation to explore if GC gamma-ray emission has a clear link to MSPs (as is the literature consensus view). I considered the relationship between gamma-ray luminosity and GC stellar encounter rate and metallicity; high values of which are thought to favor the production of MSP binary

systems in GCs and hence increase luminosity. I found that the proportionality of luminosity vs encounter rate (Γ_e) is twice that previously reported but with significant outliers, both at high and low Γ_e, whereas a plot of luminosity vs metallicity is so highly scattered that no relationship can be drawn, at odds with previous reports. On the basis that encounter rate is perhaps too crude a measure, I plotted a new quantity, derived in this thesis and introduced in my paper [181], the mass encounter rate product (MERP), which whilst correcting the outliers at high Γ_e, showed a significant high luminosity outlier at low MERP. I was able to derive a functional relationship between gamma-ray luminosity and MERP, albeit within a wide error band. In addition, I noted that GC mass alone was not of primary importance with NGC 6205 (initially predicted to be a gamma-ray emitter the equal of 47 Tuc before the *Fermi* era) being undetected whereas the smaller and equally distant GC NGC 6093 was, despite having no known MSPs. Finally, I showed that there was no correlation between resolved MSPs in GCs and gamma-ray luminosity, with GCs with no reported MSPs being similar in luminosity to those with MSPs.

These indications led me to further consider the connection between unresolved diffuse X-ray emission and gamma-ray emission in GCs (first identified in my paper [181]). I showed that 9 GCs displaying diffuse X-ray emission were detected in gamma-rays whereas 6 GCs which lack diffuse X-ray emission were not. I also identified transitional cases; 2 further GCs which lack reported diffuse X-ray emission but were detected in this work with gamma-ray luminosities of similar order to the least luminous of the 9 detected GCs above. I speculated that this correlated X-ray and gamma-ray emission could arise through the synchrotron process from a relativistic electron population produced by MSPs or alternatively from unresolved X-ray binaries and/or CVs.

The positive correlations of gamma-ray luminosity with Γ_e, MERP and unresolved diffuse X-ray emission combined with the lack of correlation with metallicity and mass allowed me to conclude that MSPs, though important, are not necessarily the sole emission mechanism in GCs.

9.1.3 Construction of a Composite MSP Spectrum

I produced my own model of stacked MSP emission, analogous to the cumulative emission of a GC MSP population using all reported gamma-ray emitting MSPs. I analysed 103 MSPs, detecting 98 and 25 MSPs in the energy range 100 MeV$-$10 GeV and 10$-$100 GeV, respectively, with no emission detected above 56 GeV. I summed the spectral fluxes of the detected MSPs to form my own stacked spectrum of gamma-ray emission and derived its functional form, ("Lloyd"), in the range 100 MeV$-$10 GeV, as a power law with super exponential cut-off, (Eqn. 6.1), in common with the model of the majority of individual

MSPs. I demonstrated that the Lloyd spectrum functional form is a very good fit, (using χ^2), to the MSP stacked spectrum between 562 MeV and 10 GeV. I also showed through the Akaike Information Criterion (AIC) statistic, that the Lloyd MSP model is the preferred model for describing the MSP stacked spectrum, when compared to alternative MSP models; Xing and Wang, and McCann, which employ just 39 MSPs. I therefore was able to use the Lloyd MSP model as the analogue of an ensemble population of MSPs in GCs for the GC spectral analysis that followed.

9.1.4 GC Spectral Analysis

I next examined the spectra of the 34 detected GCs in both a qualitative and quantitative fashion to determine the correlation of GC spectral characteristics with presumed MSP gamma-ray emission. The spectral fits produced in my *Fermi*-LAT analysis above were of varying quality with 16 and 25 GCs having a well fitted model by the χ^2 statistic at the α=0.05 and α=0.001 significance level respectively. The poorer spectral models arose from upper limit fluxes in tension with the spectral model below 250 MeV. On a qualitative level the spectral shapes of the majority of GCs were consistent with MSP emission in that they exhibited a cut-off at a few GeV , but others were not, with some showing hard emission up to 10 GeV, whilst others had a soft PL spectrum at odds with an MSP origin.

More quantitatively, I used an X-ray/gamma ray flux relation from the 2PC catalogue to estimate gamma-ray emission from 20 X-ray resolved MSPs in 47 Tuc demonstrating that they likely accounted for only half the GC gamma-ray emission.

I compared the population of GCs well fitted by the Lloyd MSP model, and those that were not, and was unable to prove using the Kolmogorov-Smirnov (KS) test that the two populations were different in GC characteristics relevant to MSP formation (encounter rate, metallicity, mass, MERP and binary encounter rate). One might expect that the GCs well-fitted by the Lloyd MSP model would have a distribution of characteristics favoring MSP formation, which would differ from that of the poorly fitted GCs. The lack of such a difference reinforced the view that other components of emission are present in addition to MSPs.

My consideration of spectral features using low energy (LE) and medium energy (ME) gamma-ray colours in GCs showed that these were also uncorrelated with factors relevant to MSP formation and that ME emission was somewhat harder in GCs than that of my MSP model. The presence of ULs below 177 MeV in the majority of GCs, although at odds with the Lloyd MSP model, was shown to be a systematic effect with UL magnitude correlated with Galactic latitude, most likely due to uncertainties in the Galactic background emission model, with the UL flux increasing with increasing latitude, until fluxes in the 133

MeV bin were observed in high latitude GCs. Furthermore my scatter plots of LE and ME colours to show the spectral differences between the individual GCs and my MSP model were unaffected by factors relevant to MSP formation, suggesting that these spectral differences were unrelated to MSPs. In order to probe if there were distinct sub-populations of MSPs spectra whose blend could account for differences between GC spectra and the Lloyd MSP model, I considered the link between LE and ME colours in MSP spectra and pulsar $\dot{E}$, which through its positive correlation with gamma-ray luminosity should be expected to change spectral shape and found no correlation.

In the very high-energy regime (VHE >50 GeV), I noted that GCs are generally under-observed with ground based gamma-ray telescopes, with only 3 of 15 GCs observed by H.E.S.S. being recognised gamma-ray emitters using *Fermi*-LAT. Terzan 5 is the only detected GC at VHE, with the H.E.S.S. results showing emission offset from the GC center. I showed that this offset emission is unlikely to be due to a proposed shock-front mechanism [54], where MSP winds interact with the denser Galactic medium at low latitudes, as the emission observed with *Fermi*-LAT, between $10-100$ GeV, is radially centered and not offset both in the case of Terzan 5, (situated in a low latitude, high density environment) and 47 Tuc (in a high latitude, lower density environment).

9.1.5 Likely Emission Candidates in GCs

To conclude, for the first time in this work, I have examined the detailed spectral characteristics of both my own stacked MSP spectrum and the spectra of gamma-ray detected GCs to determined the extent to which they agree and examine if this agreement is affected by GC characteristics relevant to MSP formation. The poor fit of my stacked MSP model to between one and two-thirds of GCs, whose characteristics relevant to MSP formation cannot be shown to be different from the well fitted cases, combined with the lack of GC spectral features which correlate with characteristics related to MSP formation, strongly suggest that other components exist in GC emission apart from MSPs.

On the basis of the evidence above the prime source of emission in GCs remains direct MSP emission by curvature radiation but the X-ray / gamma ray connection and slightly harder emission than a pure MSP model, suggests that gamma-ray emission from inverse Compton up-scattering of ambient soft photon fields by a MSP generated relativistic electron population is a major additional component. More speculatively, the very soft PL emission of some GCs, quite at odds with the spectrum of my MSP model, also hints at a role for dark matter (DM), as has been noted in 47 Tuc [63], although the exact DM candidate particle or decay channel is not examined in this work.

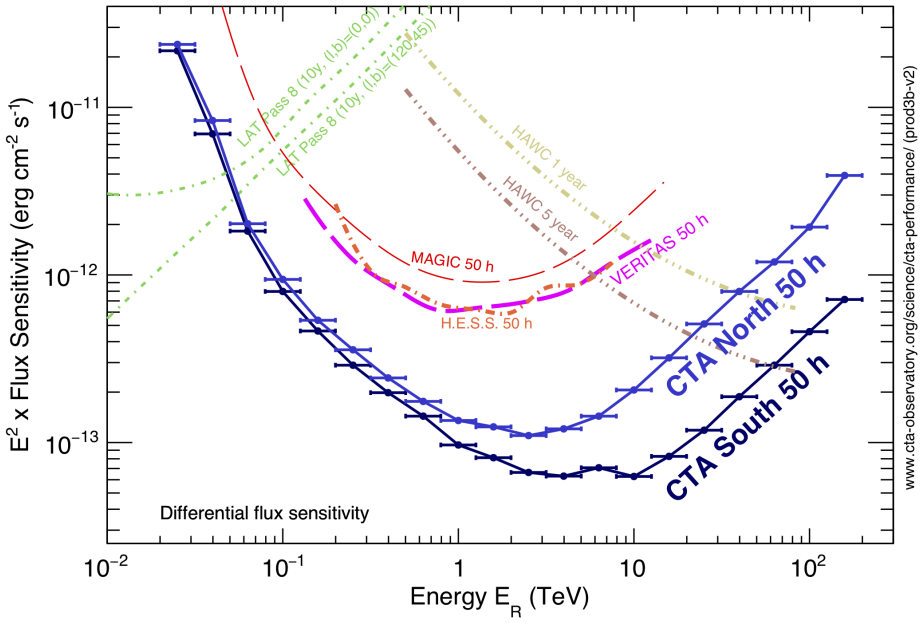

Fig. 9.1 The differential flux sensitivity of CTA-N and S for 50 h observations offers an order of magnitude increase in sensitivity compared to *Fermi*-LAT and existing IACTs: H.E.S.S, MAGIC and VERITAS and the Cherekov Water Tank experiment HAWC.

I consider alternative sources of emission such as AGN or cataclysmic variables (CVs) as less likely candidates due to the lack of variability in 6 high latitude GCs on 6 month timescales.

9.1.6 Future Work

GC Gamma-ray observations with CTA and AMEGO

In this work, I have show that *Fermi*-LAT observations are useful to constrain MSP emission models in GCs and that future VHE observations by the Cherenkov Telescope Array (CTA), with an order of magnitude increase in sensitivity (Fig. 9.1), will be required to constrain such models further. I predicted that on the basis of spectral models that GCs with hard flat spectra and fluxes $>2 \times 10^{-7}$ MeV cm^{-2} s^{-1} will be detectable by 50 h of CTA observations. The same simulations did not predict that Terzan 5 would be observable, but as the sole ground based GC detection, it will be the prime target for CTA observations to further refine the morphology and source of its offset, extended VHE emission.

The weak indications for TeV halos around MSPs using HAWC [137] should also be verified by CTA observations and if such features exist they should be observed in GCs as well.

It would also be interesting to use the ephemerides of GC MSPs, combined with gating and aperture photometry techniques to analyse which gamma-ray spectral components arise from MSP peak and inter-phase emission. This could allow the isolation of GC spectral components which arise from different sources than MSPs.

Further GC spectral analysis and detection of new GCs is also possible with the *Fermi*-LAT, which at the time of writing has nearly 1.5 years more statistics and a newer data release, PASS 8 DR2. Although there are few indications for GC variability it would be prudent to conduct a finer binned light curve analysis, on the 1 month timescale, on the most significant GC detections, Terzan 5 and 47 Tuc, to determine if variable sources contribute to the observed emission. A stacked *Fermi*-LAT spectrum of cataclysmic variables, in the outburst state, compared to the spectrum obtained in quiescence and outburst would also be useful to determine what contribution they make (if any) to GC emission and to what extent this is outburst dependent.

The Galactic latitude dependent systematics observed in GCs demonstrated that LE analysis is challenging with *Fermi*-LAT. The LE analysis could be improved considerably by using the proposed future All-sky Medium Energy Gamma-ray Observatory (AMEGO). AMEGO, if approved, could be launched in 2029 and would allow GC observations in the range 200 keV$-$ $>$10 GeV whilst improving on COMPTEL sensitivity in the MeV band by a factor of 20 as seen in Fig 9.2 [196].

Finally techniques used to detect sub-threshold point sources, such as the wavelet analysis of unresolved MSPs, which may contribute to the Galactic center excess (GCE) [47] should be applied to GC gamma-ray event data as the problem of MSP contribution to the GCE and GC emission shares many similarities.

GC MSP Radio Searches

I recommend radio pulsar search surveys of GCs to identify and characterise the complete MSP population of the detected GCs. From the Southern Hemisphere the Southerly GCs (which are in the majority) could be observed by the newly-commissioned 64-dish MeerKAT radio telescope in South Africa which has shown itself capable of determining the pulse profiles of 34 MSPs in Terzan 5 in a single 2.5 hr observation and can time 1000 pulsars per day[44]. In the Northern Hemisphere, the LOw-Frequency ARray (LOFAR) has identified 48 of the 75 known MSPs, at 110$-$188 MHz [161] and could characterise new MSPs in

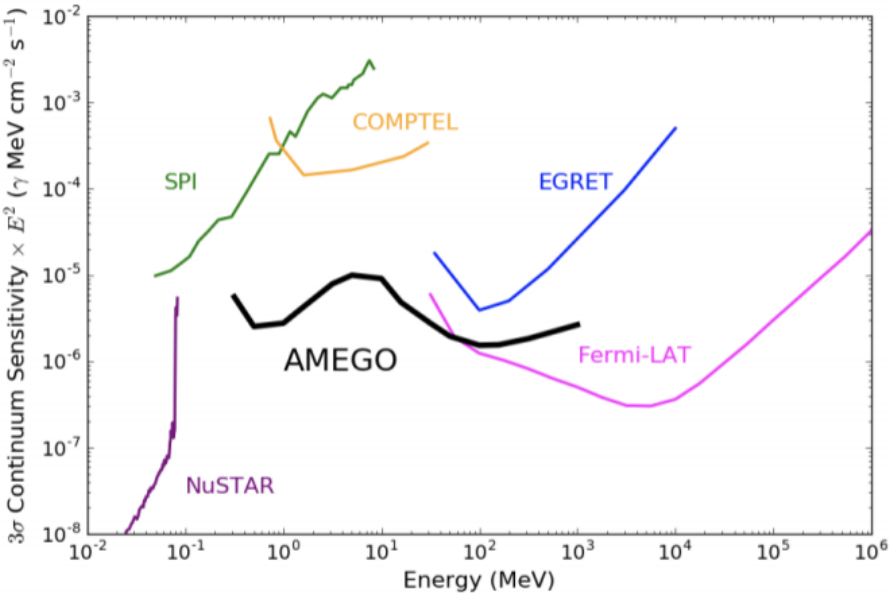

Fig. 9.2 AMEGO could provide >20 × better sensitivity in the MeV band compared to COMPTEL and extends sensitivity to the LE band which is inaccessible to *Fermi*-LAT. The AMEGO 3σ continuum sensitivity is based on an all-sky exposure during a 5-year mission. Figure taken from [196]

Northerly GCs either by direct observations or by reprocessing the LOFAR Tied-array All Sky Survey (LOTAAS), which has detected 2 new MSPs in its initial run [238].

GC Gamma-ray and X-ray Connection

The connection between unresolved diffuse X-ray emission and gamma-ray emission should be explored further. Fresh GC X-ray observations with *Chandra* or the successor satellite for *Hitomi* would be useful to determine the precise empirical relation between diffuse unresolved X-ray and gamma-ray emission along with its morphology in GCs. The gamma-ray X-ray relation was not offered in this work due to the relatively low number of GC X-ray observations and the diverse X-ray observation methods employed which hampered the validity of any direct flux comparison.

9.2 Constraints on the Axion and Axion Like Particles (ALPs)

9.2.1 Axion UL Mass from Pulsar Analysis

Whilst old millisecond pulsars are strong sources of gamma-ray emission in globular clusters, younger classical pulsars and magnetars with their stronger B fields of 10^{12} and $>10^{14}$ G, respectively, are potential sources of hypothetical cold dark matter particles, the axion and axion-like-particles. Using these pulsars, I placed very competitive constraints on the upper limit (UL) mass (m_a) of the axion, through considering gamma-ray ULs, and the use of published emission models. I used a previously published gamma-ray photon flux model, and my own analysis of 17 gamma-ray dark pulsars, to obtain an UL axion mass of 9.6×10^{-3} eV, a factor 8 improvement on the previous result. However, I also showed by considering published pulsar cooling studies and surface X-ray / core temperature relations that this result relied on an unrealistic pulsar core temperature of 20 MeV. I demonstrated the strong temperature dependence of the result through a numerical simplification and a Monte-Carlo integration method and showed that at realistic pulsar core temperatures, axion emissivity was reduced by a factor $>10^8$. These results were published in my paper [182] and listed in the PDG Review of Particle Physics 2020 (hereafter "PDG 2020", [114]).

9.2.2 ALP UL Mass from Magnetars

I then considered an alternative axion power equation model in 6 magnetars, which could have core temperatures of 10^9K ($\sim$ 86 keV) due to internal heating and a suppressed soft-gamma ray background flux, arising from their strong B fields (above the quantum critical limit), which causes splitting of the perpendicular mode of emitted photons to two parallel modes. I used a published probability of axion-to-photon conversion in the strong B field regime along with literature soft-gamma ray flux ULs in the energy range 300 keV$-$1 MeV, to obtain an average UL m_a for axion-like-particles of 8.05×10^{-3} eV, similar to my axion determination using classical pulsars above. These limits are the most competitive among the axion UL m_a values derived from nucleon coupling as listed in PDG 2020 [114] (pp 1093, Table; "Invisible A^0 (Axion) Limits from Nucleon Coupling").

9.2.3 Future Work

These axion constraints can be refined in future work using magnetar UL observations in the soft-gamma-ray regime, using the *Fermi*-Gamma Ray Burst monitor with an Earth Occultation Technique, and/or *Integral* SPI observations, combined with an energy resolved

Magnetar	Surface B Field 10^{14} G	Age kyr	Distance kpc
SGR 1806-20	19.6	0.2	8.7 [59]
1E 1547.0-5408	3.18	0.7	4.5 [256]
SGR 1900+14	7	0.9	12.5 [88]
CXOU J171405.7-381031	5.01	0.9	13.2 [255]
SGR 1627-41	2.25	2.2	11.0 [83]
PSR J1622-4950	2.74	4.0	9.0 [176]
SGR J1745-2900	2.31	4.3	8.3 [61]
Swift J1834.9-0846	1.42	4.9	4.2 [172]
XTE J1810-197	2.1	11.3	3.5 [198]
SGR 0501+4516	1.87	15.4	2.0 [180]

Table 9.1 Magnetar candidates for proposed future observations Distances are from the references shown, surface B field and age are from the online version of the McGill magnetar catalog [212].

analysis of the axion-to-gamma ray emission spectrum. These new observations can be performed not only on the 6 magnetars used in this study, but on a further 10 more recently characterised magnetars, (Table 9.1), of comparable ages and distances which have no published spectra to-date between 300 keV and 1 MeV.

9.3 Conclusion

In this work, I have presented the most complete gamma-ray study to-date of three-quarters of the entire Galactic globular cluster (GC) population to probe their sources of gamma-ray emission. I have shown that millisecond pulsars (MSPs) remain a plausible source of GC emission through broad correlations such as GC gamma-ray luminosity and the mass encounter rate product (MERP), as expected due to increased GC MSP formation (Fig. 9.3).

However the lack of luminosity correlation with other characteristics presumed to encourage MSP formation, e.g. metallicity, calls the MSP GC gamma-ray source connection into question. I have also produced the most complete best fitted composite spectrum of all known gamma-ray emitting MSPs (Fig. 9.4), as an analogue of the ensemble MSP emission in GCs, and shown that this spectral MSP model whilst a good match for many GCs cannot account for all components of emission in all GCs.

My high-quality spectra have allowed me to make colour comparisons between the MSP spectrum and a population of 34 gamma-ray detected GCs, showing that any spectral differences do not arise systematically from characteristics relevant to MSP formation (e.g

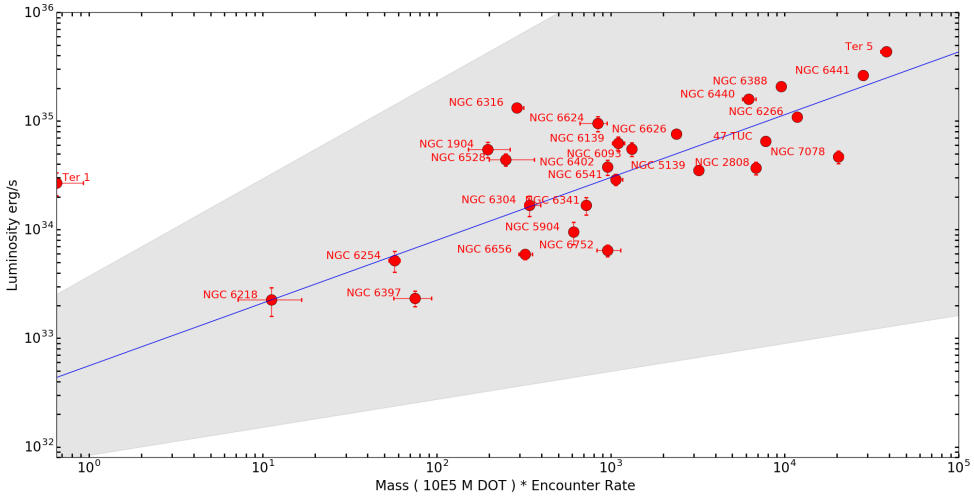

Fig. 9.3 Gamma-ray luminosity is correlated with MERP (the product of cluster mass in units of 10^5 $M_\odot$ and a normalised encounter rate from [41]) for GCs detected in this study).

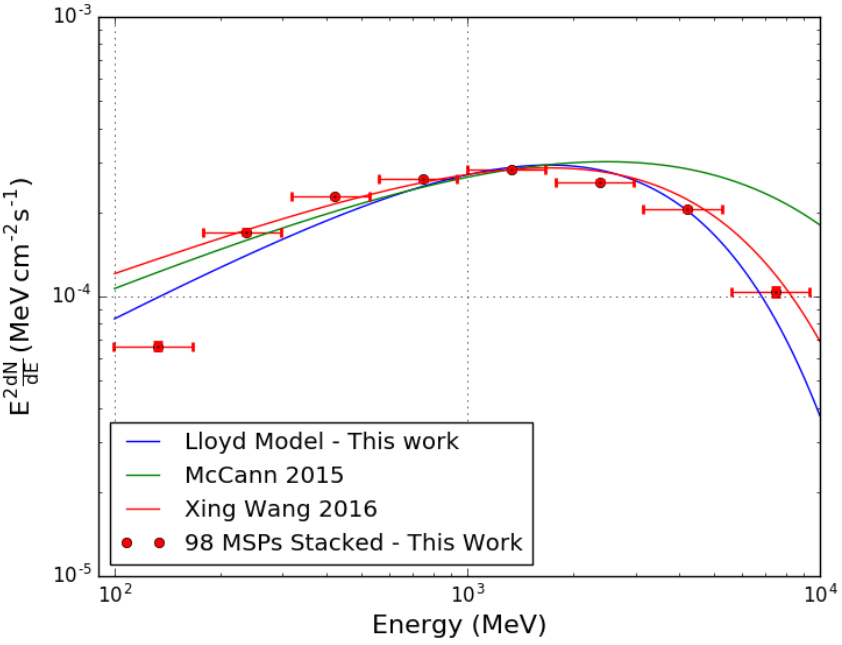

Fig. 9.4 My MSP model (Lloyd), along with literature McCann and Xing and Wang MSP models compared to the summed flux of 98 MSPs by normalising model flux to that of the summed flux at 1.3 GeV. The Lloyd model is the preferred model.

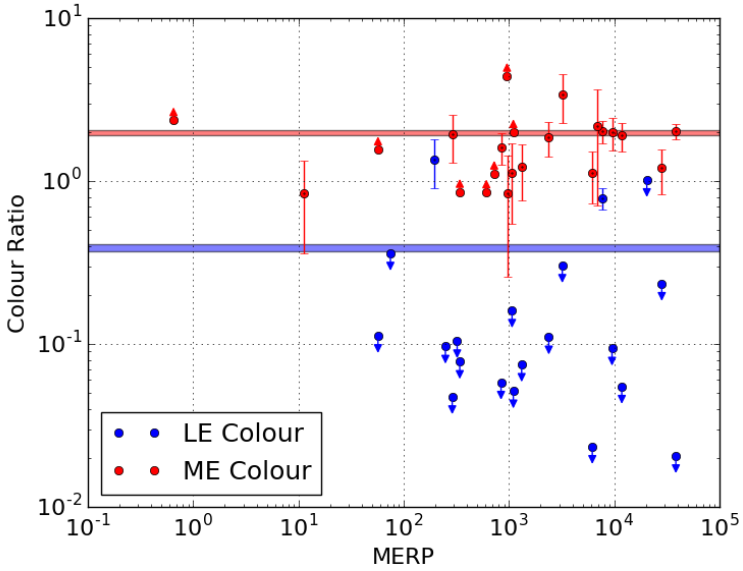

Fig. 9.5 The low energy (LE, 133/237 MeV, blue points) and medium energy (ME, 4216/7498 MeV, red points) colour bands of detected GCs and their offset from the stacked MSP model (red and blue bands) are uncorrelated with MERP.

MERP colour plot, Fig. 9.5), which again makes the case for other sources of emission in GCs.

I have also demonstrated a connection between GC gamma-ray and unresolved diffuse X-ray emission which suggests either the presence of a relativistic electron population from GC MSPs or other unresolved sources such as cataclysmic variables. It is also possible in some cases that dark matter annihilating around a central GC intermediate black hole (IMBH) could be a source of emission, although the evidence for IMBHs in GCs is not strong. Finally, I considered how the upper-limit emission of gamma-ray dark pulsars and magnetars, acting as sources of a cold dark matter particle, the axion, could be used to set competitive constraints on axion mass provided that correct core temperatures were used.

Going forward, GCs and their sources of gamma-ray emission will remain a very exciting source of study as more instruments become available allowing a co-ordinated multi-messenger approach. Recently commissioned instruments such as the radio telescope arrays, LOFAR and MeerKAT, will have the potential to detect and time many more MSPs in GCs, permitting us to relate a directly detected MSP source population to GC gamma-ray emission (as I have done in the case of the GC 47 Tuc in this work). In the gamma-ray regime CTA will shortly allow GCs to be observed at very high energies (VHE) above 50 GeV to a few TeV with an order of magnitude increase in sensitivity over existing instruments. My simulations suggest that GCs possessing hard spectra up to 100 GeV will certainly be detected by CTA in

just 50 h of observations and we should then be able to settle the question of VHE emission mechanisms in GCs, such as, but not limited to, shock fronts from MSP winds or more speculatively TeV emission halos from MSPs. Finally, *Fermi*-LAT should continue to operate into the foreseeable future, leading to increasingly refined GC spectra and possible new GC detections. The totality of these observation will allow us, in time, to put the sources of GC gamma-ray emission beyond reasonable doubt.

Appendix A

Globular Cluster Analysis

GC Name	Helio Distance (kpc)	ra (Deg.)	dec (Deg.)	l (Deg.)	b (Deg.)	Metallicity [Fe / H]	Mass x 10^5 $M_\odot$	Mass Ref
NGC 6121	2.2	245.90	-26.53	350.97	15.97	-1.16	0.97 ± 0.03	[48]
NGC 6397	2.3	265.18	-53.67	338.17	-11.96	-2.02	0.89 ± 0.02	[48]
NGC 6544	3.0	271.84	-25.00	5.84	-2.20	-1.4	0.63 ± 0.31	[48]
NGC 6656	3.2	279.10	-23.90	9.89	-7.55	-1.7	4.16 ± 0.05	[48]
NGC 6366	3.5	261.93	-5.08	18.41	16.04	-0.59	0.47 ± 0.06	[48]
2MS-GC01	3.6	272.09	-19.83	10.47	0.10	–	0.43	[132]
NGC 6752	4.0	287.72	-59.98	336.49	-25.63	-1.54	2.39 ± 0.04	[48]
NGC 6838	4.0	298.44	18.78	56.75	-4.56	-0.78	0.49 ± 0.05	[48]
GLIMPSE01	4.2	282.21	-1.50	31.30	-0.10	–	0.80 ± 0.30	[89]
NGC 6254	4.4	254.29	-4.10	15.14	23.08	-1.56	1.84 ± 0.04	[48]
NGC 104	4.5	6.02	-72.08	305.89	-44.89	-0.72	7.79 ± 0.05	[48]
NGC 6218	4.8	251.81	-1.95	15.72	26.31	-1.37	0.87 ± 0.06	[48]
Terzan 12	4.8	273.07	-22.74	8.36	-2.10	-0.5	0.28	[132]
NGC 3201	4.9	154.40	-46.41	277.23	8.64	-1.59	1.49 ± 0.09	[48]
2MS-GC02	4.9	272.40	-20.78	9.78	-0.62	-1.08	0.26	[132]
NGC 5139	5.2	201.70	-47.48	309.10	14.97	-1.53	35.50 ± 0.30	[48]
NGC 6540	5.3	271.54	-27.77	3.29	-3.31	-1.35	0.41	[132]
IC 1276	5.4	272.68	-7.21	21.83	5.67	-0.75	0.55 ± 0.26	[48]
NGC 6809	5.4	295.00	-30.96	8.79	-23.27	-1.94	1.88 ± 0.12	[48]
GLIMPSE02	5.5	274.63	-16.98	14.13	-0.65	-0.33	–	
NGC 6626	5.5	276.14	-24.87	7.80	-5.58	-1.32	3.69 ± 0.38	[48]

continued . . .

... continued

GC Name	Helio Distance (kpc)	ra (Deg.)	dec (Deg.)	l (Deg.)	b (Deg.)	Metallicity [Fe / H]	Mass x 10^5 $M_\odot$	Mass Ref
NGC 6352	5.6	261.37	-48.42	341.42	-7.17	-0.64	0.94 ± 0.35	[48]
NGC 4372	5.8	186.44	-72.66	300.99	-9.88	-2.17	2.49 ± 0.25	[48]
Pal 6	5.8	265.93	-26.22	2.09	1.78	-0.91	1.00	[132]
Terzan 10	5.8	270.90	-26.07	4.49	-1.99	-1	2.50	[132]
NGC 6304	5.9	258.63	-29.46	355.83	5.38	-0.45	2.77 ± 0.29	[48]
Pal 10	5.9	289.51	18.57	52.44	2.72	-0.1	0.50	[132]
NGC 6553	6.0	272.32	-25.91	5.25	-3.03	-0.18	2.35 ± 0.19	[48]
Djorg 2	6.3	270.45	-27.83	2.76	-2.51	-0.65	1.50	[132]
NGC 6171	6.4	248.13	-13.05	3.37	23.01	-1.02	0.87 ± 0.07	[48]
BH 261	6.5	273.53	-28.64	3.36	-5.27	-1.3	0.30	[132]
NGC 4833	6.6	194.89	-70.88	303.60	-8.02	-1.85	2.47 ± 0.32	[48]
Terzan 1	6.7	263.95	-30.47	357.57	1.00	-1.03	2.70	[132]
NGC 6266	6.8	255.30	-30.11	353.57	7.32	-1.18	7.07 ± 0.05	[48]
Terzan 6	6.8	267.69	-31.28	358.57	-2.16	-0.56	1.17 ± 0.44	[48]
NGC 6535	6.8	270.96	-0.30	27.18	10.44	-1.79	0.20 ± 0.06	[48]
Terzan 5	6.9	267.02	-24.78	3.84	1.69	-0.23	5.66 ± 0.71	[48]
NGC 6712	6.9	283.27	-8.71	25.35	-4.32	-1.02	1.27 ± 0.13	[48]
NGC 6205	7.1	250.42	36.46	59.01	40.91	-1.53	4.53 ± 0.34	[48]
Terzan 9	7.1	270.41	-26.84	3.60	-1.99	-1.05	0.46	[132]
NGC 6717	7.1	283.78	-22.70	12.88	-10.90	-1.26	0.18	[132]
Terzan 4	7.2	262.66	-31.60	356.02	1.31	-1.41	0.80	[132]
NGC 6558	7.4	272.57	-31.76	0.20	-6.02	-1.32	0.29 ± 0.11	[48]
NGC 6760	7.4	287.80	1.03	36.11	-3.92	-0.4	2.54 ± 1.08	[48]
NGC 5904	7.5	229.64	2.08	3.86	46.80	-1.29	3.72 ± 0.06	[48]
Terzan 2	7.5	261.89	-30.80	356.32	2.30	-0.69	0.40	[132]
NGC 6541	7.5	272.01	-43.71	349.29	-11.19	-1.81	2.77 ± 0.09	[48]
NGC 6362	7.6	262.98	-67.05	325.55	-17.57	-0.99	1.16	[132]
NGC 5927	7.7	232.00	-50.67	326.60	4.86	-0.49	3.54 ± 0.03	[48]
NGC 6522	7.7	270.89	-30.03	1.02	-3.93	-1.34	3.92 ± 0.54	[48]
NGC 6325	7.8	259.50	-23.77	0.97	8.00	-1.25	0.77	[132]
UKS 1	7.8	268.61	-24.15	5.13	0.76	-0.64	0.80	[132]

continued ...

. . . continued

GC Name	Helio Distance (kpc)	ra (Deg.)	dec (Deg.)	l (Deg.)	b (Deg.)	Metallicity [Fe / H]	Mass x 10^5 $M_\odot$	Mass Ref
NGC 6539	7.8	271.21	-7.59	20.79	6.78	-0.63	2.50 ± 0.35	[48]
NGC 6333	7.9	259.80	-18.52	5.54	10.71	-1.77	3.20	[132]
NGC 6528	7.9	271.21	-30.06	1.14	-4.17	-0.11	0.90 ± 0.19	[48]
NGC 6624	7.9	275.92	-30.36	2.79	-7.91	-0.44	0.73 ± 0.02	[48]
NGC 6749	7.9	286.31	1.90	36.20	-2.20	-1.6	0.57 ± 0.36	[48]
Lynga 7	8.0	242.77	-55.32	328.77	-2.80	-1.01	1.00	[132]
E 3	8.1	140.24	-77.28	292.27	-19.02	-0.83	0.31 ± 0.17	[48]
NGC 6642	8.1	277.98	-23.48	9.81	-6.44	-1.26	0.87 ± 0.55	[48]
NGC 7099	8.1	325.09	-23.18	27.18	-46.84	-2.27	1.33 ± 0.08	[48]
Terzan 3	8.2	247.17	-35.35	345.08	9.19	-0.74	0.55 ± 0.23	[48]
HP 1	8.2	262.77	-29.98	357.43	2.12	-1	1.11 ± 0.38	[48]
Liller 1	8.2	263.35	-33.39	354.84	-0.16	-0.33	6.66 ± 1.17	[48]
Ton 2	8.2	264.04	-38.55	350.80	-3.42	-0.7	0.80 ± 0.40	[48]
1636-283	8.3	249.86	-28.40	351.91	12.10	-1.5	–	
NGC 6341	8.3	259.28	43.14	68.34	34.86	-2.31	2.68 ± 0.03	[48]
NGC 6342	8.5	260.29	-19.59	4.90	9.73	-0.55	0.46 ± 0.16	[48]
NGC 6440	8.5	267.22	-20.36	7.73	3.80	-0.36	4.42 ± 0.64	[48]
NGC 362	8.6	15.81	-70.85	301.53	-46.25	-1.26	3.45 ± 0.05	[48]
NGC 6723	8.7	284.89	-36.63	0.07	-17.30	-1.1	1.57 ± 0.13	[48]
NGC 6273	8.8	255.66	-26.27	356.87	9.38	-1.74	6.80 ± 0.59	[48]
NGC 6637	8.8	277.85	-32.35	1.72	-10.27	-0.64	1.60	[132]
NGC 288	8.9	13.19	-26.58	151.28	-89.38	-1.32	1.16 ± 0.03	[48]
NGC 6144	8.9	246.81	-26.02	351.93	15.70	-1.76	0.46 ± 0.27	[48]
NGC 6681	9.0	280.80	-32.29	2.85	-12.51	-1.62	1.13 ± 0.02	[48]
NGC 6355	9.2	260.99	-26.35	359.58	5.43	-1.37	1.53 ± 0.77	[48]
NGC 6402	9.3	264.40	-3.25	21.32	14.80	-1.28	7.74 ± 0.61	[48]
NGC 6287	9.4	256.29	-22.71	0.13	11.02	-2.1	1.30	[132]
NGC 6638	9.4	277.73	-25.50	7.90	-7.15	-0.95	1.90	[132]
NGC 6779	9.4	289.15	30.18	62.66	8.34	-1.98	2.81 ± 0.52	[48]
NGC 6293	9.5	257.54	-26.58	357.62	7.83	-1.99	1.88 ± 0.18	[48]
NGC 2808	9.6	138.01	-64.86	282.19	-11.25	-1.14	7.42 ± 0.05	[48]

continued . . .

... continued

GC Name	Helio Distance (kpc)	ra (Deg.)	dec (Deg.)	l (Deg.)	b (Deg.)	Metallicity [Fe / H]	Mass x 10^5 $M_\odot$	Mass Ref
FSR 1735	9.8	253.04	-47.06	339.19	-1.85	–	0.93	[132]
NGC 6388	9.9	264.07	-44.74	345.56	-6.74	-0.55	10.60 ± 0.10	[48]
NGC 6093	10.0	244.26	-22.98	352.67	19.46	-1.75	2.49 ± 0.12	[48]
NGC 6652	10.0	278.94	-32.99	1.53	-11.38	-0.81	0.52	[132]
NGC 6139	10.1	246.92	-38.85	342.37	6.94	-1.65	3.59 ± 0.73	[48]
NGC 5272	10.2	205.55	28.38	42.22	78.71	-1.5	3.94 ± 0.23	[48]
NGC 4590	10.3	189.87	-26.74	299.63	36.05	-2.23	1.23 ± 0.12	[48]
NGC 6256	10.3	254.89	-37.12	347.79	3.31	-1.02	0.72 ± 0.33	[48]
NGC 5986	10.4	236.51	-37.79	337.02	13.27	-1.59	3.01 ± 0.31	[48]
NGC 6316	10.4	259.16	-28.14	357.18	5.76	-0.45	3.75 ± 0.69	[48]
NGC 7078	10.4	322.49	12.17	65.01	-27.31	-2.37	4.53 ± 0.05	[48]
NGC 5946	10.6	233.87	-50.66	327.58	4.19	-1.29	1.40	[132]
NGC 6401	10.6	264.65	-23.91	3.45	3.98	-1.02	3.00	[132]
NGC 6517	10.6	270.46	-8.96	19.23	6.76	-1.23	3.00	[132]
NGC 2298	10.8	102.25	-36.01	245.63	-16.01	-1.92	0.12 ± 0.07	[48]
NGC 6380	10.9	263.62	-39.07	350.18	-3.42	-0.75	2.00	[132]
NGC 6569	10.9	273.41	-31.83	0.48	-6.68	-0.76	3.02 ± 0.36	[48]
Pal 1	11.1	53.33	79.58	130.06	19.03	-0.65	0.02	[132]
NGC 6496	11.3	269.77	-44.27	348.03	-10.01	-0.46	1.06 ± 0.16	[48]
NGC 6235	11.5	253.36	-22.18	358.92	13.52	-1.28	1.00	[132]
NGC 7089	11.5	323.36	-0.82	53.37	-35.77	-1.65	5.82 ± 0.12	[48]
NGC 6441	11.6	267.55	-37.05	353.53	-5.01	-0.46	12.30 ± 0.10	[48]
NGC 6453	11.6	267.72	-34.60	355.72	-3.87	-1.5	2.30	[132]
NGC 5286	11.7	206.61	-51.37	311.61	10.57	-1.69	4.01 ± 0.19	[48]
NGC 1851	12.1	78.53	-40.05	244.51	-35.04	-1.18	3.02 ± 0.04	[48]
NGC 5897	12.5	229.35	-21.01	342.95	30.29	-1.9	2.03 ± 0.21	[48]
Pal 8	12.8	280.37	-19.83	14.10	-6.80	-0.37	0.60	[132]
NGC 1904	12.9	81.05	-24.52	227.23	-29.35	-1.6	1.69 ± 0.11	[48]

continued ...

. . . continued

GC Name	Helio Distance (kpc)	ra (Deg.)	dec (Deg.)	l (Deg.)	b (Deg.)	Metallicity [Fe / H]	Mass x 10^5 $M_\odot$	Mass Ref

Table A.1 Selection of 111 GCs ordered by increasing distance from the Sun with name, helio distance (distance from Sun) in kpc, ra and dec are right ascension and declination in degrees, l and b are Galactic longitude and latitude respectively in degrees, metallicity defined as [Fe/H]. GC masses and their errors where known are from the references listed. A "−" value for metallicity or mass indicates that no value could be found in the literature.

Globular Cluster	Energy flux UL (10^{-13} erg cm^{-2} s^{-1})	Photon flux UL (10^{-10} cm^{-2} s^{-1})
E3	6.54	8.78
NGC 4372	1564.27	2099.27
NGC 4833	4.58	6.14
NGC 362	17.96	25.29
NGC 6362	2.78	3.73
Lynga 7	10.54	14.15
NGC 5927	3049.76	5466.27
NGC 6352	11.08	14.87
FSR 1735	8.78	11.78
NGC 3201	8.97	12.04
Ton 2	25.82	34.65
NGC 5986	1.89	2.53
NGC 6256	9.66	12.97
Terzan 3	6.9	9.27
Liller 1	72.46	97.24
NGC 6637	23.83	31.97
NGC 6681	22.95	30.79
NGC 6558	54.45	73.07
Terzan 4	9.52	12.78
Terzan 6	51.93	69.69
NGC 6809	6.72	9.02
NGC 6522	15.11	20.28
HP 1	54.62	73.30

continued . . .

. . . continued

Globular Cluster	Energy flux UL (10^{-13} erg cm^{-2} s^{-1})	Photon flux UL (10^{-10} cm^{-2} s^{-1})
BH 261	4484.8	6018.66
1636-283	2807.55	4453.49
Djorg 2	32.16	43.15
NGC 6540	206.09	276.58
Terzan 9	14.79	19.85
NGC 4590	4.27	5.73
NGC 288	4.75	6.38
NGC 6293	35.07	47.06
NGC 6121	2562.14	3296.79
NGC 6355	6436.39	8637.71
NGC 6273	5.88	7.89
Pal 6	33.38	44.79
Terzan 10	2.99	4.01
NGC 6144	4.95	6.64
NGC 6553	6.85	9.20
NGC 6638	20.58	27.61
NGC 6544	12.83	17.22
UKS 1	46.23	62.04
NGC 6325	4443.48	5963.21
NGC 6642	8.54	11.46
NGC 7099	12.89	17.29
Terzan 12	2.81	3.77
NGC 6287	17.54	23.54
2MS-GC02	23751.64	32047.42
NGC 6342	25.4	34.09
NGC 6333	1.94	2.61
NGC 6171	2230.39	3614.74
NGC 6712	27.23	36.54
NGC 6539	22.97	30.83
IC 1276	7809.52	12983.21
NGC 6366	7.47	10.03
NGC 6535	4047.9	6750.22

continued . . .

. . . continued

Globular Cluster	Energy flux UL (10^{-13} erg cm^{-2} s^{-1})	Photon flux UL (10^{-10} cm^{-2} s^{-1})
NGC 6760	14.5	19.45
NGC 6749	0.14	0.19
Pal 10	0.08	0.11
NGC 5272	6.17	8.29
NGC 6779	8.05	10.80
NGC 6205	8.01	10.75
NGC 6441	4858.93	8231.95
NGC 5946	10.81	14.51
NGC 6401	29.21	39.20
NGC 6517	39.65	53.21
NGC 2298	20.32	27.27
NGC 6380	39	52.33
NGC 6569	7.62	10.23
Pal 1	1.8	2.42
NGC 6496	3.31	4.44
NGC 6235	13.77	18.47
NGC 7089	3.76	5.05
NGC 6453	40.46	54.29
NGC 5286	1543.36	2676.35
NGC 1851	23.72	48.95
NGC 5897	5.19	6.96
Pal 8	4.71	6.31

Table A.2 The flux upper limits of undetected GCs at 95 percent confidence. The GCs are modelled as PL point sources with spectral *index* 2.0 placed at the nominal GC co-ordinates

Globular Cluster	4FGL Source ID
2MS-GC01	4FGL J1808.8-1949
GLIMPSE01	4FGL J1848.7-0129
GLIMPSE02	4FGL J1818.5-1656
NGC 104 (47 Tuc)	4FGL J0024.0-7204
NGC 1904	4FGL J0524.4-2413
NGC 2808	4FGL J0912.1-6449
NGC 5139 (Omega Cen)	4FGL J1326.6-4729
NGC 5904	4FGL J1518.8+0203
NGC 6093 (M 80)	4FGL J1616.9-2257
NGC 6139	4FGL J1627.6-3852
NGC 6218	4FGL J1647.2-0154
NGC 6266 (M 62)	4FGL J1701.2-3006
NGC 6304	4FGL J1714.2-2928
NGC 6316	4FGL J1716.7-2808
NGC 6341	4FGL J1716.8+4310
NGC 6388	4FGL J1736.2-4443
NGC 6397	4FGL J1741.1-5341
NGC 6402	4FGL J1737.5-0313
NGC 6440	4FGL J1748.9-2021
NGC 6441	4FGL J1750.3-3702
NGC 6528	4FGL J1804.9-3001
NGC 6541	4FGL J1807.8-4340
NGC 6652	4FGL J1835.7-3258
NGC 6717	4FGL J1855.1-2243
NGC 6752	4FGL J1910.8-6001
NGC 6838	4FGL J1953.6+1846
NGC 7078	4FGL J2129.9+1208
Terzan 1	4FGL J1735.7-3026
Terzan 2	4FGL J1727.6-3050
Terzan 5	4FGL J1748.0-2446

Table A.3 The 30 sources of the 4FGL which are marked as associated with globular clusters by virtue of having a source type attribute of "glc" in the catalog. The names, alternative names in brackets and the 4FGL source ID are listed in name order.

GC	Core Radius (arcminutes)	Central Luminosity Density ($L_{\odot}pc^{-3}\times10^{3}$)	Binary Encounter Rate Λ ($L_{\odot}^{0.5}pc^{-1.5}$ arcminutes$^{-1}\times10^{3}$)
47 Tuc	0.36	75.86	0.77
NGC 2808	0.25	45.71	0.86
NGC 6752	0.17	109.65	1.95
NGC 6397	0.05	575.44	15.17
NGC 5139	2.37	1.41	0.02
NGC 6388	0.12	234.42	4.03
NGC 6541	0.18	44.67	1.17
NGC 6139	0.15	46.77	1.44
NGC 6441	0.13	181.97	3.28
NGC 6652	0.1	30.20	1.74
Terzan 2	0.03	72.44	8.97
Terzan 1	0.04	7.08	2.10
NGC 6624	0.06	199.53	7.44
NGC 6266	0.22	144.54	1.73
NGC 6528	0.13	58.88	1.87
NGC 6304	0.21	30.90	0.84
NGC 6316	0.17	16.98	0.77
NGC 6626	0.24	72.44	1.12
Terzan 5	0.16	138.04	2.32
NGC 1904	0.16	12.02	0.69
NGC 6656	1.33	4.27	0.05
NGC 6093	0.15	61.66	1.66
NGC 6717	0.08	38.02	2.44
NGC 6440	0.14	173.78	2.98
NGC 6254	0.77	3.47	0.08
NGC 6402	0.79	2.29	0.06
NGC 6218	0.79	1.70	0.05
NGC 5904	0.44	7.59	0.20
NGC 7078	0.14	112.20	2.39
NGC 6838	0.63	0.68	0.04
NGC 6341	0.26	19.95	0.54

Table A.4 Binary encounter rate, Λ, for detected GCs calculated as [264]. Core radius and luminosity density are from the Harris Catalogue (2010). GLIMPSE01 and 2MS-GC01 are excluded as they have no central luminosity density in the catalogue.

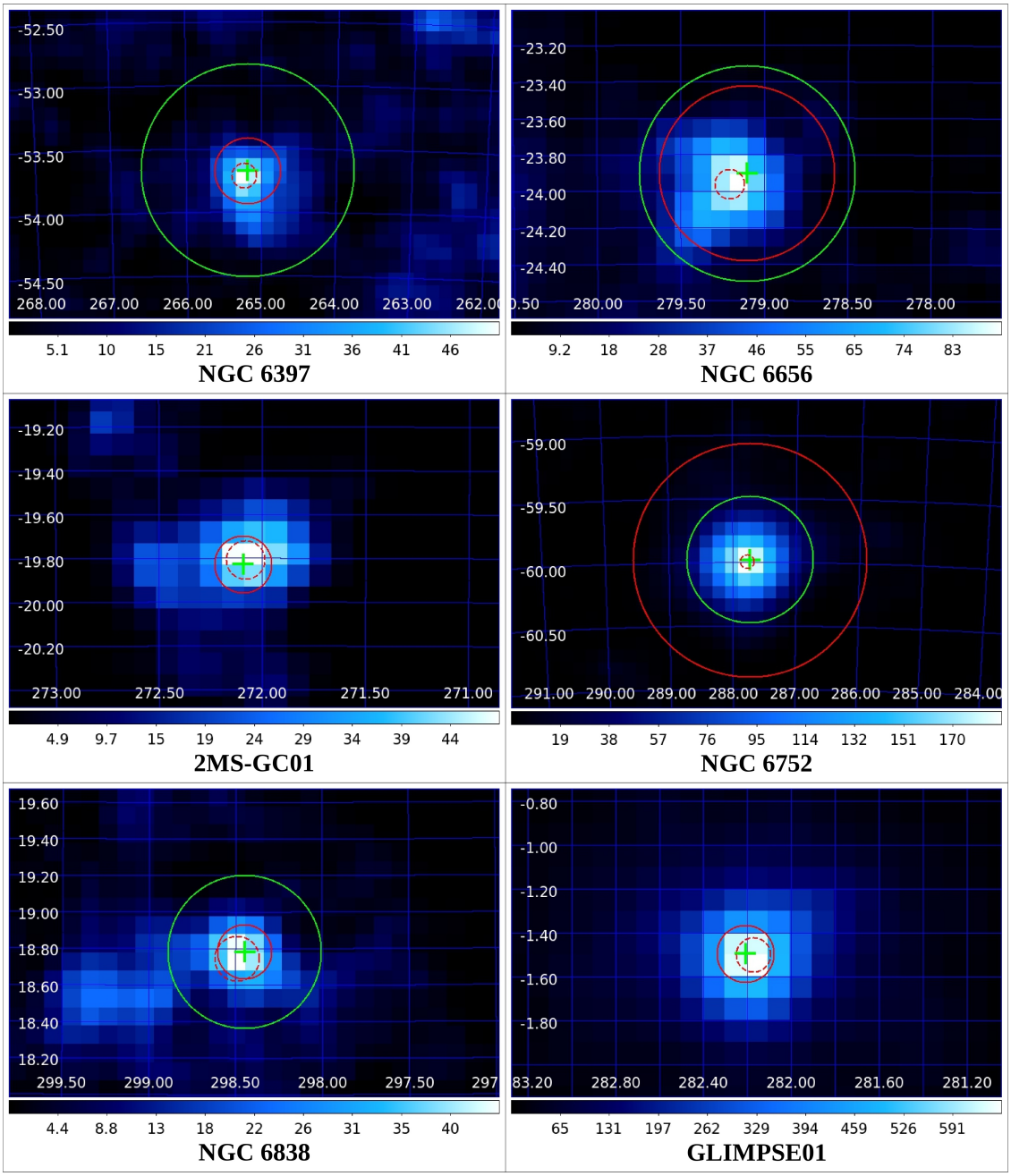

Fig. A.1 TS maps for GCs NGC 6397, NGC 6656, 2MS-GC01, NGC 6752, NGC 6838 and GLIMPSE01 with tidal radii marked as red circle from Harris 2003 (http://www.naic.edu/ pulsar/catalogs/mwgc.txt) and green circle for NGC 6397, 6656 and 6752 from [92] and NGC 6838 [200]. 2MS-GC01 and GLIMPSE01 only have Harris 2003 Tidal Radius) and gamma-ray detection localisation 95 percent containment (red dashed circle) marked. The GC catalogue co-ordinates are indicated with a green cross. Graduated color bar (bottom of each plot) shows the TS value. RA and DEC are horizontal and vertical axes respectively on the white interior scale. Spatial bin size is 0.1°.

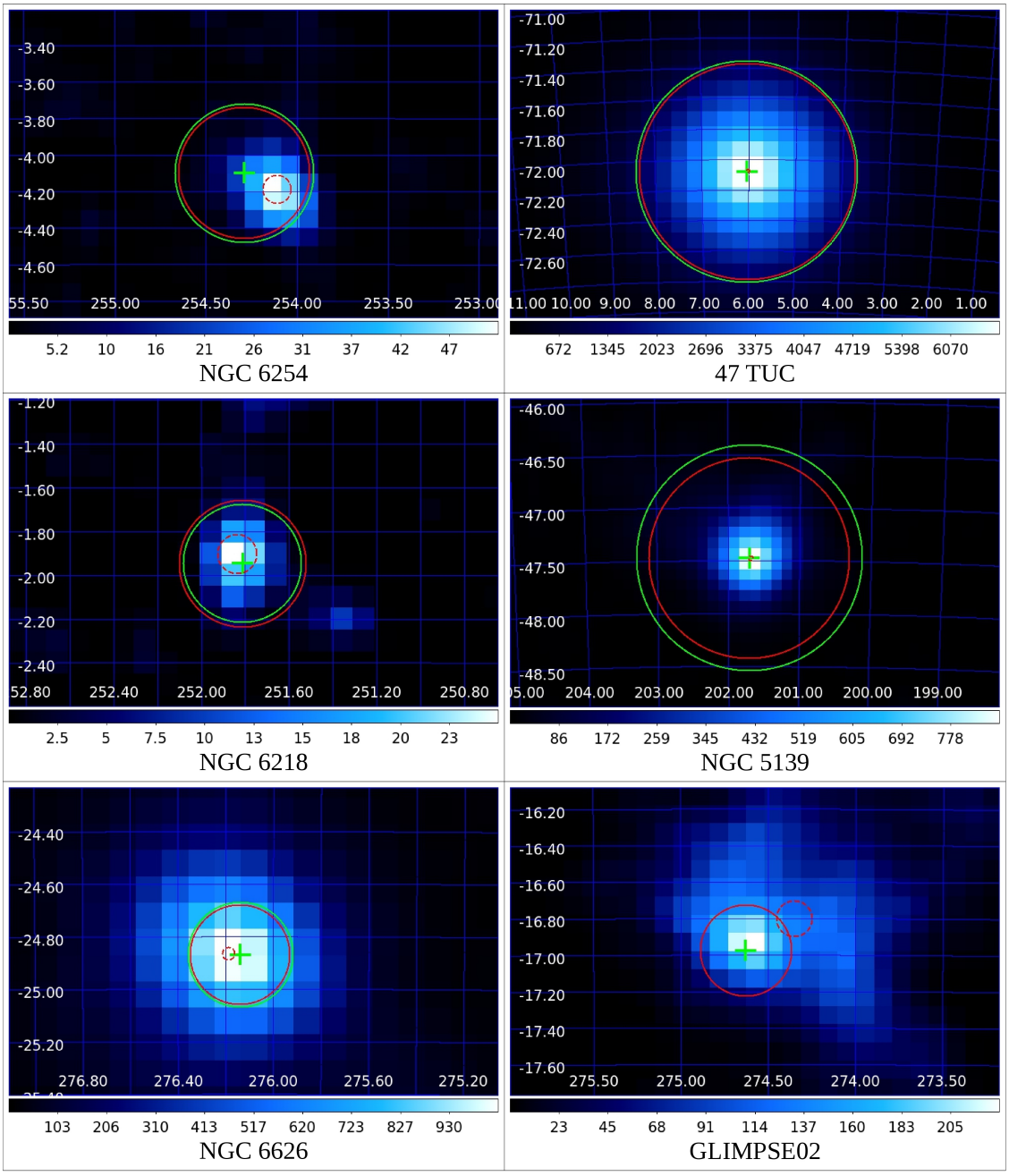

Fig. A.2 TS maps for GCs NGC 6254, 47 Tuc, NGC 6218, NGC 5139, NGC 6626 and GLIMPSE02 with tidal radii (red circle Harris 2003, green circle more recent determination of [92] for all GC except GLIMPSE02) and gamma-ray detection localisation 95 percent containment (red dashed circle) marked. This is almost too small to display for 47 Tuc and NGC 5139. The GC catalogue co-ordinates are indicated with a green cross. Graduated color bar (bottom of each plot) shows the TS value. RA and DEC are horizontal and vertical axes respectively on the white interior scale. Spatial bin size is 0.1°.

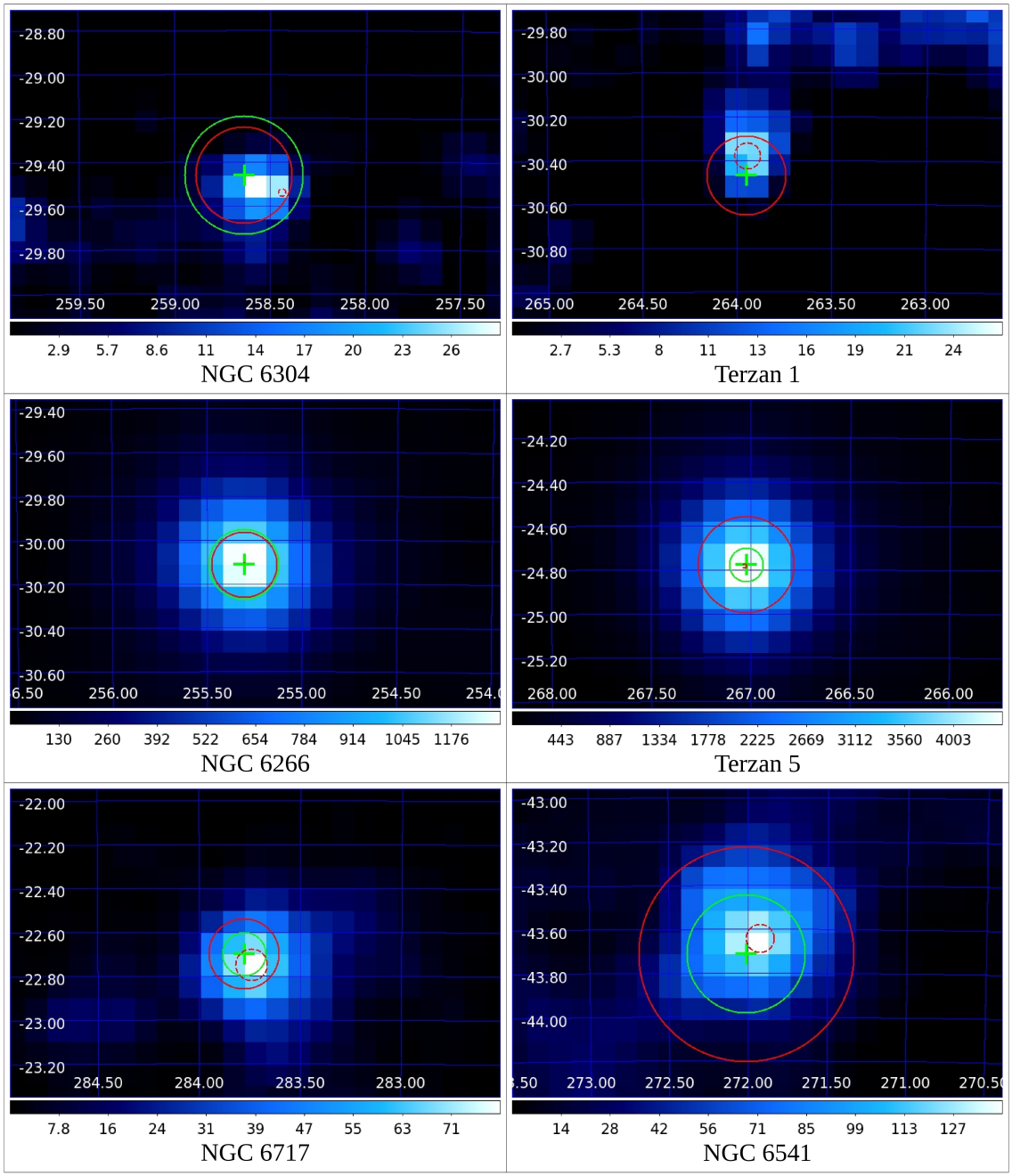

Fig. A.3 TS maps for GCs NGC 6304, Terzan 1, NGC 6266, Terzan 5, NGC 6717 and NGC 6541 with tidal radii (red circle Harris 2003), green circle more recent determination of [92] for NGC 6266, 6717 and 6541 and NGC 6304 [200] whilst Terzan 5 is [169].) and gamma-ray detection localisation 95 percent containment (red dashed circle) marked. The GC catalogue co-ordinates are indicated with a green cross. Graduated color bar (bottom of each plot) shows the TS value. RA and DEC are horizontal and vertical axes respectively on the white interior scale. Spatial bin size is 0.1°.

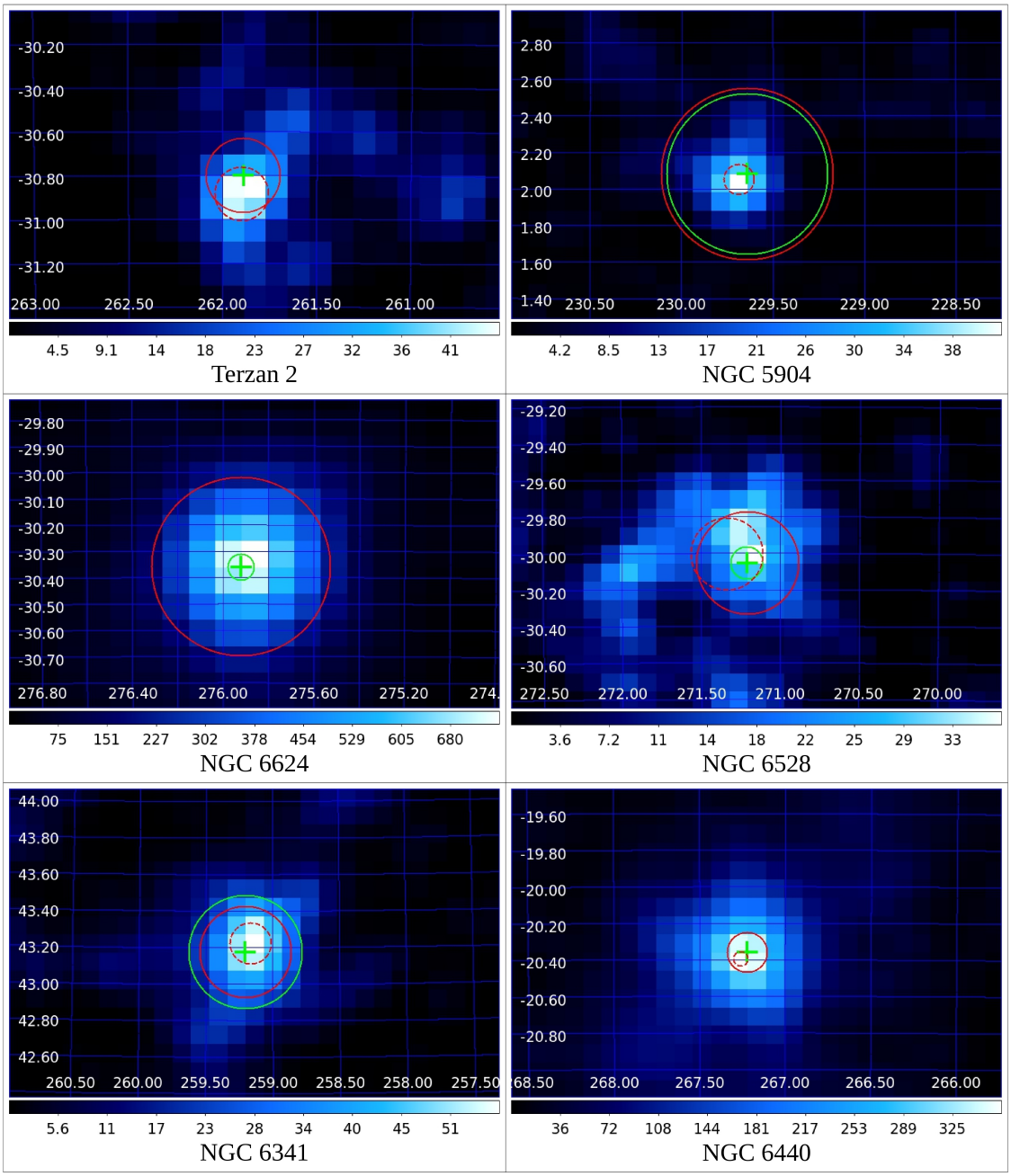

Fig. A.4 TS maps for GCs Terzan 2, NGC 5904, NGC 6624, NGC 6528, NGC 6341 and NGC 6440 with tidal radii (red circle Harris 2003, green circle more recent determination of [92] for NGC 5904, 6624 and 6341, whilst NGC 6528 is from [200]) and gamma-ray detection localisation 95 percent containment (red dashed circle) marked. The GC catalogue co-ordinates are indicated with a green cross. Graduated color bar (bottom of each plot) shows the TS value. RA and DEC are horizontal and vertical axes respectively on the white interior scale. Spatial bin size is 0.1°.

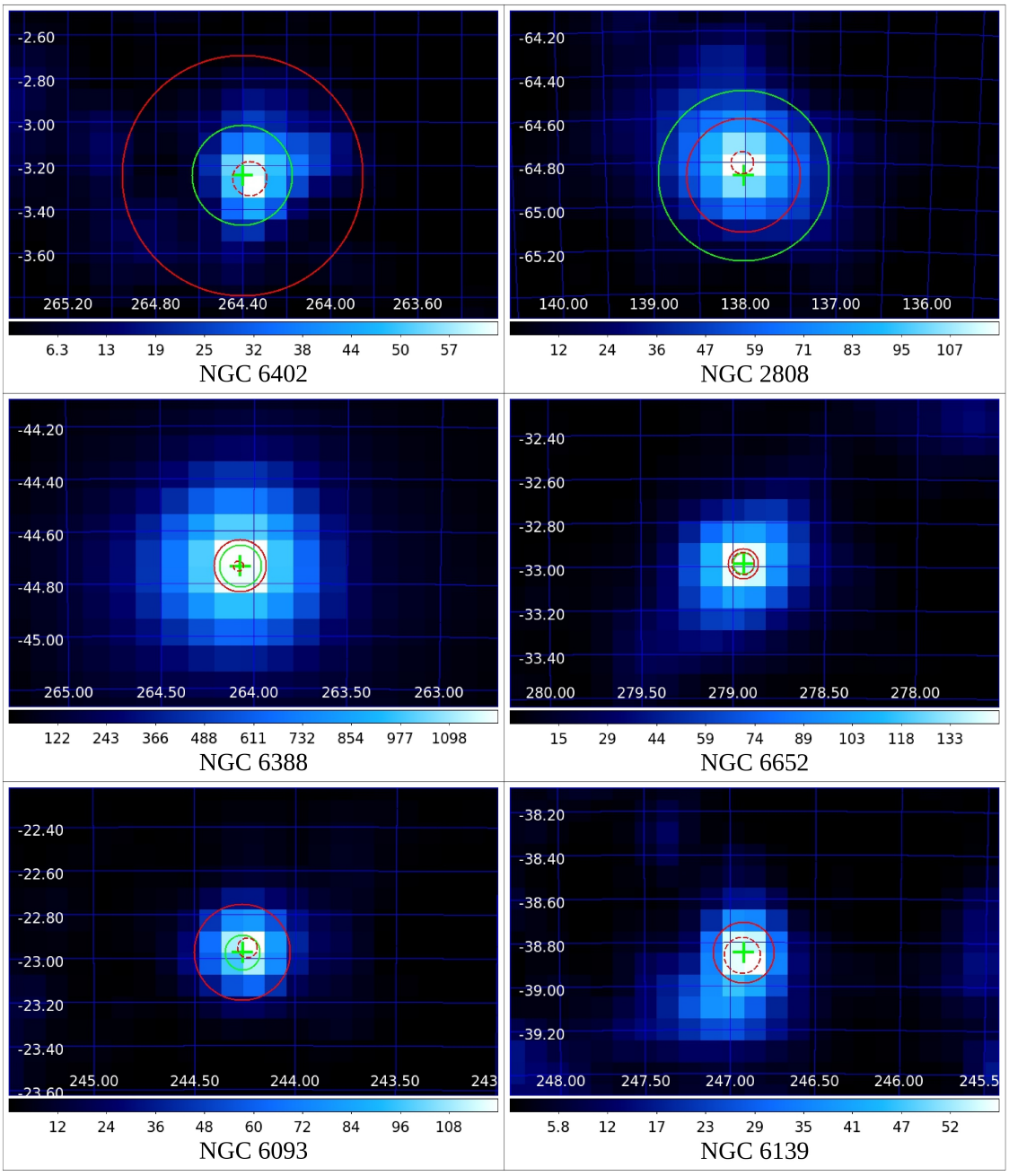

Fig. A.5 TS maps for GCs NGC 6402, NGC 2808, NGC 6388, NGC 6652, NGC 6093 and NGC 6139 with tidal radii (red circle Harris 2003, green circle more recent determination of [92]) and gamma-ray detection localisation 95 percent containment (red dashed circle) marked. The GC catalogue co-ordinates are indicated with a green cross. Graduated color bar (bottom of each plot) shows the TS value. RA and DEC are horizontal and vertical axes respectively on the white interior scale. Spatial bin size is 0.1°.

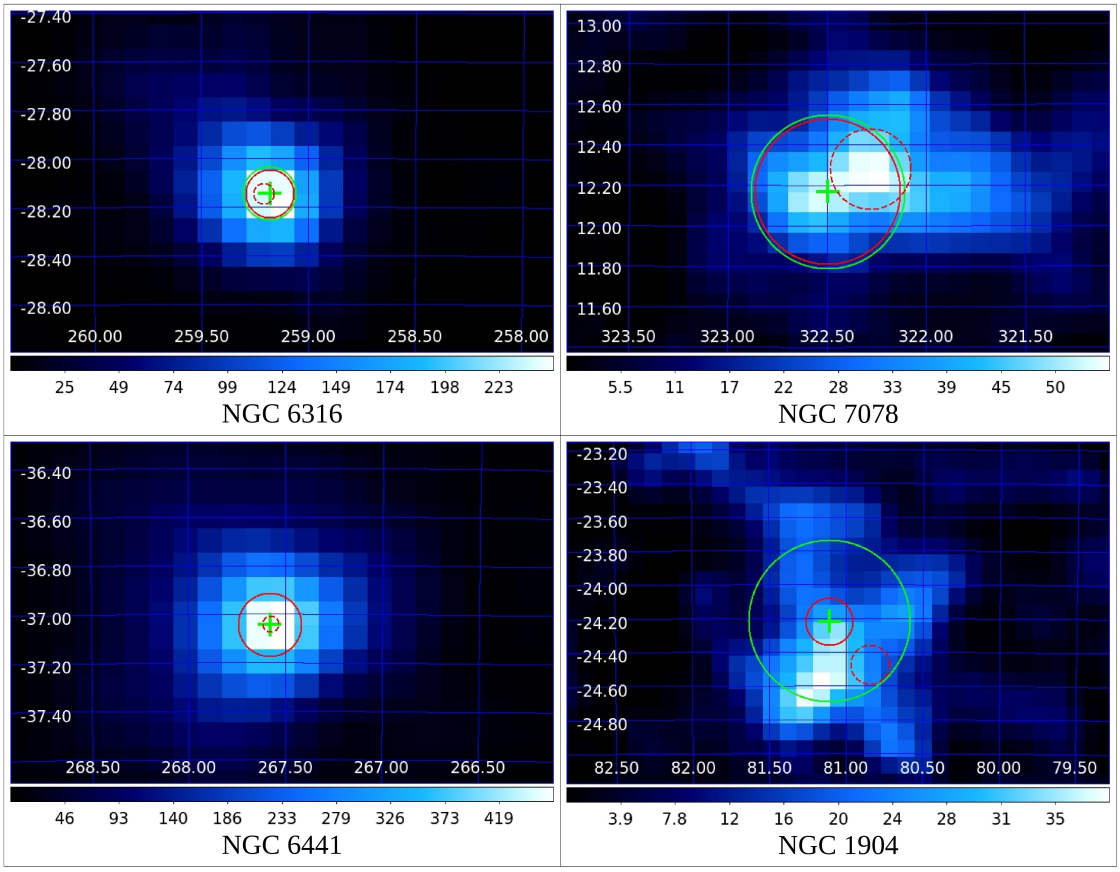

Fig. A.6 TS maps for GCs NGC 6316, NGC 7078, NGC 6441 and NGC 1904 with tidal radii (red circle Harris 2003, green circle more recent determination from RN416 for NGC 7078 and 1904 and from [200] for NGC 6316) and gamma-ray detection localisation 95 percent containment (red dashed circle) marked. The GC catalogue co-ordinates are indicated with a green cross. Graduated color bar (bottom of each plot) shows the TS value. RA and DEC are horizontal and vertical axes respectively on the white interior scale. Spatial bin size is 0.1°.

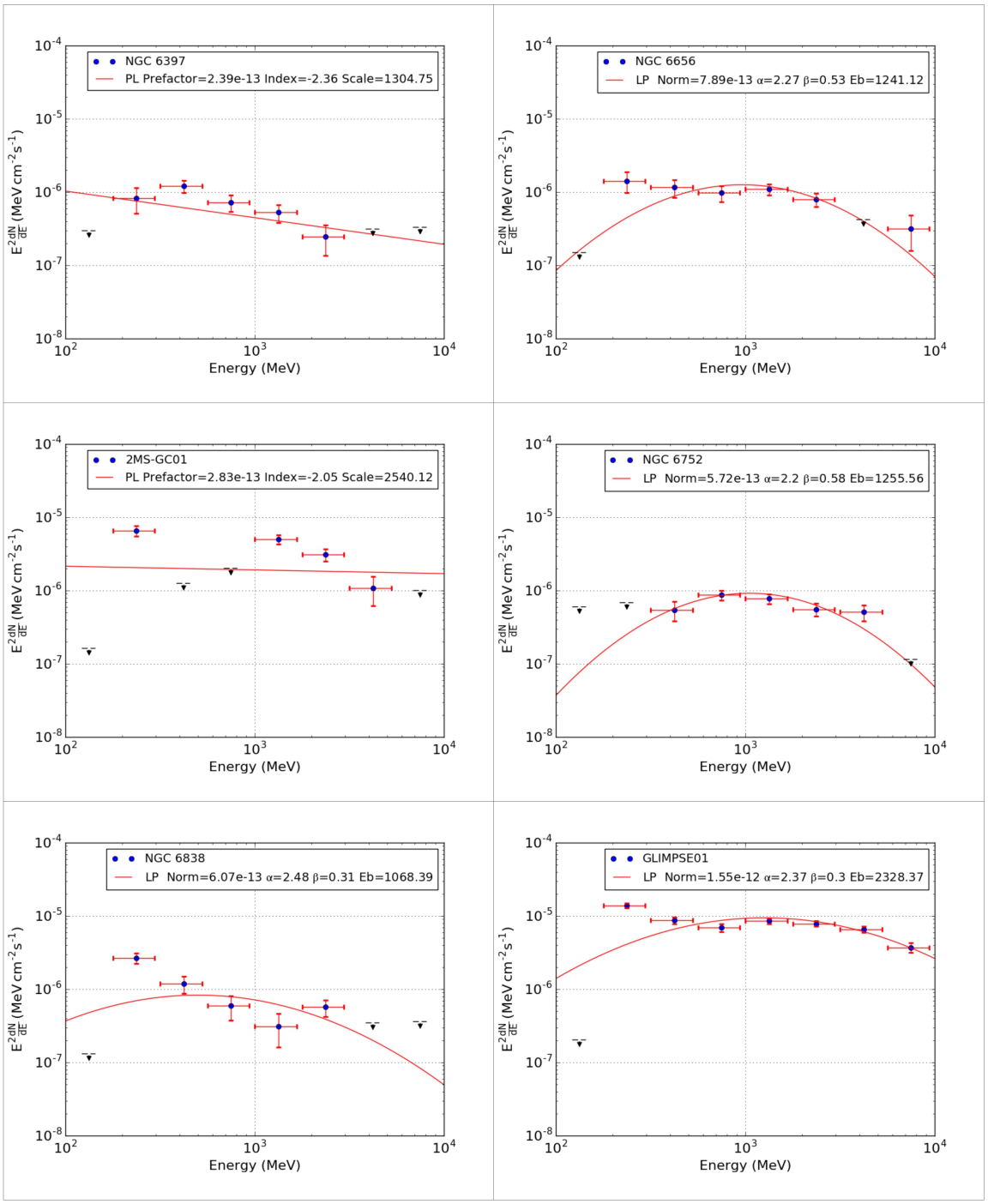

Fig. A.7 SEDs for GCs NGC 6397, NGC 6656, 2MS-GC01, NGC 6752, NGC 6838 and GLIMPSE-01. My *Fermi*-LAT observations are indicated as blue points with red error bars. ULs are marked by black symbols. The best fit model from my analysis is shown with a red line and spectral parameters and type of model are indicated in the legend as power law (PL) or Log Parabola (LP).

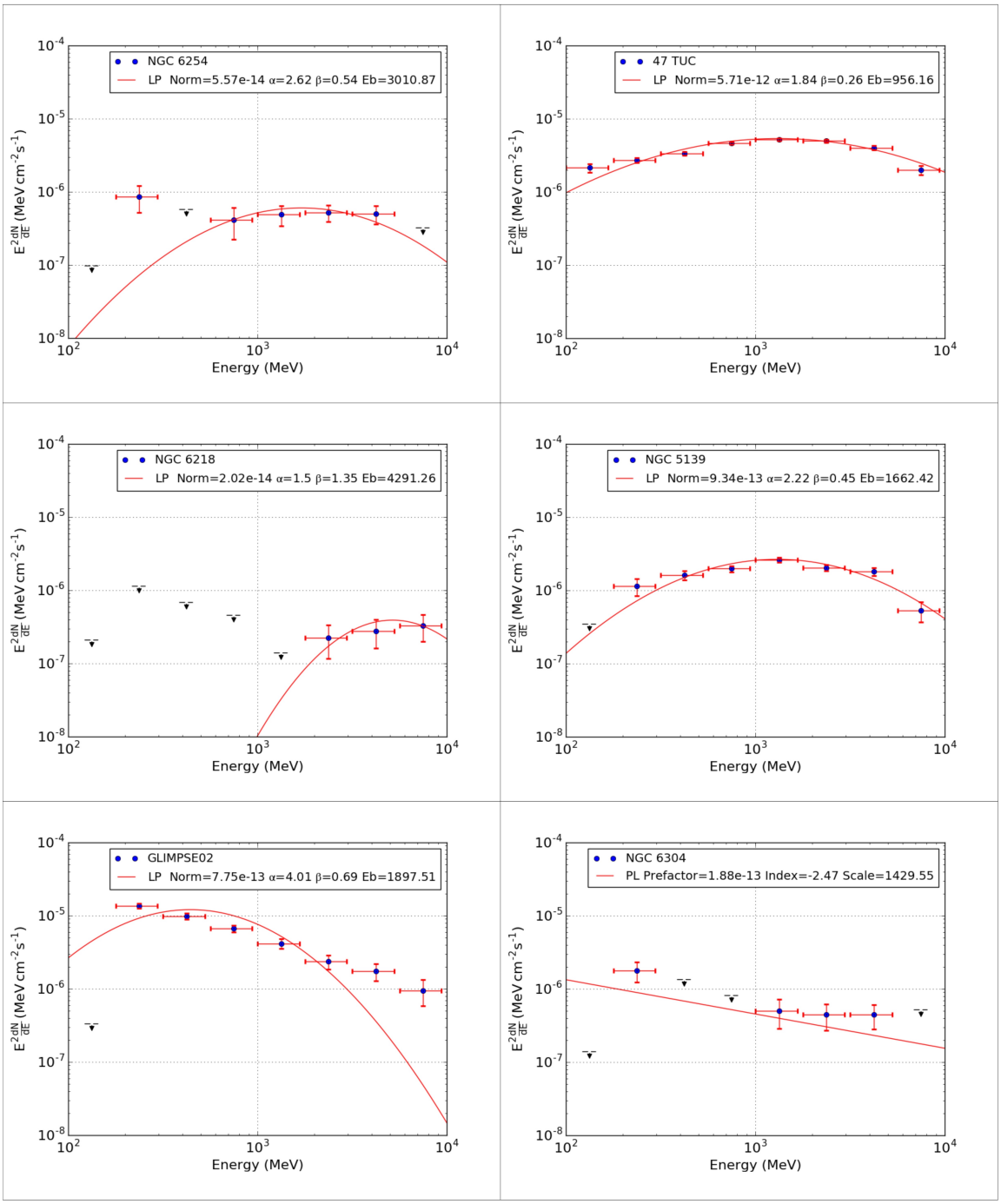

Fig. A.8 SEDs for GCs NGC 6254, 47 Tuc, NGC 6218, NGC 6139, GLIMPSE-02 and NGC 6304. My *Fermi*-LAT observations are indicated as blue points with red error bars. ULs are marked by black symbols. The best fit model from my analysis is shown with a red line and spectral parameters and type of model are indicated in the legend as power law (PL) or Log Parabola (LP).

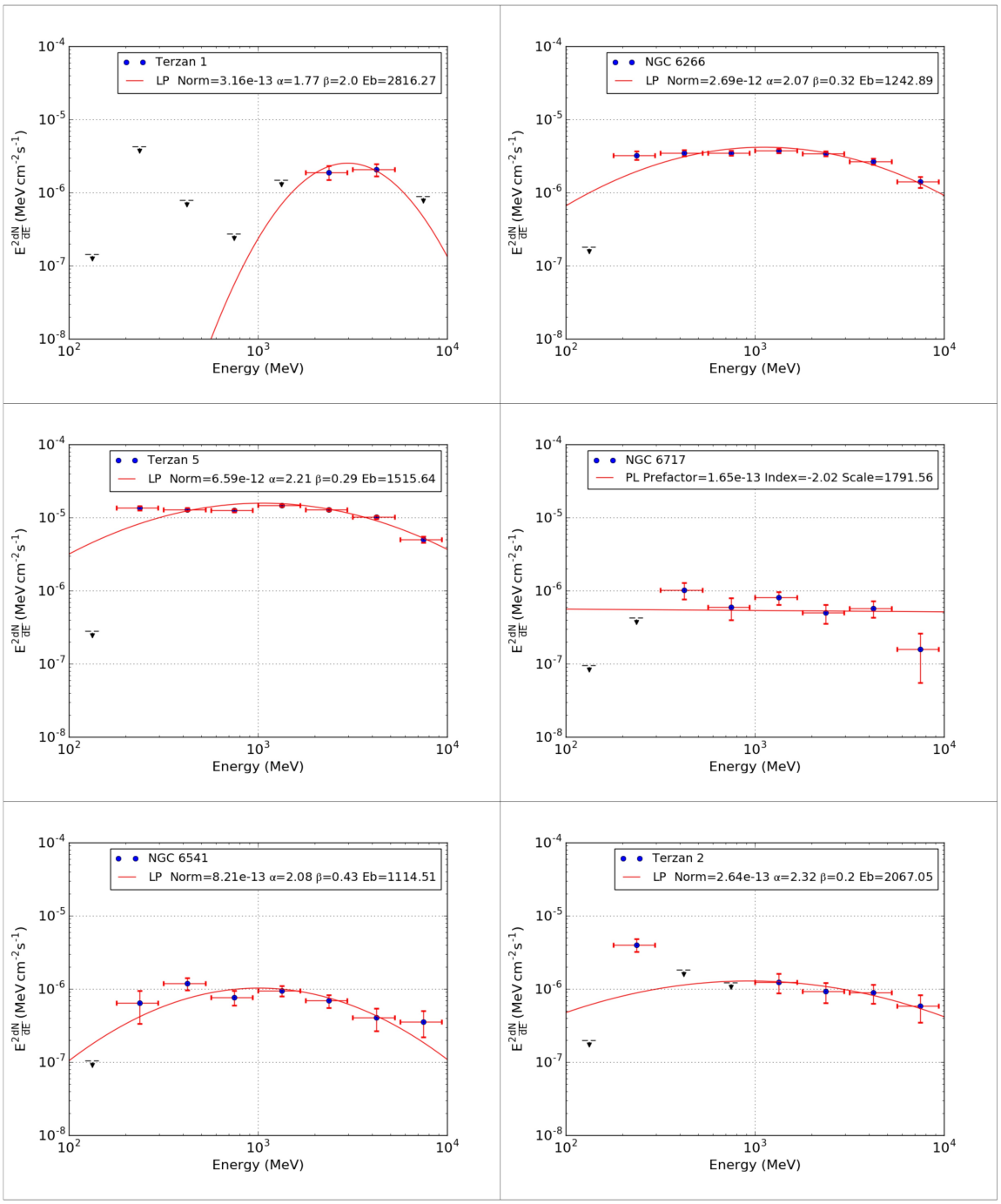

Fig. A.9 SEDs for GCs Terzan 1, NGC 6266, Terzan 5, NGC 6717, NGC 6541 and Terzan 2. My *Fermi*-LAT observations are indicated as blue points with red error bars. ULs are marked by black symbols. The best fit model from my analysis is shown with a red line and spectral parameters and type of model are indicated in the legend as power law (PL) or Log Parabola (LP).

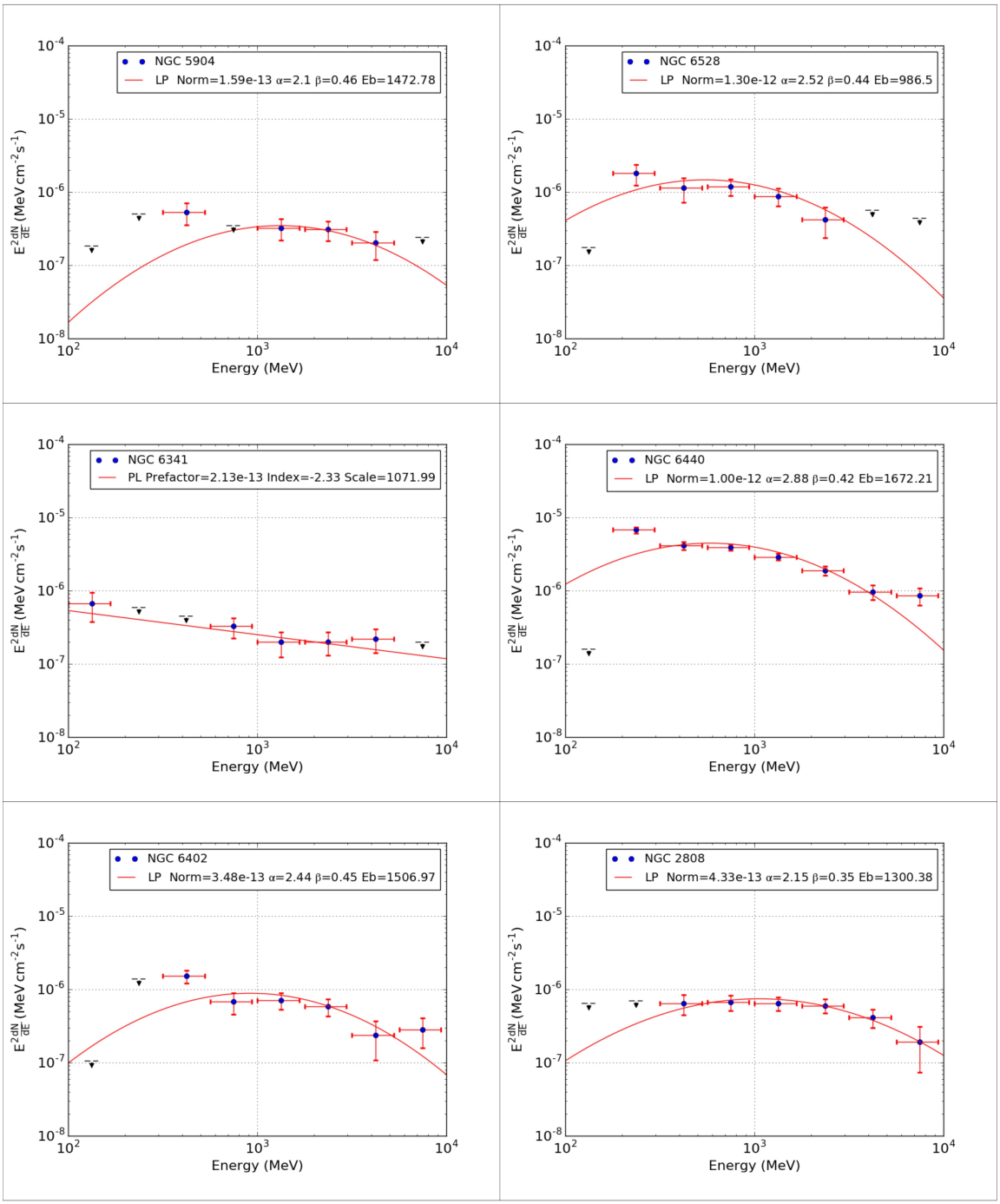

Fig. A.10 SEDs for GCs NGC 5904, NGC 6528, NGC 6341, NGC 6440, NGC 6402 and NGC 2808. My *Fermi*-LAT observations are indicated as blue points with red error bars. ULs are marked by black symbols. The best fit model from my analysis is shown with a red line and spectral parameters and type of model are indicated in the legend as power law (PL) or Log Parabola (LP).

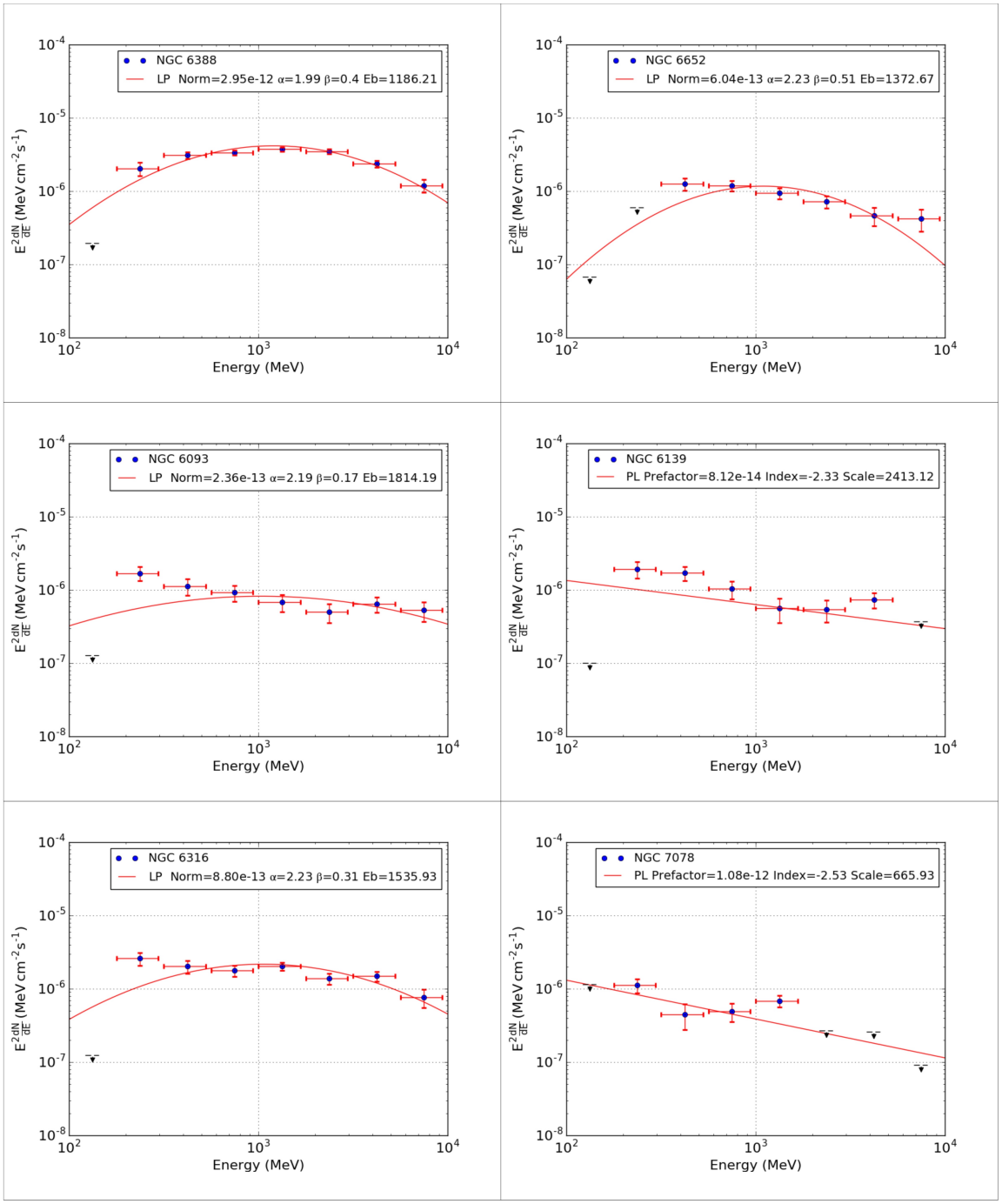

Fig. A.11 SEDs for GCs NGC 6388, NGC 6652, NGC 6093, NGC 6139, NGC 6316 and NGC 7078. My *Fermi*-LAT observations are indicated as blue points with red error bars. ULs are marked by black symbols. The best fit model from my analysis is shown with a red line and spectral parameters and type of model are indicated in the legend as power law (PL) or Log Parabola (LP).

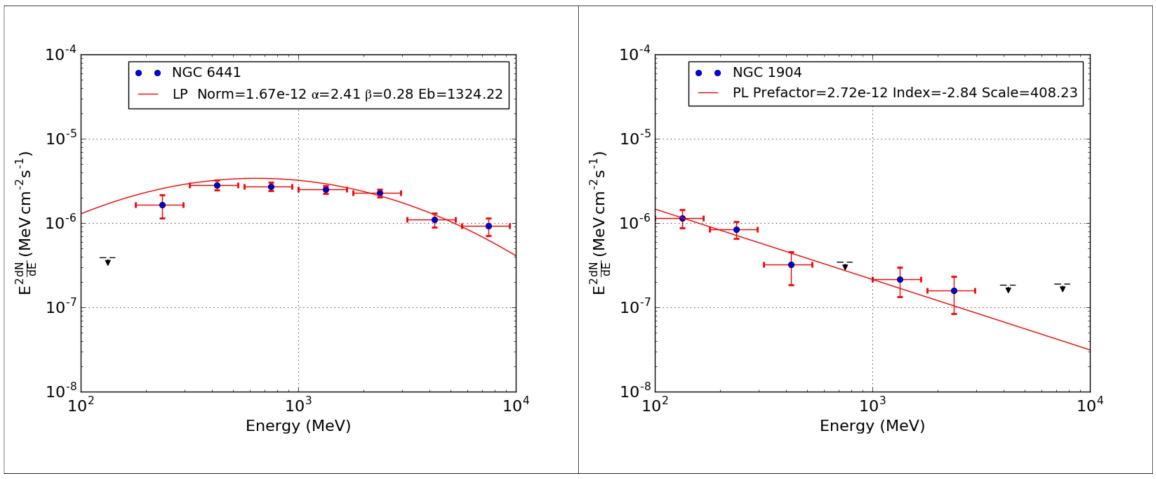

Fig. A.12 SEDs for GCs NGC 6441 and NGC 1904. My *Fermi*-LAT observations are indicated as blue points with red error bars. ULs are marked by black symbols. The best fit model from my analysis is shown with a red line and spectral parameters and type of model are indicated in the legend as power law (PL) or Log Parabola (LP).

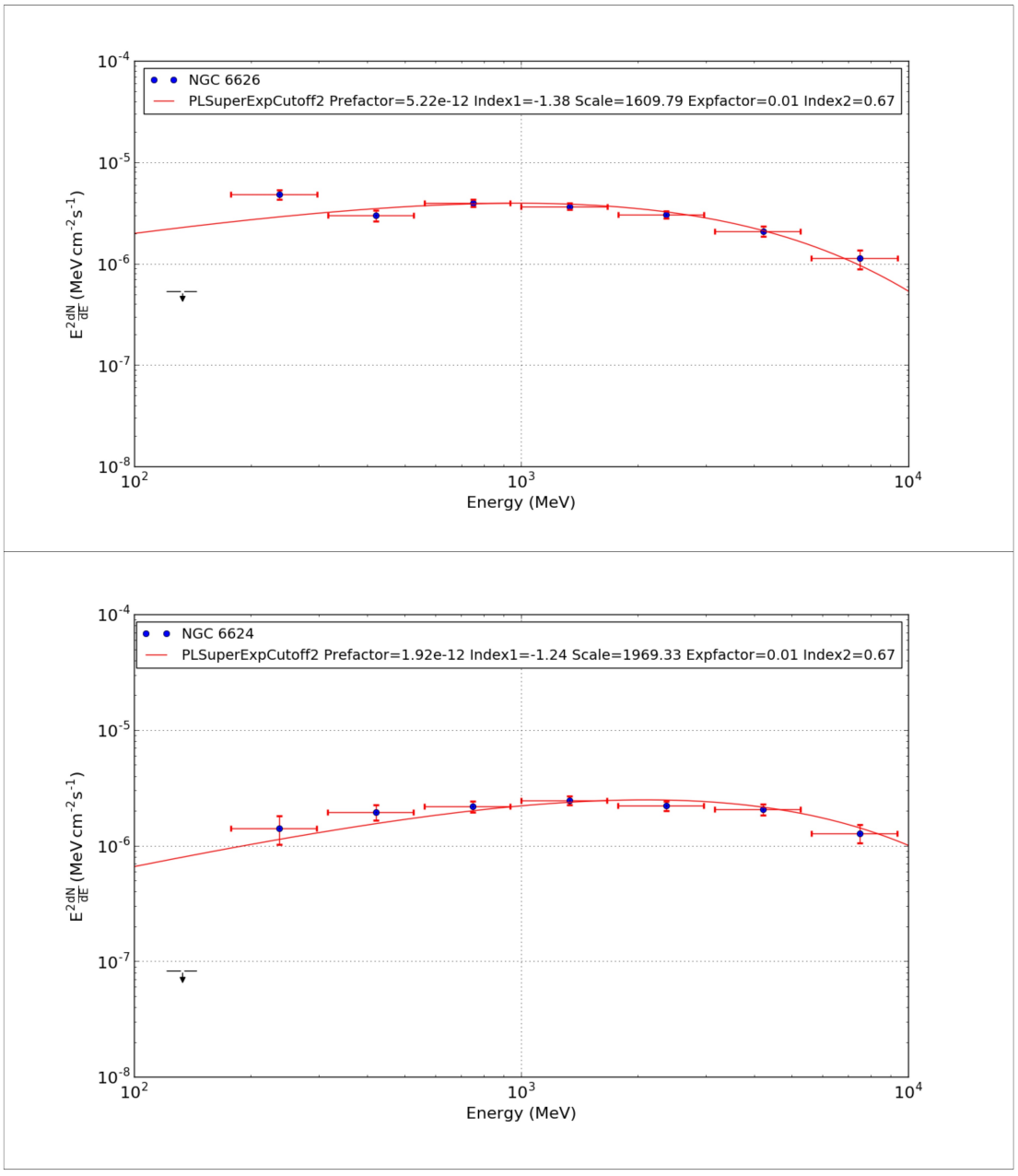

Fig. A.13 SEDs for GCs NGC 6626 and NGC 6624. My *Fermi*-LAT observations are indicated as blue points with red error bars. ULs are marked by black symbols. The best fit model of form PLSuperExpCutoff2 from my analysis is shown with a red line and spectral parameters are indicated in the legend.

Appendix B

Nucleon Phase Space Integration

The spin structure function of Eqn. 8.2 has an analytic simplification as presented by [120] of which I repeat the relevant points here. From the original 12-dimensional integral, 7 dimensions may be integrated out analytically so that a 5-dimensional integral remains to be solved through numerical integration (as opposed to numerical integration of the 4-dimensional integral of [120]).

Firstly the 3-dimensional momentum delta function is used to integrate out d^3p_4. Then, the non-relativistic nucleons have energy $E_i = p_i^2/2M_N$ and so the energy balance term is given by:

$$E_1 + E_2 - E_3 - E_4 + \omega$$

$$= \frac{-2p_3^2 - 2\mathbf{p_1}\cdot\mathbf{p_2} + 2\mathbf{p_1}\cdot\mathbf{p_3} + 2\mathbf{p_2}\cdot\mathbf{p_3}}{2M_N} + \omega \tag{B.1}$$

Next, a polar co-ordinate system is used with α and β being the polar and azimuthmal angles of p_2 relative to p_1 and θ and Φ those of p_3. The medium is isotropic so the p_1 momentum can be chosen in the z direction so $\int d^3p_1 = 4\pi \int dp_1$ with $p_1 = |p_1|$. The medium isototropy also allows the azimuthmal angle $d\Phi$ to be trivially integrated to leave three nontrivial angular integrations with the remaining angular variables expressed as follows:

$$\mathbf{p_1}\cdot\mathbf{p_2} = p_1 p_2 \cos\alpha \tag{B.2}$$

$$\mathbf{p_1}\cdot\mathbf{p_3} = p_1 p_3 \cos\theta \tag{B.3}$$

$$\mathbf{p_2} \cdot \mathbf{p_3} = p_2 p_3 \cos\alpha \cos\theta + \sin\alpha + \sin\theta + \cos\beta \tag{B.4}$$

The integration over $d\beta$ is carried out using the δ function with $f(\beta) \equiv E_1 + E_2 - E_3 - E_4 + \omega$ and β_1 being the root of $f(\beta) = 0$ in the interval [0,π] giving:

$$\int_0^{2\pi} d\beta\, \delta[f(\beta)] = \frac{2}{|df(\beta)/d\beta|_{\beta=\beta_1}} \Theta\Big(\Big|\frac{df(\beta)}{d\beta}\Big|^2_{\beta=\beta_1}\Big) \tag{B.5}$$

The derivative can be expressed as

$$\Big|\frac{df(\beta)}{d\beta}\Big|_{\beta=\beta_1} = \sqrt{az^2 + bz + c} \tag{B.6}$$

where

$$z \equiv \cos\alpha \tag{B.7}$$

$$a = p_2^2(-p_1^2 - p_3^2 + 2p_1 p_3 \cos\theta) \tag{B.8}$$

$$\begin{aligned} b = {} & 2\omega M_N p_1 p_2 - 2p_1 p_2 p_3^2 - 2\omega M_N p_2 p_3 \cos\theta \\ & + 2p_1^2 p_3 \cos\theta + 2p_2 p_3^3 \cos\theta - 2p_1 p_2 p_3^2 \cos^2\theta \end{aligned} \tag{B.9}$$

$$\begin{aligned} c = {} & \omega^2 M_N^2 + 2\omega M_N p_3^2 + p_2^2 p_3^2 - p_3^4 - 2\omega M_N p_1 p_3 \cos\theta \\ & + 2p_1 p_3^3 \cos\theta - p_1^2 p_3^2 \cos^2\theta - p_2^2 p_3^3 \cos^2\theta \end{aligned} \tag{B.10}$$

Finally the analytic simplification of equation B.5 can be solved by numerical integration through a Monte Carlo method integrating over $dp_1 dp_2 dp_3 d\cos\theta\, d\cos\alpha$.

Appendix C

MSP Analysis

Selected MSPs for Analysis

MSP Name	RA (Deg.)	DEC (Deg.)	Period (ms)	$\dot{E}$ 10^{34} erg s^{-1}
J0931-1902	142.83	-19.05	4.64	0.14
J1730-2304	262.59	-23.08	8.12	0.15
J1455-3330	223.95	-33.51	7.99	0.19
J1207-5050	181.84	-50.84	4.84	0.21
J2317+1439	349.29	14.66	3.45	0.23
J0030+0451	7.61	4.86	4.87	0.35
J1640+2224	250.07	22.4	3.16	0.35
J1713+0747	258.46	7.79	4.57	0.35
J1327-0755	201.99	-7.93	2.68	0.37
J1732-5049	263.2	-50.82	5.31	0.37
J1744-7619	266	-76.32	4.69	0.37
J2302+4442	345.7	44.71	5.19	0.37
J1946+3417	296.6	34.29	3.17	0.39
J1142+0119	175.71	1.33	5.08	0.45
J1744-1134	266.12	-11.58	4.07	0.52
J1024-0719	156.16	-7.32	5.16	0.53
J1745+1017	266.39	10.3	2.65	0.53
J1946-5403	296.64	-54.06	2.71	0.54
J2051-0827	312.78	-8.46	4.51	0.55

continued . . .

. . . continued

MSP Name	RA (Deg.)	DEC (Deg.)	Period (ms)	$\dot{E}$ 10^{34} erg s^{-1}
J0533+6759	83.48	67.99	4.39	0.57
J0636+5129	99.02	51.48	2.87	0.57
J0737-3039A	114.46	-30.66	22.7	0.59
J2042+0246	310.5	2.8	4.53	0.6
J2124-3358	321.18	-33.98	4.93	0.69
J0751+1807	117.79	18.13	3.48	0.73
J0340+4130	55.1	41.51	3.3	0.75
J1552+5437	238.22	54.62	2.43	0.77
J2017-1614	304.44	-16.24	2.31	0.78
J1137+7528	174.26	75.47	2.51	0.79
J1622-0315	245.75	-3.26	3.85	0.79
J1125-6014	171.48	-60.24	2.63	0.81
J1600-3053	240.22	-30.9	3.6	0.81
J0610-2100	92.56	-21.01	3.86	0.84
J1012-4235	153.05	-42.6	3.1	0.87
J1312+0051	198.19	0.85	4.23	0.93
J1855-1436	283.98	-14.6	3.59	0.93
J0605+3757	91.27	37.96	2.73	0.95
J0101-6422	15.3	-64.38	2.57	1.1
J1630+3734	247.65	37.58	3.32	1.1
J1858-2216	284.57	-22.28	2.38	1.1
J2047+1053	311.79	10.89	4.29	1.1
J2310-0555	347.53	-5.93	2.61	1.1
J0437-4715	69.32	-47.25	5.76	1.2
J1544+4937	236.02	49.63	2.16	1.2
J1614-2230	243.65	-22.51	3.15	1.3
J2017+0603	304.34	6.05	2.9	1.3
J0023+0923	5.82	9.39	3.05	1.5
J0613-0200	93.43	-2.01	3.06	1.5
J2043+1711	310.84	17.19	2.38	1.5
J1514-4946	228.58	-49.77	3.59	1.6
J2234+0944	338.7	9.74	3.63	1.6

continued . . .

. . . continued

MSP Name	RA (Deg.)	DEC (Deg.)	Period (ms)	$\dot{E}$ 10^{34} erg s^{-1}
J0102+4839	15.71	48.66	2.96	1.7
J1124-3653	171	-36.89	2.41	1.7
J1832-0836	278.11	-8.62	2.72	1.7
J1231-1411	187.8	-14.2	3.68	1.8
J2214+3000	333.66	30.01	3.12	1.8
J0740+6620	115.19	66.34	2.89	2
J0307+7443	46.98	74.72	3.16	2.2
J0614-3329	93.54	-33.5	3.15	2.2
J1741+1351	265.38	13.86	3.75	2.2
J1909-3744	287.45	-37.74	2.95	2.2
J2339-0533	354.91	-5.55	2.88	2.2
J2241-5236	340.43	-52.61	2.19	2.5
J1811-2405	272.83	-24.09	2.66	2.8
J0034-0534	8.59	-5.58	1.88	2.9
J1536-4948	234.1	-49.82	3.08	2.9
J1036-8317	159.17	-83.3	3.41	3.1
J1658-5324	254.66	-53.4	2.44	3.2
J0248+4230	42.13	42.51	2.6	3.8
J1446-4701	221.65	-47.02	2.19	3.8
J1810+1744	272.66	17.74	1.66	4
J0621+2514	95.3	25.23	2.72	4.8
J1311-3430	197.94	-34.51	2.56	4.9
J1921+0137	290.38	1.62	2.5	4.9
J1816+4510	274.15	45.18	3.19	5.2
J2215+5135	333.89	51.59	2.61	5.2
J1843-1113	280.92	-11.23	1.85	6
J1431-4715	217.94	-47.26	2.01	6.8
J1902-5105	285.51	-51.1	1.74	6.8
J0955-6150	148.83	-61.84	2	7
J1543-5149	235.93	-51.83	2.06	7.3
J1035-6720	158.86	-67.34	2.87	7.7
J1125-5825	171.43	-58.42	3.1	8.1

continued . . .

... continued

MSP Name	RA (Deg.)	DEC (Deg.)	Period (ms)	$\dot{E}$ 10^{34} erg s^{-1}
J1227-4853	186.99	-48.9	1.69	9
J1513-2550	228.35	-25.84	2.12	9
J1903-7051	285.91	-70.86	3.6	9.9
J1747-4036	266.95	-40.62	1.65	12
J1959+2048	299.9	20.8	1.61	16
J0218+4232	34.53	42.54	2.32	24
J1823-3021A	275.92	-30.36	5.44	83
J1939+2134	294.91	21.58	1.56	110
J1824-2452A	276.13	-24.87	3.05	220
J0251+2606	42.76	26.1	2.54	–
J0318+0253	49.56	2.88	5.19	–
J1301+0833	195.41	8.57	1.84	–
J1302-3258	195.61	-32.98	3.77	–
J1628-3205	247.03	-32.1	3.21	–
J1805+0615	271.43	6.26	2.13	–
J1908+2105	287.24	21.08	2.56	–
J2052+1218	313.2	12.33	1.99	–
J2129-0429	322.44	-4.49	7.61	–
J2205+6012	331.39	60.22	2.42	–
J2256-1024	344.23	-10.41	2.29	–

Table C.1 Analysis selection of 103 MSPs from the "Public List of LAT-Detected Gamma-Ray Pulsars" ordered by $\dot{E}$. RAJ and DECJ are right ascension and declination in degrees. 11 MSPs have no $\dot{E}$ given in the online catalogue as indicated by a "−".

MSP Analysis Results

MSP Name	Source ID	TS	Offset (Degrees)	Energy Flux 10^{-11} erg cm^{-2} s^{-1}	Photon Flux 10^{-8} cm^{-2} s^{-1}
J1455-3330	4FGL J1455.9-3332	10.3	0.050	0.08 ± 0.03	0.05 ± 0.02
J2317+1439	4FGL J2317.3+1433	12.9	0.104	0.08 ± 0.03	0.08 ± 0.03
J1137+7528	4FGL J1137.6+7527	23.7	0.043	0.07 ± 0.03	0.02 ± 0.02
J1125-6014	4FGL J1126.4-6011	29.1	0.086	0.34 ± 0.08	0.29 ± 0.06

continued ...

. . . continued

MSP Name	Source ID	TS	Offset (Degrees)	Energy Flux 10^{-11} erg cm^{-2} s^{-1}	Photon Flux 10^{-8} cm^{-2} s^{-1}
J1832-0836	4FGL J1832.4-0847	51.1	0.174	1.25 ± 0.20	0.69 ± 0.11
J0931-1902	4FGL J0931.2-1906	59.8	0.066	0.18 ± 0.03	0.12 ± 0.02
J1908+2105	4FGL J1908.9+2103	62.7	0.020	0.42 ± 0.07	0.34 ± 0.06
J0248+4230	4FGL J0248.6+4230	66.0	0.021	0.20 ± 0.10	0.19 ± 0.07
J1730-2304	4FGL J1730.8-2303	67.4	0.106	0.67 ± 0.09	0.86 ± 0.12
J1640+2224	4FGL J1640.1+2222	71.2	0.047	0.24 ± 0.05	0.31 ± 0.10
J2051-0827	4FGL J2051.0-0826	88.4	0.028	0.26 ± 0.04	0.14 ± 0.02
J1125-5825	4FGL J1125.6-5825	100.3	0.012	0.49 ± 0.07	0.27 ± 0.04
J2047+1053	4FGL J2047.3+1051	101.1	0.058	0.38 ± 0.06	0.35 ± 0.05
J0621+2514	4FGL J0621.2+2512	109.3	0.026	0.50 ± 0.08	0.32 ± 0.09
J1544+4937	4FGL J1544.0+4939	109.9	0.022	0.26 ± 0.11	0.35 ± 0.09
J1741+1351	4FGL J1741.4+1354	118.2	0.051	0.37 ± 0.05	0.27 ± 0.09
J1732-5049	4FGL J1732.7-5050	129.8	0.021	0.56 ± 0.06	0.67 ± 0.08
J1552+5437	4FGL J1553.1+5438	134.1	0.042	0.24 ± 0.03	0.19 ± 0.03
J1939+2134	4FGL J1939.6+2135	136.5	0.016	1.90 ± 0.26	3.09 ± 0.45
J1036-8317	4FGL J1036.5-8318	138.4	0.013	0.38 ± 0.16	0.30 ± 0.07
J1805+0615	4FGL J1805.6+0615	153.1	0.007	0.52 ± 0.06	0.38 ± 0.04
J0740+6620	4FGL J0741.0+6618	158.3	0.038	0.29 ± 0.03	0.30 ± 0.04
J1024-0719	4FGL J1024.5-0719	163.8	0.034	0.42 ± 0.05	0.43 ± 0.05
J1012-4235	4FGL J1012.1-4235	179.9	0.011	0.48 ± 0.20	0.46 ± 0.10
J0955-6150	4FGL J0955.4-6151	185.1	0.024	0.66 ± 0.29	0.74 ± 0.15
J1543-5149	4FGL J1543.6-5148	185.9	0.016	1.42 ± 0.96	2.07 ± 0.46
J1921+0137	4FGL J1921.4+0136	198.3	0.027	0.99 ± 0.09	1.05 ± 0.10
J0251+2606	4FGL J0251.0+2605	202.6	0.007	0.44 ± 0.05	0.32 ± 0.04
J1207-5050	4FGL J1207.4-5050	205.4	0.012	0.52 ± 0.05	0.36 ± 0.04
J1446-4701	4FGL J1446.6-4701	210.1	0.008	0.60 ± 0.06	0.50 ± 0.05
J2042+0246	4FGL J2042.2+0245	210.6	0.074	0.56 ± 0.05	0.68 ± 0.06
J2017-1614	4FGL J2017.7-1612	230.7	0.036	0.65 ± 0.06	0.79 ± 0.08
J0318+0253	4FGL J0318.2+0254	231.2	0.028	0.59 ± 0.06	0.51 ± 0.05
J1843-1113	4FGL J1843.7-1114	244.1	0.021	1.63 ± 0.22	2.88 ± 0.37
J1713+0747	4FGL J1713.8+0747	270.9	0.010	0.69 ± 0.07	0.51 ± 0.05
J1513-2550	4FGL J1513.4-2549	274.5	0.024	0.67 ± 0.06	0.69 ± 0.12

continued . . .

... continued

MSP Name	Source ID	TS	Offset (Degrees)	Energy Flux 10^{-11} erg cm^{-2} s^{-1}	Photon Flux 10^{-8} cm^{-2} s^{-1}
J2129-0429	4FGL J2129.8-0428	285.3	0.026	0.60 ± 0.06	0.58 ± 0.05
J0605+3757	4FGL J0605.1+3757	287.8	0.009	0.66 ± 0.09	0.42 ± 0.05
J1630+3734	4FGL J1630.6+3734	289.6	0.010	0.54 ± 0.06	0.53 ± 0.14
J0610-2100	4FGL J0610.2-2100	292.2	0.010	0.60 ± 0.05	0.62 ± 0.06
J1622-0315	4FGL J1623.0-0315	298.1	0.004	0.88 ± 0.23	1.04 ± 0.16
J1903-7051	4FGL J1903.4-7053	301.2	0.033	0.63 ± 0.06	0.73 ± 0.17
J1628-3205	4FGL J1628.1-3204	302.0	0.026	1.07 ± 0.25	1.52 ± 0.23
J1142+0119	4FGL J1142.8+0120	308.9	0.011	0.61 ± 0.08	0.57 ± 0.17
J0023+0923	4FGL J0023.4+0920	324.5	0.053	0.75 ± 0.06	0.81 ± 0.07
J1600-3053	4FGL J1600.9-3054	326.9	0.012	0.75 ± 0.07	0.45 ± 0.04
J1745+1017	4FGL J1745.5+1017	358.3	0.011	0.80 ± 0.07	0.57 ± 0.05
J1747-4036	4FGL J1747.7-4037	382.2	0.004	1.33 ± 0.26	1.81 ± 0.23
J1301+0833	4FGL J1301.6+0834	392.6	0.005	0.76 ± 0.19	0.83 ± 0.12
J2256-1024	4FGL J2256.8-1024	416.2	0.014	0.75 ± 0.06	0.83 ± 0.11
J1823-3021A	4FGL J1823.5-3020	456.2	0.027	1.29 ± 0.09	1.29 ± 0.09
J1858-2216	4FGL J1858.3-2216	484.7	0.005	1.03 ± 0.07	0.65 ± 0.05
J0533+6759	4FGL J0533.8+6800	487.2	0.012	0.77 ± 0.06	0.57 ± 0.04
J2234+0944	4FGL J2234.7+0943	495.7	0.012	0.94 ± 0.07	0.76 ± 0.06
J1959+2048	4FGL J1959.5+2048	501.2	0.009	1.51 ± 0.53	1.93 ± 0.30
J1824-2452A	4FGL J1824.6-2452	603.9	0.028	2.05 ± 0.54	3.03 ± 0.33
J1302-3258	4FGL J1302.4-3258	675.9	0.015	1.04 ± 0.08	0.70 ± 0.09
J0751+1807	4FGL J0751.2+1808	684.0	0.016	1.00 ± 0.10	0.66 ± 0.15
J1946-5403	4FGL J1946.5-5402	712.0	0.011	1.01 ± 0.06	1.14 ± 0.14
J1816+4510	4FGL J1816.5+4510	743.2	0.007	0.93 ± 0.06	0.88 ± 0.05
J2310-0555	4FGL J2310.0-0555	754.7	0.013	1.66 ± 0.08	4.49 ± 0.25
J1658-5324	4FGL J1658.6-5323	789.4	0.007	1.93 ± 0.09	2.61 ± 0.12
J0102+4839	4FGL J0102.8+4839	823.2	0.003	1.29 ± 0.07	1.35 ± 0.13
J1124-3653	4FGL J1124.0-3653	872.6	0.015	1.30 ± 0.07	1.17 ± 0.07
J2215+5135	4FGL J2215.6+5135	877.3	0.008	1.67 ± 0.09	1.88 ± 0.10
J1312+0051	4FGL J1312.7+0050	1021.2	0.008	1.34 ± 0.07	1.35 ± 0.07
J1035-6720	4FGL J1035.4-6720	1192.9	0.003	1.86 ± 0.09	1.53 ± 0.07
J0307+7443	4FGL J0307.8+7443	1233.5	0.004	1.52 ± 0.07	1.26 ± 0.06

continued ...

. . . continued

MSP Name	Source ID	TS	Offset (Degrees)	Energy Flux 10^{-11} erg cm^{-2} s^{-1}	Photon Flux 10^{-8} cm^{-2} s^{-1}
J1744-7619	4FGL J1744.0-7618	1274.5	0.005	1.78 ± 0.08	1.32 ± 0.06
J1810+1744	4FGL J1810.5+1744	1301.9	0.012	2.27 ± 0.30	3.98 ± 0.29
J0340+4130	4FGL J0340.3+4130	1303.2	0.001	1.74 ± 1.84	1.04 ± 0.33
J1227-4853	4FGL J1228.0-4853	1314.4	0.020	2.29 ± 0.17	3.80 ± 0.45
J0101-6422	4FGL J0101.1-6422	1436.4	0.012	1.30 ± 0.27	1.50 ± 0.14
J0034-0534	4FGL J0034.3-0534	1715.3	0.006	2.04 ± 0.48	2.76 ± 0.26
J1614-2230	4FGL J1614.5-2230	1876.6	0.010	2.44 ± 0.10	1.44 ± 0.06
J1902-5105	4FGL J1902.0-5105	1988.3	0.010	2.39 ± 0.23	3.82 ± 0.24
J2043+1711	4FGL J2043.3+1711	2000.7	0.004	2.49 ± 0.10	2.54 ± 0.17
J1744-1134	4FGL J1744.4-1135	2059.6	0.009	3.86 ± 0.12	4.55 ± 0.15
J0613-0200	4FGL J0613.7-0201	2155.5	0.014	3.60 ± 0.12	4.62 ± 0.24
J0437-4715	4FGL J0437.2-4715	2383.9	0.006	1.75 ± 0.06	2.89 ± 0.15
J2339-0533	4FGL J2339.6-0533	2430.1	0.001	2.47 ± 0.11	2.42 ± 0.16
J2017+0603	4FGL J2017.4+0602	2666.1	0.012	3.28 ± 0.14	2.03 ± 0.15
J1514-4946	4FGL J1514.3-4946	2667.2	0.003	3.93 ± 0.15	3.36 ± 0.21
J2241-5236	4FGL J2241.7-5236	2719.5	0.005	2.59 ± 0.09	2.07 ± 0.07
J2214+3000	4FGL J2214.6+3000	3795.8	0.009	3.06 ± 0.10	2.57 ± 0.08
J2302+4442	4FGL J2302.7+4443	3973.7	0.010	3.49 ± 0.11	2.80 ± 0.13
J2124-3358	4FGL J2124.7-3358	5108.8	0.010	3.93 ± 0.11	2.69 ± 0.08
J0218+4232	4FGL J0218.1+4232	5413.7	0.007	4.77 ± 0.11	8.09 ± 0.25
J1536-4948	4FGL J1536.4-4948	5437.8	0.004	7.13 ± 1.38	6.99 ± 0.39
J1311-3430	4FGL J1311.7-3430	7418.1	0.007	5.88 ± 0.55	8.35 ± 0.35
J0030+0451	4FGL J0030.4+0451	8611.2	0.001	5.67 ± 2.75	6.36 ± 1.23
J1231-1411	4FGL J1231.1-1412	15720.4	0.002	9.72 ± 0.19	7.64 ± 0.18
J0614-3329	4FGL J0614.1-3329	19856.3	0.003	10.04 ± 0.19	7.61 ± 0.16

Table C.2 Analysis results for all MSPs in the energy range 100 MeV$-$10 GeV with a PLSuperExp2 spectral model in detection significance (TS) order, with 4FGL source id, offset from catalogue co-ordinates and fluxes.

MSP Name	Source ID	TS	Offset (Degrees)	Energy Flux 10^{-11} erg cm^{-2} s^{-1}	Photon Flux 10^{-8} cm^{-2} s^{-1}
J2205+6015	4FGL J2205.5+6016	15.2	0.050	0.24 ± 0.07	0.31 ± 0.16

continued . . .

... continued

MSP Name	Source ID	TS	Offset (Degrees)	Energy Flux 10^{-11} erg cm^{-2} s^{-1}	Photon Flux 10^{-8} cm^{-2} s^{-1}
J1855-1436	4FGL J1855.9-1435	53.7	0.017	0.44 ± 0.08	0.45 ± 0.13
J1431-4715	4FGL J1431.4-4711	59.8	0.080	0.47 ± 0.07	0.99 ± 0.19
J2052+1219	4FGL J2052.7+1218	64.4	0.015	0.39 ± 0.06	0.61 ± 0.16
J1811-2405	4FGL J1811.3-2403	91.6	0.035	1.54 ± 0.20	2.86 ± 0.50

Table C.3 Analysis results for all MSPs with a PL spectral model, in the energy range 100 MeV−10 GeV , with 4FGL source id, detection significance (TS), offset from catalogue co-ordinates and fluxes.

MSP Name	Prefactor 10^{-13}	Index1	Scale	Expfactor 10^{-3}
J1455-3330	11.10 ± 4.21	-0.11	2119	19.20
J2317+1439	31.67 ± 10.98	0.00	1538	26.04
J1137+7528	2.19 ± 4.45	0.00 ± 0.01	3321	11.00 ± 7.63
J1125-6014	3.46 ± 0.78	-1.22	2465	6.29
J1832-0836	65.89 ± 10.29	-0.26	3068	13.87
J0931-1902	20.03 ± 3.83	-0.18	2172	17.76
J1908+2105	7.55 ± 1.24	-0.96	2624	9.23
J0248+4230	20.02 ± 14.49	-0.51 ± 0.42	2122	18.25 ± 0.24
J1730-2304	174.30 ± 23.81	-0.50	1361	24.81
J1640+2224	7.40 ± 1.85	-1.14 ± 0.23	2184	12.78 ± 0.52
J2051-0827	17.74 ± 2.92	-0.17	2237	14.80
J1125-5825	11.17 ± 1.57	-0.57	3096	10.11
J2047+1053	5.45 ± 0.80	-1.26	1910	6.44
J0621+2514	33.19 ± 5.26	-0.32 ± 0.22	2787	15.25 ± 0.48
J1544+4937	6.43 ± 3.11	-1.66 ± 0.35	1068	5.02 ± 0.00
J1741+1351	14.04 ± 9.80	-0.72 ± 0.46	1848	11.43 ± 4.02
J1732-5049	16.15 ± 1.87	-1.29	1541	9.68
J1552+5437	8.38 ± 1.14	-0.90	1489	9.99
J1939+2134	40.16 ± 8.03	-1.58 ± 0.11	1651	9.63 ± 0.01
J1036-8317	19.63 ± 10.71	-0.61 ± 0.34	2089	13.69 ± 0.01
J1805+0615	19.90 ± 2.36	-0.68	2071	11.90
J0740+6620	11.01 ± 1.31	-1.09	1416	10.44

continued ...

... continued

MSP Name	Prefactor 10^{-13}	Index1	Scale	Expfactor 10^{-3}
J1024-0719	22.10 ± 2.64	-1.03	1187	11.40
J1012-4235	10.65 ± 4.71	-1.24 ± 0.30	1475	7.14 ± 0.02
J0955-6150	22.33 ± 11.58	-1.24 ± 0.33	1332	9.32 ± 0.02
J1543-5149	44.86 ± 47.73	-1.40 ± 0.55	1505	10.76 ± 0.01
J1921+0137	16.97 ± 1.61	-1.27	1989	8.11
J0251+2606	87.69 ± 9.60	-0.03	1861	21.12
J1207-5050	41.95 ± 4.40	-0.36	1951	15.90
J1446-4701	27.72 ± 2.79	-0.82	1495	11.81
J2042+0246	444.94 ± 42.27	0.00	1164	33.22
J2017-1614	10.62 ± 1.03	-1.54	1476	5.64
J0318+0253	34.53 ± 3.51	-0.79	1281	12.54
J1843-1113	101.17 ± 18.64	-1.47 ± 0.12	1096	13.65 ± 0.00
J1713+0747	34.01 ± 3.20	-0.61	1845	12.90
J1513-2550	40.90 ± 3.75	-0.91 ± 0.13	1349	13.31 ± 0.01
J2129-0429	29.15 ± 2.77	-1.04	1131	10.46
J0605+3757	99.19 ± 13.68	0.00 ± 0.00	1901	19.24 ± 0.42
J1630+3734	25.72 ± 11.59	-0.83 ± 0.30	2018	13.80 ± 2.53
J0610-2100	47.23 ± 4.21	-0.86	1136	13.97
J1622-0315	18.73 ± 5.33	-1.50 ± 0.19	1281	5.89 ± 0.13
J1903-7051	5.50 ± 2.61	-1.57 ± 0.27	2004	4.68 ± 2.51
J1628-3205	84.39 ± 27.16	-1.12 ± 0.20	1232	15.44 ± 0.02
J1142+0119	8.56 ± 4.89	-1.42 ± 0.39	1492	4.52 ± 3.70
J0023+0923	67.71 ± 5.72	-0.90	976	14.00
J1600-3053	19.29 ± 1.71	-0.71	1907	9.34
J1745+1017	54.45 ± 4.52	-0.45	1881	14.77
J1747-4036	60.92 ± 16.19	-1.28 ± 0.16	1292	11.66 ± 0.00
J1301+0833	43.60 ± 11.07	-1.09 ± 0.19	1075	11.27 ± 0.01
J2256-1024	51.36 ± 4.13	-1.05 ± 0.10	1009	12.11 ± 0.01
J1823-3021A	18.91 ± 1.30	-1.29	1969	6.99
J1858-2216	150.90 ± 10.65	-0.01	2004	19.09
J0533+6759	20.55 ± 1.49	-0.95	1499	8.34
J2234+0944	44.31 ± 3.41	-0.80	1401	11.54

continued ...

. . . continued

MSP Name	Prefactor 10^{-13}	Index1	Scale	Expfactor 10^{-3}
J1959+2048	125.68 ± 61.16	-0.96 ± 0.27	1356	16.10 ± 0.02
J1824-2452A	47.03 ± 20.07	-1.50 ± 0.21	1610	9.38 ± 0.00
J1302-3258	43.41 ± 9.99	-0.64 ± 0.17	1599	11.39 ± 1.46
J0751+1807	47.47 ± 31.52	-0.52 ± 0.41	1949	12.76 ± 3.86
J1946-5403	66.23 ± 22.21	-0.91 ± 0.19	1500	14.67 ± 2.26
J1816+4510	43.74 ± 2.66	-1.05	1099	10.00
J2310-0555	4.96 ± 1.48	-2.90 ± 0.12	1247	-3.74 ± 2.17
J1658-5324	256.68 ± 12.29	-0.89	1113	18.61
J0102+4839	34.21 ± 1.96	-1.31 ± 0.06	1298	7.37 ± 0.01
J1124-3653	45.97 ± 2.59	-1.04	1333	9.41
J2215+5135	28.22 ± 1.44	-1.46	1519	5.97
J1312+0051	94.84 ± 5.21	-0.82	1348	14.23
J1035-6720	144.49 ± 6.69	-0.55	1642	15.40
J0307+7443	190.40 ± 8.38	-0.37	1506	18.24
J1744-7619	209.03 ± 9.71	-0.31	1306	17.40
J1810+1744	110.35 ± 17.77	-1.77 ± 0.10	838	7.76 ± 0.01
J0340+4130	55.21 ± 53.12	-0.67 ± 0.64	1604	9.83 ± 0.04
J1227-4853	29.06 ± 6.90	-1.92 ± 0.13	1360	4.09 ± 1.68
J0101-6422	100.87 ± 21.32	-1.07 ± 0.15	938	12.49 ± 0.01
J0034-0534	129.11 ± 27.89	-1.49 ± 0.15	739	8.04 ± 0.01
J1614-2230	210.73 ± 8.66	-0.18	1614	15.79
J1902-5105	101.77 ± 12.69	-1.57 ± 0.07	1055	9.53 ± 0.00
J2043+1711	82.12 ± 3.38	-1.21 ± 0.05	1244	8.46 ± 0.01
J1744-1134	652.83 ± 20.89	-0.61	1265	20.72
J0613-0200	172.03 ± 6.04	-1.36 ± 0.04	1001	9.30 ± 0.00
J0437-4715	447.42 ± 69.29	-1.03 ± 0.11	668	20.89 ± 1.77
J2339-0533	73.14 ± 8.83	-1.32 ± 0.08	1072	6.43 ± 0.93
J2017+0603	63.45 ± 7.84	-0.89 ± 0.09	1710	7.28 ± 0.69
J1514-4946	61.56 ± 2.79	-1.23 ± 0.05	1710	6.15 ± 0.25
J2241-5236	136.28 ± 4.61	-0.63	2000	13.71
J2214+3000	252.24 ± 7.96	-0.66	1085	14.12
J2302+4442	151.78 ± 4.58	-0.86 ± 0.04	1286	10.54 ± 0.00

continued . . .

... continued

MSP Name	Prefactor 10^{-13}	Index1	Scale	Expfactor 10^{-3}
J2124-3358	408.51 ± 11.42	-0.30	1144	16.33
J0218+4232	203.10 ± 5.02	-1.82 ± 0.02	822	6.20 ± 0.00
J1536-4948	121.02 ± 25.08	-1.39 ± 0.12	1438	5.37 ± 0.00
J1311-3430	248.31 ± 23.52	-1.66 ± 0.06	825	5.99 ± 0.00
J0030+0451	572.63 ± 252.02	-0.98 ± 0.30	808	13.45 ± 0.01
J1231-1411	667.44 ± 11.68	-0.69 ± 0.02	1047	12.66 ± 0.00
J0614-3329	331.45 ± 5.39	-1.03 ± 0.02	1075	7.58 ± 0.00

Table C.4 The spectral parameters for MSPs, in the energy range 100 MeV−10 GeV, with a PLSuperExp2 spectral model in detection significance order as from Table C.2 above. The *index2* parameter (not shown) has value 0.67 throughout.

MSP Name	Prefactor 10^{-13}	Index1	Scale
J2205+6015	0.79 ± 0.26	-1.96 ± 0.26	2052
J1855-1436	1.80 ± 0.33	-1.81 ± 0.15	1905
J1431-4715	10.47 ± 1.64	-2.41 ± 0.12	765
J2052+1219	3.61 ± 0.59	-2.11 ± 0.14	1197
J1811-2405	2.40 ± 0.34	-2.26 ± 0.08	2532

Table C.5 The spectral parameters for MSPs, in the energy range 100 MeV−10 GeV , with a PL spectral model in detection significance order as Table C.3 above.

MSP Name	Source ID	TS	Offset (Degrees)	Energy Flux 10^{-11} erg cm^{-2} s^{-1}	Photon Flux 10^{-8} cm^{-2} s^{-1}
J1810+1744	4FGL J1810.5+1744	9.0	0.015	0.07 ± 0.05	0.003 ± 0.002
J1816+4510	4FGL J1816.5+4510	9.8	0.012	0.07 ± 0.10	0.003 ± 0.004
J1431-4715	4FGL J1431.4-4711	10.4	0.011	0.02 ± 0.02	0.001 ± 0.001
J1614-2230	4FGL J1614.5-2230	10.7	0.020	0.03 ± 0.02	0.001 ± 0.001
J1125-5825	4FGL J1125.6-5825	12.6	0.002	0.12 ± 0.05	0.006 ± 0.003
J1302-3258	4FGL J1302.4-3258	12.7	0.015	0.02 ± 0.02	0.001 ± 0.001
J2302+4442	4FGL J2302.7+4443	13.6	0.007	0.14 ± 0.06	0.007 ± 0.003
J0533+6759	4FGL J0533.8+6800	13.6	0.080	0.13 ± 0.10	0.002 ± 0.001

continued ...

... continued

MSP Name	Source ID	TS	Offset (Degrees)	Energy Flux 10^{-11} erg cm^{-2} s^{-1}	Photon Flux 10^{-8} cm^{-2} s^{-1}
J1855-1436	4FGL J1855.9-1435	13.7	0.003	0.16 ± 0.10	0.006 ± 0.004
J1823-3021A	4FGL J1823.5-3020	14.4	0.004	0.46 ± 0.09	0.019 ± 0.004
J1124-3653	4FGL J1124.0-3653	16.2	0.010	0.02 ± 0.02	0.001 ± 0.001
J0101-6422	4FGL J0101.1-6422	21.2	0.010	0.02 ± 0.02	0.001 ± 0.001
J2234+0944	4FGL J2234.7+0943	23.0	0.012	0.02 ± 0.04	0.001 ± 0.002
J0102+4839	4FGL J0102.8+4839	23.6	0.007	0.01 ± 0.01	0.001 ± 0.001
J0340+4130	4FGL J0340.3+4130	24.3	0.027	0.04 ± 0.02	0.002 ± 0.001
J2215+5135	4FGL J2215.6+5135	24.3	0.028	0.09 ± 0.10	0.003 ± 0.002
J1514-4946	4FGL J1514.3-4946	28.7	0.017	0.05 ± 0.05	0.002 ± 0.003
J2043+1711	4FGL J2043.3+1711	29.4	0.027	0.02 ± 0.02	0.001 ± 0.001
J0030+0451	4FGL J0030.4+0451	36.3	0.012	0.22 ± 0.06	0.010 ± 0.003
J2339-0533	4FGL J2339.6-0533	41.3	0.004	0.10 ± 0.09	0.004 ± 0.003
J1311-3430	4FGL J1311.7-3430	68.6	0.008	0.10 ± 0.06	0.003 ± 0.002
J2017+0603	4FGL J2017.4+0602	85.5	0.012	0.09 ± 0.08	0.004 ± 0.003
J1231-1411	4FGL J1231.1-1412	102.7	0.005	0.01 ± 0.02	0.001 ± 0.001
J1536-4948	4FGL J1536.4-4948	146.6	0.010	0.07 ± 0.06	0.003 ± 0.002
J0614-3329	4FGL J0614.1-3329	452.7	0.001	0.15 ± 0.09	0.005 ± 0.002

Table C.6 Analysis results for all MSPs, ordered by detection significance (TS), in the energy range $10-100$ GeV , with 4FGL source id, detection significance, offset from catalogue co-ordinates and fluxes.

References

[1] 2010. URL https://fermi.gsfc.nasa.gov/ssc/data/analysis/scitools/source_models.html.

[2] Veritas specification. https://veritas.sao.arizona.edu/about-veritas-mainmenu-81/veritas-specifications-mainmenu-111, 2020. Accessed: 2020-06-14.

[3] R. Abbott, T. D. Abbott, S. Abraham, F. Acernese, K. Ackley, C. Adams, R. X. Adhikari, V. B. Adya, C. Affeldt, M. Agathos, K. Agatsuma, N. Aggarwal, O. D. Aguiar, A. Aich, L. Aiello, A. Ain, P. Ajith, S. Akcay, G. Allen, A. Allocca, P. A. Altin, A. Amato, S. Anand, A. Ananyeva, S. B. Anderson, W. G. Anderson, S. V. Angelova, S. Ansoldi, S. Antier, S. Appert, K. Arai, M. C. Araya, J. S. Areeda, M. Arène, N. Arnaud, S. M. Aronson, K. G. Arun, Y. Asali, S. Ascenzi, G. Ashton, S. M. Aston, P. Astone, F. Aubin, P. Aufmuth, K. AultONeal, C. Austin, V. Avendano, S. Babak, P. Bacon, F. Badaracco, M. K. M. Bader, S. Bae, A. M. Baer, J. Baird, F. Baldaccini, G. Ballardin, S. W. Ballmer, A. Bals, A. Balsamo, G. Baltus, S. Banagiri, D. Bankar, R. S. Bankar, J. C. Barayoga, C. Barbieri, B. C. Barish, D. Barker, K. Barkett, P. Barneo, F. Barone, B. Barr, L. Barsotti, M. Barsuglia, D. Barta, J. Bartlett, I. Bartos, R. Bassiri, A. Basti, M. Bawaj, J. C. Bayley, M. Bazzan, B. Bécsy, M. Bejger, I. Belahcene, A. S. Bell, D. Beniwal, M. G. Benjamin, J. D. Bentley, F. Bergamin, B. K. Berger, G. Bergmann, S. Bernuzzi, C. P. L. Berry, D. Bersanetti, A. Bertolini, J. Betzwieser, R. Bhandare, A. V. Bhandari, J. Bidler, E. Biggs, I. A. Bilenko, G. Billingsley, R. Birney, O. Birnholtz, S. Biscans, M. Bischi, S. Biscoveanu, A. Bisht, G. Bissenbayeva, M. Bitossi, M. A. Bizouard, J. K. Blackburn, J. Blackman, C. D. Blair, D. G. Blair, R. M. Blair, F. Bobba, N. Bode, M. Boer, Y. Boetzel, G. Bogaert, F. Bondu, E. Bonilla, R. Bonnand, P. Booker, B. A. Boom, R. Bork, V. Boschi, S. Bose, V. Bossilkov, J. Bosveld, Y. Bouffanais, A. Bozzi, C. Bradaschia, P. R. Brady, A. Bramley, M. Branchesi, J. E. Brau, M. Breschi, T. Briant, J. H. Briggs, F. Brighenti, A. Brillet, M. Brinkmann, P. Brockill, A. F. Brooks, J. Brooks, D. D. Brown, S. Brunett, G. Bruno, R. Bruntz, A. Buikema, T. Bulik, H. J. Bulten, A. Buonanno, R. Buscicchio, D. Buskulic, R. L. Byer, M. Cabero, L. Cadonati, G. Cagnoli, C. Cahillane, J. Calderón Bustillo, J. D.

Callaghan, T. A. Callister, E. Calloni, J. B. Camp, M. Canepa, K. C. Cannon, H. Cao, J. Cao, G. Carapella, F. Carbognani, S. Caride, M. F. Carney, G. Carullo, J. Casanueva Diaz, C. Casentini, J. Castañeda, S. Caudill, M. Cavaglià, F. Cavalier, R. Cavalieri, G. Cella, P. Cerdá-Durán, E. Cesarini, O. Chaibi, K. Chakravarti, C. Chan, M. Chan, S. Chao, P. Charlton, E. A. Chase, E. Chassande-Mottin, D. Chatterjee, M. Chaturvedi, K. Chatziioannou, H. Y. Chen, X. Chen, Y. Chen, H.-P. Cheng, C. K. Cheong, H. Y. Chia, F. Chiadini, R. Chierici, A. Chincarini, A. Chiummo, G. Cho, H. S. Cho, M. Cho, N. Christensen, Q. Chu, S. Chua, K. W. Chung, S. Chung, G. Ciani, P. Ciecielag, M. Cieślar, A. A. Ciobanu, R. Ciolfi, F. Cipriano, A. Cirone, F. Clara, J. A. Clark, P. Clearwater, S. Clesse, F. Cleva, E. Coccia, P.-F. Cohadon, D. Cohen, M. Colleoni, C. G. Collette, C. Collins, M. Colpi, M. Constancio, L. Conti, S. J. Cooper, P. Corban, T. R. Corbitt, I. Cordero-Carrión, S. Corezzi, K. R. Corley, N. Cornish, D. Corre, A. Corsi, S. Cortese, C. A. Costa, R. Cotesta, M. W. Coughlin, S. B. Coughlin, J.-P. Coulon, S. T. Countryman, P. Couvares, P. B. Covas, D. M. Coward, M. J. Cowart, D. C. Coyne, R. Coyne, J. D. E. Creighton, T. D. Creighton, J. Cripe, M. Croquette, S. G. Crowder, J.-R. Cudell, T. J. Cullen, A. Cumming, R. Cummings, L. Cunningham, E. Cuoco, M. Curylo, T. Dal Canton, G. Dálya, A. Dana, L. M. Daneshgaran-Bajastani, B. D'Angelo, S. L. Danilishin, S. D'Antonio, K. Danzmann, C. Darsow-Fromm, A. Dasgupta, L. E. H. Datrier, V. Dattilo, I. Dave, M. Davier, G. S. Davies, D. Davis, E. J. Daw, D. DeBra, M. Deenadayalan, J. Degallaix, M. De Laurentis, S. Deléglise, M. Delfavero, N. De Lillo, W. Del Pozzo, L. M. DeMarchi, V. D'Emilio, N. Demos, T. Dent, R. De Pietri, R. De Rosa, C. De Rossi, R. DeSalvo, O. de Varona, S. Dhurandhar, M. C. Díaz, M. Diaz-Ortiz, T. Dietrich, L. Di Fiore, C. Di Fronzo, C. Di Giorgio, F. Di Giovanni, M. Di Giovanni, T. Di Girolamo, A. Di Lieto, B. Ding, S. Di Pace, I. Di Palma, F. Di Renzo, A. K. Divakarla, A. Dmitriev, Z. Doctor, F. Donovan, K. L. Dooley, S. Doravari, I. Dorrington, T. P. Downes, M. Drago, J. C. Driggers, Z. Du, J.-G. Ducoin, P. Dupej, O. Durante, D. D'Urso, S. E. Dwyer, P. J. Easter, G. Eddolls, B. Edelman, T. B. Edo, O. Edy, A. Effler, P. Ehrens, J. Eichholz, S. S. Eikenberry, M. Eisenmann, R. A. Eisenstein, A. Ejlli, L. Errico, R. C. Essick, H. Estelles, D. Estevez, Z. B. Etienne, T. Etzel, M. Evans, T. M. Evans, B. E. Ewing, V. Fafone, S. Fairhurst, X. Fan, S. Farinon, B. Farr, W. M. Farr, E. J. Fauchon-Jones, M. Favata, M. Fays, M. Fazio, J. Feicht, M. M. Fejer, F. Feng, E. Fenyvesi, D. L. Ferguson, A. Fernandez-Galiana, I. Ferrante, E. C. Ferreira, T. A. Ferreira, F. Fidecaro, I. Fiori, D. Fiorucci, M. Fishbach, R. P. Fisher, R. Fittipaldi, M. Fitz-Axen, V. Fiumara, R. Flaminio, E. Floden, E. Flynn, H. Fong, J. A. Font, P. W. F. Forsyth, J.-D. Fournier, S. Frasca, F. Frasconi, Z. Frei, A. Freise, R. Frey, V. Frey, P. Fritschel, V. V. Frolov,

G. Fronzè, P. Fulda, M. Fyffe, H. A. Gabbard, B. U. Gadre, S. M. Gaebel, J. R. Gair, S. Galaudage, D. Ganapathy, S. G. Gaonkar, C. García-Quirós, F. Garufi, B. Gateley, S. Gaudio, V. Gayathri, G. Gemme, E. Genin, A. Gennai, D. George, J. George, L. Gergely, S. Ghonge, Abhirup Ghosh, Archisman Ghosh, S. Ghosh, B. Giacomazzo, J. A. Giaime, K. D. Giardina, D. R. Gibson, C. Gier, K. Gill, J. Glanzer, J. Gniesmer, P. Godwin, E. Goetz, R. Goetz, N. Gohlke, B. Goncharov, G. González, A. Gopakumar, S. E. Gossan, M. Gosselin, R. Gouaty, B. Grace, A. Grado, M. Granata, A. Grant, S. Gras, P. Grassia, C. Gray, R. Gray, G. Greco, A. C. Green, R. Green, E. M. Gretarsson, H. L. Griggs, G. Grignani, A. Grimaldi, S. J. Grimm, H. Grote, S. Grunewald, P. Gruning, G. M. Guidi, A. R. Guimaraes, G. Guixé, H. K. Gulati, Y. Guo, A. Gupta, Anchal Gupta, P. Gupta, E. K. Gustafson, R. Gustafson, L. Haegel, O. Halim, E. D. Hall, E. Z. Hamilton, G. Hammond, M. Haney, M. M. Hanke, J. Hanks, C. Hanna, M. D. Hannam, O. A. Hannuksela, T. J. Hansen, J. Hanson, T. Harder, T. Hardwick, K. Haris, J. Harms, G. M. Harry, I. W. Harry, R. K. Hasskew, C.-J. Haster, K. Haughian, F. J. Hayes, J. Healy, A. Heidmann, M. C. Heintze, J. Heinze, H. Heitmann, F. Hellman, P. Hello, G. Hemming, M. Hendry, I. S. Heng, E. Hennes, J. Hennig, M. Heurs, S. Hild, T. Hinderer, S. Y. Hoback, S. Hochheim, E. Hofgard, D. Hofman, A. M. Holgado, N. A. Holland, K. Holt, D. E. Holz, P. Hopkins, C. Horst, J. Hough, E. J. Howell, C. G. Hoy, Y. Huang, M. T. Hübner, E. A. Huerta, D. Huet, B. Hughey, V. Hui, S. Husa, S. H. Huttner, R. Huxford, T. Huynh-Dinh, B. Idzkowski, A. Iess, H. Inchauspe, C. Ingram, G. Intini, J.-M. Isac, M. Isi, B. R. Iyer, T. Jacqmin, S. J. Jadhav, S. P. Jadhav, A. L. James, K. Jani, N. N. Janthalur, P. Jaranowski, D. Jariwala, R. Jaume, A. C. Jenkins, J. Jiang, G. R. Johns, N. K. Johnson-McDaniel, A. W. Jones, D. I. Jones, J. D. Jones, P. Jones, R. Jones, R. J. G. Jonker, L. Ju, J. Junker, C. V. Kalaghatgi, V. Kalogera, B. Kamai, S. Kandhasamy, G. Kang, J. B. Kanner, S. J. Kapadia, S. Karki, R. Kashyap, M. Kasprzack, W. Kastaun, S. Katsanevas, E. Katsavounidis, W. Katzman, S. Kaufer, K. Kawabe, F. Kéfélian, D. Keitel, A. Keivani, R. Kennedy, J. S. Key, S. Khadka, F. Y. Khalili, I. Khan, S. Khan, Z. A. Khan, E. A. Khazanov, N. Khetan, M. Khursheed, N. Kijbunchoo, Chunglee Kim, G. J. Kim, J. C. Kim, K. Kim, W. Kim, W. S. Kim, Y.-M. Kim, C. Kimball, P. J. King, M. Kinley-Hanlon, R. Kirchhoff, J. S. Kissel, L. Kleybolte, S. Klimenko, T. D. Knowles, E. Knyazev, P. Koch, S. M. Koehlenbeck, G. Koekoek, S. Koley, V. Kondrashov, A. Kontos, N. Koper, M. Korobko, W. Z. Korth, M. Kovalam, D. B. Kozak, V. Kringel, N. V. Krishnendu, A. Królak, N. Krupinski, G. Kuehn, A. Kumar, P. Kumar, Rahul Kumar, Rakesh Kumar, S. Kumar, L. Kuo, A. Kutynia, B. D. Lackey, D. Laghi, E. Lalande, T. L. Lam, A. Lamberts, M. Landry, B. B. Lane, R. N. Lang, J. Lange, B. Lantz, R. K. Lanza, I. La Rosa, A. Lartaux-

Vollard, P. D. Lasky, M. Laxen, A. Lazzarini, C. Lazzaro, P. Leaci, S. Leavey, Y. K. Lecoeuche, C. H. Lee, H. M. Lee, H. W. Lee, J. Lee, K. Lee, J. Lehmann, N. Leroy, N. Letendre, Y. Levin, A. K. Y. Li, J. Li, K. li, T. G. F. Li, X. Li, F. Linde, S. D. Linker, J. N. Linley, T. B. Littenberg, J. Liu, X. Liu, M. Llorens-Monteagudo, R. K. L. Lo, A. Lockwood, L. T. London, A. Longo, M. Lorenzini, V. Loriette, M. Lormand, G. Losurdo, J. D. Lough, C. O. Lousto, G. Lovelace, H. Lück, D. Lumaca, A. P. Lundgren, Y. Ma, R. Macas, S. Macfoy, M. MacInnis, D. M. Macleod, I. A. O. MacMillan, A. Macquet, I. Magaña Hernandez, F. Magaña-Sandoval, R. M. Magee, E. Majorana, I. Maksimovic, A. Malik, N. Man, V. Mandic, V. Mangano, G. L. Mansell, M. Manske, M. Mantovani, M. Mapelli, F. Marchesoni, F. Marion, S. Márka, Z. Márka, C. Markakis, A. S. Markosyan, A. Markowitz, E. Maros, A. Marquina, S. Marsat, F. Martelli, I. W. Martin, R. M. Martin, V. Martinez, D. V. Martynov, H. Masalehdan, K. Mason, E. Massera, A. Masserot, T. J. Massinger, M. Masso-Reid, S. Mastrogiovanni, A. Matas, F. Matichard, N. Mavalvala, E. Maynard, J. J. McCann, R. McCarthy, D. E. McClelland, S. McCormick, L. McCuller, S. C. McGuire, C. McIsaac, J. McIver, D. J. McManus, T. McRae, S. T. McWilliams, D. Meacher, G. D. Meadors, M. Mehmet, A. K. Mehta, E. Mejuto Villa, A. Melatos, G. Mendell, R. A. Mercer, L. Mereni, K. Merfeld, E. L. Merilh, J. D. Merritt, M. Merzougui, S. Meshkov, C. Messenger, C. Messick, R. Metzdorff, P. M. Meyers, F. Meylahn, A. Mhaske, A. Miani, H. Miao, I. Michaloliakos, C. Michel, H. Middleton, L. Milano, A. L. Miller, M. Millhouse, J. C. Mills, E. Milotti, M. C. Milovich-Goff, O. Minazzoli, Y. Minenkov, A. Mishkin, C. Mishra, T. Mistry, S. Mitra, V. P. Mitrofanov, G. Mitselmakher, R. Mittleman, G. Mo, K. Mogushi, S. R. P. Mohapatra, S. R. Mohite, M. Molina-Ruiz, M. Mondin, M. Montani, C. J. Moore, D. Moraru, F. Morawski, G. Moreno, S. Morisaki, B. Mours, C. M. Mow-Lowry, S. Mozzon, F. Muciaccia, Arunava Mukherjee, D. Mukherjee, S. Mukherjee, Subroto Mukherjee, N. Mukund, A. Mullavey, J. Munch, E. A. Muñiz, P. G. Murray, A. Nagar, I. Nardecchia, L. Naticchioni, R. K. Nayak, B. F. Neil, J. Neilson, G. Nelemans, T. J. N. Nelson, M. Nery, A. Neunzert, K. Y. Ng, S. Ng, C. Nguyen, P. Nguyen, D. Nichols, S. A. Nichols, S. Nissanke, F. Nocera, M. Noh, C. North, D. Nothard, L. K. Nuttall, J. Oberling, B. D. O'Brien, G. Oganesyan, G. H. Ogin, J. J. Oh, S. H. Oh, F. Ohme, H. Ohta, M. A. Okada, M. Oliver, C. Olivetto, P. Oppermann, Richard J. Oram, B. O'Reilly, R. G. Ormiston, L. F. Ortega, R. O'Shaughnessy, S. Ossokine, C. Osthelder, D. J. Ottaway, H. Overmier, B. J. Owen, A. E. Pace, G. Pagano, M. A. Page, G. Pagliaroli, A. Pai, S. A. Pai, J. R. Palamos, O. Palashov, C. Palomba, H. Pan, P. K. Panda, P. T. H. Pang, C. Pankow, F. Pannarale, B. C. Pant, F. Paoletti, A. Paoli, A. Parida, W. Parker,

D. Pascucci, A. Pasqualetti, R. Passaquieti, D. Passuello, B. Patricelli, E. Payne, B. L. Pearlstone, T. C. Pechsiri, A. J. Pedersen, M. Pedraza, A. Pele, S. Penn, A. Perego, C. J. Perez, C. Périgois, A. Perreca, S. Perriès, J. Petermann, H. P. Pfeiffer, M. Phelps, K. S. Phukon, O. J. Piccinni, M. Pichot, M. Piendibene, F. Piergiovanni, V. Pierro, G. Pillant, L. Pinard, I. M. Pinto, K. Piotrzkowski, M. Pirello, M. Pitkin, W. Plastino, R. Poggiani, D. Y. T. Pong, S. Ponrathnam, P. Popolizio, E. K. Porter, J. Powell, A. K. Prajapati, K. Prasai, R. Prasanna, G. Pratten, T. Prestegard, M. Principe, G. A. Prodi, L. Prokhorov, M. Punturo, P. Puppo, M. Pürrer, H. Qi, V. Quetschke, P. J. Quinonez, F. J. Raab, G. Raaijmakers, H. Radkins, N. Radulesco, P. Raffai, H. Rafferty, S. Raja, C. Rajan, B. Rajbhandari, M. Rakhmanov, K. E. Ramirez, A. Ramos-Buades, Javed Rana, K. Rao, P. Rapagnani, V. Raymond, M. Razzano, J. Read, T. Regimbau, L. Rei, S. Reid, D. H. Reitze, P. Rettegno, F. Ricci, C. J. Richardson, J. W. Richardson, P. M. Ricker, G. Riemenschneider, K. Riles, M. Rizzo, N. A. Robertson, F. Robinet, A. Rocchi, R. D. Rodriguez-Soto, L. Rolland, J. G. Rollins, V. J. Roma, M. Romanelli, R. Romano, C. L. Romel, I. M. Romero-Shaw, J. H. Romie, C. A. Rose, D. Rose, K. Rose, D. Rosińska, S. G. Rosofsky, M. P. Ross, S. Rowan, S. J. Rowlinson, P. K. Roy, Santosh Roy, Soumen Roy, P. Ruggi, G. Rutins, K. Ryan, S. Sachdev, T. Sadecki, M. Sakellariadou, O. S. Salafia, L. Salconi, M. Saleem, A. Samajdar, E. J. Sanchez, L. E. Sanchez, N. Sanchis-Gual, J. R. Sanders, K. A. Santiago, E. Santos, N. Sarin, B. Sassolas, B. S. Sathyaprakash, O. Sauter, R. L. Savage, V. Savant, D. Sawant, S. Sayah, D. Schaetzl, P. Schale, M. Scheel, J. Scheuer, P. Schmidt, R. Schnabel, R. M. S. Schofield, A. Schönbeck, E. Schreiber, B. W. Schulte, B. F. Schutz, O. Schwarm, E. Schwartz, J. Scott, S. M. Scott, E. Seidel, D. Sellers, A. S. Sengupta, N. Sennett, D. Sentenac, V. Sequino, A. Sergeev, Y. Setyawati, D. A. Shaddock, T. Shaffer, M. S. Shahriar, S. Sharifi, A. Sharma, P. Sharma, P. Shawhan, H. Shen, M. Shikauchi, R. Shink, D. H. Shoemaker, D. M. Shoemaker, K. Shukla, S. ShyamSundar, K. Siellez, M. Sieniawska, D. Sigg, L. P. Singer, D. Singh, N. Singh, A. Singha, A. Singhal, A. M. Sintes, V. Sipala, V. Skliris, B. J. J. Slagmolen, T. J. Slaven-Blair, J. Smetana, J. R. Smith, R. J. E. Smith, S. Somala, E. J. Son, S. Soni, B. Sorazu, V. Sordini, F. Sorrentino, T. Souradeep, E. Sowell, A. P. Spencer, M. Spera, A. K. Srivastava, V. Srivastava, K. Staats, C. Stachie, M. Standke, D. A. Steer, M. Steinke, J. Steinlechner, S. Steinlechner, D. Steinmeyer, S. Stevenson, D. Stocks, D. J. Stops, M. Stover, K. A. Strain, G. Stratta, A. Strunk, R. Sturani, A. L. Stuver, S. Sudhagar, V. Sudhir, T. Z. Summerscales, L. Sun, S. Sunil, A. Sur, J. Suresh, P. J. Sutton, B. L. Swinkels, M. J. Szczepańczyk, M. Tacca, S. C. Tait, C. Talbot, A. J. Tanasijczuk, D. B. Tanner, D. Tao, M. Tápai, A. Tapia, E. N. Tapia San Martin, J. D. Tasson, R. Taylor,

R. Tenorio, L. Terkowski, M. P. Thirugnanasambandam, M. Thomas, P. Thomas, J. E. Thompson, S. R. Thondapu, K. A. Thorne, E. Thrane, C. L. Tinsman, T. R. Saravanan, Shubhanshu Tiwari, S. Tiwari, V. Tiwari, K. Toland, M. Tonelli, Z. Tornasi, A. Torres-Forné, C. I. Torrie, I. Tosta e Melo, D. Töyrä, E. A. Trail, F. Travasso, G. Traylor, M. C. Tringali, A. Tripathee, A. Trovato, R. J. Trudeau, K. W. Tsang, M. Tse, R. Tso, L. Tsukada, D. Tsuna, T. Tsutsui, M. Turconi, A. S. Ubhi, R. Udall, K. Ueno, D. Ugolini, C. S. Unnikrishnan, A. L. Urban, S. A. Usman, A. C. Utina, H. Vahlbruch, G. Vajente, G. Valdes, M. Valentini, N. van Bakel, M. van Beuzekom, J. F. J. van den Brand, C. Van Den Broeck, D. C. Vander-Hyde, L. van der Schaaf, J. V. Van Heijningen, A. A. van Veggel, M. Vardaro, V. Varma, S. Vass, M. Vasúth, A. Vecchio, G. Vedovato, J. Veitch, P. J. Veitch, K. Venkateswara, G. Venugopalan, D. Verkindt, D. Veske, F. Vetrano, A. Viceré, A. D. Viets, S. Vinciguerra, D. J. Vine, J.-Y. Vinet, S. Vitale, Francisco Hernandez Vivanco, T. Vo, H. Vocca, C. Vorvick, S. P. Vyatchanin, A. R. Wade, L. E. Wade, M. Wade, R. Walet, M. Walker, G. S. Wallace, L. Wallace, S. Walsh, J. Z. Wang, S. Wang, W. H. Wang, R. L. Ward, Z. A. Warden, J. Warner, M. Was, J. Watchi, B. Weaver, L.-W. Wei, M. Weinert, A. J. Weinstein, R. Weiss, F. Wellmann, L. Wen, P. Weßels, J. W. Westhouse, K. Wette, J. T. Whelan, B. F. Whiting, C. Whittle, D. M. Wilken, D. Williams, J. L. Willis, B. Willke, W. Winkler, C. C. Wipf, H. Wittel, G. Woan, J. Woehler, J. K. Wofford, C. Wong, J. L. Wright, D. S. Wu, D. M. Wysocki, L. Xiao, H. Yamamoto, L. Yang, Y. Yang, Z. Yang, M. J. Yap, M. Yazback, D. W. Yeeles, Hang Yu, Haocun Yu, S. H. R. Yuen, A. K. Zadrożny, A. Zadrożny, M. Zanolin, T. Zelenova, J.-P. Zendri, M. Zevin, J. Zhang, L. Zhang, T. Zhang, C. Zhao, G. Zhao, M. Zhou, Z. Zhou, X. J. Zhu, A. B. Zimmerman, Y. Zlochower, M. E. Zucker, and J. Zweizig and. Properties and astrophysical implications of the 150 m $\odot$ binary black hole merger GW190521. *The Astrophysical Journal*, 900(1):L13, sep 2020. doi: 10.3847/2041-8213/aba493. URL https://doi.org/10.3847%2F2041-8213%2Faba493.

[4] H. Abdalla, A. Abramowski, F. Aharonian, F. A. Benkhali, E. O. Anguner, M. Arakawa, M. Arrieta, P. Aubert, M. Backes, A. Balzer, M. Barnard, Y. Becherini, J. B. Tjus, D. Berge, S. Bernhard, K. Bernlohr, R. Blackwell, M. Bottcher, C. Boisson, J. Bolmont, S. Bonnefoy, P. Bordas, J. Bregeon, F. Brun, P. Brun, M. Bryan, M. Buchele, T. Bulik, M. Capasso, S. Carrigan, S. Caroff, A. Carosi, S. Casanova, M. Cerruti, N. Chakraborty, R. C. G. Chaves, A. Chen, J. Chevalier, S. Colafrancesco, B. Condon, J. Conrad, I. D. Davids, J. Decock, C. Deil, J. Devin, P. deWilt, L. Dirson, A. Djannati-Atai, W. Domainko, A. Donath, L. O. Drury, K. Dutson, J. Dyks, T. Edwards, K. Egberts, P. Eger, G. Emery, J. P. Ernenwein, S. Eschbach, C. Farnier,

S. Fegan, M. V. Fernandes, A. Fiasson, G. Fontaine, A. Forster, S. Funk, M. Fussling, S. Gabici, Y. A. Gallant, T. Garrigoux, H. Gast, F. Gate, G. Giavitto, B. Giebels, D. Glawion, J. F. Glicenstein, D. Gottschall, M. H. Grondin, J. Hahn, M. Haupt, J. Hawkes, G. Heinzelmann, G. Henri, G. Hermann, J. A. Hinton, W. Hofmann, C. Hoischen, T. L. Holch, M. Holler, D. Horns, A. Ivascenko, H. Iwasaki, A. Jacholkowska, M. Jamrozy, D. Jankowsky, F. Jankowsky, M. Jingo, L. Jouvin, I. Jung-Richardt, M. A. Kastendieck, et al. The hess galactic plane survey. *Astronomy Astrophysics*, 612, 2018. ISSN 1432-0746. doi: 10.1051/0004-6361/201732098. URL <GotoISI>://WOS:000429404700001.

[5] A. A. Abdo, M. Ackermann, M. Ajello, J. Ampe, B. Anderson, W. B. Atwood, M. Axelsson, R. Bagagli, L. Baldini, J. Ballet, G. Barbiellini, J. Bartelt, D. Bastieri, B. M. Baughman, K. Bechtol, D. Bederede, F. Bellardi, R. Bellazzini, F. Belli, B. Berenji, D. Bisello, E. Bissaldi, E. D. Bloom, G. Bogaert, J. R. Bogart, E. Bonamente, A. W. Borgland, P. Bourgeois, A. Bouvier, J. Bregeon, A. Brez, M. Brigida, P. Bruel, T. H. Burnett, G. Busetto, G. A. Caliandro, R. A. Cameron, M. Campell, P. A. Caraveo, S. Carius, P. Carlson, J. M. Casandjian, E. Cavazzuti, M. Ceccanti, C. Cecchi, E. Charles, A. Chekhtman, C. C. Cheung, J. Chiang, R. Chipaux, A. N. Cillis, S. Ciprini, R. Claus, J. Cohen-Tanugi, S. Condamoor, J. Conrad, R. Corbet, S. Cutini, D. S. Davis, M. DeKlotz, C. D. Dermer, A. de Angelis, F. de Palma, S. W. Digel, P. Dizon, M. Dormody, E. D. E. Silva, P. S. Drell, R. Dubois, D. Dumora, Y. Edmonds, D. Fabiani, C. Farnier, C. Favuzzi, E. C. Ferrara, O. Ferreira, Z. Fewtrell, D. L. Flath, P. Fleury, W. B. Focke, K. Fouts, M. Frailis, D. Freytag, Y. Fukazawa, S. Funk, P. Fusco, F. Garganov, D. Gasparrini, N. Gehrelscao, S. Germani, B. Giebels, N. Giglietto, F. Giordano, T. Glanzman, G. Godfrey, J. Goodman, I. A. Grenier, M. H. Grondin, J. E. Grove, L. Guillemot, et al. The on-orbit calibration of the fermi large area telescope. *Astroparticle Physics*, 32(3-4):193–219, 2009. ISSN 0927-6505. doi: 10.1016/j.astropartphys.2009.08.002. URL <GotoISI>://WOS:000272276400005.

[6] A. A. Abdo, M. Ackermann, M. Ajello, W. B. Atwood, M. Axelsson, L. Baldini, J. Ballet, G. Barbiellini, M. G. Baring, D. Bastieri, B. M. Baughman, K. Bechtol, R. Bellazzini, B. Berenji, G. F. Bignami, R. D. Blandford, E. D. Bloom, E. Bonamente, A. W. Borgland, J. Bregeon, A. Brez, M. Brigida, P. Bruel, T. H. Burnett, G. A. Caliandro, R. A. Cameron, F. Camilo, P. A. Caraveo, P. Carlson, J. M. Casandjian, C. Cecchi, O. Celik, E. Charles, A. Chekhtman, C. C. Cheung, J. Chiang, S. Ciprini, R. Claus, I. Cognard, J. Cohen-Tanugi, L. R. Cominsky, J. Conrad, R. Corbet, S. Cutini, C. D. Dermer, G. Desvignes, A. de Angelis, A. de Luca, F. de Palma, S. W. Digel,

M. Dormody, E. D. E. Silva, P. S. Drell, R. Dubois, D. Dumora, Y. Edmonds, C. Farnier, C. Favuzzi, S. J. Fegan, W. B. Focke, M. Frailis, P. C. C. Freire, Y. Fukazawa, S. Funk, P. Fusco, F. Gargano, D. Gasparrini, N. Gehrels, S. Germani, B. Giebels, N. Giglietto, F. Giordano, T. Glanzman, G. Godfrey, I. A. Grenier, M. H. Grondin, J. E. Grove, L. Guillemot, S. Guiriec, Y. Hanabata, A. K. Harding, M. Hayashida, E. Hays, G. Hobbs, R. E. Hughes, G. Johannesson, A. S. Johnson, R. P. Johnson, T. J. Johnson, W. N. Johnson, S. Johnston, T. Kamae, H. Katagiri, J. Kataoka, N. Kawai, M. Kerr, J. Knodlseder, M. L. Kocian, M. Kramer, M. Kuss, et al. A population of gamma-ray millisecond pulsars seen with the fermi large area telescope. *Science*, 325 (5942):848–852, 2009. ISSN 0036-8075. doi: 10.1126/science.1176113.

[7] A. A. Abdo, M. Ackermann, M. Ajello, W. B. Atwood, M. Axelsson, L. Baldini, J. Ballet, G. Barbiellini, D. Bastieri, B. M. Baughman, K. Bechtol, R. Bellazzini, B. Berenji, R. D. Blandford, E. D. Bloom, E. Bonamente, A. W. Borgland, J. Bregeon, A. Brez, M. Brigida, P. Bruel, T. H. Burnett, G. A. Caliandro, R. A. Cameron, P. A. Caraveo, J. M. Casandjian, C. Cecchi, O. Celik, E. Charles, S. Chaty, A. Chekhtman, C. C. Cheung, J. Chiang, S. Ciprini, R. Claus, J. Cohen-Tanugi, J. Conrad, S. Cutini, C. D. Dermer, F. de Palma, S. W. Digel, M. Dormody, E. D. E. Silva, P. S. Drell, R. Dubois, D. Dumora, C. Farnier, C. Favuzzi, S. J. Fegan, W. B. Focke, M. Frailis, Y. Fukazawa, P. Fusco, F. Gargano, D. Gasparrini, N. Gehrels, S. Germani, B. Giebels, N. Giglietto, F. Giordano, T. Glanzman, G. Godfrey, I. A. Grenier, J. E. Grove, L. Guillemot, S. Guiriec, Y. Hanabata, A. K. Harding, M. Hayashida, E. Hays, D. Horan, R. E. Hughes, G. Johannesson, A. S. Johnson, R. P. Johnson, T. J. Johnson, W. N. Johnson, T. Kamae, H. Katagiri, N. Kawai, M. Kerr, J. Knodlseder, F. Kuehn, M. Kuss, J. Lande, L. Latronico, M. Lemoine-Goumard, F. Longo, F. Loparco, B. Lott, M. N. Lovellette, P. Lubrano, A. Makeev, M. N. Mazziotta, W. McConville, J. E. McEnery, C. Meurer, P. F. Michelson, W. Mitthumsiri, T. Mizuno, et al. Detection of high-energy gamma-ray emission from the globular cluster 47 tucanae with fermi. *Science*, 325(5942):845–848, 2009. ISSN 0036-8075. doi: 10.1126/science.1177023. URL <GotoISI>://WOS:000269242400038.

[8] A. A. Abdo, M. Ackermann, M. Ajello, A. Allafort, E. Antolini, W. B. Atwood, M. Axelsson, L. Baldini, J. Ballet, G. Barbiellini, D. Bastieri, B. M. Baughman, K. Bechtol, R. Bellazzini, F. Belli, B. Berenji, D. Bisello, R. D. Blandford, E. D. Bloom, E. Bonamente, J. Bonnell, A. W. Borgland, A. Bouvier, J. Bregeon, A. Brez, M. Brigida, P. Bruel, T. H. Burnett, G. Busetto, S. Buson, G. A. Caliandro, R. A. Cameron, R. Campana, B. Canadas, P. A. Caraveo, S. Carrigan, J. M. Casandjian,

E. Cavazzuti, M. Ceccanti, C. Cecchi, O. Celik, E. Charles, A. Chekhtman, C. C. Cheung, J. Chiang, A. N. Cillis, S. Ciprini, R. Claus, J. Cohen-Tanugi, J. Conrad, R. Corbet, D. S. Davis, M. DeKlotz, P. R. den Hartog, C. D. Dermer, A. de Angelis, A. de Luca, F. de Palma, S. W. Digel, M. Dormody, E. D. E. Silva, P. S. Drell, R. Dubois, D. Dumora, D. Fabiani, C. Farnier, C. Favuzzi, S. J. Fegan, E. C. Ferrara, W. B. Focke, P. Fortin, M. Frailis, Y. Fukazawa, S. Funk, P. Fusco, F. Gargano, D. Gasparrini, N. Gehrels, S. Germani, G. Giavitto, B. Giebels, N. Giglietto, P. Giommi, F. Giordano, M. Giroletti, T. Glanzman, G. Godfrey, I. A. Grenier, M. H. Grondin, J. E. Grove, L. Guillemot, S. Guiriec, M. Gustafsson, D. Hadasch, Y. Hanabata, A. K. Harding, M. Hayashida, E. Hays, S. E. Healey, A. B. Hill, et al. Fermi large area telescope first source catalog. *Astrophysical Journal Supplement Series*, 188 (2):405–436, 2010. ISSN 0067-0049. doi: 10.1088/0067-0049/188/2/405. URL <GotoISI>://WOS:000278969400004.

[9] A. A. Abdo, M. Ackermann, M. Ajello, W. B. Atwood, L. Baldini, J. Ballet, G. Barbiellini, D. Bastieri, K. Bechtol, R. Bellazzini, B. Berenji, R. D. Blandford, E. D. Bloom, E. Bonamente, A. W. Borgland, A. Bouvier, T. J. Brandt, J. Bregeon, A. Brez, M. Brigida, P. Bruel, R. Buehler, T. H. Burnett, S. Buson, G. A. Caliandro, R. A. Cameron, P. A. Caraveo, S. Carrigan, J. M. Casandjian, C. Cecchi, O. Celik, E. Charles, S. Chaty, A. Chekhtman, C. C. Cheung, J. Chiang, S. Ciprini, R. Claus, J. Cohen-Tanugi, J. Conrad, S. Corbel, R. Corbet, M. E. DeCesar, P. R. den Hartog, C. D. Dermer, F. de Palma, S. W. Digel, D. Donato, E. D. E. Silva, P. S. Drell, R. Dubois, G. Dubus, D. Dumora, C. Favuzzi, S. J. Fegan, E. C. Ferrara, P. Fortin, M. Frailis, L. Fuhrmann, Y. Fukazawa, S. Funk, P. Fusco, F. Gargano, D. Gasparrini, N. Gehrels, S. Germani, N. Giglietto, F. Giordano, M. Giroletti, T. Glanzman, G. Godfrey, I. A. Grenier, M. H. Grondin, J. E. Grove, S. Guiriec, D. Hadasch, A. K. Harding, M. Hayashida, E. Hays, S. E. Healey, A. B. Hill, D. Horan, R. E. Hughes, R. Itoh, P. Jean, G. Johannesson, A. S. Johnson, R. P. Johnson, T. J. Johnson, W. N. Johnson, T. Kamae, H. Katagiri, J. Kataoka, M. Kerr, J. Knodlseder, E. Koerding, M. Kuss, J. Lande, S. H. Lee, M. Lemoine-Goumard, et al. Gamma-ray emission concurrent with the nova in the symbiotic binary v407 cygni. *Science*, 329(5993):817–821, 2010. ISSN 0036-8075. doi: 10.1126/science.1192537. URL <GotoISI>://WOS:000280809900044.

[10] A. A. Abdo, M. Ackermann, M. Ajello, L. Baldini, J. Ballet, G. Barbiellini, D. Bastieri, R. Bellazzini, R. D. Blandford, E. D. Bloom, E. Bonamente, A. W. Borgland, A. Bouvier, T. J. Brandt, J. Bregeon, M. Brigida, P. Bruel, R. Buehler, S. Buson, G. A. Caliandro, R. A. Cameron, P. A. Caraveo, S. Carrigan, J. M. Casandjian,

E. Charles, S. Chaty, A. Chekhtman, C. C. Cheung, J. Chiang, S. Ciprini, R. Claus, J. Cohen-Tanugi, J. Conrad, M. E. DeCesar, C. D. Dermer, F. de Palma, S. W. Digel, E. D. E. Silva, P. S. Drell, R. Dubois, D. Dumora, C. Favuzzi, P. Fortin, M. Frailis, Y. Fukazawa, P. Fusco, F. Gargano, D. Gasparrini, N. Gehrels, S. Germani, N. Giglietto, F. Giordano, T. Glanzman, G. Godfrey, I. Grenier, M. H. Grondin, J. E. Grove, L. Guillemot, S. Guiriec, D. Hadasch, A. K. Harding, E. Hays, P. Jean, G. Johannesson, T. J. Johnson, W. N. Johnson, T. Kamae, H. Katagiri, J. Kataoka, M. Kerr, J. Knodlseder, M. Kuss, J. Lande, L. Latronico, S. H. Lee, M. Lemoine-Goumard, M. L. Garde, F. Longo, F. Loparco, M. N. Lovellette, P. Lubrano, A. Makeev, M. N. Mazziotta, P. F. Michelson, W. Mitthumsiri, T. Mizuno, C. Monte, M. E. Monzani, A. Morselli, I. V. Moskalenko, S. Murgia, M. Naumann-Godo, P. L. Nolan, J. P. Norris, E. Nuss, T. Ohsugi, N. Omodei, E. Orlando, J. F. Ormes, B. Pancrazi, et al. A population of gamma-ray emitting globular clusters seen with the fermi large area telescope. *Astronomy Astrophysics*, 524:11, 2010. ISSN 0004-6361. doi: 10.1051/0004-6361/201014458. URL <GotoISI>://WOS:000284625300024.

[11] A. A. Abdo, M. Ajello, A. Allafort, L. Baldini, J. Ballet, G. Barbiellini, M. G. Baring, D. Bastieri, A. Belfiore, R. Bellazzini, B. Bhattacharyya, E. Bissaldi, E. D. Bloom, E. Bonamente, E. Bottacini, T. J. Brandt, J. Bregeon, M. Brigida, P. Bruel, R. Buehler, M. Burgay, T. H. Burnett, G. Busetto, S. Buson, G. A. Caliandro, R. A. Cameron, F. Camilo, P. A. Caraveo, J. M. Casandjian, C. Cecchi, O. Celik, E. Charles, S. Chaty, R. C. G. Chaves, A. Chekhtman, A. W. Chen, J. Chiang, G. Chiaro, S. Ciprini, R. Claus, I. Cognard, J. Cohen-Tanugi, L. R. Cominsky, J. Conrad, S. Cutini, F. D'Ammando, A. De Angelis, M. E. DeCesar, A. De Luca, P. R. Den Hartog, F. De Palma, C. D. Dermer, G. Desvignes, S. W. Digel, L. Di Venere, P. S. Drell, A. Drlica-Wagner, R. Dubois, D. Dumora, C. M. Espinoza, L. Falletti, C. Favuzzi, E. C. Ferrara, W. B. Focke, A. Franckowiak, P. C. C. Freire, S. Funk, P. Fusco, F. Gargano, D. Gasparrini, S. Germani, N. Giglietto, P. Giommi, F. Giordano, M. Giroletti, T. Glanzman, G. Godfrey, E. V. Gotthelf, I. A. Grenier, M. H. Grondin, J. E. Grove, L. Guillemot, S. Guiriec, D. Hadasch, Y. Hanabata, A. K. Harding, M. Hayashida, E. Hays, J. Hessels, J. Hewitt, A. B. Hill, D. Horan, X. Hou, R. E. Hughes, M. S. Jackson, G. H. Janssen, T. Jogler, G. Johannesson, R. P. Johnson, A. S. Johnson, et al. The second fermi large area telescope catalog of gamma-ray pulsars. *Astrophysical Journal Supplement Series*, 208(2):59, 2013. ISSN 0067-0049. doi: 10.1088/0067-0049/208/2/17. URL <GotoISI>://WOS:000325276600004.

[12] S. Abdollahi, F. Acero, M. Ackermann, M. Ajello, W. B. Atwood, M. Axelsson, L. Baldini, J. Ballet, G. Barbiellini, D. Bastieri, and et al. Fermi large area telescope fourth source catalog. *The Astrophysical Journal Supplement Series*, 247(1):33, Mar 2020. ISSN 1538-4365. doi: 10.3847/1538-4365/ab6bcb. URL http://dx.doi.org/10.3847/1538-4365/ab6bcb.

[13] S. Abdollahi, F. Acero, M. Ackermann, M. Ajello, W. B. Atwood, M. Axelsson, L. Baldini, J. Ballet, G. Barbiellini, D. Bastieri, J. B. Gonzalez, R. Bellazzini, A. Berretta, E. Bissaldi, R. D. Blandford, E. D. Bloom, R. Bonino, E. Bottacini, T. J. Brandt, J. Bregeon, P. Bruel, R. Buehler, T. H. Burnett, S. Buson, R. A. Cameron, R. Caputo, P. A. Caraveo, J. M. Casandjian, D. Castro, E. Cavazzuti, E. Charles, S. Chaty, S. Chen, C. C. Cheung, G. Chiaro, S. Ciprini, J. Cohen-Tanugi, L. R. Cominsky, J. Coronado-Blazquez, D. Costantin, A. Cuoco, S. Cutini, F. D'Ammando, M. DeKlotz, P. D. Luque, F. de Palma, A. Desai, S. W. Digel, N. Di Lalla, M. Di Mauro, L. Di Venere, A. Dominguez, D. Dumora, F. F. Dirirsa, S. J. Fegan, E. C. Ferrara, A. Franckowiak, Y. Fukazawa, S. Funk, P. Fusco, F. Gargano, D. Gaspanini, N. Giglietto, P. Giommi, F. Giordano, M. Giroletti, T. Glanzman, D. Green, I. A. Grenier, S. Griffin, M. H. Grondin, J. E. Grove, S. Guiriec, A. K. Harding, K. Hayashi, E. Hays, J. W. Hewitt, D. Horan, G. Johannesson, T. J. Johnson, T. Kamae, M. Kerr, D. Kocevski, M. Kovac'evic, M. Kuss, D. Landriu, S. Larsson, L. Latronico, M. Lemoine-Goumard, J. Li, I. Liodakis, F. Longo, F. Loparco, B. Lott, M. N. Lovellette, P. Lubrano, G. M. Madejski, S. Maldera, D. Malyshev, A. Manfreda, et al. Fermi large area telescope fourth source catalog. *Astrophysical Journal Supplement Series*, 247(1), 2020. ISSN 0067-0049. doi: 10.3847/1538-4365/ab6bcb. URL <GotoISI>://WOS:000520200200001.

[14] A. U. Abeysekara, A. Albert, R. Alfaro, C. Alvarez, J. D. Alvarez, R. Arceo, J. C. Arteaga-Velazquez, H. A. A. Solares, A. S. Barber, B. Baughman, N. Bautista-Elivar, J. B. Gonzalez, A. Becerril, E. Belmont-Moreno, S. Y. BenZvi, D. Berley, A. Bernal, J. Braun, C. Brisbois, K. S. Caballero-Mora, T. Capistran, A. Carraminana, S. Casanova, M. Castillo, U. Cotti, J. Cotzomi, S. C. de Leon, E. de la Fuente, C. De Leon, R. D. Hernandez, B. L. Dingus, M. A. DuVernois, J. C. Diaz-Velez, R. W. Ellsworth, K. Engel, D. W. Fiorino, N. Fraija, J. A. Garcia-Gonzalez, F. Garfias, M. Gerhardt, A. G. Munoz, M. M. Gonzalez, J. A. Goodman, Z. Hampel-Arias, J. P. Harding, S. Hernandez, A. Hernandez-Almada, J. Hinton, C. M. Hui, P. Huntemeyer, A. Iriarte, A. Jardin-Blicq, V. Joshi, S. Kaufmann, D. Kieda, A. Lara, R. J. Lauer, W. H. Lee, D. Lennarz, H. L. Vargas, J. T. Linnemann, A. L. Longinotti, G. L. Raya, R. Luna-Garcia, R. Lopez-Coto, K. Malone, S. S. Marinelli, O. Martinez,

I. Martinez-Castellanos, J. Martinez-Castro, H. Martinez-Huerta, J. A. Matthews, P. Miranda-Romagnoli, E. Moreno, M. Mostafa, L. Nellen, M. Newbold, M. U. Nisa, R. Noriega-Papaqui, R. Pelayo, J. Pretz, E. G. Perez-Perez, Z. Ren, C. D. Rho, C. Riviere, D. Rosa-Gonzalez, M. Rosenberg, E. Ruiz-Velasco, H. Salazar, F. S. Greus, A. Sandoval, M. Schneider, H. Schoorlemmer, G. Sinnis, A. J. Smith, R. W. Springer, P. Surajbali, I. Taboada, O. Tibolla, K. Tollefson, et al. The 2hwc hawc observatory gamma-ray catalog. *Astrophysical Journal*, 843(1), 2017. ISSN 0004-637X. doi: 10.3847/1538-4357/aa7556. URL <GotoISI>://WOS:000404605200004.

[15] A. Abramowski, F. Acero, F. Aharonian, A. G. Akhperjanian, G. Anton, A. Balzer, A. Barnacka, U. B. de Almeida, Y. Becherini, J. Becker, B. Behera, K. Bernlohr, A. Bochow, C. Boisson, J. Bolmont, P. Bordas, J. Brucker, F. Brun, P. Brun, T. Bulik, I. Busching, S. Carrigan, S. Casanova, M. Cerruti, P. M. Chadwick, A. Charbonnier, R. C. G. Chaves, A. Cheesebrough, L. M. Chounet, A. C. Clapson, G. Coignet, G. Cologna, J. Conrad, M. Dalton, M. K. Daniel, I. D. Davids, B. Degrange, C. Deil, H. J. Dickinson, A. Djannati-Atai, W. Domainko, L. O. Drury, F. Dubois, G. Dubus, K. Dutson, J. Dyks, M. Dyrda, K. Egberts, P. Eger, P. Espigat, L. Fallon, C. Farnier, S. Fegan, F. Feinstein, M. V. Fernandes, A. Fiasson, G. Fontaine, A. Forster, M. Fussling, Y. A. Gallant, H. Gast, L. Gerard, D. Gerbig, B. Giebels, J. F. Glicenstein, B. Gluck, P. Goret, D. Goring, S. Haffner, J. D. Hague, D. Hampf, M. Hauser, S. Heinz, G. Heinzelmann, G. Henri, G. Hermann, J. A. Hinton, A. Hoffmann, W. Hofmann, P. Hofverberg, M. Holler, D. Horns, A. Jacholkowska, O. C. de Jager, C. Jahn, M. Jamrozy, I. Jung, M. A. Kastendieck, K. Katarzynski, U. Katz, S. Kaufmann, D. Keogh, D. Khangulyan, B. Khelifi, D. Klochkov, W. Kluzniak, T. Kneiske, N. Komin, K. Kosack, R. Kossakowski, et al. Very-high-energy gamma-ray emission from the direction of the galactic globular cluster terzan 5. *Astronomy Astrophysics*, 531:5, 2011. ISSN 1432-0746. doi: 10.1051/0004-6361/201117171. URL <GotoISI>://WOS:000293017700184.

[16] A. Abramowski, F. Acero, F. Aharonian, A. G. Akhperjanian, G. Anton, S. Balenderan, A. Balzer, A. Barnacka, Y. Becherini, J. B. Tjus, K. Bernlohr, E. Birsin, J. Biteau, A. Bochow, C. Boisson, J. Bolmont, P. Bordas, J. Brucker, F. Brun, P. Brun, T. Bulik, S. Carrigan, S. Casanova, M. Cerruti, P. M. Chadwick, R. C. G. Chaves, A. Cheesebrough, S. Colafrancesco, G. Cologna, J. Conrad, C. Couturier, M. Dalton, M. K. Daniel, I. D. Davids, B. Degrange, C. Deil, P. deWilt, H. J. Dickinson, A. Djannati-Atai, W. Domainko, L. O. Drury, G. Dubus, K. Dutson, J. Dyks, M. Dyrda, K. Egberts, P. Eger, P. Espigat, L. Fallon, C. Farnier, S. Fegan, F. Feinstein, M. V.

Fernandes, D. Fernandez, A. Fiasson, G. Fontaine, A. Forster, M. Fussling, M. Gajdus, Y. A. Gallant, T. Garrigoux, H. Gast, B. Giebels, J. F. Glicenstein, B. Gluck, D. Goring, M. H. Grondin, M. Grudzinska, S. Haffner, J. D. Hague, J. Hahn, D. Hampf, J. Harris, S. Heinz, G. Heinzelmann, G. Henri, G. Hermann, A. Hillert, J. A. Hinton, W. Hofmann, P. Hofverberg, M. Holler, D. Horns, A. Jacholkowska, C. Jahn, M. Jamrozy, I. Jung, M. A. Kastendieck, K. Katarzynski, U. Katz, S. Kaufmann, B. Khelifi, S. Klepser, D. Klochkov, W. Kluzniak, T. Kneiske, D. Kolitzus, N. Komin, K. Kosack, R. Kossakowski, et al. Search for very-high-energy gamma-ray emission from galactic globular clusters with hess. *Astronomy Astrophysics*, 551:8, 2013. ISSN 0004-6361. doi: 10.1051/0004-6361/201220719.

[17] V. A. Acciari, S. Ansoldi, L. A. Antonelli, A. A. Engels, D. Baack, A. Babic, B. Banerjee, U. B. de Almeida, J. A. Barrio, J. B. Gonzalez, W. Bednarek, E. Bernardini, A. Berti, J. Besenrieder, W. Bhattacharyya, C. Bigongiari, A. Biland, O. Blanch, G. Bonnoli, G. Busetto, R. Carosi, G. Ceribella, S. Cikota, S. M. Colak, P. Colin, E. Colombo, J. L. Contreras, J. Cortina, S. Covino, V. D'Elia, P. Da Vela, F. Dazzi, A. De Angelis, B. De Lotto, M. Delfino, J. Delgado, F. Di Pierro, E. D. Espinera, A. Dominguez, D. D. Prester, D. Dorner, M. Doro, S. Einecke, D. Elsaesser, V. F. Ramazani, A. Fattorini, A. Fernandez-Barral, G. Ferrara, D. Fidalgo, L. Foffano, M. V. Fonseca, L. Font, C. Fruck, D. Galindo, S. Gallozzi, R. J. G. Lopez, M. Garczarczyk, S. Gasparyan, M. Gaug, P. Giammaria, N. Godinovic, D. Green, D. Guberman, D. Hadasch, A. Hahn, J. Herrera, J. Hoang, D. Hrupec, S. Inoue, K. Ishio, Y. Iwamura, H. Kubo, J. Kushida, D. Kuvezdic, A. Lamastra, D. Lelas, F. Leone, E. Lindfors, S. Lombardi, F. Longo, M. Lopez, A. Lopez-Oramas, B. M. D. Fraga, C. Maggio, P. Majumdar, M. Makariev, M. Mallamaci, G. Maneva, M. Manganaro, K. Mannheim, L. Maraschi, M. Mariotti, M. Martinez, S. Masuda, D. Mazin, M. Minev, J. M. Miranda, R. Mirzoyan, E. Molina, A. Moralejo, et al. Deep observations of the globular cluster m15 with the magic telescopes. *Monthly Notices of the Royal Astronomical Society*, 484(2):2876–2885, 2019. ISSN 0035-8711. doi: 10.1093/mnras/stz179. URL <GotoISI>://WOS:000462302600103.

[18] F. Acero, M. Ackermann, M. Ajello, A. Albert, W. B. Atwood, M. Axelsson, L. Baldini, J. Ballet, G. Barbiellini, D. Bastieri, A. Belfiore, R. Bellazzini, E. Bissaldi, R. D. Blandford, E. D. Bloom, J. R. Bogart, R. Bonino, E. Bottacini, J. Bregeon, R. J. Britto, P. Bruel, R. Buehler, T. H. Burnett, S. Buson, G. A. Caliandro, R. A. Cameron, R. Caputo, M. Caragiulo, P. A. Caraveo, J. M. Casandjian, E. Cavazzuti, E. Charles, R. C. G. Chaves, A. Chekhtman, C. C. Cheung, J. Chiang, G. Chiaro, S. Ciprini, R. Claus,

J. Cohen-Tanugi, L. R. Cominsky, J. Conrad, S. Cutini, F. D'Ammando, A. de Angelis, M. DeKlotz, F. de Palma, R. Desiante, S. W. Digel, L. Di Venere, P. S. Drell, R. Dubois, D. Dumora, C. Favuzzi, S. J. Fegan, E. C. Ferrara, J. Finke, A. Franckowiak, Y. Fukazawa, S. Funk, P. Fusco, F. Gargano, D. Gasparrini, B. Giebels, N. Giglietto, P. Giommi, F. Giordano, M. Giroletti, T. Glanzman, G. Godfrey, I. A. Grenier, M. H. Grondin, J. E. Grove, L. Guillemot, S. Guiriec, D. Hadasch, A. K. Harding, E. Hays, J. W. Hewitt, A. B. Hill, D. Horan, G. Iafrate, T. Jogler, G. Johannesson, R. P. Johnson, A. S. Johnson, T. J. Johnson, W. N. Johnson, T. Kamae, J. Kataoka, J. Katsuta, M. Kuss, G. La Mura, D. Landriu, S. Larsson, L. Latronico, M. Lemoine-Goumard, J. Li, L. Li, F. Longo, et al. Fermi large area telescope third source catalog. *Astrophysical Journal Supplement Series*, 218(2):41, 2015. ISSN 0067-0049. doi: 10.1088/0067-0049/218/2/23. URL <GotoISI>://WOS:000357122200009.

[19] F. Acero, M. Ackermann, M. Ajello, A. Albert, W. B. Atwood, M. Axelsson, L. Baldini, J. Ballet, G. Barbiellini, D. Bastieri, A. Belfiore, R. Bellazzini, E. Bissaldi, R. D. Blandford, E. D. Bloom, J. R. Bogart, R. Bonino, E. Bottacini, J. Bregeon, R. J. Britto, P. Bruel, R. Buehler, T. H. Burnett, S. Buson, G. A. Caliandro, R. A. Cameron, R. Caputo, M. Caragiulo, P. A. Caraveo, J. M. Casandjian, E. Cavazzuti, E. Charles, R. C. G. Chaves, A. Chekhtman, C. C. Cheung, J. Chiang, G. Chiaro, S. Ciprini, R. Claus, J. Cohen-Tanugi, L. R. Cominsky, J. Conrad, S. Cutini, F. D'Ammando, A. de Angelis, M. DeKlotz, F. de Palma, R. Desiante, S. W. Digel, L. Di Venere, P. S. Drell, R. Dubois, D. Dumora, C. Favuzzi, S. J. Fegan, E. C. Ferrara, J. Finke, A. Franckowiak, Y. Fukazawa, S. Funk, P. Fusco, F. Gargano, D. Gasparrini, B. Giebels, N. Giglietto, P. Giommi, F. Giordano, M. Giroletti, T. Glanzman, G. Godfrey, I. A. Grenier, M. H. Grondin, J. E. Grove, L. Guillemot, S. Guiriec, D. Hadasch, A. K. Harding, E. Hays, J. W. Hewitt, A. B. Hill, D. Horan, G. Iafrate, T. Jogler, G. Johannesson, R. P. Johnson, A. S. Johnson, T. J. Johnson, W. N. Johnson, T. Kamae, J. Kataoka, J. Katsuta, M. Kuss, G. La Mura, D. Landriu, S. Larsson, L. Latronico, M. Lemoine-Goumard, J. Li, L. Li, F. Longo, et al. Fermi large area telescope third source catalog. *Astrophysical Journal Supplement Series*, 218(2):41, 2015. ISSN 0067-0049. doi: 10.1088/0067-0049/218/2/23. URL <GotoISI>://WOS:000357122200009.

[20] M. Ackermann, M. Ajello, A. Albert, A. Allafort, W. B. Atwood, M. Axelsson, L. Baldini, J. Ballet, G. Barbiellini, D. Bastieri, K. Bechtol, R. Bellazzini, E. Bissaldi, R. D. Blandford, E. D. Bloom, J. R. Bogart, E. Bonamente, A. W. Borgland, E. Bottacini, A. Bouvier, T. J. Brandt, J. Bregeon, M. Brigida, P. Bruel, R. Buehler, T. H. Burnett, S. Buson, G. A. Caliandro, R. A. Cameron, P. A. Caraveo, J. M. Casandjian, E. Cavaz-

zuti, C. Cecchi, O. Celik, E. Charles, R. C. G. Chaves, A. Chekhtman, C. C. Cheung, J. Chiang, S. Ciprini, R. Claus, J. Cohen-Tanugi, J. Conrad, R. Corbet, S. Cutini, F. D'Ammando, D. S. Davis, A. de Angelis, M. DeKlotz, F. de Palma, C. D. Dermer, S. W. Digel, E. do Couto e Silva, P. S. Drell, A. Drlica-Wagner, R. Dubois, C. Favuzzi, S. J. Fegan, E. C. Ferrara, W. B. Focke, P. Fortin, Y. Fukazawa, S. Funk, P. Fusco, F. Gargano, D. Gasparrini, N. Gehrels, B. Giebels, N. Giglietto, F. Giordano, M. Giroletti, T. Glanzman, G. Godfrey, I. A. Grenier, J. E. Grove, S. Guiriec, D. Hadasch, M. Hayashida, E. Hays, D. Horan, X. Hou, R. E. Hughes, M. S. Jackson, T. Jogler, G. Johannesson, R. P. Johnson, T. J. Johnson, W. N. Johnson, T. Kamae, H. Katagiri, J. Kataoka, M. Kerr, J. Knoedlseder, M. Kuss, J. Lande, S. Larsson, L. Latronico, C. Lavalley, M. Lemoine-Goumard, F. Longo, et al. The fermi large area telescope on orbit: Event classification, instrument response functions, and calibration. *Astrophysical Journal Supplement Series*, 203(1):4–4, 2012. ISSN 0067-0049. URL <GotoISI>://CCC:000310908300004.

[21] M. Ackermann, M. Ajello, A. Albert, A. Allafort, E. Antolini, L. Baldini, J. Ballet, G. Barbiellini, D. Bastieri, K. Bechtol, R. Bellazzini, R. D. Blandford, E. D. Bloom, E. Bonamente, E. Bottacini, A. Bouvier, T. J. Brandt, J. Bregeon, M. Brigida, P. Bruel, R. Buehler, S. Buson, G. A. Caliandro, R. A. Cameron, P. A. Caraveo, E. Cavazzuti, C. Cecchi, E. Charles, A. Chekhtman, C. C. Cheung, J. Chiang, G. Chiaro, S. Ciprini, R. Claus, J. Cohen-Tanugi, J. Conrad, S. Cutini, M. Dalton, F. D'Ammando, A. de Angelis, F. de Palma, C. D. Dermer, L. Di Venere, P. S. Drell, A. Drlica-Wagner, C. Favuzzi, S. J. Fegan, E. C. Ferrara, W. B. Focke, A. Franckowiak, Y. Fukazawa, S. Funk, P. Fusco, F. Gargano, D. Gasparrini, S. Germani, N. Giglietto, F. Giordano, M. Giroletti, T. Glanzman, G. Godfrey, I. A. Grenier, M. H. Grondin, J. E. Grove, S. Guiriec, D. Hadasch, Y. Hanabata, A. K. Harding, M. Hayashida, E. Hays, J. Hewitt, A. B. Hill, D. Horan, X. Hou, R. E. Hughes, Y. Inoue, M. S. Jackson, T. Jogler, G. Johannesson, W. N. Johnson, T. Kamae, J. Kataoka, T. Kawano, J. Knoedlseder, M. Kuss, J. Lande, S. Larsson, L. Latronico, M. Lemoine-Goumard, F. Longo, F. Loparco, B. Lott, M. N. Lovellette, P. Lubrano, M. Mayer, M. N. Mazziotta, J. E. McEnery, P. F. Michelson, W. Mitthumsiri, T. Mizuno, et al. The fermi all-sky variability analysis: A list of flaring gamma-ray sources and the search for transients in our galaxy. *Astrophysical Journal*, 771(1), 2013. ISSN 0004-637X. doi: 10.1088/0004-637x/771/1/57. URL <GotoISI>://WOS:000321274200057.

[22] F. Aharonian, A. G. Akhperjanian, A. R. Bazer-Bachi, M. Beilicke, W. Benbow, D. Berge, K. Bernlohr, C. Boisson, O. Bolz, V. Borrel, I. Braun, F. Breitling,

A. M. Brown, R. Buhler, I. Busching, S. Carrigan, P. M. Chadwick, L. M. Chounet, R. Cornils, L. Costamante, B. Degrange, H. J. Dickinson, A. Djannati-Atai, L. O. C. Drury, G. Dubus, K. Egberts, D. Emmanoulopoulos, P. Espigat, F. Feinstein, E. Ferrero, A. Fiasson, G. Fontaine, S. Funk, Y. A. Gallant, B. Giebels, J. F. Glicenstein, P. Goret, C. Hadjichristidis, D. Hauser, M. Hauser, G. Heinzelmann, G. Henri, G. Hermann, J. A. Hinton, W. Hofmann, M. Holleran, D. Horns, A. Jacholkowska, O. C. de Jager, B. Khelifi, N. Komin, A. Konopelko, K. Kosack, I. J. Latham, R. Le Gallou, A. Lemiere, M. Lemoine-Goumard, T. Lohse, J. M. Martin, O. Martineau-Huynh, A. Marcowith, C. Masterson, T. J. L. McComb, M. de Naurois, D. Nedbal, S. J. Nolan, A. Noutsos, K. J. Orford, J. L. Osborne, M. Ouchrif, M. Panter, G. Pelletier, S. Pita, G. Puhlhofer, M. Punch, B. C. Raubenheimer, M. Raue, S. M. Rayner, A. Reimer, O. Reimer, J. Ripken, L. Rob, L. Rolland, G. Rowell, V. Sahakian, L. Sauge, S. Schlenker, R. Schlickeiser, U. Schwanke, H. Sol, D. Spangler, F. Spanier, R. Steenkamp, C. Stegmann, G. Superina, J. P. Tavernet, R. Terrier, C. G. Theoret, M. Tluczykont, C. van Eldik, et al. Observations of the crab nebula with hess. *Astronomy Astrophysics*, 457 (3):899–915, 2006. ISSN 0004-6361. doi: 10.1051/0004-6361:20065351. URL <GotoISI>://WOS:000240785500018.

[23] F. Aharonian, A. Akhperjanian, G. Anton, Ulisses Barres de Almeida, A. Bazer-Bachi, Y. Becherini, Bagmeet Behera, K. Bernlöhr, Cb Boisson, A. Bochow, V. Borrel, Isabel Braun, E. Brion, J. Brucker, Pierre Brun, R. Bühler, Tomasz Bulik, I. Büsching, T. Boutelier, and A. Zech. Hess upper limit on the very high energy -ray emission from the globular cluster 47 tucanae. *Astronomy and Astrophysics*, 499:273, 05 2009. doi: 10.1051/0004-6361/200811564.

[24] M. L. Ahnen, S. Ansoldi, L. A. Antonelli, C. Arcaro, A. Babic, B. Banerjee, P. Bangale, U. B. de Almeida, J. A. Barrio, J. B. Gonzalez, W. Bednarek, E. Bernardini, A. Berti, B. Biasuzzi, A. Biland, O. Blanch, S. Bonnefoy, G. Bonnoli, F. Borracci, T. Bretz, R. Carosi, A. Carosi, A. Chatterjee, P. Colin, E. Colombo, J. L. Contreras, J. Cortina, S. Covino, P. Cumani, P. Da Vela, F. Dazzi, A. De Angelis, B. De Lotto, E. D. Wilhelmi, F. Di Pierro, M. Doert, A. Dominguez, D. D. Prester, D. Dorner, M. Doro, S. Einecke, D. E. Glawion, D. Elsaesser, M. Engelkemeier, V. F. Ramazani, A. Fernandez-Barral, D. Fidalgo, M. V. Fonseca, L. Font, C. Fruck, D. Galindo, R. J. G. Lopez, M. Garczarczyk, M. Gaug, P. Giammaria, N. Godinovic, D. Gora, S. R. Gozzini, S. Griffiths, D. Guberman, D. Hadasch, A. Hahn, T. Hassan, M. Hayashida, J. Herrera, J. Hose, D. Hrupec, G. Hughes, K. Ishio, Y. Konno, H. Kubo, J. Kushida, D. Kuvezdic, D. Lelas, E. Lindfors, S. Lombardi, F. Longo, M. Lopez, P. Majumdar,

M. Makariev, G. Maneva, M. Manganaro, K. Mannheim, L. Maraschi, M. Mariotti, M. Martinez, D. Mazin, U. Menzel, R. Mirzoyan, A. Moralejo, V. Moreno, E. Moretti, V. Neustroev, A. Niedzwiecki, M. N. Rosillo, K. Nilsson, K. Nishijima, K. Noda, L. Nogues, S. Paiano, et al. Observation of the black widow b1957+20 millisecond pulsar binary system with the magic telescopes. *Monthly Notices of the Royal Astronomical Society*, 470(4):4608–4617, 2017. ISSN 0035-8711. doi: 10.1093/mnras/stx1405. URL <GotoISI>://WOS:000408207600060.

[25] M. Ajello, W. B. Atwood, L. Baldini, J. Ballet, G. Barbiellini, D. Bastieri, R. Bellazzini, E. Bissaldi, R. D. Blandford, E. D. Bloom, R. Bonino, J. Bregeon, R. J. Britto, P. Bruel, R. Buehler, S. Buson, R. A. Cameron, R. Caputo, M. Caragiulo, P. A. Caraveo, E. Cavazzuti, C. Cecchi, E. Charles, A. Chekhtman, C. C. Cheung, G. Chiaro, S. Ciprini, J. M. Cohen, D. Costantin, F. Costanza, A. Cuoco, S. Cutini, F. D'Ammando, F. de Palma, R. Desiante, S. W. Digel, N. Di Lalla, M. Di Mauro, L. Di Venere, A. Dominguez, P. S. Drell, D. Dumora, C. Favuzzi, S. J. Fegan, E. C. Ferrara, P. Fortin, A. Franckowiak, Y. Fukazawa, S. Funk, P. Fusco, F. Gargano, D. Gasparrini, N. Giglietto, P. Giommi, F. Giordano, M. Giroletti, T. Glanzman, D. Green, I. A. Grenier, M. H. Grondin, J. E. Grove, L. Guillemot, S. Guiriec, A. K. Harding, E. Hays, J. W. Hewitt, D. Horan, G. Johannesson, S. Kensei, M. Kuss, G. La Mura, S. Larsson, L. Latronico, M. Lemoine-Goumard, J. Li, F. Longo, F. Loparco, B. Lott, P. Lubrano, J. D. Magill, S. Maldera, A. Manfreda, M. N. Mazziotta, J. E. McEnery, M. Meyer, P. F. Michelson, N. Mirabal, W. Mitthumsiri, T. Mizuno, A. A. Moiseev, M. E. Monzani, A. Morselli, I. V. Moskalenko, M. Negro, E. Nuss, T. Ohsugi, N. Omodei, M. Orienti, E. Orlando, M. Palatiello, et al. 3fhl: The third catalog of hard fermi-lat sources. *Astrophysical Journal Supplement Series*, 232(2), 2017. ISSN 0067-0049. doi: 10.3847/1538-4365/aa8221. URL <GotoISI>://WOS:000411892800001.

[26] H. Akaike. A New Look at the Statistical Model Identification. *IEEE Transactions on Automatic Control*, 19:716–723, January 1974.

[27] A. Akmal, V. R. Pandharipande, and D. G. Ravenhall. Equation of state of nucleon matter and neutron star structure. *Physical Review C*, 58(3):1804–1828, 1998. ISSN 0556-2813. doi: 10.1103/PhysRevC.58.1804. URL <GotoISI>://WOS:000075896700051.

[28] J. Aleksic, S. Ansoldi, L. A. Antonelli, P. Antoranz, A. Babic, P. Bangale, M. Barcelo, J. A. Barrio, J. B. Gonzalez, W. Bednarek, E. Bernardini, B. Biasuzzi, A. Biland, M. Bitossi, O. Blanch, S. Bonnefoy, G. Bonnolic, F. Borracci, T. Bretzl, E. Carmona, A. Carosi, R. Cecchi, P. Colin, E. Colombo, J. L. Contreras, D. Corti, J. Cortina,

S. Covino, P. Da Vela, F. Dazzi, A. De Angelis, G. De Caneva, B. De Lotto, E. D. Wilhelmi, C. D. Mendez, A. Dettlaff, D. D. Prester, D. Dorner, M. Doro, S. Einecke, D. Eisenacher, D. Elsaesser, D. Fidalgo, D. Fink, M. V. Fonseca, L. Font, K. Frantzen, C. Fruck, D. Galindo, R. J. G. Lopez, M. Garczarczyk, D. G. Terrats, M. Gaug, G. Giavitto, N. Godinovic, A. G. Munoz, S. R. Gozzini, W. Haberer, D. Hadasch, Y. Hanabata, M. Hayashida, J. Herrera, D. Hildebrand, J. Hose, D. Hrupec, W. Idec, J. M. Illa, V. Kadenius, H. Kellermann, M. L. Knoetig, K. Kodani, Y. Konno, J. Krause, H. Kubo, J. Kushida, A. La Barbera, D. Lelas, J. L. Lemus, N. Lewandowska, E. Lindfors, S. Lombardi, F. Longo, M. Lopez, R. Lopez-Coto, A. Lopez-Oramas, A. Lorca, E. Lorenz, I. Lozano, M. Makariev, K. Mallot, G. Maneva, N. Mankuzhiyil, K. Mannheim, L. Maraschi, B. Marcote, M. Mariotti, M. Martinez, D. Mazin, U. Menzel, J. M. Miranda, et al. The major upgrade of the magic telescopes, part ii: A performance study using observations of the crab nebula. *Astroparticle Physics*, 72:76–94, 2016. ISSN 0927-6505. doi: 10.1016/j.astropartphys.2015.02.005. URL <GotoISI>://WOS:000362143000008.

[29] E. Aliu, H. Anderhub, L. A. Antonelli, P. Antoranz, M. Backes, C. Baixeras, J. A. Barrio, H. Bartko, D. Bastieri, J. K. Becker, W. Bednarek, K. Berger, E. Bernardini, C. Bigongiari, A. Biland, R. K. Bock, G. Bonnoli, P. Bordas, V. Bosch-Ramon, T. Bretz, I. Britvitch, M. Camara, E. Carmona, A. Chilingarian, S. Commichau, J. L. Contreras, J. Cortina, M. T. Costado, S. Covino, V. Curtef, F. Dazzi, A. De Angelis, E. D. C. del Pozo, R. de los Reyes, B. De Lotto, M. De Maria, F. De Sabata, C. D. Mendez, A. Dominguez, D. Dorner, M. Doro, D. Elsasser, M. Errando, M. Fagiolini, D. Ferenc, E. Fernandez, R. Firpo, M. V. Fonseca, L. Font, N. Galante, R. J. G. Lopez, M. Garczarczyk, M. Gaug, F. Goebel, D. Hadasch, M. Hayashida, A. Herrero, D. Hohne, J. Hose, C. C. Hsu, S. Huber, T. Jogler, D. Kranich, A. La Barbera, A. Laille, E. Leonardo, E. Lindfors, S. Lombardi, F. Longo, M. Lopez, E. Lorenz, P. Majumdar, G. Maneva, N. Mankuzhiyil, K. Mannheim, L. Maraschi, M. Mariotti, M. Martinez, D. Mazin, M. Meucci, M. Meyer, J. M. Miranda, R. Mirzoyan, M. Moles, A. Moralejo, D. Nieto, K. Nilsson, J. Ninkovic, N. Otte, I. Oya, R. Paoletti, J. M. Paredes, M. Pasanen, D. Pascoli, F. Pauss, R. G. Pegna, M. A. Perez-Torres, M. Persic, L. Peruzzo, A. Piccioli, et al. Observation of pulsed gamma-rays above 25 gev from the crab pulsar with magic. *Science*, 322(5905):1221–1224, 2008. ISSN 0036-8075. doi: 10.1126/science.1164718. URL <GotoISI>://WOS:000261033400034.

[30] M. A. Alpar, A. F. Cheng, M. A. Ruderman, and J. Shaham. A new class of radio pulsars. *Nature*, 300(5894):728–730, 1982. ISSN 0028-0836. doi: 10.1038/300728a0.

URL <GotoISI>://WOS:A1982PU97700046.

[31] R. Amato, A. D'Ai, M. Del Santo, D. de Martino, A. Marino, T. Di Salvo, R. Iaria, and T. Mineo. Search for multiwavelength emission from the binary millisecond pulsar psr j1836-2354a in the globular cluster m22. *Monthly Notices of the Royal Astronomical Society*, 486(3):3992–4000, 2019. ISSN 0035-8711. doi: 10.1093/mnras/stz1100. URL <GotoISI>://WOS:000474903500078.

[32] V. Anastassopoulos et al. New CAST Limit on the Axion-Photon Interaction. *Nature Phys.*, 13:584–590, 2017. doi: 10.1038/nphys4109.

[33] A. De Angelis, V. Tatischeff, I.A. Grenier, J. McEnery, M. Mallamaci, M. Tavani, U. Oberlack, L. Hanlon, R. Walter, A. Argan, P. Von Ballmoos, A. Bulgarelli, A. Bykov, M. Hernanz, G. Kanbach, I. Kuvvetli, M. Pearce, A. Zdziarski, J. Conrad, G. Ghisellini, A. Harding, J. Isern, M. Leising, F. Longo, G. Madejski, M. Martinez, M.N. Mazziotta, J.M. Paredes, M. Pohl, R. Rando, M. Razzano, A. Aboudan, M. Ackermann, A. Addazi, M. Ajello, C. Albertus, et al. Science with e-astrogam: A space mission for mev–gev gamma-ray astrophysics. *Journal of High Energy Astrophysics*, 19:1 – 106, 2018. ISSN 2214-4048. doi: https://doi.org/10.1016/j.jheap.2018.07.001. URL http://www.sciencedirect.com/science/article/pii/S2214404818300168.

[34] N. R. Arakelyan, S. V. Pilipenko, and N. I. Libeskind. Spatial distribution of globular clusters in the galaxy. *Monthly Notices of the Royal Astronomical Society*, 481(1): 918–929, 2018. ISSN 0035-8711. doi: 10.1093/mnras/sty2320. URL <GotoISI>://WOS:000449651400063.

[35] S. Archambault, A. Archer, W. Benbow, R. Bird, E. Bourbeau, A. Bouvier, M. Buchovecky, V. Bugaev, J.V. Cardenzana, M. Cerruti, and et al. Gamma-ray observations under bright moonlight with veritas. *Astroparticle Physics*, 91:34–43, May 2017. ISSN 0927-6505. doi: 10.1016/j.astropartphys.2017.03.001. URL http://dx.doi.org/10.1016/j.astropartphys.2017.03.001.

[36] Z. Arzoumanian, D. J. Nice, J. H. Taylor, and S. E. Thorsett. Timing behavior of 96 radio pulsars. *Astrophysical Journal*, 422(2):671–680, 1994. ISSN 0004-637X. doi: 10.1086/173760. URL <GotoISI>://WOS:A1994MZ63600023.

[37] S. J. Asztalos, G. Carosi, C. Hagmann, D. Kinion, K. van Bibber, M. Hotz, L. J Rosenberg, G. Rybka, J. Hoskins, J. Hwang, P. Sikivie, D. B. Tanner, R. Bradley, and J. Clarke. Squid-based microwave cavity search for dark-matter axions. *Phys.*

Rev. Lett., 104:041301, Jan 2010. doi: 10.1103/PhysRevLett.104.041301. URL https://link.aps.org/doi/10.1103/PhysRevLett.104.041301.

[38] W. Atwood, A. Albert, L. Baldini, M. Tinivella, J. Bregeon, M. Pesce-Rollins, C. Sgrò, P. Bruel, E. Charles, A. Drlica-Wagner, A. Franckowiak, T. Jogler, L. Rochester, T. Usher, M. Wood, J. Cohen-Tanugi, and S. Zimmer. Pass 8: Toward the full realization of the fermi-lat scientific potential, 2013.

[39] W. B. Atwood, A. A. Abdo, M. Ackermann, W. Althouse, B. Anderson, M. Axelsson, L. Baldini, J. Ballet, D. L. Band, G. Barbiellini, J. Bartelt, D. Bastieri, B. M. Baughman, K. Bechtol, D. Bederede, F. Bellardi, R. Bellazzini, B. Berenji, G. F. Bignami, D. Bisello, E. Bissaldi, R. D. Blandford, E. D. Bloom, J. R. Bogart, E. Bonamente, J. Bonnell, A. W. Borgland, A. Bouvier, J. Bregeon, A. Brez, M. Brigida, P. Bruel, T. H. Burnett, G. Busetto, G. A. Caliandro, R. A. Cameron, P. A. Caraveo, S. Carius, P. Carlson, J. M. Casandjian, E. Cavazzuti, M. Ceccanti, C. Cecchi, E. Charles, A. Chekhtman, C. C. Cheung, J. Chiang, R. Chipaux, A. N. Cillis, S. Ciprini, R. Claus, J. Cohen-Tanugi, S. Condamoor, J. Conrad, R. Corbet, L. Corucci, L. Costamante, S. Cutini, D. S. Davis, D. Decotigny, M. DeKlotz, C. D. Dermer, A. De Angelis, S. W. Digel, Edce Silva, P. S. Drell, R. Dubois, D. Dumora, Y. Edmonds, D. Fabiani, C. Farnier, C. Favuzzi, D. L. Flath, P. Fleury, W. B. Focke, S. Funk, P. Fusco, F. Gargano, D. Gasparrini, N. Gehrels, F. X. Gentit, S. Germani, B. Giebels, N. Giglietto, P. Giommi, F. Giordano, T. Glanzman, G. Godfrey, I. A. Grenier, M. H. Grondin, J. E. Grove, L. Guillemot, S. Guiriec, G. Haller, A. K. Harding, P. A. Hart, E. Hays, S. E. Healey, M. Hirayama, L. Hjalmarsdotter, et al. The large area telescope on the fermi gamma-ray space telescope mission. *Astrophysical Journal*, 697(2): 1071–1102, 2009. ISSN 0004-637X. doi: 10.1088/0004-637x/697/2/1071. URL <GotoISI>://WOS:000266159500012.

[40] A. Ayala, I. Dominguez, M. Giannotti, A. Mirizzi, and O. Straniero. Revisiting the bound on axion-photon coupling from globular clusters. *Physical Review Letters*, 113(19):5, 2014. ISSN 0031-9007. doi: 10.1103/PhysRevLett.113.191302. URL <GotoISI>://WOS:000344496600003.

[41] A. Bahramian, C. O. Heinke, G. R. Sivakoff, and J. C. Gladstone. Stellar encounter rate in galactic globular clusters. *Astrophysical Journal*, 766(2):10, 2013. ISSN 0004-637X. doi: 10.1088/0004-637x/766/2/136. URL <GotoISI>://WOS:000316320900070.

[42] X. Bai, B. Y. Bi, X. J. Bi, Z. Cao, S. Z. Chen, Y. Chen, A. Chiavassa, X. H. Cui, Z. G. Dai, D. della Volpe, T. Di Girolamo, Giuseppe Di Sciascio, Y. Z. Fan, J. Giacalone,

Y. Q. Guo, H. H. He, T. L. He, M. Heller, D. Huang, Y. F. Huang, H. Jia, L. T. Ksenofontov, D. Leahy, F. Li, Z. Li, E. W. Liang, P. Lipari, R. Y. Liu, Y. Liu, S. Liu, X. Ma, O. Martineau-Huynh, D. Martraire, T. Montaruli, D. Ruffolo, Y. V. Stenkin, H. Q. Su, T. Tam, Q. W. Tang, W. W. Tian, P. Vallania, S. Vernetto, C. Vigorito, J. . C. Wang, L. Z. Wang, X. Wang, X. Y. Wang, X. J. Wang, Z. X. Wang, D. M. Wei, J. J. Wei, D. Wu, H. R. Wu, X. F. Wu, D. H. Yan, A. Y. Yang, R. Z. Yang, Z. G. Yao, L. Q. Yin, Q. Yuan, B. Zhang, B. Zhang, L. Zhang, M. F. Zhang, S. S. Zhang, X. Zhang, Y. Zhao, X. X. Zhou, F. R. Zhu, and H. Zhu. The large high altitude air shower observatory (lhaaso) science white paper, 2019.

[43] M. Bailes, S. Johnston, J. F. Bell, D. R. Lorimer, B. W. Stappers, R. N. Manchester, A. G. Lyne, L. Nicastro, N. Damico, and B. M. Gaensler. Discovery of four isolated millisecond pulsars. *Astrophysical Journal*, 481(1):386–391, 1997. ISSN 0004-637X. doi: 10.1086/304041. URL <GotoISI>://WOS:A1997XA54400031.

[44] M. Bailes, A. Jameson, F. Abbate, E. D. Barr, N. D. R. Bhat, L. Bondonneau, M. Burgay, S. J. Buchner, F. Camilo, D. J. Champion, and et al. The meerkat telescope as a pulsar facility: System verification and early science results from meertime. *Publications of the Astronomical Society of Australia*, 37, 2020. ISSN 1448-6083. doi: 10.1017/pasa.2020.19. URL http://dx.doi.org/10.1017/pasa.2020.19.

[45] M. G. Baring and A. K. Harding. Resonant compton upscattering in anomalous x-ray pulsars. *Astrophysics and Space Science*, 308(1-4):109–118, 2007. ISSN 0004-640X. doi: 10.1007/s10509-007-9326-x. URL <GotoISI>://WOS:000246351000015.

[46] Roger Barlow. Asymmetric systematic errors, 2003. URL https://arxiv.org/abs/physics/0306138.

[47] R. Bartels, S. Krishnamurthy, and C. Weniger. Strong support for the millisecond pulsar origin of the galactic center gev excess. *Physical Review Letters*, 116(5), 2016. ISSN 0031-9007. doi: 10.1103/PhysRevLett.116.051102. URL <GotoISI>://WOS:000369492600001.

[48] H. Baumgardt and M. Hilker. A catalogue of masses, structural parameters, and velocity dispersion profiles of 112 milky way globular clusters. *Monthly Notices of the Royal Astronomical Society*, 478(2):1520–1557, 2018. ISSN 0035-8711. doi: 10.1093/mnras/sty1057. URL <GotoISI>://WOS:000439547400008.

[49] H. Baumgardt, G. De Marchi, and P. Kroupa. Evidence for primordial mass segregation in globular clusters. *Astrophysical Journal*, 685(1):247–253, 2008. ISSN 0004-637X. doi: 10.1086/590488. URL <GotoISI>://WOS:000259314200019.

[50] H. Baumgardt, C. He, S. M. Sweet, M. Drinkwater, A. Sollima, J. Hurley, C. Usher, S. Kamann, H. Dalgleish, S. Dreizler, and T. O. Husser. No evidence for intermediate-mass black holes in the globular clusters omega cen and ngc 6624. *Monthly Notices of the Royal Astronomical Society*, 488(4):5340–5351, 2019. ISSN 0035-8711. doi: 10.1093/mnras/stz2060. URL <GotoISI>://WOS:000484349700069.

[51] W. Becker, H. H. Huang, and T. Prinz. X-ray counterparts of millisecond pulsars in globular clusters, 2010. URL https://arxiv.org/abs/1006.0335.

[52] W. Bednarek and J. Sitarek. High-energy gamma-rays from globular clusters. *Monthly Notices of the Royal Astronomical Society*, 377(2):920–930, 2007. ISSN 0035-8711. doi: 10.1111/j.1365-2966.2007.11664.x. URL <GotoISI>://WOS:000246032400039.

[53] W. Bednarek and J. Sitarek. High-energy emission from the nebula around the black widow binary system containing millisecond pulsar b1957+20. *Astronomy Astrophysics*, 550, 2013. ISSN 0004-6361. doi: 10.1051/0004-6361/201220711. URL <GotoISI>://WOS:000314879700039.

[54] W. Bednarek and T. Sobczak. Misaligned tev gamma-ray sources in the vicinity of globular clusters. *Monthly Notices of the Royal Astronomical Society*, 445(3): 2842–2847, 2014. ISSN 0035-8711. doi: 10.1093/mnras/stu1966.

[55] W. Bednarek, J. Sitarek, and T. Sobczak. Tev gamma-ray emission initiated by the population or individual millisecond pulsars within globular clusters. *Monthly Notices of the Royal Astronomical Society*, 458(1):1083–1095, 2016. ISSN 0035-8711. doi: 10.1093/mnras/stw367.

[56] A. M. Beloborodov. On the mechanism of hard x-ray emission from magnetars. *Astrophysical Journal*, 762(1), 2013. ISSN 0004-637X. doi: 10.1088/0004-637x/762/1/13. URL <GotoISI>://WOS:000313007900013.

[57] A. M. Beloborodov and X. Y. Li. Magnetar heating. *Astrophysical Journal*, 833(2): 20, 2016. ISSN 0004-637X. doi: 10.3847/1538-4357/833/2/261. URL <GotoISI>://WOS:000391169600136.

[58] B. Berenji, J. Gaskins, and M. Meyer. Constraints on axions and axionlike particles from fermi large area telescope observations of neutron stars. *Physical Review*

D, 93(4):13, 2016. ISSN 2470-0010. doi: 10.1103/PhysRevD.93.045019. URL <GotoISI>://WOS:000370247600020.

[59] J. L. Bibby, P. A. Crowther, J. P. Furness, and J. S. Clark. A downward revision to the distance of the 1806-20 cluster and associated magnetar from Gemini Near-Infrared Spectroscopy. , 386(1):L23–L27, May 2008. doi: 10.1111/j.1745-3933.2008.00453.x.

[60] S. Bogdanov, J. E. Grindlay, C. O. Heinke, F. Camilo, P. C. C. Freire, and W. Becker. Chandra x-ray observations of 19 millisecond pulsars in the globular cluster 47 tucanae. *Astrophysical Journal*, 646(2):1104–1115, 2006. ISSN 0004-637X. doi: 10.1086/505133. URL <GotoISI>://WOS:000239647400036.

[61] Geoffrey C. Bower, Adam Deller, Paul Demorest, Andreas Brunthaler, Ralph Eatough, Heino Falcke, Michael Kramer, K. J. Lee, and Laura Spitler. The Angular Broadening of the Galactic Center Pulsar SGR J1745-29: A New Constraint on the Scattering Medium. , 780(1):L2, January 2014. doi: 10.1088/2041-8205/780/1/L2.

[62] R. P. Brinkmann and M. S. Turner. Numerical rates for nucleon-nucleon, axion bremsstrahlung. *Physical Review D*, 38(8):2338–2348, 1988. ISSN 0556-2821. doi: 10.1103/PhysRevD.38.2338. URL <GotoISI>://WOS:A1988Q529100004.

[63] A. M. Brown, T. Lacroix, S. Lloyd, C. Boehm, and P. Chadwick. Understanding the gamma-ray emission from the globular cluster 47 tuc: Evidence for dark matter? *Physical Review D*, 98(4), 2018. ISSN 2470-0010. doi: 10.1103/PhysRevD.98.041301. URL <GotoISI>://WOS:000440719500001.

[64] P. Bruel, T. H. Burnett, S. W. Digel, G. Johannesson, N. Omodei, and M. Wood. Fermi-lat improved pass 8 event selection, 2018. URL https://arxiv.org/abs/1810.11394.

[65] M. Burgay, B. C. Joshi, N. D'Amico, A. Possenti, A. G. Lyne, R. N. Manchester, M. A. McLaughlin, M. Kramer, F. Camilo, and P. C. C. Freire. The Parkes high-latitude pulsar survey. *Monthly Notices of the Royal Astronomical Society*, 368(1): 283–292, 2006. ISSN 0035-8711. doi: 10.1111/j.1365-2966.2006.10100.x. URL <GotoISI>://WOS:000236797600039.

[66] S. Burke-Spolaor and M. Bailes. The millisecond radio sky: transients from a blind single-pulse search. *Monthly Notices of the Royal Astronomical Society*, 402(2): 855–866, 2010. ISSN 0035-8711. doi: 10.1111/j.1365-2966.2009.15965.x. URL <GotoISI>://WOS:000274242900012.

[67] F. Camilo and D. J. Nice. Timing parameters of 29 pulsars. *Astrophysical Journal*, 445(2):756–761, 1995. ISSN 0004-637X. doi: 10.1086/175737. URL <GotoISI>://WOS:A1995RA62500021.

[68] F. Camilo, D. J. Nice, and J. H. Taylor. A search for millisecond pulsars at Galactic latitudes -50 degrees $<$ b $<$ -20 degrees. *Astrophysical Journal*, 461(2):812–819, 1996. ISSN 0004-637X. doi: 10.1086/177103. URL <GotoISI>://WOS:A1996UE57000027.

[69] A. Caputo and M. Reig. Cosmic implications of a low-scale solution to the axion domain wall problem. *Physical Review D*, 100(6), 2019. ISSN 2470-0010. doi: 10.1103/PhysRevD.100.063530. URL <GotoISI>://WOS:000487735200009.

[70] W. Cash. Parameter estimation in astronomy through application of the likelihood ratio. *Astrophysical Journal*, 228:939–947, March 1979. doi: 10.1086/156922.

[71] D. Cerri-Serim, M. M. Serim, S. Sahiner, S. C. Inam, and A. Baykal. Pulse frequency fluctuations of magnetars. *Monthly Notices of the Royal Astronomical Society*, 485(1):2–12, 2019. ISSN 0035-8711. doi: 10.1093/mnras/sty3213. URL <GotoISI>://WOS:000466786400001.

[72] B. Cerutti. Gamma-ray pulsars: what have we learned from ab initio kinetic simulations? *Rendiconti Lincei-Scienze Fisiche E Naturali*, 30(SUPPL 1):89–92, 2019. ISSN 2037-4631. doi: 10.1007/s12210-019-00864-y. URL <GotoISI>://WOS:000501308500011.

[73] B. Cerutti, A. A. Philippov, and A. Spitkovsky. Modelling high-energy pulsar light curves from first principles. *Monthly Notices of the Royal Astronomical Society*, 457(3):2401–2414, 2016. ISSN 0035-8711. doi: 10.1093/mnras/stw124. URL <GotoISI>://WOS:000373583900010.

[74] S. Chang and L. Zhang. Revisiting of pulsed gamma-ray properties of millisecond pulsars in the pulsar striped winds. *Monthly Notices of the Royal Astronomical Society*, 483(2):1796–1801, 2019. ISSN 0035-8711. doi: 10.1093/mnras/sty2815. URL <GotoISI>://WOS:000462258200028.

[75] S. Chang, L. Zhang, X. Li, and Z. J. Jiang. Modelling pulsed gamma-ray emissions from millisecond pulsars with double peaks. *Monthly Notices of the Royal Astronomical Society*, 488(3):4288–4306, 2019. ISSN 0035-8711. doi: 10.1093/mnras/stz1957. URL <GotoISI>://WOS:000485158400096.

[76] R. C. G. Chaves. Extending the h.e.s.s. galactic plane survey, 2009. URL https://arxiv.org/abs/0907.0768.

[77] A. Y. Chen and A. M. Beloborodov. Electrodynamics of axisymmetric pulsar magnetosphere with electron-positron discharge: A numerical experiment. *Astrophysical Journal Letters*, 795(1), 2014. ISSN 2041-8205. doi: 10.1088/2041-8205/795/1/l22. URL <GotoISI>://WOS:000345455500022.

[78] K. S. Cheng, C. Ho, and M. Ruderman. Energetic Radiation from Rapidly Spinning Pulsars. I. Outer Magnetosphere Gaps. , 300:500, January 1986. doi: 10.1086/163829.

[79] T. W. Cole and J. D. Pilkington. Search for pulsating radio sources in declination range + 44 degrees delta + 90 degrees. *Nature*, 219(5154):574–+, 1968. ISSN 0028-0836. doi: 10.1038/219574a0. URL <GotoISI>://WOS:A1968B569000008.

[80] Cast Collaboration. New cast limit on the axion-photon interaction. *Nature Physics*, 13(6):584–590, 2017. ISSN 1745-2473. doi: 10.1038/nphys4109. URL <GotoISI>://WOS:000402604200020.

[81] Hess Collaboration, A. Abramowski, F. Aharonian, F. A. Benkhali, A. G. Akhperjanian, E. Anguner, G. Anton, S. Balenderan, A. Balzer, A. Barnacka, Y. Becherini, J. B. Tjus, K. Bernlohr, E. Birsin, E. Bissaldi, J. Biteau, M. Bottcher, C. Boisson, J. Bolmont, P. Bordas, J. Brucker, F. Brun, P. Brun, T. Bulik, S. Carrigan, S. Casanova, M. Cerruti, P. M. Chadwick, R. Chalme-Calvet, R. C. G. Chaves, A. Cheesebrough, M. Chretien, S. Colafrancesco, G. Cologna, J. Conrad, C. Couturier, Y. Cui, M. Dalton, M. K. Daniel, I. D. Davids, B. Degrange, C. Deil, P. de Wilt, H. J. Dickinson, A. Djannati-Ataii, W. Domainko, L. O. Drury, G. Dubus, K. Dutson, J. Dyks, M. Dyrda, T. Edwards, K. Egberts, P. Eger, P. Espigat, C. Farnier, S. Fegan, F. Feinstein, M. V. Fernandes, D. Fernandez, A. Fiasson, G. Fontaine, A. Forster, M. Fussling, M. Gajdus, Y. A. Gallant, T. Garrigoux, G. Giavitto, B. Giebels, J. F. Glicenstein, M. H. Grondin, M. Grudzinska, S. Haffner, J. Hahn, J. Harris, G. Heinzelmann, G. Henri, G. Hermann, O. Hervet, A. Hillert, J. A. Hinton, W. Hofmann, P. Hofverberg, M. Holler, D. Horns, A. Jacholkowska, C. Jahn, M. Jamrozy, M. Janiak, F. Jankowsky, I. Jung, M. A. Kastendieck, K. Katarzynski, U. Katz, S. Kaufmann, B. Khelifi, M. Kieffer, S. Klepser, D. Klochkov, W. Kluzniak, et al. Hess observations of the crab during its march 2013 gev gamma-ray flare. *Astronomy Astrophysics*, 562, 2014. ISSN 1432-0746. doi: 10.1051/0004-6361/201323013. URL <GotoISI>://WOS:000332161800140.

[82] A. C. Collazzi, C. Kouveliotou, A. J. van der Horst, G. A. Younes, Y. Kaneko, E. Gogus, L. Lin, J. Granot, M. H. Finger, V. L. Chaplin, D. Huppenkothen, A. L. Watts, A. von Kienlin, M. G. Baring, D. Gruber, P. N. Bhat, M. H. Gibby, N. Gehrels, J. McEnery, M. van der Klis, and Ramj Wijers. The five year fermi/gbm magnetar burst catalog. *Astrophysical Journal Supplement Series*, 218(1), 2015. ISSN 0067-0049. doi: 10.1088/0067-0049/218/1/11. URL <GotoISI>://WOS:000354999200011.

[83] S. Corbel, C. Chapuis, T. M. Dame, and P. Durouchoux. The Distance to the Soft Gamma Repeater SGR 1627-41. , 526(1):L29–L32, November 1999. doi: 10.1086/312359.

[84] H.D. Craft, R.V.E. Lovelace, and J.M. Sutton. New pulsar. iau circ., 2100. 2100, 1968. URL http://adsabs.harvard.edu/abs/1968IAUC.2100....1C.

[85] P. Creasey, L. V. Sales, E. W. Peng, and O. Sameie. Globular clusters formed within dark haloes i: present-day abundance, distribution, and kinematics. *Monthly Notices of the Royal Astronomical Society*, 482(1):219–230, 2019. ISSN 0035-8711. doi: 10.1093/mnras/sty2701. URL <GotoISI>://WOS:000454575300017.

[86] S. Dall'Osso, S. N. Shore, and L. Stella. Early evolution of newly born magnetars with a strong toroidal field. *Monthly Notices of the Royal Astronomical Society*, 398(4): 1869–1885, 2009. ISSN 0035-8711. doi: 10.1111/j.1365-2966.2008.14054.x. URL <GotoISI>://WOS:000269906400021.

[87] J. K. Daugherty and A. K. Harding. Polar-cap models of gamma-ray pulsars - emission from single poles of nearly aligned rotators. *Astrophysical Journal*, 429(1):325–330, 1994. ISSN 0004-637X. doi: 10.1086/174321. URL <GotoISI>://WOS:A1994NT95800026.

[88] Ben Davies, Don F. Figer, Rolf-Peter Kudritzki, Christine Trombley, Chryssa Kouveliotou, and Stefanie Wachter. The Progenitor Mass of the Magnetar SGR1900+14. , 707(1):844–851, December 2009. doi: 10.1088/0004-637X/707/1/844.

[89] Ben Davies, Nate Bastian, Mark Gieles, Anil C. Seth, Sabine Mengel, and Iraklis S. Konstantopoulos. Glimpse-co1: the most massive intermediate-age stellar cluster in the galaxy. *Monthly Notices of the Royal Astronomical Society*, 411(2):1386–1394, Nov 2010. ISSN 0035-8711. doi: 10.1111/j.1365-2966.2010.17777.x. URL http://dx.doi.org/10.1111/j.1365-2966.2010.17777.x.

[90] J. M. Davies and E. S. Cotton. Design of the quartermaster solar furnace. *Solar Energy*, 1(2-3):16–22, 1957. ISSN 0038-092X. doi: 10.1016/0038-092x(57)90116-0. URL <GotoISI>://WOS:A1957XG99900003.

[91] M. B. Davies and B. M. S. Hansen. Neutron star retention and millisecond pulsar production in globular clusters. *Monthly Notices of the Royal Astronomical Society*, 301(1):15–24, 1998. ISSN 0035-8711. doi: 10.1046/j.1365-8711.1998.01923.x. URL <GotoISI>://WOS:000077570600007.

[92] T. J. L. de Boer, M. Gieles, E. Balbinot, V. Henault-Brunet, A. Sollima, L. L. Watkins, and I. Claydon. Globular cluster number density profiles using gaia dr2. *Monthly Notices of the Royal Astronomical Society*, 485(4):4906–4935, 2019. ISSN 0035-8711. doi: 10.1093/mnras/stz651. URL <GotoISI>://WOS:000474880400035.

[93] de Martino, D., Falanga, M., Bonnet-Bidaud, J.-M., Belloni, T., Mouchet, M., Masetti, N., Andruchow, I., Cellone, S. A., Mukai, K., and Matt, G. The intriguing nature of the high-energy gamma ray source xssj12270-4859*. *AA*, 515:A25, 2010. doi: 10.1051/0004-6361/200913802. URL https://doi.org/10.1051/0004-6361/200913802.

[94] R. de Menezes, F. Cafardo, and R. Nemmen. Milky way globular clusters in gamma-rays: analysing the dynamical formation of millisecond pulsars. *Monthly Notices of the Royal Astronomical Society*, 486(1):851–867, 2019. ISSN 0035-8711. doi: 10.1093/mnras/stz898. URL <GotoISI>://WOS:000474894100065.

[95] Christoph Deil et al. Gammapy - A prototype for the CTA science tools. *PoS*, ICRC2017:766, 2018. doi: 10.22323/1.301.0766.

[96] P. R. den Hartog, L. Kuiper, and W. Hermsen. Detailed high-energy characteristics of axp 1rxs j170849-400910 - probing the magnetosphere using integral, rxte, and xmm-newton. *Astronomy Astrophysics*, 489(1):263–279, 2008. ISSN 1432-0746. doi: 10.1051/0004-6361:200809772. URL <GotoISI>://WOS:000259347400022.

[97] P. R. den Hartog, L. Kuiper, W. Hermsen, V. M. Kaspi, R. Dib, J. Knodlseder, and F. P. Gavriil. Detailed high-energy characteristics of axp 4u 0142+61 - multi-year observations with integral, rxte, xmm-newton, and asca. *Astronomy Astrophysics*, 489(1):245–261, 2008. ISSN 1432-0746. doi: 10.1051/0004-6361:200809390. URL <GotoISI>://WOS:000259347400021.

[98] Michael Dine, Willy Fischler, and Mark Srednicki. A Simple Solution to the Strong CP Problem with a Harmless Axion. *Phys. Lett.*, 104B:199–202, 1981. doi: 10.1016/0370-2693(81)90590-6.

[99] N. Du, N. Force, R. Khatiwada, E. Lentz, R. Ottens, L. J Rosenberg, G. Rybka, G. Carosi, N. Woollett, D. Bowring, A. S. Chou, A. Sonnenschein, W. Wester, C. Boutan, N. S. Oblath, R. Bradley, E. J. Daw, A. V. Dixit, J. Clarke, S. R. O'Kelley, N. Crisosto, J. R. Gleason, S. Jois, P. Sikivie, I. Stern, N. S. Sullivan, D. B Tanner, and G. C. Hilton. Search for invisible axion dark matter with the axion dark matter experiment. *Phys. Rev. Lett.*, 120:151301, Apr 2018. doi: 10.1103/PhysRevLett.120.151301. URL https://link.aps.org/doi/10.1103/PhysRevLett.120.151301.

[100] L. D. Duffy, P. Sikivie, D. B. Tanner, S. J. Asztalos, C. Hagmann, D. Kinion, L. J Rosenberg, K. van Bibber, D. B. Yu, and R. F. Bradley. High resolution search for dark-matter axions. *Phys. Rev. D*, 74:012006, Jul 2006. doi: 10.1103/PhysRevD.74.012006. URL https://link.aps.org/doi/10.1103/PhysRevD.74.012006.

[101] M. Durant and M. H. van Kerkwijk. Distances to anomalous x-ray pulsars using red clump stars. *Astrophysical Journal*, 650(2):1070–1081, 2006. ISSN 0004-637X. doi: 10.1086/506380. URL <GotoISI>://WOS:000241497700044.

[102] K. Ebisawa, M. Tsujimoto, A. Paizis, K. Hamaguchi, A. Bamba, R. Cutri, H. Kaneda, Y. Maeda, G. Sato, A. Senda, M. Ueno, S. Yamauchi, V. Beckmann, T. J. L. Courvoisier, P. Dubath, and E. Nishihara. Chandra deep x-ray observation of a typical galactic plane region and near-infrared identification. *Astrophysical Journal*, 635(1):214–242, 2005. ISSN 0004-637X. doi: 10.1086/497284. URL <GotoISI>://WOS:000233929600018.

[103] P. Eger and W. Domainko. A search for diffuse x-ray emission from gev-detected galactic globular clusters. *Astronomy Astrophysics*, 540:8, 2012. ISSN 0004-6361. doi: 10.1051/0004-6361/201118628. URL <GotoISI>://WOS:000303315400031.

[104] P. Eger, W. Domainko, and A. C. Clapson. Chandra detection of diffuse x-ray emission from the globular cluster terzan 5. *Astronomy Astrophysics*, 513:6, 2010. ISSN 0004-6361. doi: 10.1051/0004-6361/200913732. URL <GotoISI>://WOS:000285581500025.

[105] R. Engel, D. Heck, and T. Pierog. Extensive air showers and hadronic interactions at high energy. *Annual Review of Nuclear and Particle Science, Vol 61*, 61:467–489, 2011. ISSN 0163-8998. doi: 10.1146/annurev.nucl.012809.104544. URL <GotoISI>://WOS:000299231300019.

[106] T. Enoto, S. Kisaka, and S. Shibata. Observational diversity of magnetized neutron stars. *Reports on Progress in Physics*, 82(10), 2019. ISSN 0034-4885. doi: 10.1088/1361-6633/ab3def. URL <GotoISI>://WOS:000488006300001.

[107] J. F. Fortin and K. Sinha. Constraining axion-like-particles with hard x-ray emission from magnetars. *Journal of High Energy Physics*, (6):22, 2018. ISSN 1029-8479. doi: 10.1007/jhep06(2018)048. URL <GotoISI>://WOS:000435023100005.

[108] A. Franckowiak, P. Jean, M. Wood, C. C. Cheung, and S. Buson. Search for gamma-ray emission from galactic novae with the fermi-lat. *Astronomy Astrophysics*, 609, 2018. ISSN 1432-0746. doi: 10.1051/0004-6361/201731516. URL <GotoISI>://WOS:000429203900001.

[109] P. C. C. Freire, A. A. Abdo, M. Ajello, A. Allafort, J. Ballet, G. Barbiellini, D. Bastieri, K. Bechtol, R. Bellazzini, R. D. Blandford, E. D. Bloom, E. Bonamente, A. W. Borgland, M. Brigida, P. Bruel, R. Buehler, S. Buson, G. A. Caliandro, R. A. Cameron, F. Camilo, P. A. Caraveo, C. Cecchi, O. Celik, E. Charles, A. Chekhtman, C. C. Cheung, J. Chiang, S. Ciprini, R. Claus, I. Cognard, J. Cohen-Tanugi, L. R. Cominsky, F. de Palma, C. D. Dermer, E. D. E. Silva, M. Dormody, P. S. Drell, R. Dubois, D. Dumora, C. M. Espinoza, C. Favuzzi, S. J. Fegan, E. C. Ferrara, W. B. Focke, P. Fortin, Y. Fukazawa, P. Fusco, F. Gargano, D. Gasparrini, N. Gehrels, S. Germani, N. Giglietto, F. Giordano, M. Giroletti, T. Glanzman, G. Godfrey, I. A. Grenier, M. H. Grondin, J. E. Grove, L. Guillemot, S. Guiriec, D. Hadasch, A. K. Harding, G. Johannesson, A. S. Johnson, T. J. Johnson, S. Johnston, H. Katagiri, J. Kataoka, M. Keith, M. Kerr, J. Knodlseder, M. Kramer, M. Kuss, J. Lande, L. Latronico, S. H. Lee, M. Lemoine-Goumard, F. Longo, F. Loparco, M. N. Lovellette, P. Lubrano, A. G. Lyne, R. N. Manchester, M. Marelli, M. N. Mazziotta, J. E. McEnery, P. F. Michelson, T. Mizuno, A. A. Moiseev, C. Monte, M. E. Monzani, A. Morselli, I. V. Moskalenko, S. Murgia, T. Nakamori, P. L. Nolan, J. P. Norris, E. Nuss, T. Ohsugi, et al. Fermi detection of a luminous gamma-ray pulsar in a globular cluster. *Science*, 334(6059): 1107–1110, 2011. ISSN 0036-8075. doi: 10.1126/science.1207141.

[110] Georg G. Raffelt. Stars as laboratories for fundamental physics: The astrophysics of neutrinos, axions, and other weakly interacting particles. *Bibliovault OAI Repository, the University of Chicago Press*, 01 1996.

[111] P. L. Gonthier, A. K. Harding, E. C. Ferrara, S. E. Frederick, V. E. Mohr, and Y. M. Koh. Population syntheses of millisecond pulsars from the galactic disk and bulge. *Astrophysical Journal*, 863(2), 2018. ISSN 0004-637X. doi: 10.3847/1538-4357/aad08d. URL <GotoISI>://WOS:000442628400035.

[112] D. Gotz, S. Mereghetti, A. Tiengo, and P. Esposito. Magnetars as persistent hard x-ray sources: Integral discovery of a hard tail in sgr 1900+14. *Astronomy Astrophysics*,

449(2):L31–L34, 2006. ISSN 0004-6361. doi: 10.1051/0004-6361:20064870. URL <GotoISI>://WOS:000236198600006.

[113] P. W. Graham, I. G. Irastorza, S. K. Lamoreaux, A. Lindner, and K. A. van Bibber. *Experimental Searches for the Axion and Axion-Like Particles*, volume 65 of *Annual Review of Nuclear and Particle Science*, pages 485–514. Annual Reviews, Palo Alto, 2015. ISBN 978-0-8243-1565-8. doi: 10.1146/annurev-nucl-102014-022120. URL <GotoISI>://WOS:000363473100020.

[114] Particle Data Group, P A Zyla, R M Barnett, J Beringer, O Dahl, D A Dwyer, D E Groom, C J Lin, K S Lugovsky, E Pianori, D J Robinson, C G Wohl, W M Yao, K Agashe, G Aielli, B C Allanach, C Amsler, M Antonelli, E C Aschenauer, D M Asner, H Baer, Sw Banerjee, L Baudis, C W Bauer, J J Beatty, V I Belousov, S Bethke, A Bettini, O Biebel, K M Black, E Blucher, O Buchmuller, V Burkert, M A Bychkov, R N Cahn, M Carena, A Ceccucci, A Cerri, D Chakraborty, R Sekhar Chivukula, G Cowan, G D'Ambrosio, T Damour, D de Florian, A de Gouvêa, T DeGrand, P de Jong, G Dissertori, B A Dobrescu, M D'Onofrio, M Doser, M Drees, H K Dreiner, P Eerola, U Egede, S Eidelman, J Ellis, J Erler, V V Ezhela, W Fetscher, B D Fields, B Foster, A Freitas, H Gallagher, L Garren, H J Gerber, G Gerbier, T Gershon, Y Gershtein, T Gherghetta, A A Godizov, M C Gonzalez-Garcia, M Goodman, C Grab, A V Gritsan, C Grojean, M Grünewald, A Gurtu, T Gutsche, H E Haber, C Hanhart, S Hashimoto, Y Hayato, A Hebecker, S Heinemeyer, B Heltsley, J J Hernández-Rey, K Hikasa, J Hisano, A Höcker, J Holder, A Holtkamp, J Huston, T Hyodo, K F Johnson, M Kado, M Karliner, U F Katz, M Kenzie, V A Khoze, S R Klein, E Klempt, R V Kowalewski, F Krauss, M Kreps, B Krusche, Y Kwon, O Lahav, J Laiho, L P Lellouch, J Lesgourgues, A R Liddle, Z Ligeti, C Lippmann, T M Liss, L Littenberg, C Lourengo, S B Lugovsky, A Lusiani, Y Makida, F Maltoni, T Mannel, A V Manohar, W J Marciano, A Masoni, J Matthews, U G Meißner, M Mikhasenko, D J Miller, D Milstead, R E Mitchell, K Mönig, P Molaro, F Moortgat, M Moskovic, K Nakamura, M Narain, P Nason, S Navas, M Neubert, P Nevski, Y Nir, K A Olive, C Patrignani, J A Peacock, S T Petcov, V A Petrov, A Pich, A Piepke, A Pomarol, S Profumo, A Quadt, K Rabbertz, J Rademacker, G Raffelt, H Ramani, M Ramsey-Musolf, B N Ratcliff, P Richardson, A Ringwald, S Roesler, S Rolli, A Romaniouk, L J Rosenberg, J L Rosner, G Rybka, M Ryskin, R A Ryutin, Y Sakai, G P Salam, S Sarkar, F Sauli, O Schneider, K Scholberg, A J Schwartz, J Schwiening, D Scott, V Sharma, S R Sharpe, T Shutt, M Silari, T Sjöstrand, P Skands, T Skwarnicki, G F Smoot, A Soffer, M S Sozzi, S Spanier, C Spiering, A Stahl, S L Stone, Y Sumino, T Sumiyoshi, M J

Syphers, F Takahashi, M Tanabashi, J Tanaka, M Taševský, K Terashi, J Terning, U Thoma, R S Thorne, L Tiator, M Titov, N P Tkachenko, D R Tovey, K Trabelsi, P Urquijo, G Valencia, R Van de Water, N Varelas, G Venanzoni, L Verde, M G Vincter, P Vogel, W Vogelsang, A Vogt, V Vorobyev, S P Wakely, W Walkowiak, C W Walter, D Wands, M O Wascko, D H Weinberg, E J Weinberg, M White, L R Wiencke, S Willocq, C L Woody, R L Workman, M Yokoyama, R Yoshida, G Zanderighi, G P Zeller, O V Zenin, R Y Zhu, S L Zhu, F Zimmermann, J Anderson, T Basaglia, V S Lugovsky, P Schaffner, and W Zheng. Review of Particle Physics. *Progress of Theoretical and Experimental Physics*, 2020(8), 08 2020. ISSN 2050-3911. doi: 10.1093/ptep/ptaa104. URL https://doi.org/10.1093/ptep/ptaa104. 083C01.

[115] E. H. Gudmundsson, C. J. Pethick, and R. I. Epstein. Neutron star envelopes. *Astrophysical Journal*, 259(1):L19–L23, 1982. ISSN 0004-637X. doi: 10.1086/183840. URL <GotoISI>://WOS:A1982PB24500004.

[116] L. Guillemot, M. Kramer, T. J. Johnson, H. A. Craig, R. W. Romani, C. Venter, A. K. Harding, R. D. Ferdman, I. H. Stairs, and M. Kerr. Fermi lat pulsed detection of psr j0737-3039a in the double pulsar system. *Astrophysical Journal*, 768(2), 2013. ISSN 0004-637X. doi: 10.1088/0004-637x/768/2/169. URL <GotoISI>://WOS:000318228400072.

[117] L. Guillemot, D. A. Smith, H. Laffon, G. H. Janssen, I. Cognard, G. Theureau, G. Desvignes, E. C. Ferrara, and P. S. Ray. The gamma-ray millisecond pulsar deathline, revisited new velocity and distance measurements. *Astronomy Astrophysics*, 587, 2016. ISSN 1432-0746. doi: 10.1051/0004-6361/201527847. URL <GotoISI>://WOS:000371589800120.

[118] C. Hagmann, D. Kinion, W. Stoeffl, K. van Bibber, E. Daw, H. Peng, Leslie J Rosenberg, J. LaVeigne, P. Sikivie, N. S. Sullivan, D. B. Tanner, F. Nezrick, Michael S. Turner, D. M. Moltz, J. Powell, and N. A. Golubev. Results from a high-sensitivity search for cosmic axions. *Phys. Rev. Lett.*, 80:2043–2046, Mar 1998. doi: 10.1103/PhysRevLett.80.2043. URL https://link.aps.org/doi/10.1103/PhysRevLett.80.2043.

[119] C. Hanhart, D. R. Phillips, and S. Reddy. Neutrino and axion emissivities of neutron stars from nucleon-nucleon scattering data. *Physics Letters B*, 499(1-2):9–15, 2001. ISSN 0370-2693. doi: 10.1016/s0370-2693(00)01382-4. URL <GotoISI>://WOS:000166949100002.

[120] S. Hannestad and G. Raffelt. Supernova neutrino opacity from nucleon-nucleon bremsstrahlung and related processes. *Astrophysical Journal*, 507(1):339–352, 1998. ISSN 0004-637X. doi: 10.1086/306303. URL <GotoISI>://WOS:000077779400033.

[121] A. K. Harding and J. K. Daugherty. Pulse profiles and spectra of gamma ray pulsars in the polar cap model. *Space Based Astronomy: Iso, Agn, Radiopulsars and the Sun*, 21 (1-2):251–254, 1998. ISSN 0273-1177. doi: 10.1016/s0273-1177(97)00811-9. URL <GotoISI>://WOS:000072736800032.

[122] A. K. Harding and C. Kalapotharakos. Synchrotron self-compton emission from the crab and other pulsars. *Astrophysical Journal*, 811(1), 2015. ISSN 0004-637X. doi: 10.1088/0004-637x/811/1/63. URL <GotoISI>://WOS:000363471600064.

[123] A. K. Harding, V. V. Usov, and A. G. Muslimov. High-energy emission from millisecond pulsars. *Astrophysical Journal*, 622(1):531–543, 2005. ISSN 0004-637X. doi: 10.1086/427840. URL <GotoISI>://WOS:000227740900043.

[124] W. E. Harris. A catalog of parameters for globular clusters in the milky way. *Astronomical Journal*, 112(4):1487–1488, 1996. ISSN 0004-6256. doi: 10.1086/118116. URL <GotoISI>://WOS:A1996VK84000012.

[125] William E. Harris. A new catalog of globular clusters in the milky way, 2010. URL https://arxiv.org/abs/1012.3224.

[126] C. O. Heinke and W. C. G. Ho. Direct observation of the cooling of the cassiopeia a neutron star. *Astrophysical Journal Letters*, 719(2):L167–L171, 2010. ISSN 2041-8205. doi: 10.1088/2041-8205/719/2/l167. URL <GotoISI>://WOS:000281199900013.

[127] C. O. Heinke, J. E. Grindlay, P. D. Edmonds, D. A. Lloyd, S. S. Murray, H. N. Cohn, and P. M. Lugger. A chandra x-ray study of the globular cluster m80. *Astrophysical Journal*, 598(1):516–526, 2003. ISSN 0004-637X. doi: 10.1086/378884. URL <GotoISI>://WOS:000186688700043.

[128] S. Henleywillis, A. M. Cool, D. Haggard, C. Heinke, P. Callanan, and Y. Zhao. A deep x-ray survey of the globular cluster omega centauri. *Monthly Notices of the Royal Astronomical Society*, 479(2):2834–2852, 2018. ISSN 0035-8711. doi: 10.1093/mnras/sty675. URL <GotoISI>://WOS:000441380100097.

[129] H.E.S.S. Collaboration, A. Abramowski, F. Acero, F. Aharonian, A. G. Akhperjanian, G. Anton, A. Balzer, A. Barnacka, U. Barres de Almeida, Y. Becherini, J. Becker,

B. Behera, K. Bernlöhr, A. Bochow, C. Boisson, J. Bolmont, P. Bordas, J. Brucker, F. Brun, P. Brun, T. Bulik, I. Büsching, S. Carrigan, S. Casanova, M. Cerruti, P. M. Chadwick, A. Charbonnier, R. C. G. Chaves, A. Cheesebrough, L.-M. Chounet, A. C. Clapson, G. Coignet, G. Cologna, J. Conrad, M. Dalton, M. K. Daniel, I. D. Davids, B. Degrange, C. Deil, H. J. Dickinson, A. Djannati-Ataï, W. Domainko, L. O. Drury, F. Dubois, G. Dubus, K. Dutson, J. Dyks, M. Dyrda, K. Egberts, P. Eger, P. Espigat, L. Fallon, C. Farnier, S. Fegan, F. Feinstein, M. V. Fernandes, A. Fiasson, G. Fontaine, A. Förster, M. Füßling, Y. A. Gallant, H. Gast, L. Gérard, D. Gerbig, B. Giebels, J. F. Glicenstein, B. Glück, P. Goret, D. Göring, S. Häffner, J. D. Hague, D. Hampf, M. Hauser, S. Heinz, G. Heinzelmann, G. Henri, G. Hermann, J. A. Hinton, A. Hoffmann, W. Hofmann, P. Hofverberg, M. Holler, D. Horns, A. Jacholkowska, O. C. de Jager, C. Jahn, M. Jamrozy, I. Jung, M. A. Kastendieck, K. Katarzyński, U. Katz, S. Kaufmann, D. Keogh, D. Khangulyan, B. Khélifi, D. Klochkov, W. Kluźniak, T. Kneiske, N. Komin, K. Kosack, R. Kossakowski, H. Laffon, G. Lamanna, D. Lennarz, T. Lohse, A. Lopatin, C.-C. Lu, V. Marandon, A. Marcowith, J. Masbou, D. Maurin, N. Maxted, T. J. L. McComb, M. C. Medina, J. Méhault, R. Moderski, E. Moulin, C. L. Naumann, M. Naumann-Godo, M. de Naurois, D. Nedbal, D. Nekrassov, N. Nguyen, B. Nicholas, J. Niemiec, S. J. Nolan, S. Ohm, D. de Oña Wilhelmi, B. Opitz, M. Ostrowski, I. Oya, M. Panter, M. Paz Arribas, G. Pedaletti, G. Pelletier, P.-O. Petrucci, S. Pita, G. Pühlhofer, M. Punch, A. Quirrenbach, M. Raue, S. M. Rayner, A. Reimer, O. Reimer, M. Renaud, R. de los Reyes, F. Rieger, J. Ripken, L. Rob, S. Rosier-Lees, G. Rowell, B. Rudak, C. B. Rulten, J. Ruppel, F. Ryde, V. Sahakian, A. Santangelo, R. Schlickeiser, F. M. Schöck, A. Schulz, U. Schwanke, S. Schwarzburg, S. Schwemmer, M. Sikora, J. L. Skilton, H. Sol, G. Spengler, Ł. Stawarz, R. Steenkamp, C. Stegmann, F. Stinzing, K. Stycz, I. Sushch, A. Szostek, J.-P. Tavernet, R. Terrier, M. Tluczykont, K. Valerius, C. van Eldik, G. Vasileiadis, C. Venter, J. P. Vialle, A. Viana, P. Vincent, H. J. Völk, F. Volpe, S. Vorobiov, M. Vorster, S. J. Wagner, M. Ward, R. White, A. Wierzcholska, M. Zacharias, A. Zajczyk, A. A. Zdziarski, A. Zech, and H.-S. Zechlin. Very-high-energy gamma-ray emission from the direction of the Galactic globular cluster Terzan 5. , 531:L18, July 2011. doi: 10.1051/0004-6361/201117171.

[130] H.E.S.S. Collaboration, A. Abramowski, F. Acero, F. Aharonian, A. G. Akhperjanian, G. Anton, S. Balenderan, A. Balzer, A. Barnacka, Y. Becherini, J. Becker Tjus, K. Bernlöhr, E. Birsin, J. Biteau, A. Bochow, C. Boisson, J. Bolmont, P. Bordas, J. Brucker, F. Brun, P. Brun, T. Bulik, S. Carrigan, S. Casanova, M. Cerruti, P. M. Chadwick, R. C. G. Chaves, A. Cheesebrough, S. Colafrancesco, G. Cologna, J. Con-

rad, C. Couturier, M. Dalton, M. K. Daniel, I. D. Davids, B. Degrange, C. Deil, P. deWilt, H. J. Dickinson, A. Djannati-Ataï, W. Domainko, L. O'C. Drury, G. Dubus, K. Dutson, J. Dyks, M. Dyrda, K. Egberts, P. Eger, P. Espigat, L. Fallon, C. Farnier, S. Fegan, F. Feinstein, M. V. Fernandes, D. Fernandez, A. Fiasson, G. Fontaine, A. Förster, M. Füßling, M. Gajdus, Y. A. Gallant, T. Garrigoux, H. Gast, B. Giebels, J. F. Glicenstein, B. Glück, D. Göring, M.-H. Grondin, M. Grudzińska, S. Häffner, J. D. Hague, J. Hahn, D. Hampf, J. Harris, S. Heinz, G. Heinzelmann, G. Henri, G. Hermann, A. Hillert, J. A. Hinton, W. Hofmann, P. Hofverberg, M. Holler, D. Horns, A. Jacholkowska, C. Jahn, M. Jamrozy, I. Jung, M. A. Kastendieck, K. Katarzyński, U. Katz, S. Kaufmann, B. Khélifi, S. Klepser, D. Klochkov, W. Kluźniak, T. Kneiske, D. Kolitzus, N. Komin, K. Kosack, R. Kossakowski, F. Krayzel, P. P. Krüger, H. Laffon, G. Lamanna, J. Lefaucheur, M. Lemoine-Goumard, J.-P. Lenain, D. Lennarz, T. Lohse, A. Lopatin, C.-C. Lu, V. Marandon, A. Marcowith, J. Masbou, G. Maurin, N. Maxted, M. Mayer, T. J. L. McComb, M. C. Medina, J. Méhault, U. Menzler, R. Moderski, M. Mohamed, E. Moulin, C. L. Naumann, M. Naumann-Godo, M. de Naurois, D. Nedbal, N. Nguyen, J. Niemiec, S. J. Nolan, S. Ohm, E. de Oña Wilhelmi, B. Opitz, M. Ostrowski, I. Oya, M. Panter, R. D. Parsons, M. Paz Arribas, N. W. Pekeur, G. Pelletier, J. Perez, P.-O. Petrucci, B. Peyaud, S. Pita, G. Pühlhofer, M. Punch, A. Quirrenbach, S. Raab, M. Raue, A. Reimer, O. Reimer, M. Renaud, R. de los Reyes, F. Rieger, J. Ripken, L. Rob, S. Rosier-Lees, G. Rowell, B. Rudak, C. B. Rulten, V. Sahakian, D. A. Sanchez, A. Santangelo, R. Schlickeiser, A. Schulz, U. Schwanke, S. Schwarzburg, S. Schwemmer, F. Sheidaei, J. L. Skilton, H. Sol, G. Spengler, Ł. Stawarz, R. Steenkamp, C. Stegmann, F. Stinzing, K. Stycz, I. Sushch, A. Szostek, J.-P. Tavernet, R. Terrier, M. Tluczykont, C. Trichard, K. Valerius, C. van Eldik, G. Vasileiadis, C. Venter, A. Viana, P. Vincent, H. J. Völk, F. Volpe, S. Vorobiov, M. Vorster, S. J. Wagner, M. Ward, R. White, A. Wierzcholska, D. Wouters, M. Zacharias, A. Zajczyk, A. A. Zdziarski, A. Zech, and H.-S. G Zechlin. Search for very-high-energy γ-ray emission from Galactic globular clusters with H.E.S.S. , 551: A26, March 2013. doi: 10.1051/0004-6361/201220719.

[131] J. W. T. Hessels, S. M. Ransom, I. H. Stairs, V. M. Kaspi, and P. C. C. Freire. A 1.4 ghz arecibo survey for pulsars in globular clusters. *Astrophysical Journal*, 670(1): 363–378, 2007. ISSN 0004-637X. doi: 10.1086/521780. URL <GotoISI>://WOS: 000250965400026.

[132] Michael Hilker, Holger Baumgardt, Antonio Sollima, and Andrea Bellini. Galactic globular clusters: A new catalog of masses, structural parameters, velocity

dispersion profiles, proper motions and space orbits. *Proceedings of the International Astronomical Union*, 14(S351):451–454, May 2019. ISSN 1743-9221. doi: 10.1017/s1743921319006823. URL http://dx.doi.org/10.1017/S1743921319006823.

[133] A. M. Hillas. Cerenkov Light Images of EAS Produced by Primary Gamma Rays and by Nuclei. In *19th International Cosmic Ray Conference (ICRC19), Volume 3*, volume 3 of *International Cosmic Ray Conference*, page 445, August 1985.

[134] W. C. G. Ho, K. Glampedakis, and N. Andersson. Magnetars: super(ficially) hot and super(fluid) cool. *Monthly Notices of the Royal Astronomical Society*, 422(3): 2632–2641, 2012. ISSN 0035-8711. doi: 10.1111/j.1365-2966.2012.20826.x. URL <GotoISI>://WOS:000303858400065.

[135] G. Hobbs, A. G. Lyne, M. Kramer, C. E. Martin, and C. Jordan. Long-term timing observations of 374 pulsars. *Monthly Notices of the Royal Astronomical Society*, 353 (4):1311–1344, 2004. ISSN 0035-8711. doi: 10.1111/j.1365-2966.2004.08157.x. URL <GotoISI>://WOS:000224385800027.

[136] M. Holler, D. Berge, C. Eldik, Jean-Philippe Lenain, V. Marandon, Thomas Murach, Mathieu de Naurois, R. Parsons, H. Prokoph, and D. Zaborov. Observations of the crab nebula with h.e.s.s. phase ii. 09 2015.

[137] D. Hooper and T. Linden. Millisecond pulsars, tev halos, and implications for the galactic center gamma-ray excess. *Physical Review D*, 98(4), 2018. ISSN 2470-0010. doi: 10.1103/PhysRevD.98.043005. URL <GotoISI>://WOS:000440824800004.

[138] D. Hooper and G. Mohlabeng. The gamma-ray luminosity function of millisecond pulsars and implications for the gev excess. *Journal of Cosmology and Astroparticle Physics*, (3), 2016. ISSN 1475-7516. doi: 10.1088/1475-7516/2016/03/049. URL <GotoISI>://WOS:000375608200051.

[139] S. Horiuchi and S. Ando. Dark matter annihilation from intermediate-mass black holes: Contribution to the extragalactic gamma-ray background. *Physical Review D*, 74(10):11, 2006. ISSN 1550-7998. doi: 10.1103/PhysRevD.74.103504. URL <GotoISI>://WOS:000242409800012.

[140] J. Hoskins, J. Hwang, C. Martin, P. Sikivie, N. S. Sullivan, D. B. Tanner, M. Hotz, L. J Rosenberg, G. Rybka, A. Wagner, S. J. Asztalos, G. Carosi, C. Hagmann, D. Kinion, K. van Bibber, R. Bradley, and J. Clarke. Search for nonvirialized axionic dark

matter. *Phys. Rev. D*, 84:121302, Dec 2011. doi: 10.1103/PhysRevD.84.121302. URL https://link.aps.org/doi/10.1103/PhysRevD.84.121302.

[141] K. Hu, M. G. Baring, Z. Wadiasingh, and A. K. Harding. Opacities for photon splitting and pair creation in neutron star magnetospheres. *Monthly Notices of the Royal Astronomical Society*, 486(3):3327–3349, 2019. ISSN 0035-8711. doi: 10.1093/mnras/stz995. URL <GotoISI>://WOS:000474903500025.

[142] C. Y. Hui, K. S. Cheng, and R. E. Taam. Diffuse x-ray emission in globular cluster cores. *Astrophysical Journal*, 700(2):1233–1241, 2009. ISSN 0004-637X. doi: 10.1088/0004-637x/700/2/1233. URL <GotoISI>://WOS:000268098100032.

[143] C. Y. Hui, K. S. Cheng, Y. Wang, P. H. T. Tam, A. K. H. Kong, D. O. Chernyshov, and V. A. Dogiel. The fundamental plane of gamma-ray globular clusters. *Astrophysical Journal*, 726(2), 2011. ISSN 0004-637X. doi: 10.1088/0004-637x/726/2/100.

[144] V Hénault-Brunet, M Gieles, J Strader, M Peuten, E Balbinot, and K E K Douglas. On the black hole content and initial mass function of 47 tuc. *Monthly Notices of the Royal Astronomical Society*, 491(1):113–128, Oct 2019. ISSN 1365-2966. doi: 10.1093/mnras/stz2995. URL http://dx.doi.org/10.1093/mnras/stz2995.

[145] N. Ivanova. Low-mass x-ray binaries and metallicity dependence: Story of failures. *Astrophysical Journal*, 636(2):979–984, 2006. ISSN 0004-637X. doi: 10.1086/498054. URL <GotoISI>://WOS:000234469400036.

[146] N. Iwamoto. Axion emission from neutron stars. *Physical Review Letters*, 53(12): 1198–1201, 1984. ISSN 0031-9007. doi: 10.1103/PhysRevLett.53.1198. URL <GotoISI>://WOS:A1984TH67800021.

[147] N. Iwamoto. Nucleon-nucleon bremsstrahlung of axions and pseudoscalar particles from neutron-star matter. *Physical Review D*, 64(4):10, 2001. ISSN 0556-2821. doi: 10.1103/PhysRevD.64.043002. URL <GotoISI>://WOS:000170467600009.

[148] B. A. Jacoby, M. Bailes, S. M. Ord, R. T. Edwards, and S. R. Kulkarni. A large-area survey for radio pulsars at high Galactic latitudes. *Astrophysical Journal*, 699(2): 2009–2016, 2009. ISSN 0004-637X. doi: 10.1088/0004-637x/699/2/2009. URL <GotoISI>://WOS:000267401500096.

[149] Hans-Thomas Janka, Wolfgang Keil, Georg Raffelt, and David Seckel. Nucleon spin fluctuations and the supernova emission of neutrinos and axions. *Phys. Rev.*

Lett., 76:2621–2624, Apr 1996. doi: 10.1103/PhysRevLett.76.2621. URL https://link.aps.org/doi/10.1103/PhysRevLett.76.2621.

[150] M. Jiang, B. Y. Cui, N. A. Schmid, M. A. McLaughlin, and Z. C. Cao. Wavelet denoising of radio observations of rotating radio transients (rrats): Improved timing parameters for eight rrats. *Astrophysical Journal*, 847(1):13, 2017. ISSN 0004-637X. doi: 10.3847/1538-4357/aa88c3. URL <GotoISI>://WOS:000411520600003.

[151] T. J. Johnson, L. Guillemot, M. Kerr, I. Cognard, P. S. Ray, M. T. Wolff, S. Begin, G. H. Janssen, R. W. Romani, C. Venter, J. E. Grove, P. C. C. Freire, M. Wood, C. C. Cheung, J. M. Casandjian, I. H. Stairs, F. Camilo, C. M. Espinoza, E. C. Ferrara, A. K. Harding, S. Johnston, M. Kramer, A. G. Lyne, P. F. Michelson, S. M. Ransom, R. Shannon, D. A. Smith, B. W. Stappers, G. Theureau, and S. E. Thorsett. Broadband pulsations from psr b1821-24: Implications for emission models and the pulsar population of m28. *Astrophysical Journal*, 778(2), 2013. ISSN 0004-637X. doi: 10.1088/0004-637x/778/2/106. URL <GotoISI>://WOS:000327762800021.

[152] T. J. Johnson, C. Venter, A. K. Harding, L. Guillemot, D. A. Smith, M. Kramer, O. Celik, P. R. Den Hartog, E. C. Ferrara, X. Hou, J. Lande, and P. S. Ray. Constraints on the emission geometries and spin evolution of gamma-ray millisecond pulsars. *Astrophysical Journal Supplement Series*, 213(1), 2014. ISSN 0067-0049. doi: 10.1088/0067-0049/213/1/6.

[153] C. Kalapotharakos, G. Brambilla, A. Timokhin, A. K. Harding, and D. Kazanas. Three-dimensional kinetic pulsar magnetosphere models: Connecting to gamma-ray observations. *Astrophysical Journal*, 857(1), 2018. ISSN 0004-637X. doi: 10.3847/1538-4357/aab550. URL <GotoISI>://WOS:000429836900009.

[154] J. Kaluzny and I. B. Thompson. Variable stars in the globular cluster ngc 6752. *Acta Astronomica*, 59(3):273–289, 2009. ISSN 0001-5237. URL <GotoISI>://WOS:000271215800003.

[155] A. D. Kaminker, D. G. Yakovlev, A. Y. Potekhin, N. Shibazaki, P. S. Shternin, and O. Y. Gnedin. Magnetars as cooling neutron stars with internal heating. *Monthly Notices of the Royal Astronomical Society*, 371(1):477–483, 2006. ISSN 0035-8711. doi: 10.1111/j.1365-2966.2006.10680.x. URL <GotoISI>://WOS:000239863700063.

[156] V. M. Kaspi and A. M. Beloborodov. Magnetars. *Annual Review of Astronomy and Astrophysics, Vol 55*, 55:261–301, 2017. ISSN 0066-4146. doi: 10.1146/annurev-astro-081915-023329. URL <GotoISI>://WOS:000410544500008.

[157] Wolfgang Keil, Hans-Thomas Janka, David N. Schramm, Günter Sigl, Michael S. Turner, and John Ellis. Fresh look at axions and sn 1987a. *Phys. Rev. D*, 56:2419–2432, Aug 1997. doi: 10.1103/PhysRevD.56.2419. URL https://link.aps.org/doi/10.1103/PhysRevD.56.2419.

[158] F. Kirsten, W. Vlemmings, P. Freire, M. Kramer, H. Rottmann, and R. M. Campbell. Precision astrometry of pulsars and other compact radio sources in the globular cluster m15. *Astronomy Astrophysics*, 565:10, 2014. ISSN 1432-0746. doi: 10.1051/0004-6361/201323239. URL <GotoISI>://WOS:000336730900043.

[159] B. Kiziltan, H. Baumgardt, and A. Loeb. An intermediate-mass black hole in the centre of the globular cluster 47 tucanae. *Nature*, 542(7640):203–205, 2017. ISSN 0028-0836. doi: 10.1038/nature21361. URL <GotoISI>://WOS:000393737500034.

[160] J. Knodlseder, M. Mayer, C. Deil, J. B. Cayrou, E. Owen, N. Kelley-Hoskins, C. C. Lu, R. Buehler, F. Forest, T. Louge, H. Siejkowski, K. Kosack, L. Gerard, A. Schulz, P. Martin, D. Sanchez, S. Ohm, T. Hassan, and S. Brau-Nogue. Gammalib and ctools a software framework for the analysis of astronomical gamma-ray data. *Astronomy Astrophysics*, 593, 2016. ISSN 1432-0746. doi: 10.1051/0004-6361/201628822. URL <GotoISI>://WOS:000385820100122.

[161] V. I. Kondratiev, J. P. W. Verbiest, J. W. T. Hessels, A. V. Bilous, B. W. Stappers, M. Kramer, E. F. Keane, A. Noutsos, S. Oslowski, R. P. Breton, T. E. Hassall, A. Alexov, S. Cooper, H. Falcke, J. M. Griessmeier, A. Karastergiou, M. Kuniyoshi, M. Pilia, C. Sobey, S. ter Veen, J. van Leeuwen, P. Weltevrede, M. E. Bell, J. W. Broderick, S. Corbel, J. Eisloffel, S. Markoff, A. Rowlinson, J. D. Swinbank, Ramj Wijers, R. Wijnands, and P. Zarka. A lofar census of millisecond pulsars. *Astronomy Astrophysics*, 585, 2016. ISSN 0004-6361. doi: 10.1051/0004-6361/201527178. URL <GotoISI>://WOS:000369710300135.

[162] A. Kopp, C. Venter, I. Busching, and O. C. de Jager. Multi-wavelength modeling of globular clusters-the millisecond pulsar scenario. *Astrophysical Journal*, 779(2), 2013. ISSN 0004-637X. doi: 10.1088/0004-637x/779/2/126. URL <GotoISI>://WOS:000328187200036.

[163] R. Kothes and T. Foster. A thorough investigation of the distance to the supernova remnant ctb109 and its pulsar axp j2301+5852. *Astrophysical Journal Letters*, 746(1), 2012. ISSN 2041-8205. doi: 10.1088/2041-8205/746/1/l4. URL <GotoISI>://WOS:000300323500004.

[164] L. Kuiper, W. Hermsen, F. Verbunt, D. J. Thompson, I. H. Stairs, A. G. Lyne, M. S. Strickman, and G. Cusumano. The likely detection of pulsed high-energy gamma-ray emission from millisecond pulsar psr j0218+4232. *Astronomy Astrophysics*, 359(2): 615–626, 2000. ISSN 0004-6361. URL <GotoISI>://WOS:000088587000025.

[165] L. Kuiper, W. Hermsen, and M. Mendez. Discovery of hard nonthermal pulsed x-ray emission from the anomalous x-ray pulsar 1e 1841-045. *Astrophysical Journal*, 613 (2):1173–1178, 2004. ISSN 0004-637X. doi: 10.1086/423129. URL <GotoISI>: //WOS:000224303200042.

[166] L. Kuiper, W. Hermsen, P. R. den Hartog, and W. Collmar. Discovery of luminous pulsed hard x-ray emission from anomalous x-ray pulsars 1rxs j1708-4009, 4u 0142+61, and 1e 2259-586 by integral and rxte. *Astrophysical Journal*, 645(1): 556–575, 2006. ISSN 0004-637X. doi: 10.1086/504317. URL <GotoISI>://WOS: 000238832900046.

[167] S. R. Kulkarni and J. J. Hester. Discovery of a nebula around psr1957+20. *Nature*, 335 (6193):801–803, 1988. ISSN 0028-0836. doi: 10.1038/335801a0. URL <GotoISI>: //WOS:A1988Q634600051.

[168] R. Kurtev, V. D. Ivanov, J. Borissova, and S. Ortolani. Obscured clusters. ii. glimpse-c02 - a new metal rich globular cluster in the milky way. *Astronomy Astrophysics*, 489(2):583–587, 2008. ISSN 0004-6361. doi: 10.1051/0004-6361:200809425. URL <GotoISI>://WOS:000259601500018.

[169] B. Lanzoni, F. R. Ferraro, E. Dalessandro, A. Mucciarelli, G. Beccari, P. Miocchi, M. Bellazzini, R. M. Rich, L. Origlia, E. Valenti, R. T. Rood, and S. M. Ransom. New density profile and structural parameters of the complex stellar system terzan 5. *Astrophysical Journal*, 717(2):653–657, 2010. ISSN 0004-637X. doi: 10.1088/ 0004-637x/717/2/653. URL <GotoISI>://WOS:000280650800004.

[170] M. I. Large, A. E. Vaughan, and R. Wielebinski. Highly dispersed pulsar and 3 others. *Nature*, 223(5212):1249–+, 1969. ISSN 0028-0836. doi: 10.1038/2231249a0. URL <GotoISI>://WOS:A1969E173500028.

[171] M. B. Larson and B. Link. Superfluid friction and late-time thermal evolution of neutron stars. *Astrophysical Journal*, 521(1):271–280, 1999. ISSN 0004-637X. doi: 10.1086/307532. URL <GotoISI>://WOS:000081868300025.

[172] D. A. Leahy and W. W. Tian. The Distances of SNR W41 and Overlapping H II Regions. , 135(1):167–172, January 2008. doi: 10.1088/0004-6256/135/1/167.

[173] F. Lebrun, J. P. Leray, P. Lavocat, J. Cretolle, M. Arques, C. Blondel, C. Bonnin, A. Bouere, C. Cara, T. Chaleil, F. Daly, F. Desages, H. Dzitko, B. Horeau, P. Laurent, O. Limousin, F. Mathy, V. Mauguen, F. Meignier, F. Molinie, E. Poindron, M. Rouger, A. Sauvageon, and T. Tourrette. Isgri: The integral soft gamma-ray imager. *Astronomy Astrophysics*, 411(1):L141–L148, 2003. ISSN 0004-6361. doi: 10.1051/0004-6361:20031367. URL <GotoISI>://WOS:000186227800024.

[174] L. B. Leinson. Axion mass limit from observations of the neutron star in cassiopeia a. *Journal of Cosmology and Astroparticle Physics*, (8):11, 2014. ISSN 1475-7516. doi: 10.1088/1475-7516/2014/08/031. URL <GotoISI>://WOS:000341848800031.

[175] N. Leroy, O. Bolz, J. Guy, I. Jung, I. Redondo, L. Rolland, J. P. Tavernet, K. M. Aye, P. Berghaus, K. Bernleohr, K. Bernlöhr, P. M. Chadwick, V. Chitnis, M. de Naurois, A. Djannati-Ataì, P. Espigat, G. Hermann, J. Hinton, B. Khelifi, A. Kohnle, R. Le Gallou, C. Masterson, S. Pita, T. Saito, C. Théoret, P. Vincent, and H. E. S. S. Collaboration. Calibration Results for the First Two H.E.S.S. Array Telescopes. In *International Cosmic Ray Conference*, volume 5 of *International Cosmic Ray Conference*, page 2895, July 2003.

[176] Lina Levin, Matthew Bailes, Samuel Bates, N. D. Ramesh Bhat, Marta Burgay, Sarah Burke-Spolaor, Nichi D'Amico, Simon Johnston, Michael Keith, Michael Kramer, Sabrina Milia, Andrea Possenti, Nanda Rea, Ben Stappers, and Willem van Straten. A Radio-loud Magnetar in X-ray Quiescence. , 721(1):L33–L37, September 2010. doi: 10.1088/2041-8205/721/1/L33.

[177] J. Li, N. Rea, D. F. Torres, and E. de Ona-Wilhelmi. Gamma-ray upper limits on magnetars with six years of fermi-lat observations. *Astrophysical Journal*, 835(1):10, 2017. ISSN 0004-637X. doi: 10.3847/1538-4357/835/1/30. URL <GotoISI>://WOS:000393455400030.

[178] T. P. Li and Y. Q. Ma. Analysis methods for results in gamma-ray astronomy. , 272:317–324, September 1983. doi: 10.1086/161295.

[179] Brent Limyansky. The Third Fermi Pulsar Catalog. In *AAS/High Energy Astrophysics Division*, AAS/High Energy Astrophysics Division, page 109.32, March 2019.

[180] Lin Lin, Chryssa Kouveliotou, Matthew G. Baring, Alexander J. van der Horst, Sylvain Guiriec, Peter M. Woods, Ersin Göğüş, Yuki Kaneko, Jeffrey Scargle, Jonathan Granot, Robert Preece, Andreas von Kienlin, Vandiver Chaplin, Anna L. Watts, Ralph A. M. J. Wijers, Shuang Nan Zhang, Narayan Bhat, Mark H. Finger, Neil Gehrels, Alice Harding, Lex Kaper, Victoria Kaspi, Julie Mcenery, Charles A. Meegan, William S. Paciesas, Asaf Pe'er, Enrico Ramirez-Ruiz, Michiel van der Klis, Stefanie Wachter, and Colleen Wilson-Hodge. Fermi/Gamma-Ray Burst Monitor Observations of SGR J0501+4516 Bursts. , 739(2):87, October 2011. doi: 10.1088/0004-637X/739/2/87.

[181] S. J. Lloyd, P. M. Chadwick, and A. M. Brown. Gamma-ray emission from high galactic latitude globular clusters. *Monthly Notices of the Royal Astronomical Society*, 480(4):4782–4796, 2018. ISSN 0035-8711. doi: 10.1093/mnras/sty2150. URL <GotoISI>://WOS:000449617100040.

[182] S. J. Lloyd, P. M. Chadwick, and A. M. Brown. Constraining the axion mass through gamma-ray observations of pulsars. *Physical Review D*, 100(6), 2019. ISSN 2470-0010. doi: 10.1103/PhysRevD.100.063005. URL <GotoISI>://WOS: 000485197900004.

[183] Sheridan J. Lloyd, Paula M. Chadwick, Anthony M. Brown, Huai ke Guo, and Kuver Sinha. Axion constraints from quiescent soft gamma-ray emission from magnetars, 2020. URL https://arxiv.org/abs/2001.10849.

[184] R. Lopez-Coto and Hawc Collaboration. Very high energy gamma-ray astronomy with hawc. *Nuclear Instruments Methods in Physics Research Section a-Accelerators Spectrometers Detectors and Associated Equipment*, 876:39–41, 2017. ISSN 0168-9002. doi: 10.1016/j.nima.2016.12.058. URL <GotoISI>://WOS:000418267300011.

[185] Ting-Ni Lu, Albert K. H. Kong, Cees Bassa, Frank Verbunt, Walter H. G. Lewin, Scott F. Anderson, and David Pooley. X-ray sources and their optical counterparts in the galactic globular cluster m12 (ngc 6218). *The Astrophysical Journal*, 705(1):175, 2009. URL http://stacks.iop.org/0004-637X/705/i=1/a=175.

[186] P. M. Lugger, H. N. Cohn, A. M. Cool, C. O. Heinke, and J. Anderson. Identification of faint chandra x-ray sources in the core-collapsed globular cluster ngc 6752. *Astrophysical Journal*, 841(1):23, 2017. ISSN 0004-637X. doi: 10.3847/1538-4357/aa6c56. URL <GotoISI>://WOS:000402310500039.

[187] Jhilik Majumdar, Francesca Calore, and Dieter Horns. Search for gamma-ray spectral modulations in galactic pulsars. *Journal of Cosmology and Astroparticle Physics*,

2018(04):048–048, apr 2018. doi: 10.1088/1475-7516/2018/04/048. URL https://doi.org/10.1088%2F1475-7516%2F2018%2F04%2F048.

[188] R. N. Manchester, A. G. Lyne, J. H. Taylor, J. M. Durdin, M. I. Large, and A. G. Little. 2nd Molonglo pulsar survey - discovery of 155 pulsars. *Monthly Notices of the Royal Astronomical Society*, 185(2):409–421, 1978. ISSN 0035-8711. doi: 10.1093/mnras/185.2.409. URL <GotoISI>://WOS:A1978FU94600009.

[189] R. N. Manchester, A. G. Lyne, N. Damico, M. Bailes, S. Johnston, D. R. Lorimer, P. A. Harrison, L. Nicastro, and J. F. Bell. The Parkes southern pulsar survey .1. observing and data analysis systems and initial results. *Monthly Notices of the Royal Astronomical Society*, 279(4):1235–1250, 1996. ISSN 0035-8711. doi: 10.1093/mnras/279.4.1235. URL <GotoISI>://WOS:A1996UG55300020.

[190] R. N. Manchester, G. B. Hobbs, A. Teoh, and M. Hobbs. The Australia Telescope National Facility Pulsar Catalogue. *The Astronomical Journal*, 129:1993–2006, April 2005. doi: 10.1086/428488.

[191] J. R. Mattox, D. L. Bertsch, J. Chiang, B. L. Dingus, S. W. Digel, J. A. Esposito, J. M. Fierro, R. C. Hartman, S. D. Hunter, G. Kanbach, D. A. Kniffen, Y. C. Lin, D. J. Macomb, H. A. MayerHasselwander, P. F. Michelson, C. vonMontigny, R. Mukherjee, P. L. Nolan, P. V. Ramanamurthy, E. Schneid, P. Sreekumar, D. J. Thompson, and T. D. Willis. The likelihood analysis of egret data. *Astrophysical Journal*, 461(1):396–407, 1996. ISSN 0004-637X. doi: 10.1086/177068. URL <GotoISI>://WOS:A1996UD64600035.

[192] M. Mayer, R. Buehler, E. Hays, C. C. Cheung, M. S. Dutka, J. E. Grove, M. Kerr, and R. Ojha. Rapid gamma-ray flux variability during the 2013 march crab nebula flare. *Astrophysical Journal Letters*, 775(2):6, 2013. ISSN 2041-8205. doi: 10.1088/2041-8205/775/2/l37. URL <GotoISI>://WOS:000324626700004.

[193] Ron Mayle, James R. Wilson, John Ellis, Keith Olive, David N. Schramm, and Gary Steigman. Constraints on axions from sn 1987a. *Physics Letters B*, 203(1):188 – 196, 1988. ISSN 0370-2693. doi: https://doi.org/10.1016/0370-2693(88)91595-X. URL http://www.sciencedirect.com/science/article/pii/037026938891595X.

[194] A. McCann. A stacked analysis of 115 pulsars observed by the fermi lat. *Astrophysical Journal*, 804(2):10, 2015. ISSN 0004-637X. doi: 10.1088/0004-637x/804/2/86. URL <GotoISI>://WOS:000354905000008.

[195] Michael McCutcheon. Veritas observations of globular clusters, 2009. URL https://arxiv.org/abs/0907.4974.

[196] Julie McEnery, Juan Abel Barrio, Ivan Agudo, Marco Ajello, José-Manuel Álvarez, Stefano Ansoldi, Sonia Anton, Natalia Auricchio, John B. Stephen, Luca Baldini, Cosimo Bambi, Matthew Baring, Ulisses Barres, Denis Bastieri, John Beacom, Volker Beckmann, Wlodek Bednarek, Denis Bernard, Elisabetta Bissaldi, Peter Bloser, Harsha Blumer, Markus Boettcher, Steven Boggs, Aleksey Bolotnikov, Eugenio Bottacini, Vladimir Bozhilov, Enrico Bozzo, Michael Briggs, Jim Buckley, Eric Burns, Sara Buson, Riccardo Campana, Regina Caputo, Martina Cardillo, Ezio Caroli, Daniel Castro, S. Brad Cenko, Eric Charles, Wenlei Chen, Teddy Cheung, Stefano Ciprini, Paolo Coppi, Rui Curado da Silva, Sara Cutini, Filippo D'Ammando, Alessandro De Angelis, Michaël De Becker, Georgia De Nolfo, Stefano Del Sordo, Mattia Di Mauro, Leonardo Di Venere, Stefano Dietrich, Seth Digel, Alberto Dominguez, Michele Doro, Elizabeth Ferrara, Brian Fields, Justin Finke, Luca Foffano, Chris Fryer, Yasushi Fukazawa, Stefan Funk, Dario Gasparrini, Joseph Gelfand, Markos Georganopoulos, Francesco Giordano, Andrea Giuliani, Christian Gouiffes, Brian Grefenstette, Isabelle Grenier, Sean Griffin, Eric Grove, Sylvain Guiriec, Alice Harding, Pat Harding, Dieter Hartmann, Elizabeth Hays, Margarita Hernanz, Jack Hewitt, Jamie Holder, Michelle Hui, Andrew Inglis, Robert Johnson, Sam Jones, Gottfried Kanbach, Oleg Kargaltsev, Sarah Kaufmann, Matthew Kerr, Carolyn Kierans, Fabian Kislat, Alexei V. Klimenko, Jurgen Knodlseder, Daniel Kocveski, Joachim Kopp, Henric Krawczynsiki, John Krizmanic, Hidetoshi Kubo, Naoko Kurahashi Neilson, Philippe Laurent, Jean-Philippe Lenain, Hui Li, Amy Lien, Tim Linden, Jan Lommler, Francesco Longo, Michael Lovellette, Marcos López, Antonios Manousakis, Lea Marcotulli, Alexandre Marcowith, Manel Martinez, Marc McConnell, Jessica Metcalfe, Eileen Meyer, Manuel Meyer, Roberto Mignani, John Mitchell, Tsunefumi Mizuno, Alexander Moiseev, Daniel Morcuende, Igor Moskalenko, Michael Moss, Kazuhiro Nakazawa, M. Nicola Mazziotta, Uwe Oberlack, Masanori Ohno, Foteini Oikonomou, Roopesh Ojha, Nicola Omodei, Elena Orlando, Nepomuk Otte, Vaidehi S Paliya, Lucas Parker, Barbara Patricelli, Jeremy Perkins, Maria Petropoulou, Carlotta Pittori, Martin Pohl, Troy Porter, Elisa Prandini, Chanda Prescod-Weinstein, Judith Racusin, Riccardo Rando, Bindu Rani, Marc Ribó, James Rodi, Miguel A. Sanchez-Conde, Pablo Saz Parkinson, Richard Schirato, Peter Shawhan, Chris Shrader, Jacob Smith, Karl Smith, Antonio Stamerra, Lukasz Stawarz, Andy Strong, Inga Stumke, Hiro Tajima, Hiromitsu Takahashi, Yasuyuki Tanaka, Vincent Tatischeff, Lih-Sin The, David Thompson, Luigi Tibaldo, John Tomsick, Lucas Uhm, Tonia Venters, Tom Vestrand, Giacomo Vianello,

Zorawar Wadiasingh, Roland Walter, Xilu Wang, David Williams, Colleen Wilson-Hodge, Matthew Wood, Richard Woolf, Eric Wulf, George Younes, Luca Zampieri, Silvia Zane, Bing Zhang, Haocheng Zhang, Stephan Zimmer, Andreas Zoglauer, and Alexander van der Horst. All-sky medium energy gamma-ray observatory: Exploring the extreme multimessenger universe, 2019.

[197] C. Meegan, G. Lichti, P. N. Bhat, E. Bissaldi, M. S. Briggs, V. Connaughton, R. Diehl, G. Fishman, J. Greiner, A. S. Hoover, A. J. van der Horst, A. Von Kienlin, R. M. Kippen, C. Kouveliotou, S. McBreen, W. S. Paciesas, R. Preece, H. Steinle, M. S. Wallace, R. B. Wilson, and C. Wilson-Hodge. The fermi gamma-ray burst monitor. *Astrophysical Journal*, 702(1):791–804, 2009. ISSN 0004-637X. doi: 10.1088/0004-637x/702/1/791. URL <GotoISI>://WOS:000269244500065.

[198] Anthony H. Minter, Fernando Camilo, Scott M. Ransom, Jules P. Halpern, and Neil Zimmerman. Neutral Hydrogen Absorption toward XTE J1810-197: The Distance to a Radio-emitting Magnetar. , 676(2):1189–1199, April 2008. doi: 10.1086/529005.

[199] L. Mohrmann, A. Specovius, D. Tiziani, S. Funk, D. Malyshev, K. Nakashima, and C. van Eldik. Validation of open-source science tools and background model construction in gamma-ray astronomy. *Astronomy Astrophysics*, 632, 2019. ISSN 0004-6361. doi: 10.1051/0004-6361/201936452. URL <GotoISI>://WOS:000505727500002.

[200] E. Moreno, B. Pichardo, and H. Velazquez. Tidal radii and destruction rates of globular clusters in the milky way due to bulge-bar and disk shocking. *Astrophysical Journal*, 793(2), 2014. ISSN 0004-637X. doi: 10.1088/0004-637x/793/2/110. URL <GotoISI>://WOS:000341965300041.

[201] Paul J. Morris, Garret Cotter, Anthony M. Brown, and Paula M. Chadwick. Gamma-ray novae: rare or nearby? *Monthly Notices of the Royal Astronomical Society*, 465 (1):1218–1226, 2017. doi: 10.1093/mnras/stw2776. URL +http://dx.doi.org/10.1093/mnras/stw2776.

[202] A. G. Muslimov and A. K. Harding. Extended acceleration in slot gaps and pulsar high-energy emission. *Astrophysical Journal*, 588(1):430–440, 2003. ISSN 0004-637X. doi: 10.1086/368162. URL <GotoISI>://WOS:000182451800036.

[203] A. G. Muslimov and A. K. Harding. High-altitude particle acceleration and radiation in pulsar slot gaps. *Astrophysical Journal*, 606(2):1143–1153, 2004. ISSN 0004-637X. doi: 10.1086/383079. URL <GotoISI>://WOS:000221261900043.

[204] Ken'ichiro Nakazato, Hideyuki Suzuki, and Hajime Togashi. Heavy nuclei as thermal insulation for protoneutron stars. *Phys. Rev. C*, 97:035804, Mar 2018. doi: 10.1103/PhysRevC.97.035804. URL https://link.aps.org/doi/10.1103/PhysRevC.97.035804.

[205] H. Ndiyavala, P. P. Kruger, and C. Venter. Identifying the brightest galactic globular clusters for future observations by hess and cta. *Monthly Notices of the Royal Astronomical Society*, 473(1):897–908, 2018. ISSN 0035-8711. doi: 10.1093/mnras/stx2336. URL <GotoISI>://WOS:000415653600072.

[206] H. Ndiyavala, C. Venter, T. J. Johnson, A. K. Harding, D. A. Smith, P. Eger, A. Kopp, and D. J. van der Walt. Probing the pulsar population of terzan 5 via spectral modeling. *Astrophysical Journal*, 880(1):12, 2019. ISSN 0004-637X. doi: 10.3847/1538-4357/ab24ca. URL <GotoISI>://WOS:000477571400010.

[207] R. Negreiros, V. A. Dexheimer, and S. Schramm. Quark core impact on hybrid star cooling. *Physical Review C*, 85(3):7, 2012. ISSN 2469-9985. doi: 10.1103/PhysRevC.85.035805. URL <GotoISI>://WOS:000301573000004.

[208] H. I. Nel and O. C. Dejager. Gamma-ray pulsars - polar-cap or outer gap emission. *Astrophysics and Space Science*, 230(1-2):299–306, 1995. ISSN 0004-640X. doi: 10.1007/bf00658187. URL <GotoISI>://WOS:A1995TD81200027.

[209] P. L. Nolan, A. A. Abdo, M. Ackermann, M. Ajello, A. Allafort, E. Antolini, W. B. Atwood, M. Axelsson, L. Baldini, J. Ballet, G. Barbiellini, D. Bastieri, K. Bechtol, A. Belfiore, R. Bellazzini, B. Berenji, G. F. Bignami, R. D. Blandford, E. D. Bloom, E. Bonamente, J. Bonnell, A. W. Borgland, E. Bottacini, A. Bouvier, T. J. Brandt, J. Bregeon, M. Brigida, P. Bruel, R. Buehler, T. H. Burnett, S. Buson, G. A. Caliandro, R. A. Cameron, R. Campana, B. Canadas, A. Cannon, P. A. Caraveo, J. M. Casandjian, E. Cavazzuti, M. Ceccanti, C. Cecchi, O. Celik, E. Charles, A. Chekhtman, C. C. Cheung, J. Chiang, R. Chipaux, S. Ciprini, R. Claus, J. Cohen-Tanugi, L. R. Cominsky, J. Conrad, R. Corbet, S. Cutini, F. D'Ammando, D. S. Davis, A. de Angelis, M. E. DeCesar, M. DeKlotz, A. De Luca, P. R. den Hartog, F. de Palma, C. D. Dermer, S. W. Digel, E. D. E. Silva, P. S. Drell, A. Drlica-Wagner, R. Dubois, D. Dumora, T. Enoto, L. Escande, D. Fabiani, L. Falletti, C. Favuzzi, S. J. Fegan, E. C. Ferrara, W. B. Focke, P. Fortin, M. Frailis, Y. Fukazawa, S. Funk, P. Fusco, F. Gargano, D. Gasparrini, N. Gehrels, S. Germani, B. Giebels, N. Giglietto, P. Giommi, F. Giordano, M. Giroletti, T. Glanzman, G. Godfrey, I. A. Grenier, M. H. Grondin, J. E. Grove, L. Guillemot, S. Guiriec, M. Gustafsson, D. Hadasch, et al. Fermi large area telescope second source

catalog. *Astrophysical Journal Supplement Series*, 199(2), 2012. ISSN 0067-0049. doi: 10.1088/0067-0049/199/2/31. URL <GotoISI>://WOS:000303105400007.

[210] K. Nomoto and S. Tsuruta. Cooling of neutron-stars - effects of the finite-time scale of thermal conduction. *Astrophysical Journal*, 312(2):711–726, 1987. ISSN 0004-637X. doi: 10.1086/164914. URL <GotoISI>://WOS:A1987F864700021.

[211] Y. Okada, M. Kokubun, T. Yuasa, and K. Makishima. Chandra detections of diffuse x-ray emission from globular clusters. *Publications of the Astronomical Society of Japan*, 59(4):727–742, 2007. ISSN 0004-6264. doi: 10.1093/pasj/59.4.727. URL <GotoISI>://WOS:000249977200008.

[212] S. A. Olausen and V. M. Kaspi. The mcgill magnetar catalog. *Astrophysical Journal Supplement Series*, 212(1), 2014. ISSN 0067-0049. doi: 10.1088/0067-0049/212/1/6. URL <GotoISI>://WOS:000339232600006.

[213] G. G. Pavlov, G. S. Stringfellow, and F. A. Cordova. Hubble space telescope observations of isolated pulsars. *Astrophysical Journal*, 467(1):370–+, 1996. ISSN 0004-637X. doi: 10.1086/177612. URL <GotoISI>://WOS:A1996VB70300033.

[214] G. G. Pavlov, B. Rangelov, O. Kargaltsev, A. Reisenegger, S. Guillot, and C. Reyes. Old but still warm: Far-uv detection of psr b0950+08. *Astrophysical Journal*, 850(1): 7, 2017. ISSN 0004-637X. doi: 10.3847/1538-4357/aa947c. URL <GotoISI>://WOS: 000415827600005.

[215] R. D. Peccei and Helen R. Quinn. CP conservation in the presence of pseudoparticles. *Phys. Rev. Lett.*, 38:1440–1443, Jun 1977. doi: 10.1103/PhysRevLett.38.1440. URL https://link.aps.org/doi/10.1103/PhysRevLett.38.1440.

[216] P. J. E. Peebles. Dark matter and the origin of galaxies and globular star clusters. , 277:470–477, February 1984. doi: 10.1086/161714.

[217] B. B. P. Perera, B. W. Stappers, A. G. Lyne, C. G. Bassa, I. Cognard, L. Guillemot, M. Kramer, G. Theureau, and G. Desvignes. Evidence for an intermediate-mass black hole in the globular cluster ngc 6624. *Monthly Notices of the Royal Astronomical Society*, 468(2):2114–2127, 2017. ISSN 0035-8711. doi: 10.1093/mnras/stx501.

[218] R. Perna, W. C. G. Ho, L. Verde, M. van Adelsberg, and R. Jimenez. Signatures of photon-axion conversion in the thermal spectra and polarization of neutron stars. *Astrophysical Journal*, 748(2):17, 2012. ISSN 0004-637X. doi: 10.1088/0004-637x/748/2/116. URL <GotoISI>://WOS:000302135200044.

[219] J. Petri. Pulsar gamma-ray emission in the radiation reaction regime. *Monthly Notices of the Royal Astronomical Society*, 484(4):5669–5691, 2019. ISSN 0035-8711. doi: 10.1093/mnras/stz360. URL <GotoISI>://WOS:000462414400085.

[220] A. A. Philippov and A. Spitkovsky. Ab initio pulsar magnetosphere: Three-dimensional particle-in-cell simulations of axisymmetric pulsars. *Astrophysical Journal Letters*, 785(2), 2014. ISSN 2041-8205. doi: 10.1088/2041-8205/785/2/l33. URL <GotoISI>://WOS:000334359800014.

[221] J. D. Pilkington, A. Hewish, S. J. Bell, and T. W. Cole. Observations of some further pulsed radio sources. *Nature*, 218(5137):126–+, 1968. ISSN 0028-0836. doi: 10.1038/218126a0. URL <GotoISI>://WOS:A1968A935500004.

[222] J. A. Pons, S. Reddy, M. Prakash, J. M. Lattimer, and J. A. Miralles. Evolution of proto-neutron stars. *Astrophysical Journal*, 513(2):780–804, 1999. ISSN 0004-637X. doi: 10.1086/306889. URL <GotoISI>://WOS:000079816000024.

[223] L. Posti and A. Helmi. Mass and shape of the milky way's dark matter halo with globular clusters from gaia and hubble. *Astronomy Astrophysics*, 621, 2019. ISSN 1432-0746. doi: 10.1051/0004-6361/201833355. URL <GotoISI>://WOS:000455076900005.

[224] A. Y. Potekhin, G. Chabrier, and D. G. Yakovlev. Heat blanketing envelopes and thermal radiation of strongly magnetized neutron stars. *Astrophysics and Space Science*, 308(1-4):353–361, 2007. ISSN 0004-640X. doi: 10.1007/s10509-007-9362-6. URL <GotoISI>://WOS:000246351000044.

[225] B. J. Prager, S. M. Ransom, P. C. C. Freire, J. W. T. Hessels, I. H. Stairs, P. Arras, and M. Cadelano. Using long-term millisecond pulsar timing to obtain physical characteristics of the bulge globular cluster terzan 5. *Astrophysical Journal*, 845(2):24, 2017. ISSN 0004-637X. doi: 10.3847/1538-4357/aa7ed7. URL <GotoISI>://WOS:000408111400034.

[226] G. G. Raffelt. Astrophysical axion bounds. *Axions: Theory, Cosmology, and Experimental Searches*, 741:51–71, 2008. ISSN 0075-8450. doi: 10.1007/978-3-540-73518-2-3. URL <GotoISI>://WOS:000253561800003.

[227] J. F. Rajotte and Veritas Collaboration. Upgrade and performance of the veritas telescope array. *Nuclear Instruments Methods in Physics Research Section a-Accelerators*

Spectrometers Detectors and Associated Equipment, 766:61–64, 2014. ISSN 0168-9002. doi: 10.1016/j.nima.2014.04.075. URL <GotoISI>://WOS:000344622200015.

[228] B. Rajput, C. S. Stalin, and S. Rakshit. Long term gamma-ray variability of blazars. *Astronomy Astrophysics*, 634, 2020. ISSN 0004-6361. doi: 10.1051/0004-6361/201936769. URL <GotoISI>://WOS:000514887200001.

[229] R. Rando. The all-sky medium energy gamma-ray observatory. *Journal of Instrumentation*, 12(11):C11024, 2017. URL http://stacks.iop.org/1748-0221/12/i=11/a=C11024.

[230] S. Raso, C. Pallanca, F. R. Ferraro, B. Lanzoni, A. Mucciarelli, L. Origlia, E. Dalessandro, A. Bellini, M. Libralato, and J. Anderson. Spectral energy distribution of blue stragglers in the core of 47 tucanae. *Astrophysical Journal*, 879(1), 2019. ISSN 0004-637X. doi: 10.3847/1538-4357/ab2637. URL <GotoISI>://WOS:000474384700001.

[231] D. J. Reardon, G. Hobbs, W. Coles, Y. Levin, M. J. Keith, M. Bailes, N. D. R. Bhat, S. Burke-Spolaor, S. Dai, M. Kerr, P. D. Lasky, R. N. Manchester, S. Oslowski, V. Ravi, R. M. Shannon, W. van Straten, L. Toomey, J. Wang, L. Wen, X. P. You, and X. J. Zhu. Timing analysis for 20 millisecond pulsars in the Parkes pulsar timing array. *Monthly Notices of the Royal Astronomical Society*, 455(2):1751–1769, 2016. ISSN 0035-8711. doi: 10.1093/mnras/stv2395. URL <GotoISI>://WOS:000368007100046.

[232] Florent Renaud, Oscar Agertz, and Mark Gieles. The origin of the Milky Way globular clusters. *Monthly Notices of the Royal Astronomical Society*, 465(3):3622–3636, 11 2016. ISSN 0035-8711. doi: 10.1093/mnras/stw2969. URL https://doi.org/10.1093/mnras/stw2969.

[233] A. Ridolfi, P. C. C. Freire, P. Torne, C. O. Heinke, M. Van Den Berg, C. Jordan, M. Kramer, C. G. Bassa, J. Sarkissian, N. D'Amico, D. Lorimer, F. Camilo, R. N. Manchester, and A. Lyne. Long-term observations of the pulsars in 47 tucanae - i. a study of four elusive binary systems. *Monthly Notices of the Royal Astronomical Society*, 462(3):2918–2933, 2016. ISSN 0035-8711. doi: 10.1093/mnras/stw1850. URL <GotoISI>://WOS:000384676000044.

[234] J. Rodi, M. L. Cherry, G. L. Case, A. Camero-Arranz, V. Chaplin, M. H. Finger, P. Jenke, and C. A. Wilson-Hodge. Earth occultation imaging of the low energy gamma-ray sky with gbm. *Astronomy Astrophysics*, 562, 2014. ISSN 1432-0746. doi: 10.1051/0004-6361/201321637. URL <GotoISI>://WOS:000332161800024.

[235] S. B. Ruster, V. Werth, M. Buballa, I. A. Shovkovy, and D. H. Rischke. Phase diagram of neutral quark matter: Self-consistent treatment of quark masses. *Physical Review D*, 72(3):13, 2005. ISSN 2470-0010. doi: 10.1103/PhysRevD.72.034004. URL <GotoISI>://WOS:000231564900032.

[236] Gray Rybka. Direct detection searches for axion dark matter. *Physics of the Dark Universe*, 4:14 – 16, 2014. ISSN 2212-6864. doi: https://doi.org/10.1016/j.dark.2014.05.003. URL http://www.sciencedirect.com/science/article/pii/S2212686414000156. DARK TAUP2013.

[237] L. E. R. Sandoval, M. van den Berg, C. O. Heinke, H. N. Cohn, P. M. Lugger, J. Anderson, A. M. Cool, P. D. Edmonds, R. Wijnands, N. Ivanova, and J. E. Grindlay. New cataclysmic variables and other exotic binaries in the globular cluster 47 tucanae. *Monthly Notices of the Royal Astronomical Society*, 475(4):4841–4867, 2018. ISSN 0035-8711. doi: 10.1093/mnras/sty058. URL <GotoISI>://WOS:000428835700038.

[238] S. Sanidas, S. Cooper, C. G. Bassa, J. W. T. Hessels, V. I. Kondratiev, D. Michilli, B. W. Stappers, C. M. Tan, J. van Leeuwen, L. Cerrigone, R. A. Fallows, M. Iacobelli, E. Orrú, R. F. Pizzo, A. Shulevski, M. C. Toribio, S. ter Veen, P. Zucca, L. Bondonneau, J. M. Grießmeier, A. Karastergiou, M. Kramer, and C. Sobey. The LOFAR Tied-Array All-Sky Survey (LOTAAS): Survey overview and initial pulsar discoveries. , 626: A104, June 2019. doi: 10.1051/0004-6361/201935609.

[239] V. Schonfelder, H. Aarts, K. Bennett, H. Deboer, J. Clear, W. Collmar, A. Connors, A. Deerenberg, R. Diehl, A. Vondordrecht, J. W. Denherder, W. Hermsen, M. Kippen, L. Kuiper, G. Lichti, J. Lockwood, J. Macri, M. McConnell, D. Morris, R. Much, J. Ryan, G. Simpson, M. Snelling, G. Stacy, H. Steinle, A. Strong, B. N. Swanenburg, B. Taylor, C. Devries, and C. Winkler. Instrument description and performance of the imaging gamma-ray telescope comptel aboard the compton gamma-ray observatory. *Astrophysical Journal Supplement Series*, 86(2):657–692, 1993. ISSN 0067-0049. doi: 10.1086/191794. URL <GotoISI>://WOS:A1993LD67400013.

[240] Armen Sedrakian. Axion cooling of neutron stars. *Phys. Rev. D*, 93:065044, Mar 2016. doi: 10.1103/PhysRevD.93.065044. URL https://link.aps.org/doi/10.1103/PhysRevD.93.065044.

[241] H. Shen, H. Toki, K. Oyamatsu, and K. Sumiyoshi. Relativistic equation of state of nuclear matter for supernova and neutron star. *Nuclear Physics A*, 637(3):435–450,

1998. ISSN 0375-9474. doi: 10.1016/s0375-9474(98)00236-x. URL <GotoISI>://WOS:000075680900007.

[242] B. C. Siegman, R. N. Manchester, and J. M. Durdin. Timing parameters for 59 pulsars. *Monthly Notices of the Royal Astronomical Society*, 262(2):449–455, 1993. ISSN 0035-8711. doi: 10.1093/mnras/262.2.449. URL <GotoISI>://WOS:A1993LC06400021.

[243] D. A. Smith, P. Bruel, I. Cognard, A. D. Cameron, F. Camilo, S. Dai, L. Guillemot, T. J. Johnson, S. Johnston, M. J. Keith, M. Kerr, M. Kramer, A. G. Lyne, R. N. Manchester, R. Shannon, C. Sobey, B. W. Stappers, and P. Weltevrede. Searching a thousand radio pulsars for gamma-ray emission. *Astrophysical Journal*, 871(1), 2019. ISSN 0004-637X. doi: 10.3847/1538-4357/aaf57d. URL <GotoISI>://WOS:000456837000027.

[244] David A. Smith, Lucas Guillemot, Matthew Kerr, Cherry Ng, and Ewan Barr. Gamma-ray pulsars with fermi, 2017. URL https://arxiv.org/abs/1706.03592.

[245] A. Sollima. The eye of gaia on globular clusters structure: tidal tails. *Monthly Notices of the Royal Astronomical Society*, 495(2):2222–2233, 2020. ISSN 0035-8711. doi: 10.1093/mnras/staa1209. URL <GotoISI>://WOS:000543015800050.

[246] M. Su, T. R. Slatyer, and D. P. Finkbeiner. Giant gamma-ray bubbles from fermi-lat: Active galactic nucleus activity or bipolar galactic wind? *Astrophysical Journal*, 724 (2):1044–1082, 2010. ISSN 0004-637X. doi: 10.1088/0004-637x/724/2/1044. URL <GotoISI>://WOS:000284149000018.

[247] K. Sumiyoshi, S. Yamada, H. Suzuki, H. Shen, S. Chiba, and H. Toki. Postbounce evolution of core-collapse supernovae: Long-term effects of the equation of state. *Astrophysical Journal*, 629(2):922–932, 2005. ISSN 0004-637X. doi: 10.1086/431788. URL <GotoISI>://WOS:000231159500030.

[248] J. Takata, C. W. Ng, and K. S. Cheng. Probing gamma-ray emissions of fermi-lat pulsars with a non-stationary outer gap model. *Monthly Notices of the Royal Astronomical Society*, 455(4):4249–4266, 2016. ISSN 0035-8711. doi: 10.1093/mnras/stv2612. URL <GotoISI>://WOS:000368009300064.

[249] P. H. T. Tam, A. K. H. Kong, C. Y. Hui, K. S. Cheng, C. Li, and T. N. Lu. Gamma-ray emission from the globular clusters liller 1, m80, ngc 6139, ngc 6541, ngc 6624, and ngc 6752. *Astrophysical Journal*, 729(2):8, 2011. ISSN 0004-637X. doi: 10.1088/0004-637x/729/2/90.

[250] T. M. Tauris, L. Nicastro, S. Johnston, R. N. Manchester, M. Bailes, A. G. Lyne, J. Glowacki, D. R. Lorimer, and N. Damico. Discovery of psr j0108-1431 - the closest known neutron-star. *Astrophysical Journal*, 428(2):L53–L55, 1994. ISSN 0004-637X. doi: 10.1086/187391. URL <GotoISI>://WOS:A1994NQ75300003.

[251] Felix ter Beek. *FERMI GBM detections of four AXPs at soft gamma-rays*. Thesis, 2012. URL https://esc.fnwi.uva.nl/thesis/centraal/files/f750556480.pdf.

[252] *Fermi* LAT Collaboration. Galactic interstellar emission model for the 4fgl catalog analysis. 2019. URL https://fermi.gsfc.nasa.gov/ssc/data/analysis/software/aux/4fgl/Galactic_Diffuse_Emission_Model_for_the_4FGL_Catalog_Analysis.pdf.

[253] G. S. Thomson, C. Knigge, A. Dieball, T. J. Maccarone, A. Dolphin, D. Zurek, K. S. Long, M. Shara, and A. Sarajedini. A multiwavelength survey of ngc 6752: X-ray counterparts, two new dwarf novae and a core-collapsed radial profile. *Monthly Notices of the Royal Astronomical Society*, 423(3):2901–2916, 2012. ISSN 0035-8711. doi: 10.1111/j.1365-2966.2012.21104.x. URL <GotoISI>://WOS:000305470100074.

[254] W. W. Tian and D. A. Leahy. The distance and age of the supernova remnants kes 73 and axp 1e 1841-045. *Astrophysical Journal*, 677(1):292–296, 2008. ISSN 0004-637X. doi: 10.1086/529120. URL <GotoISI>://WOS:000254754300021.

[255] W. W. Tian and D. A. Leahy. Distances of the TeV supernova remnant complex CTB 37 towards the Galactic bar. , 421(3):2593–2597, April 2012. doi: 10.1111/j.1365-2966.2012.20491.x.

[256] A. Tiengo, G. Vianello, P. Esposito, S. Mereghetti, A. Giuliani, E. Costantini, G. L. Israel, L. Stella, R. Turolla, S. Zane, N. Rea, D. Götz, F. Bernardini, A. Moretti, P. Romano, M. Ehle, and N. Gehrels. The Dust-scattering X-ray Rings of the Anomalous X-ray Pulsar 1E 1547.0-5408. , 710(1):227–235, February 2010. doi: 10.1088/0004-637X/710/1/227.

[257] A. Tiengo, G. Vianello, P. Esposito, S. Mereghetti, A. Giuliani, E. Costantini, G. L. Israel, L. Stella, R. Turolla, S. Zane, N. Rea, D. Gotz, F. Bernardini, A. Moretti, P. Romano, M. Ehle, and N. Gehrels. The dust-scattering x-ray rings of the anomalous x-ray pulsar 1e 1547.0-5408. *Astrophysical Journal*, 710(1):227–235, 2010. ISSN 0004-637X. doi: 10.1088/0004-637x/710/1/227. URL <GotoISI>://WOS:000273850800022.

[258] E. Tremou, J. Strader, L. Chomiuk, L. Shishkovsky, T. J. Maccarone, J. C. A. Miller-Jones, V. Tudor, C. O. Heinke, G. R. Sivakoff, A. C. Seth, and E. Noyola. The maveric survey: Still no evidence for accreting intermediate-mass black holes in globular clusters. *Astrophysical Journal*, 862(1), 2018. ISSN 0004-637X. doi: 10.3847/1538-4357/aac9b9. URL <GotoISI>://WOS:000439184900006.

[259] K. E. Turver and T. C. Weekes. Gamma-ray Astronomy From 10 To 100 Gev. *Nuovo Cimento Della Societa Italiana Di Fisica B-General Physics Relativity Astronomy and Mathematical Physics and Methods*, 45(1):99–108, 1978. ISSN 0369-3554. doi: 10.1007/bf02904077. URL <GotoISI>://WOS:A1978FC38500008.

[260] D. A. Uzdensky and A. Spitkovsky. Physical conditions in the reconnection layer in pulsar magnetospheres. *Astrophysical Journal*, 780(1), 2014. ISSN 0004-637X. doi: 10.1088/0004-637x/780/1/3. URL <GotoISI>://WOS:000328937100003.

[261] Large M. I. Wielebinski R. Vaughan, A. E. Three new pulsars. *Nature*, 222:963, 1969. doi: 10.1038/222963a0. URL <GotoISI>://WOS:A1994NQ75300003.

[262] G. Vedrenne, J. P. Roques, V. Schonfelder, P. Mandrou, G. G. Lichti, A. von Kienlin, B. Cordier, S. Schanne, J. Knodlseder, G. Skinner, P. Jean, F. Sanchez, P. Caraveo, B. Teegarden, P. von Ballmoos, L. Bouchet, P. Paul, J. Matteson, S. Boggs, C. Wunderer, P. Leleux, G. Weidenspointner, P. Durouchoux, R. Diehl, A. Strong, M. Casse, M. A. Clair, and Y. Andre. Spi: The spectrometer aboard integral. *Astronomy Astrophysics*, 411(1):L63–L70, 2003. ISSN 0004-6361. doi: 10.1051/0004-6361:20031482. URL <GotoISI>://WOS:000186227800012.

[263] C. Venter and O. C. De Jager. Accelerating high-energy pulsar radiation codes. *Astrophysical Journal*, 725(2):1903–1909, 2010. ISSN 0004-637X. doi: 10.1088/0004-637x/725/2/1903. URL <GotoISI>://WOS:000285501300043.

[264] F. Verbunt and P. C. C. Freire. On the disruption of pulsar and x-ray binaries in globular clusters. *Astronomy Astrophysics*, 561:10, 2014. ISSN 0004-6361. doi: 10.1051/0004-6361/201321177. URL <GotoISI>://WOS:000330584000011.

[265] D. Vigano, D. F. Torres, K. Hirotani, and M. E. Pessah. An assessment of the pulsar outer gap model - i. assumptions, uncertainties, and implications on the gap size and the accelerating field. *Monthly Notices of the Royal Astronomical Society*, 447(3):2631–2648, 2015. ISSN 0035-8711. doi: 10.1093/mnras/stu2564. URL <GotoISI>://WOS:000350273200043.

[266] D. Vigano, D. F. Torres, and J. Martin. A systematic synchro-curvature modelling of pulsar gamma-ray spectra unveils hidden trends. *Monthly Notices of the Royal Astronomical Society*, 453(3):2599–2621, 2015. ISSN 0035-8711. doi: 10.1093/mnras/stv1582. URL <GotoISI>://WOS:000363649000032.

[267] H. Volk and K. Bernlohr. Imaging very high energy gamma-ray telescopes. *Experimental Astronomy*, 25(1-3):173–191, 2009. ISSN 0922-6435. doi: 10.1007/s10686-009-9151-z. URL <GotoISI>://WOS:000267896100013.

[268] Z. Wadiasingh, M. G. Baring, P. L. Gonthier, and A. K. Harding. Resonant inverse compton scattering spectra from highly magnetized neutron stars. *Astrophysical Journal*, 854(2), 2018. ISSN 0004-637X. doi: 10.3847/1538-4357/aaa460. URL <GotoISI>://WOS:000425306100021.

[269] N. C. Weatherford, S. Chatterjee, K. Kremer, and F. A. Rasio. A dynamical survey of stellar-mass black holes in 50 milky way globular clusters. *Astrophysical Journal*, 898(2), 2020. ISSN 0004-637X. doi: 10.3847/1538-4357/ab9f98. URL <GotoISI>://WOS:000560046200001.

[270] Weekes. *Very High Energy Gamma-Ray Astronomy*. CRC Press, 2003. ISBN 9780429093241. doi: 10.1201/9781420033199.

[271] T. C. Weekes, M. F. Cawley, D. J. Fegan, K. G. Gibbs, A. M. Hillas, P. W. Kwok, R. C. Lamb, D. A. Lewis, D. Macomb, N. A. Porter, P. T. Reynolds, and G. Vacanti. Observation of tev gamma-rays from the crab-nebula using the atmospheric cerenkov imaging technique. *Astrophysical Journal*, 342(1):379–395, 1989. ISSN 0004-637X. doi: 10.1086/167599. URL <GotoISI>://WOS:A1989AD79900029.

[272] Steven Weinberg. A new light boson? *Phys. Rev. Lett.*, 40:223–226, Jan 1978. doi: 10.1103/PhysRevLett.40.223. URL https://link.aps.org/doi/10.1103/PhysRevLett.40.223.

[273] S. S. Wilks. The large-sample distribution of the likelihood ratio for testing composite hypotheses. *Ann. Math. Statist.*, 9(1):60–62, 03 1938. doi: 10.1214/aoms/1177732360. URL https://doi.org/10.1214/aoms/1177732360.

[274] C. A. Wilson-Hodge, G. L. Case, M. L. Cherry, J. Rodi, A. Camero-Arranz, P. Jenke, V. Chaplin, E. Beklen, M. Finger, N. Bhat, M. S. Briggs, V. Connaughton, J. Greiner, R. M. Kippen, C. A. Meegan, W. S. Paciesas, R. Preece, and A. von Kienlin. Three years of fermi gbm earth occultation monitoring: Observations of hard x-ray/soft gamma-ray sources. *Astrophysical Journal Supplement Series*, 201(2), 2012.

ISSN 0067-0049. doi: 10.1088/0067-0049/201/2/33. URL <GotoISI>://WOS: 000309555900026.

[275] M. Wood, R. Caputo, E. Charles, M. Di Mauro, J. Magill, and Jeremy Perkins for the Fermi-LAT Collaboration. Fermipy: An open-source Python package for analysis of Fermi-LAT Data. *ArXiv e-prints*, July 2017.

[276] E. M. H. Wu, C. Y. Hui, A. K. H. Kong, P. H. T. Tam, K. S. Cheng, and V. A. Dogiel. Chandra detection of a new diffuse x-ray component from the globular cluster 47 tucanae. *Astrophysical Journal Letters*, 788(2), 2014. ISSN 2041-8205. doi: 10.1088/2041-8205/788/2/l40. URL <GotoISI>://WOS:000338504500021.

[277] J. H. K. Wu, C. Y. Hui, E. M. H. Wu, A. K. H. Kong, R. H. H. Huang, P. H. T. Tam, J. Takata, and K. S. Cheng. Search for pulsed gamma-ray emission from globular cluster m28. *Astrophysical Journal Letters*, 765(2):4, 2013. ISSN 2041-8205. doi: 10.1088/2041-8205/765/2/l47. URL <GotoISI>://WOS:000315489100023.

[278] Y. Xing and Z. X. Wang. Fermi study of gamma-ray millisecond pulsars: The spectral shape and pulsed emission from j0614-3329 up to 60 gev. *Astrophysical Journal*, 831(2):8, 2016. ISSN 0004-637X. doi: 10.3847/0004-637x/831/2/143. URL <GotoISI>://WOS:000400474300007.

[279] D.G. Yakovlev and C.J. Pethick. Neutron star cooling. *Annual Review of Astronomy and Astrophysics*, 42(1):169–210, 2004.

[280] T. Yuasa, K. Nakazawa, and K. Makishima. The origin of an extended x-ray emission apparently associated with the globular cluster 47 tucanae. *Publications of the Astronomical Society of Japan*, 61(5):1107–1115, 2009. ISSN 0004-6264. doi: 10.1093/pasj/61.5.1107. URL <GotoISI>://WOS:000271364100018.

[281] A. Zajczyk, W. Bednarek, and B. Rudak. Numerical modelling of gamma-ray emission produced by electrons originating from the magnetospheres of millisecond pulsars in globular clusters. *Monthly Notices of the Royal Astronomical Society*, 432(4): 3462–3473, 2013. ISSN 0035-8711. doi: 10.1093/mnras/stt704. URL <GotoISI>: //WOS:000321053500069.

[282] S. Zane, R. Turolla, L. Nobili, and N. Rea. Modeling the broadband persistent emission of magnetars. *Advances in Space Research*, 47(8):1298–1304, 2011. ISSN 0273-1177. doi: 10.1016/j.asr.2010.08.003. URL <GotoISI>://WOS:000290136700003.

[283] P. F. Zhang, Y. L. Xin, L. Fu, J. N. Zhou, J. Z. Yan, Q. Z. Liu, and L. Zhang. Detection of gamma-ray emission from globular clusters m15, ngc 6397, 5904, 6218 and 6139 with fermi-lat. *Monthly Notices of the Royal Astronomical Society*, 459(1):99–107, 2016. ISSN 0035-8711. doi: 10.1093/mnras/stw567.

[284] J. N. Zhou, P. F. Zhang, X. Y. Huang, X. Li, Y. F. Liang, L. Fu, J. Z. Yan, and Q. Z. Liu. Gamma-ray emission from globular clusters 2ms-gc01, ic 1257, fsr 1735, ngc 5904 and 6656. *Monthly Notices of the Royal Astronomical Society*, 448(4):3215–3220, 2015. ISSN 0035-8711. doi: 10.1093/mnras/stv185. URL <GotoISI>://WOS:000351529500018.

[285] L. G. Zhu, J. L. Lu, and L. Wang. Effects of temperature on the structure of neutron stars at high temperature. *General Relativity and Gravitation*, 50(1):18, 2018. ISSN 0001-7701. doi: 10.1007/s10714-017-2327-3. URL <GotoISI>://WOS:000422697900007.